First biological validation of the efficacy of radioactive ion beams in high-precision image-guided tumour treatment of a murine model

at the Biology Faculty

of the Technische Universität Darmstadt

submitted in fulfilment of the requirements

for the degree of Doctor rerum naturalium

(Dr. rer. nat.)

Doctoral thesis

by Tamara Vitacchio

First assessor: Prof. Dr. Marco Durante

Second assessor: Prof. Dr. M. Cristina Cardoso

Darmstadt, 2026

Tamara Vitacchio, “First biological validation of the efficacy of radioactive ion beams in high-precision image-guided tumour treatment of a murine model”

Darmstadt, Technische Universität Darmstadt
Year thesis published in TUprints: 2026
Date of the viva voce: 9th of July, 2026

DOI: https://doi.org/10.26083/tuda-8235

URL: https://tuprints.ulb.tu-darmstadt.de/handle/tuda/15814

Ehrenwörtliche Erklärung

Stand: April 2026

Ich erkläre hiermit, dass ich die vorliegende Arbeit ohne unzulässige Hilfe Dritter angefertigt habe. Sämtliche aus fremden Quellen direkt oder indirekt übernommenen Gedanken sowie sämtliche von Anderen direkt oder indirekt übernommenen Daten, Techniken und Materialien sind als solche kenntlich gemacht.

Ferner erkläre ich, dass ich bei der Verfassung der Dissertation die "Grundsätze zur Sicherung guter wissenschaftlicher Praxis an der Technischen Universität Darmstadt" und die "Leitlinien zum Umgang mit digitalen Forschungsdaten an der TU Darmstadt" in den jeweils aktuellen Versionen beachtet habe. Die Arbeit wurde bisher bei keiner anderen Hochschule zu Prüfungszwecken eingereicht.

Darmstadt, 28/04/2026

Tamara Vitacchio

Zusammenfassung

Seit der Entdeckung der Röntgenstrahlen ist die Strahlentherapie als wirksame Behandlungsmethode für Krebspatienten bekannt. Die wissenschaftlichen Entdeckungen, die dazu geführt haben, dass sie zu einer der wichtigsten Behandlungsmethoden für diese Patienten geworden ist (etwa 50 %), umfassten mehrere Durchbrüche in der Kernphysik. Eine der wichtigsten Entdeckungen war die Verwendung geladener Teilchen: Im Gegensatz zu Photonen in der konventionellen Strahlentherapie neigen geladene Teilchen wie Protonen oder Kohlenstoffionen aufgrund des sogenannten Bragg-Peaks dazu, ihre Energie in einem sehr engen Bereich abzugeben. Diese vorteilhafte Dosisabgabe ermöglicht es, einen größeren Bereich des gesunden Gewebes um den Tumor herum zu schonen. Auch aufgrund einer höheren relativen biologischen Wirksamkeit im Vergleich zu Röntgenstrahlen wurde die Therapie mit geladenen Teilchen zu einer etablierten und wirksamen klinischen Praxis, mit der auch Probleme wie Strahlenresistenz und Tumorhypoxie behandelt werden können.

Eine große Herausforderung ist jedoch die Unsicherheit hinsichtlich der Reichweite der Dosisabgabe, die, die Vorteile des Bragg-Peaks zunichtemacht. Diese Unsicherheiten sind auf zwei Faktoren zurückzuführen: erstens auf anatomische Veränderungen im Körper des Patienten während der Behandlung, auf Veränderungen der Tumorgröße sowie auf Änderungen der Positionierung zwischen den einzelnen Bestrahlungssitzungen. Zweitens durch die Ungenauigkeit bei der Umrechnung der auf Röntgenwerten basierenden Hounsfield-Einheiten (HU) der Computertomographie (CT) in die wasseräquivalente Weglänge (WEPL) der Schwerionen. Die Reichweitenunsicherheiten führen zu einer zusätzlichen Dosisabgabe in das gesunde Gewebe, da um den Tumor herum beträchtliche Sicherheitsabstände hinzugefügt werden, um eine Unterdosierung der bösartigen Tumoren und ein Wiederauftreten der Erkrankung zu verhindern. Durch den Einsatz radioaktiver $ß^+$-emittierender Ionen (RIBs) in Verbindung mit der Positronen-Emissions-Tomographie (PET) könnten die Tumorsicherheitsabstände durch Echtzeit-Bildgebung reduziert werden, indem die Dosis gleichzeitig abgegeben und die Reichweite der Partikel zuverlässig überwacht wird, wodurch so viel gesundes Gewebe wie möglich geschont wird.

Im Rahmen der BARB-Versuchskampagne (Biomedizinische Anwendung radioaktiver Ionenstrahlen) an der GSI haben wir die erste Behandlung eines Tumors bei Mäusen mit radioaktiven Ionenstrahlen ($ß^+$-emittierende ^{11}C-Ionen) in Verbindung mit einer Online-Bildgebung durchgeführt. Es wurde ein spezifisches Mausmodell unter Verwendung von C3H/HeNRj-Mäusen entwickelt, die ein syngenes LM8-Osteosarkom oberhalb des zervikalen Rückenmarks aufweisen. Dieses Modell wurde zunächst mit Röntgenstrahlen getestet, um die zu erwartenden Gesundheitsergebnisse zu ermitteln, und anschließend mit ^{11}C-Ionen. Angesichts der Nähe des Tumors zum Rückenmark und zur Speiseröhre kann eine Abweichung von wenigen Millimetern von der geplanten Behandlung zu schweren Toxizitäten wie strahleninduzierter Myelopathie oder Speiseröhrenschäden führen.

Im Verlauf von zwei Experimenten konnte die Machbarkeit der Bildgebung der vom ^{11}C-Primärstrahl abgeleiteten $ß^+$-Aktivität nachgewiesen werden, die zur Anpassung der Dosisverteilung verwendet wurde, um das Tumorgewebe präzise abzudecken und die Tumore mit einer Dosis von 20 Gy zu behandeln, ohne schwere Nebenwirkungen bei den Tieren zu verursachen. Darüber hinaus ermöglichten die Online-Aktivitätskarten die

Gewinnung von Daten über das biologische Auswaschen der Aktivität in Echtzeit, wodurch die Rolle von Ischämie-Reperfusionsschäden in der Strahlentherapie untersucht werden konnte. Die gewonnenen Daten deuteten auf eine mögliche Komponente von Gefäßschäden hin, wenn die Dosis von 20 Gy verwendet wurde, im Vergleich zu einer niedrigeren Dosis von 5 Gy, bei der keine Gefäßschäden beobachtet wurden.

Es war auch möglich, eine Demonstration zu erhalten, wie RIBs in einer adaptiven Therapieumgebung eingesetzt werden können, in der der Behandlungsplan angepasst werden muss, um Veränderungen in der Anatomie des Patienten und der Tumorposition Rechnung zu tragen. Durch die Echtzeit-Überprüfung der Strahlenreichweite im Körper der Tiere mit einem ^{11}C- Strahl konnte der Bereich, in dem die Dosis während der Behandlung abgegeben wurde, genau bestimmt werden. Diese Präzision wurde mit einem „Goldilocks"-Experiment getestet, bei dem zwei unerwünschte Ergebnisse (unkontrolliertes Tumorwachstum und Toxizität für normales Gewebe) und das positive Ergebnis, nämlich die Behandlung des Tumors unter Schonung des gesunden Gewebes, möglich waren. Wenn die bestrahlten Tumore nur teilweise vom Bestrahlungsfeld abgedeckt waren, was einen Fall von Unterdosierung simulierte, führte dies zu einem Tumorrezidiv, während es zu Komplikationen im normalen Gewebe kam, wenn das Feld zu tief in den Körper der Tiere eindrang, indem es den Tumor durchquerte und das Rückenmark und die Speiseröhre erreichte. Das perfekte Ergebnis wäre die vollständige Beseitigung des Tumors ohne Nebenwirkungen auf gesundes Gewebe, und dieses Ergebnis wurde während dieser Versuchsserie zum ersten Mal erzielt. Diese Ergebnisse unterstreichen die wichtige Rolle radioaktiver Ionenstrahlen in der Teilchentherapie und ebnen den Weg für zukünftige klinische Anwendungen.

Das Experiment wurde durch den ERC Advanced Grant 883425 an Prof. M. Durante unterstützt und umfasste den Einsatz des SIRMIO-PET-Detektors der Gruppe von Prof. K. Parodi, Ludwig-Maximilians-Universität, München.

Abstract

Radiotherapy has been known to be an effective way to treat cancer-burdened patients since the discovery of X-rays. The scientific discoveries that led it to become one of the main ways to treat these patients (approximately 50%) involved several breakthroughs in nuclear physics. One of these main discoveries was the use of charged particles: unlike the photons, in conventional radiotherapy, charged particles like protons or carbon ions tend to deposit their energy in a very narrow area, thanks to the so-called Bragg Peak. This advantageous dose deposition permits to spare a larger area of the healthy tissue surrounding the tumour. Owing also to a higher relative biological effectiveness when compared to X-rays, charged particle therapy became a well-established and effective clinical practice, capable of targeting also issues like radioresistance and tumour hypoxia.

On the other hand, a major drawback is the range uncertainty in dose delivery, which jeopardizes the advantages of the sharp Bragg peak. These uncertainties can be attributed to two factors: firstly, anatomical changes in the body of the patient during treatment, changes in tumour size, and changes in positioning between individual radiotherapy sessions. Secondly, by the inaccuracy in the conversion of the Computed Tomography (CT) Hounsfield units (HU), which are based on X-rays values, into the water-equivalent path length (WEPL) of the heavy ions. The range uncertainties lead to additional dose delivery in the healthy tissues, because considerable margins are added around the tumour to prevent underdosage of the malignancy and disease recurrence. By using radioactive ß+-emitting ions (RIBs) coupled with Positron Emission Tomography (PET) imaging, the tumour margins could be reduced with real-time imaging by simultaneously delivering the dose and reliably monitoring the range of the particles, sparing as much healthy tissue as possible.

In the context of the Biomedical Application of Radioactive Ion Beams (BARB) experimental campaign held at GSI, we performed the first treatment of a murine tumour using radioactive ion beams (ß+-emitting ^{11}C ions) coupled with online image-guidance. A specific murine model was developed using C3H/HeNRj mice bearing a syngeneic LM8 osteosarcoma above the cervical spinal cord, which was tested first with X-rays to benchmark the expected health outcomes, then with ^{11}C ions. Given the proximity of the tumour to the spinal cord and the oesophagus, a few millimetres of deviation from the planned treatment can result in severe toxicities, like radiation-induced myelopathy or oesophageal damage.

During the course of two experiments, it was possible to demonstrate the feasibility of imaging the ß+ activity derived from the ^{11}C primary beam, utilising it to adjust the dose distribution to precisely cover the tumour tissue and to treat the tumours with a dose of 20 Gy without causing severe side effects in the animals. Furthermore, the online activity maps permitted to obtain data about the biological washout of the activity in real-time, exploring the role of ischaemia-reperfusion damage in radiotherapy. The obtained data hinted at a possible component of vascular damage when the dose of 20 Gy was used, with comparison with a lower dose of 5 Gy where no vascular damage has been observed.

It was also possible to obtain a demonstration of how RIBs can be used in an adaptive therapy setting, where the treatment plan requires adaptation to account for changes in patient anatomy and tumour position. By testing the beam range in the body of the animals

in real-time, with a probe beam of ^{11}C, it was possible to accurately determine the area where the dose would be deposited during treatment. This precision was tested with a "Goldilocks" type of experiment, with two undesirable outcomes (uncontrolled tumour growth and normal tissue toxicity) and the positive outcome, tumour treatment and healthy tissue sparing. When the irradiated tumours were only partially covered by the irradiation field, mimicking a case of underdosage, this led to tumour recurrence, while if the field entered too deep in the body of the animals by traversing the tumour and reaching the spinal cord and oesophagus, normal tissues complications arose. The perfect outcome would be tumour eradication and absence of healthy tissues side effects, and it was obtained for the first time during this experimental campaign. These findings mark the important role of radioactive ion beams in charged particle therapy and pave the way for future clinical applications.

The experiment was supported by the ERC Advanced Grant 883425 to Prof. M. Durante and involved the use of the SIRMIO PET detector from Prof. K. Parodi's group, Ludwig-Maximilians Universität, Münich.

Contents

List of Figures

List of Tables

List of Abbreviations

ALARA	As Low As Reasonably Achievable
ART	Adaptive Radiotherapy
BARB	Biomedical Application of Radioactive Ion Beams
BER	Base Excision Repair
CAs	Chromosomal Aberrations
CBCT	Cone Beam Computed Tomography
CIRT	Carbon Ions Radiotherapy
CNS	Central Nervous System
CPT	Charged Particle Therapy
CSA	Colony Survival Assay
CT	Computed Tomography
CTRL	Control
CTV	Clinical Target Volume
DNA	Deoxyribonucleic Acid
DSB	Double Strand Breaks
EDTA	Ethylenediaminetetraacetic Acid
EoEHSS	Eosinophilic Esophagitis histologic scoring system
EtOH	Ethanol
FAIR	Facility for Antiproton and Ion Research
FDG	Fluorodeoxyglucose
FRS	Fragment Separator
FSU	Functional Sub-Units
GSI	Helmholtz Centre for Heavy Ion Research
GTV	Gross Tumour Volume
GV-SOLAS	Gesellschaft für Versuchstierkunde
HRR	Homologous Recombination Repair
HE	Haematoxylin-Eosin staining
HU	Hounsfield Units

ICRP	International Commission on Radiological Protection
IHC	Immunohistochemistry
LET	Linear Energy Transfer
LQ	Linear-Quadratic model
LR	Long Range
MC	Monte Carlo Simulation Method
MLEM	Maximum Likelihood Expectation Maximization model
NER	Nucleotide Excision Repair
NHEJ	Non-Homologous End-Joining
NTCP	Normal Tissue Complication Probability
OAR	Organ At Risk
OER	Oxygen Enhancement Ratio
OCT	Optimal Cutting Temperature Compound
PBS	Phosphate Buffer Saline solution
PET	Positron Emission Tomography
PrAnCER	Paw Print analysis of Contrast-Enhanced Recordings
PTV	Planned Target Volume
RIBs	Radioactive Ion Beams
RNS	Reactive Nitrogen Species
ROS	Reactive Oxygen Species
RR	Right Range
RT	Radiotherapy
RTOG	Radiation Therapy Oncology Group
SARRP	Small Animal Radiation Therapy Platform
SDRT	Single-Dose Radiotherapy
SIRMIO	Small animal proton Irradiator for Research in Molecular Image-guided Radiation-oncology
SOBP	Spread-Out Bragg Peak
SR	Short Range
SSB	Single Strand Breaks
TCP	Tumour Control Probability

"I am life that wants to live, in the midst of life that wants to live."

- Albert Schweitzer -

This thesis is dedicated to all the animals that gave their lives in this study, without whom all the experiments would have not been possible.

With respect,

Tamara

1 Introduction

From the discoveries of X-rays and radioactivity, respectively in 1895 and 1898, a large amount of knowledge about the effect of ionizing radiation on biological beings has been uncovered. In particular, the fact that this kind of radiation can kill living cells opened the door to the possibility of treating cancer and relieving the life of affected patients. On the other side, however, radiation researchers and people exposed to radiations because of their jobs started to show how the prolonged exposure was actually causing them to develop diseases, like cancer itself. It became clear that the ionizing radiations could be of great use to healthcare, but also a major threat to avoid as much as possible. This duplicity sparked to study of radiation effects on human health, creating a new research field: radiobiology[1].

1.1 Radiobiology

Radiobiology studies the interaction of ionizing radiation with biological matter, and specifically how this interaction leads to damage. The radiation causes damage in a direct or indirect fashion[2]: in the first case, the targets are molecules such as DNA and proteins, while in the latter the radiation is interacting with the water molecules present in the cells, causing radiolysis. This reaction generates reactive oxygen species (ROS), which are highly reactive and high-energy molecules that can target the cell´s structures, especially when coupled with the reactive nitrogen species (RNS). The direct effects are produced by both high and low linear energy transfer (LET) radiation, but radiation with high LET, like alpha particles, neutrons and heavy ions such as carbon or oxygen, are the main cause of the direct damage. The indirect effects, instead, contribute to about two-thirds of the damage produced by low LET radiation, such as X-rays, gamma-rays, and beta particles. The LET is defined as the average energy locally imparted to a medium by a charged particle of specified energy in traversing a distance (in units of $keV/\mu m$), and as the particles travels through the medium they slow down, while the LET increases[1].

Radiation damage goes through different time stages as it happens[2], as represented in Figure 1. The first is the physical stage, which lasts less than 10^{-16}–10^{-15} s and it´s when the energy is transferred to the electrons of the targets, resulting in ionization and/or excitation and the subsequent formation of ions. The following stage is the physicochemical (10^{-12} s), when the ions diffuse in the medium and form radical species. Afterwards, in the chemical stage (10^{-6} s), the formed radicals and ions recombine and interact with the cellular molecules, causing changes to their structures and impairing their functions. At the end, the biological stage is a consequence of the diffusion of the chemical reactions happening in the cell and may last seconds to decades. At this stage, the cell´s repair mechanisms are activated as a response to the damage, but they differ in the repair effectiveness and are also dependent on the type of radiation, dose and dose rate, the type of damage resulting and the radiosensitivity of the irradiated tissue[1], which can greatly vary between different ones.

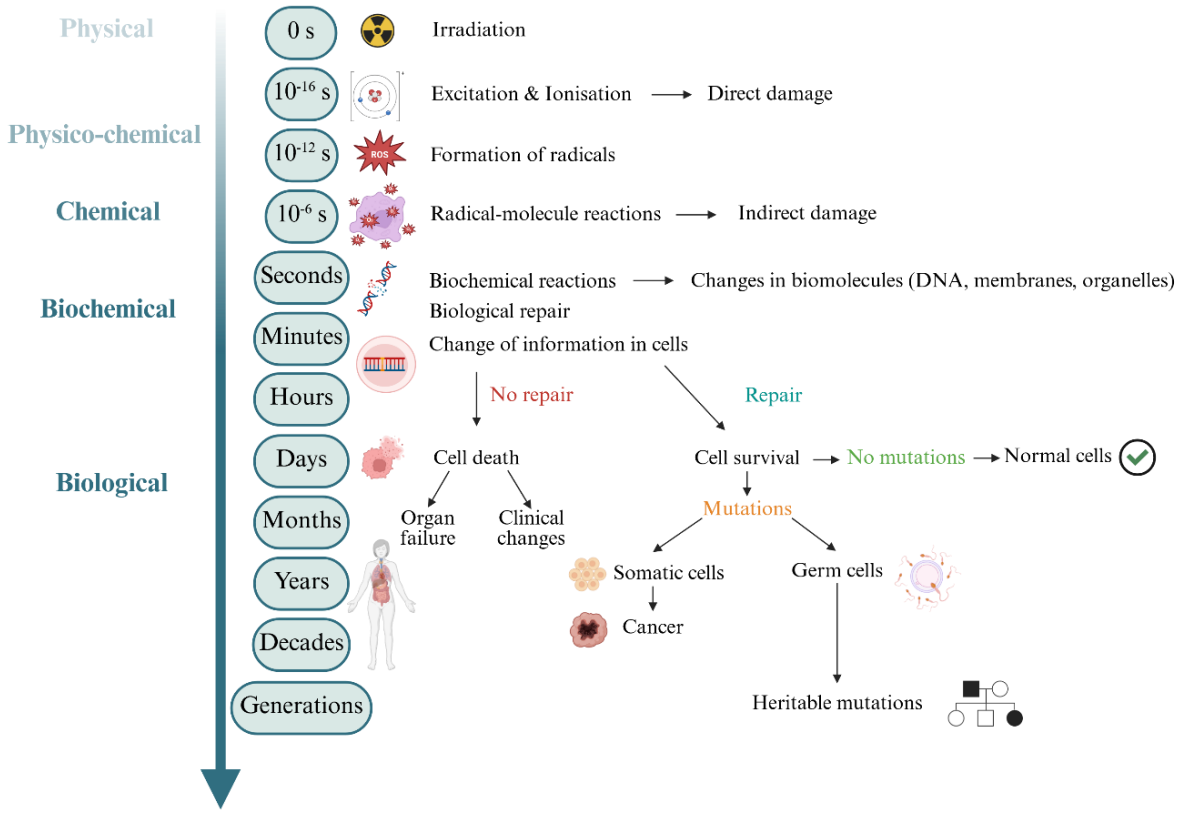

Figure 1. Timeline of radiation effects. Created with BioRender.

1.1.1 Dose, dose rates and equivalent dose

Different units are used in radiobiology and radiation protection. The dose (or absorbed dose) is the mean energy (E) imparted by ionizing radiation to a material of a certain mass (m):

$$Dose = \frac{dE}{dm}$$

The SI unit of the dose is measured in *Gray* (Gy), and is defined as the absorbed energy per unit of mass of a tissue, given by one J per kg. The dose rate, instead, is defined as the dose of ionizing radiation absorbed or delivered per unit time, and is measured in *Gray per hour*. The dose rate effect explains the biological effect a certain dose has on biological matter: if the exposure time to a given dose is extended, and if the dose rate is lowered, its biological effect is reduced because the biological system has time to repair sub-lethal damage that occurs in the case of long radiation exposure. On the contrary, when the dose rate lowers and an increased biological effects occurs, this is defined as inverse dose rate effect[1]. The second "dose" definition is the equivalent dose, used to describe the different effects caused by different types of radiation, and how these may harm a biological tissue. This is because, even if the same amount of dose is absorbed, the density of the ionization events and the pattern of dose distribution are different between different radiation qualities. Hence, the equivalent dose is defined as[1]:

$$H_T = w_R D_T$$

Where D_T is the absorbed dose, and w_R is the radiation weighting factor, which is dependent on the type and energy of radiation involved. Still expressed in J per kg, the unit for the equivalent dose is the *Sievert* (Sv). Lastly, the effective dose is the addiction of equivalent doses to all organs, and is defined as the equivalent dose in a tissue or organ (T) multiplied by the tissue weighting factor (w_T). It represents the relative contribution of each tissue or organ to the total effect resulting from uniform irradiation of the whole body[3]:

$$E = \Sigma w_T H_T$$

For both the radiation and the tissue weighting factors, the ICRP (International Commission on Radiological Protection) published reference tables regarding their values[4].

1.1.2 DNA damage and repair

When radiation is directly hitting the molecules present in the cell their structures may be altered, which leads to their impairment. The DNA molecule, contrary of the others cell´s structures (mitochondria, Golgi apparatus etc.), is present in a single copy, and since it carries most of the information about the biological processes, when damaged it might lead the cell to die, or mutate and become cancerogenic[1]. The structure of the DNA is composed by two polynucleotide chains that coil around each other to form a double helical structure, created by the hydrogen bonds between two pyrimidine-purine bases coupling across two opposite strands. On one strand, instead, nucleotides are joined to one another by covalent bonds between the sugar (deoxyribose) of one nucleotide and the phosphate group of the next one. From this structural organization, it comes that the damage to the DNA can occur in one strand or both: these are defined as Single Strand Breaks (SSB) and Double Strand Breaks (DSB). In the first case, the biological consequence of the damage is usually very little, since the cells possess repair mechanisms that use the opposite strand as a template to repair the broken strand. Sometimes the damage is mis-repaired, which might result in a mutation. In the second case, instead, the damage occurs in both the strands in the same area, or just a few bases of difference. In this case, the breakage might lead to the separation of chromatin in two pieces, creating a type of damage that is more difficult to repair. Some examples of different DNA repair mechanisms are: Base Excision Repair (BER), Nucleotide Excision Repair (NER), DNA Double-Strand Break Repair, that is divided in Homologous Recombination Repair (HRR, occurs in S and G_2 phase of the cell cycle) and Non-Homologous End-Joining (NHEJ, occurs in the G_1 phase)[2]. Mutations in genes associated with DSB repair, like BRCA-1 and BRCA-2, increase the risk for developing breast cancers and other neoplasias[5].

The damage to the DNA can also consist in base damage due to indirect effects (see paragraph 1.1), caused by the formation of ROS that generate apurinic/apyrimidinic (abasic) sites in the DNA, sugar modification and deaminated bases. If the damages following radiation are repaired the cell might become radioresistant[6] and will continue to survive and replicate, otherwise the repair mechanisms will induce apoptosis (controlled cell death, cells visibly shrink and have condensed chromatin with nuclear margination and DNA fragmentation, plus blebbing of cell membrane) to avoid the accumulation of mutations in the daughter cells[5]. Other types of cell death are mitotic catastrophe, necrosis, autophagy and cell senescence, which consists in the loss of replicative capability of the cell. Mitotic catastrophe typically occurs after or during mitosis and is probably caused by mis-segregation of chromosomes and/or cell fusion, with cells showing an enlarged size with the presence of multiple nuclei. Necrosis, instead, shows early breakdown of the cell

membrane, atypical nuclear shape and non-condensed chromatin, with disintegrated cellular organelles. Autophagy, on the other hand, is a genetically regulated form of programmed cell death in which the cell digests itself and is characterised by the formation of double-membrane vacuoles in the cytoplasm[7]. An important reason for cell death are chromosomal aberrations (CAs): these happen following an unrepaired or misrepaired DSB, which causes the chromosome to undergo deletions, inversions, insertions, substitutions, duplications or translocations. There are various types of aberrations, based on how the chromatids (S-G_2 phase exposure) or chromosomes (G_0-G_1 exposure) are rejoined[8]: they can be classified in intrachanges and interchanges, symmetrical or asymmetrical, simple or complex type. The complexity of the aberration depends also on the number of break sites, and the frequency of radiation-induced CAs rises with increasing radiation dose to the cells[1].

1.1.3 Radiobiology of X-rays and heavy ions

DNA lesions can be both direct and indirect, and the relevance of the damage is dependent on the radiation type. Different kinds of radiation are characterised by different physical properties and effects on the biological sample that receive them. Between these, the LET is influenced by both particle species and energy, it accounts for the density of energy transfer occurring along the track of charged particles and it determines DNA damage quality and quantity[9]. The important radiobiological advantage of the heavy ions is that their LET is higher (densely ionizing radiation) than the one of X-rays (sparsely ionizing radiation), which means higher direct damage to the DNA[10]. The so-called track structures of heavy ions are peculiar, because they are characterised by a high level of energy deposition clustering[11], as it can be seen in Figure 2. The optimal LET value for cell killing is around 100 keV/µm, because the average separation of ionization events at this LET is about the same as the diameter of the DNA´s structure (2 nm)[1]. This means that a relevant fraction of the DNA can be damaged and the damage is usually complex, *e. g.* DSBs, which are more difficult for the cell to repair[11].

Another important concept is the energy loss of the particle traversing a medium, *e. g.* water or a patient´s body, because while doing so, it ionizes the atoms of the encountered material by depositing a dose along its path, therefore losing energy. For low LET radiation, like photons and electrons, the highest amount of energy is released closer to the entrance point of the medium (*e. g.* the skin), and then it slowly decreases, as it can be seen in Figure 3. In the case of protons and heavy ions, instead, the deposited dose increases with the depth and the curve assumes the shape of a sharp peak, the so-called Bragg Peak[1]. The sharpness implies that the energy is discharged quickly and in a short tract of the beam pathway, delivering a high amount of it. The higher the primary energy of the beam, the deeper it can penetrate the medium. In the treatment of deep-seated malignancies with a given volume, a series of peaks with variable energies are combined to cover the entire volume, creating a Spread-Out Bragg Peak (SOBP). In this region, were the dose distribution is highly favourable, the Relative Biological Effectiveness (RBE) is also increased[12].

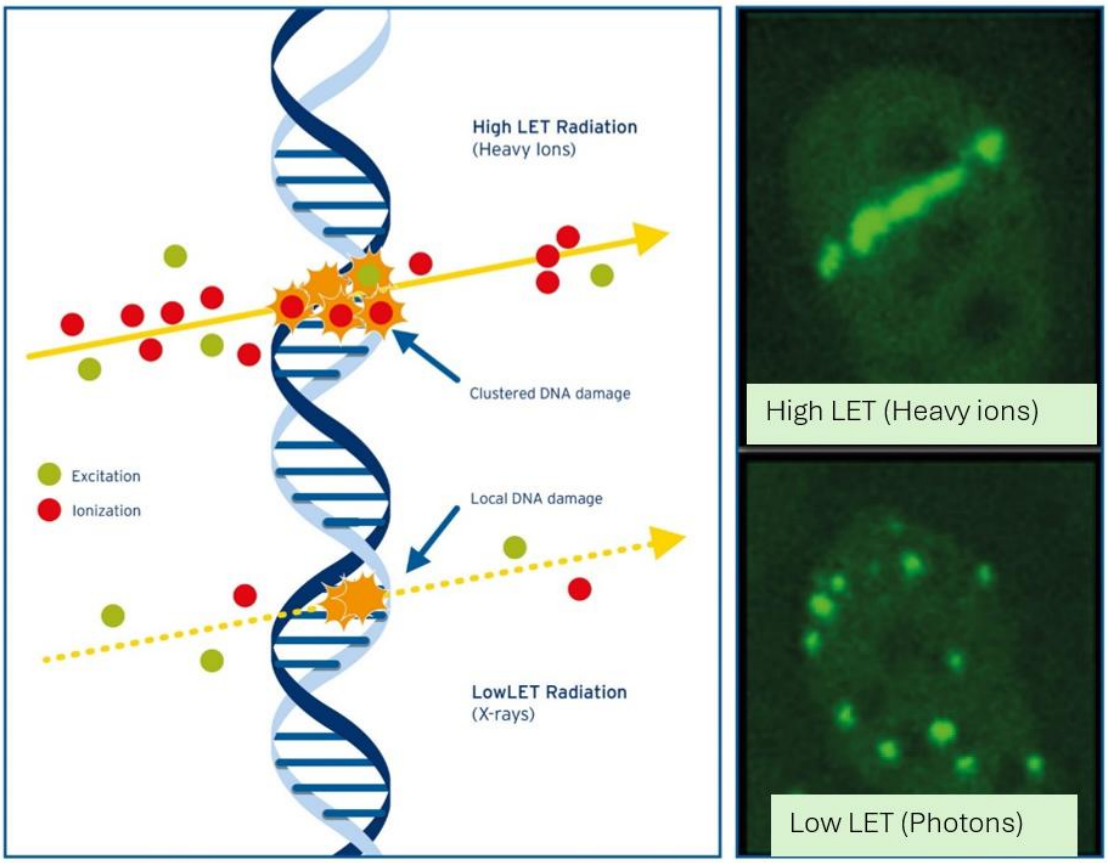

Figure 2. Representative picture of the different damage produced by high LET and low LET radiation. Iron ions and photons hitting a cells' nucleus (top and bottom panels) respectively (adapted from Jakob *et al.*[13,14]) shown with immunofluorescence. The cell nucleus is highlighted in dark green, with the areas where the DNA is bind by the repair complexes is shown in brighter green, showing the differences between an ion traversing a cell nuclei (continuous track, clustered DNA damage) and the sparsely arranged local DNA damage repair points caused by X-rays.

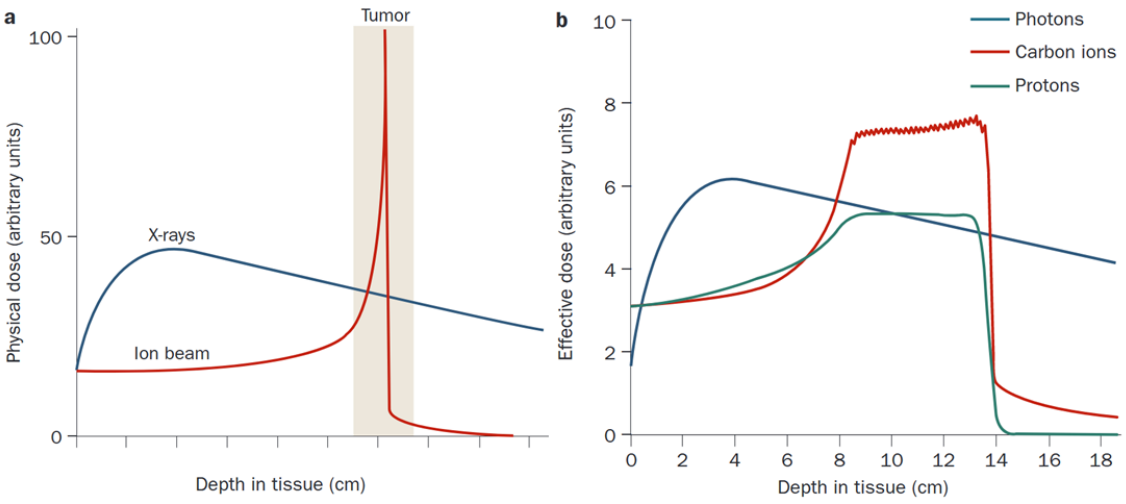

Figure 3. A) Charged particles show an advantageous radiation dose-tissue depth profile compared to photons. B) When the tumour to treat has a large volume, the SOBP aims to deliver the same biologically effective dose to all the volume. From Durante and Loeffler[15]. The X-axis in A is the same as B.

1.1.4 Relative Biological Effectiveness (RBE)

The relative biological effectiveness is a concept used to quantify and compare the biological damage of different types of radiation. The RBE is a dimensionless quantity, and is defined as the ratio between the absorbed dose of a reference radiation (typically X-rays) to an absorbed dose of the test radiation needed for an iso-effect in a given biological system. The RBE is required to define the effective dose and varies with the LET and radiation quality, dose, dose rate, fractionation regimes, the biological system in study and the endpoint taken into account. The induced biological effects depend on the LET, and a great proof of this phenomenon is the Colony Survival Assay (CSA) in Figure 4.

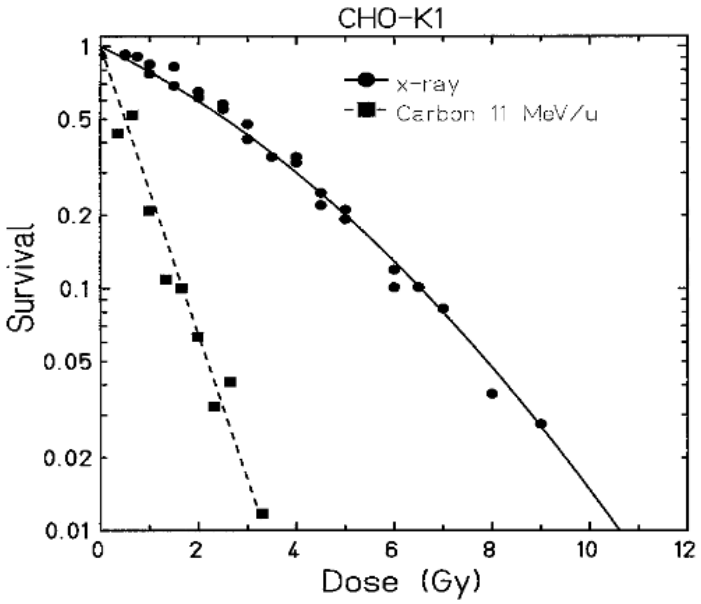

Figure 4. Survival of Chinese Hamster Ovary (CHO) cells as a function of dose measured for X-rays and 11 MeV/u carbon ions from Weyrather *et al.*[16].

This test is used to determine the radiosensitivity of a cell line to different types of radiation and its survival capability, and is extremely important in radiotherapy. A variety of experimental and clinical data have been validating the Linear-Quadratic model (LQ), which describes the surviving fraction (SF) of clonogenic or stem cells as a function of radiation dose (D):

$$SF\ (D) = e^{-\alpha \cdot D - \beta \cdot D\hat{}2}$$

α and β determine, respectively, the linear and quadratic component of cellular damage. The α/β ratio represents the intrinsic radiosensitivity of cells: the higher the α and β, the higher the radiosensitivity. The LET determines the shape of the curves, and cells irradiated with the same dose but different LET (which induces different biological effects) show different survival, derived from the capacity of the cells to repair different damages. As a general rule, the more the LET increases, the steeper the curves become, meaning a higher α/β ratio[17].

1.1.5 Deterministic and stochastic effects

The effect of radiation on human's health can happen in two different ways. In the case of the deterministic effects, these are characterized by a threshold, below which no damage is detected and above which the damage increases in relation with the dose. These effects are

mainly caused by the direct cell killing caused by radiation. On the other hand, the stochastic effects are characterised by the probability of the effect manifestation increasing with the dose, but their severity is independent of the dose received and are mostly relying on the mutations happening in the cells that survive the irradiation and their progeny. An example of deterministic effect is the acute radiation syndrome, which occurs immediately after irradiation with high doses and damages to the tissues. For the stochastic effects, instead, an example is the risk to develop cancer[1].

1.2 Radiotherapy

Between all the applications of radiation research in the medical field, there are a plethora of possibilities to diagnose and treat human and veterinarian diseases by radiation based devices and protocols[1]. Radiation therapy is defined as the use of high-energy radiation from X-rays, gamma rays, neutrons, protons, or heavy ions to kill cancer cells and shrink tumours. Radiation may come from a machine outside the body (external-beam radiation therapy), or from radioactive material placed in the body near the cancer mass (internal radiation therapy or brachytherapy). The ideal scenario would be to deliver the highest possible dose to a malignancy to eradicate it permanently, but to completely spare the normal tissues that surround it, especially in the case of radiosensitive ones.

Nowadays, approximately 50% of cancer patients are treated with either radiotherapy alone, or a combination of radiotherapy, surgery and/or chemotherapy[18,19]. When a tumour is diagnosed, a proper clinical treatment has to be planned to maximize the dose it receives[20]. Despite the advances in modern precision radiotherapy (RT), it is basically impossible to completely avoid some dose deposition in the healthy tissue. The goal is to minimize it as much as possible, balancing the therapeutic effectiveness with the normal tissues adverse effects[1]. The tumour might be extending over what is seen with the common imaging techniques; what is called Gross Tumour Volume (GTV) is extended in the clinical practice, to ensure coverage at the microscopical level of the tumour's microenvironment and disease spread: this is defined as the Clinical Tumour Volume (CTV). To guarantee tumour coverage and allow for uncertainties in planning and treatment delivery, further margins are added to create the Planning Target Volume (PTV), which extend in the healthy tissue[21].

The dose selected for the treatment is actually determined by the tolerance dose of the normal tissues or the organs at risk; unlike tumour cells, healthy cells have a fully functional DNA damage repair machinery. Here lies the main difference in the tissues' response to radiation, and this is where the therapeutic window concept arises. This concept shows the difference between Tumour Control Probability (TCP) and Normal Tissue Complication Probability (NTCP)[22]. The aim of radiotherapy is to widen the window (therapeutic index, see Figure 5), delivering enough dose to kill the tumour cells while avoiding severe side effects in the normal tissue.

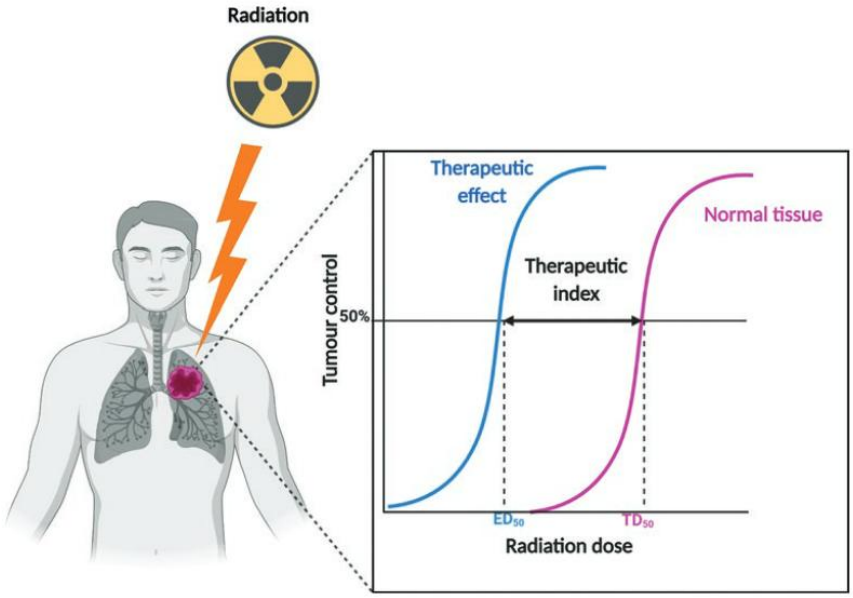

Figure 5. Therapeutic window concept based on the differences between tumour control probability (TCP) and normal tissue complication probability (NTCP) as functions of radiation dose, described with sigmoid curves, from Baatout *et al.*[1].

The therapeutic ratio, or therapeutic index, is the efficacy/toxicity ratio, and represents how a treatment planning is made using a certain quantity of radiation for the purpose of treating the disease without complications[1]. To create a treatment plan, first a computed tomography (CT) scan of the malignancy and the surrounding anatomy is acquired, to be used as the base for treatment planning and treatment delivery. Although geometrically robust, the CT images can´t describe the motion of the organs inside the patient´s body, like the respiratory or cardiac cycles. Those create uncertainties in the anatomy[20], which are a very important factor for treatment planning and are further discussed in paragraph 1.3. A typical photon radiotherapy treatment plan is delivered on a linear accelerator, which uses high-powered X-rays focused by collimators that shape the radiation beam. Beam parameters like the energy, intensity, number of beams and dose parameters like the location of areas of high and low dose level need to be carefully adapted to avoid under-coverage of the target. The radiation oncologist creates and reviews the plan working in collaboration with a radiation physicist, which ensures the plan meets hospital relevant criteria via quality assurance tools (plan complexity, robustness and dose distribution analysis including dose-volume control)[1]. Another important parameter is the number of fractions to deliver for a full treatment. Fractionation is the delivery of small doses (usually 2 Gy) daily over different days, to let the normal tissue repair the DNA damages while the tumour cells are eradicated[23]. This also causes the reoxygenation of the external layers of the tumour mass, which has important implications for the treatment of hypoxic tumours[24] (see 1.2.2.).

Nowadays, the treatment planning technology is increasingly incorporating the Monte Carlo simulation method (MC), a numerical calculation used to estimate how particles interact in a medium, and consequently the dose deposited, through simulations of the stochastic events through which radiation deposits energy[1].

1.2.1 From the 4Rs of radiobiology, to the 6Rs and beyond: tumour cells

Cancer is a complex, multifaceted and multifactorial disease, where tumour development proceeds via a process analogous to the one characterising Darwinian evolution[25], namely the differential survival based on advantageous genetic changes in a certain cell or subpopulation of cells. The changing cell takes advantage of the newly found characteristics by starting to act against the self (the rest of the human body) and behaving not as part of a consortium, but as a solitary individual acting on its own survival interest. There are numerous evidences that show how tumorigenesis is a multistep process, involving different genetic mutations in key genes like those that control cell division, replication, and resistance to apoptosis. Cancer cells have to acquire certain capabilities in order to survive, proliferate and remain hidden from the immune system, and this is given by their characteristic genomic instability, the proneness to have mutations happening in the genome. These capabilities are defined as the "hallmarks of cancer"[25] and in the latest ampliation of the theory[26] they are described as follows. Tumour cells have resistance to cell death, being capable of escaping pathways as apoptosis, necrosis etcetera. They support their proliferation by inducing angiogenesis, creating new vessels to receive nutrients from the bloodstream[27]. These new vessels are not well formed and functional, though, which often leads to formation of hypoxia in the tumour mass not perfused by them[28]. Hypoxia is an important factor in radiobiology, since it can influence the cells' radioresistance[1]; this concept is discussed in detail in the paragraph 1.2.2. The proliferation itself is sustained by a very active proliferation signalling, combined with the evasion from the growth suppressors and a deregulation of cellular energetics to support their very fast growth[29]. Avoiding immune destruction by masking themselves as normal cells, they manage to extravasate from the tumour's location and travel through the bloodstream and landing in other organs, where, if a suitable niche is found, they can invade the tissues and form metastases[30].

From these evidences, a very important concept emerges: if a tumour is treated, but one or a few of the cells are resistant to the treatment or are not covered by a radiation field, there might be survivors that will proliferate again[31]. Hence, the necessity to deposit a very high dose in the treatment area to create as much DNA damage as possible, but also the need to ensure that the tumour is completely covered by the radiotherapy treatment field, to avoid missing malignant cells.

To fully understand how the process of sterilizing cancer cells works, the first theory of the 4Rs was proposed[32]. The 4Rs stands for ´Repair´ of the sublethal DNA damage in healthy and tumour cells, ´Reoxygenation´ which transforms initially resistant hypoxic regions into a more radiosensitive state[33], ´Redistribution´ of the cells in the cell cycle, and ´Repopulation´ due to the proliferation of the remaining cells in the niche left empty from the dead cells. Lately, the theory was expanded to the 6Rs in these works[26,34] (Figure 6) and the added Rs were ´Radiosensitivity´, which explains how different cells might be more or less radioresistant based on their own different cell-specific mechanisms (*e. g.* metabolic adaptations, ROS detoxification), and ´Reactivation´ of the immune system, where after the radiation treatment the immune system is capable of recognising again the cancer cells and attack them. In the last update of the theory, the 7R added is ´Reinforcement´[35], where the complex interactions between the cancer cells and the surrounding tumours microenvironment can reinforce the cancer cells radioresistance.

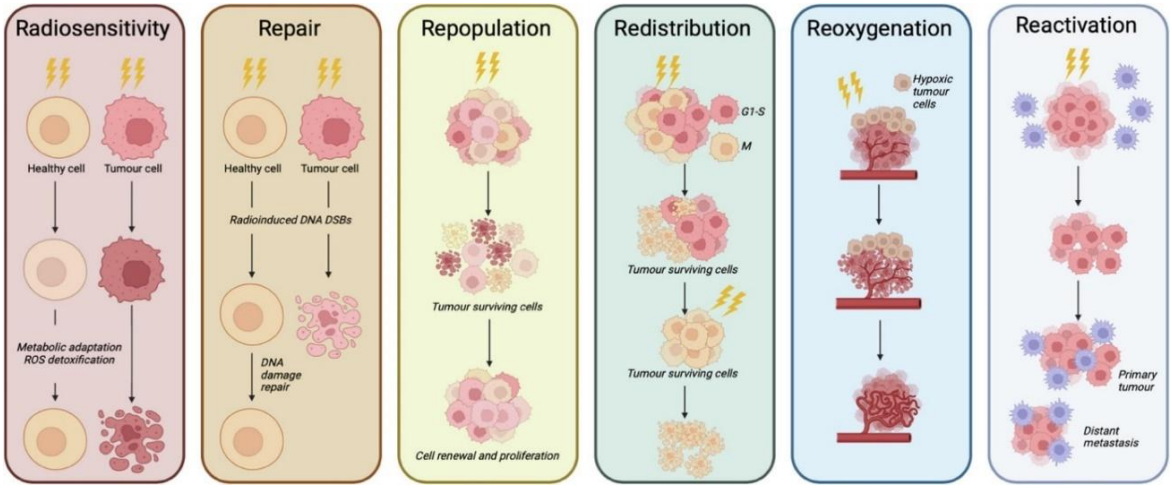

Figure 6. 6Rs of Radiobiology. The response to radiotherapy is based on six major responses of the cells to radiation, and every different cell-line manifests different sensitivity to radiation based on these factors (from Ripoll-Viladomiu *et al.*[33]).

1.2.2 Tumour hypoxia and radioresistance

In radiation therapy, the oxygenation of a tissue is an important parameter that modifies its biological responses. Hypoxia is a condition where the oxygen concentration is low: normally in the majority of the human body the oxygen concentration is between 5-7%, and the tissues considered to be hypoxic are below 3%[36]. The oxygen concentration in a tissue can diffuse as far as 150 µm from the arterial end of the capillaries, so in the areas further away the tissue undergoes chronic (diffusion-limited) hypoxia, caused by the limitations in oxygen diffusion[37]. Acute (perfusion-limited) hypoxia, instead, relates to a temporary disturbance in the normal tissue perfusion and can be reverted by regaining the blood flow[38]. The vessels nourishing a tumour are usually growing in a chaotic and leaky fashion, caused by the incapability of the tumour to balance between pro- and antiangiogenic signals. Hence, there are usually hypoxic areas within its volume[24].

It was demonstrated already in the 1950s that tissues with a higher oxygenation, compared to hypoxic ones, are more radiosensitive[24]. In the clinical setting, hypoxia in solid tumours correlates with poor prognosis in patients[37], making it a field of interest for finding new and more effective ways to eradicate tumours which are resistant to both chemotherapy and radiotherapy[39]. The oxygen fixation hypothesis postulates that the majority of the radiation-induced DNA damage caused by radicals can be repaired, but it becomes more difficult or even impossible to repair when the damage is caused by the product of a radical and an oxygen molecule[24]. In radiotherapy, the Oxygen Enhancement Ratio (OER) describes hypoxia-induced radioresistance (Figure 7). The OER is defined as the influence of the oxygen effect, namely the ratio between the dose that produces a given biological response under hypoxic conditions, and the dose that produces the same response under aerobic conditions[1]. It varies with the LET, having usually a value > 1 for low LET radiation like photons, and decreasing as the LET increases, dropping to almost 1 over a few hundreds of keV/µm[39]. This is because high LET radiation mostly induces direct damage, which is less sensitive to the presence of molecular oxygen, while there are also lesions that are more difficult to repair (*e. g.* DSBs)[1] and an increased production of molecular oxygen, which can react with the DNA and create further damage (oxygen in track hypothesis)[39].

Given these characteristics, added to the increased RBE, heavy ions such as carbon seem a promising treatment in achieving tumour control of hypoxic tumours[40].

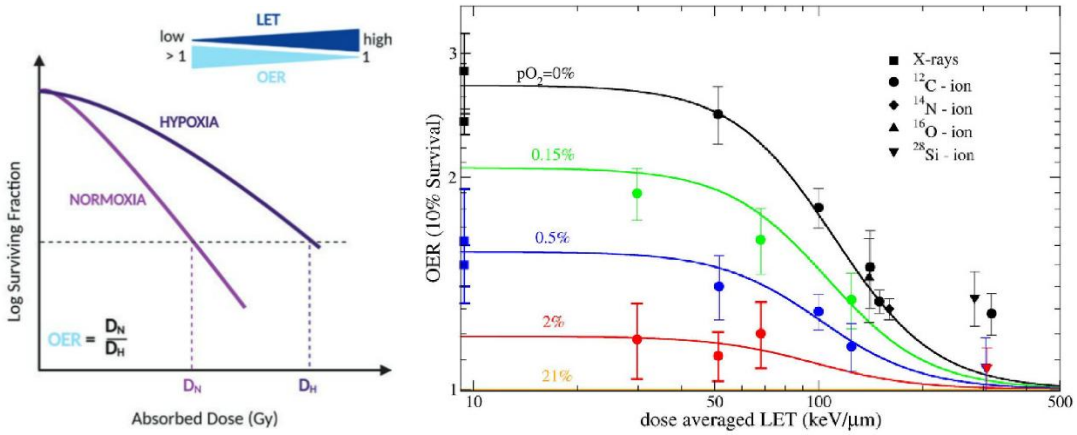

Figure 7. The survival of irradiated cells depends on their oxygenation status. The figure on the left show the impact of the oxygenation status on the survival of the cells (from Baatout *et al.*[1]). On the right, the OER is plotted against the LET to show their relationship for different oxygenation levels based on *in vitro* measurements (from Tinganelli *et al.*[39]).

An interesting correlation is also the one between hypoxic regions and ischaemia-reperfusion damage. This kind of damage occurs when an ischaemic region, which is hypoxic since a sustained period of time, suddenly becomes flooded by blood again. The prolonged reduction of tumour blood flow deteriorates the hypoxic and acidic microenvironment, which leads to cytotoxicity; this, in turn, becomes even worse when the tissue is re-perfused, and by consequences, reoxygenated again[41]. Tackling the importance of the oxygen level in a tumour tissue is extremely important to improve the outcome of a radiotherapy treatment, and in this sense, heavy ion therapy (carbon ion therapy, in particular) seems very promising[37].

1.2.3 Photon versus heavy ion radiotherapy

Conventional radiotherapy with X-rays (photons) is the most common radiotherapy treatment since its first application with a breast cancer patient in 1896. X-rays are usually generated by a device that excites electrons (*e. g.* cathode ray tubes and linear accelerators)[42]. However, due to the continual energy release of the photon´s radiation tracks both during entrance and exit of the tissue they traverse, there can be unnecessary dose delivery to the surrounding healthy tissues and organs at risk, which might lead to acute and long-term adverse effect[19]. To mitigate these disadvantages, radiotherapy is usually delivered in small, daily fractions (1,5-3 Gy) for several weeks to avoid overexposure of the normal tissues and to achieve better tumour control[1,42]. Considering the high energy release in the entrance channel, it's a valid technique for the treatment of superficial lesions, like skin cancers. To reach deep seated malignancies, instead, several beams need to be shoot from different direction, summing them up to reach a high dose in the tumour volume (see Figure 8).

Compared to photons, particle beam therapy is characterized by a lower entrance and exit dose, relying mostly on the Bragg Peak for tumour cells killing. The dose distribution created by the Bragg peak is particularly suitable for treating deep-seated tumours. Coupled

with higher LET, it allows to reduce the number of beams necessary to achieve a high dose in the tumour volume while better sparing the healthy tissues[37].

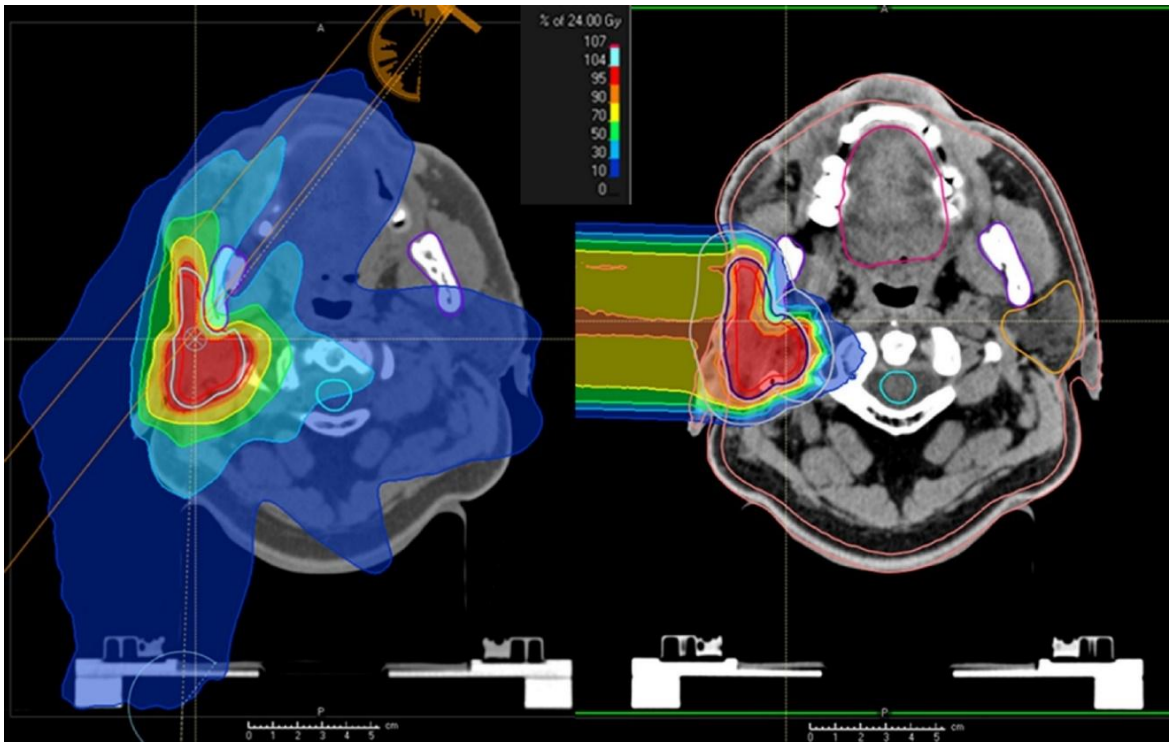

Figure 8. Healthy tissue sparing in photon versus carbon ion therapy from Eichkorn *et al.*[43].

Particle therapy was initially proposed by Robert Wilson in 1946, who recognised how the physical advantages of heavy particles, compared with photons, could be interesting in the radiotherapy setting[44]. The dose distribution of particle therapy treatments are especially advantageous in the case of risk to expose radiosensitive organs to the radiation. The other main reason to use heavy ions in radiotherapy comes from the higher RBE[16], which is indicated for treating radioresistant tumours like sarcomas, glioblastomas, prostate and cervical adenocarcinomas, ovarian cancers etc.[45,46]. The biological advantages of heavy ions are summarised in Figure 9.

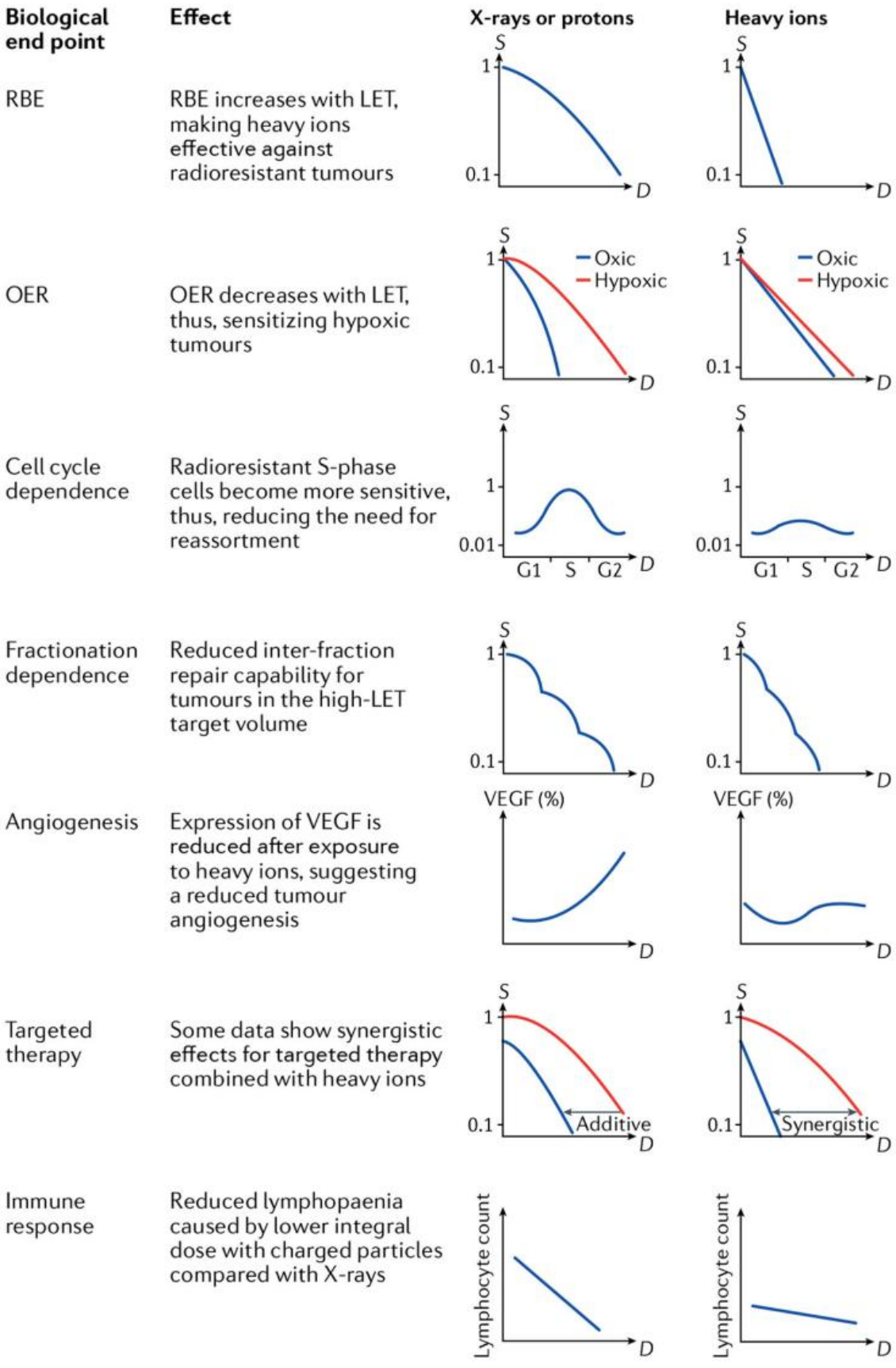

Figure 9. Biological advantages of heavy ions from Durante, Debus and Loeffler[47].

1.2.4 Carbon ion centres

With 17 centres already in operation around the world and an additional 3 more currently under construction[48], plus over 20,000 patients already treated all around the world, there is a growing interest in the clinical application of heavy ions therapy[49]. These facilities need to have a source of ions, a linear accelerator to bring them to a synchrotron for acceleration, a high energy beam transport line made of magnets that focus the beam, one or more horizontal beamlines equipped with instruments like the raster scanner, and if possible, an ion gantry that can rotate the beam around the patient couch[50].

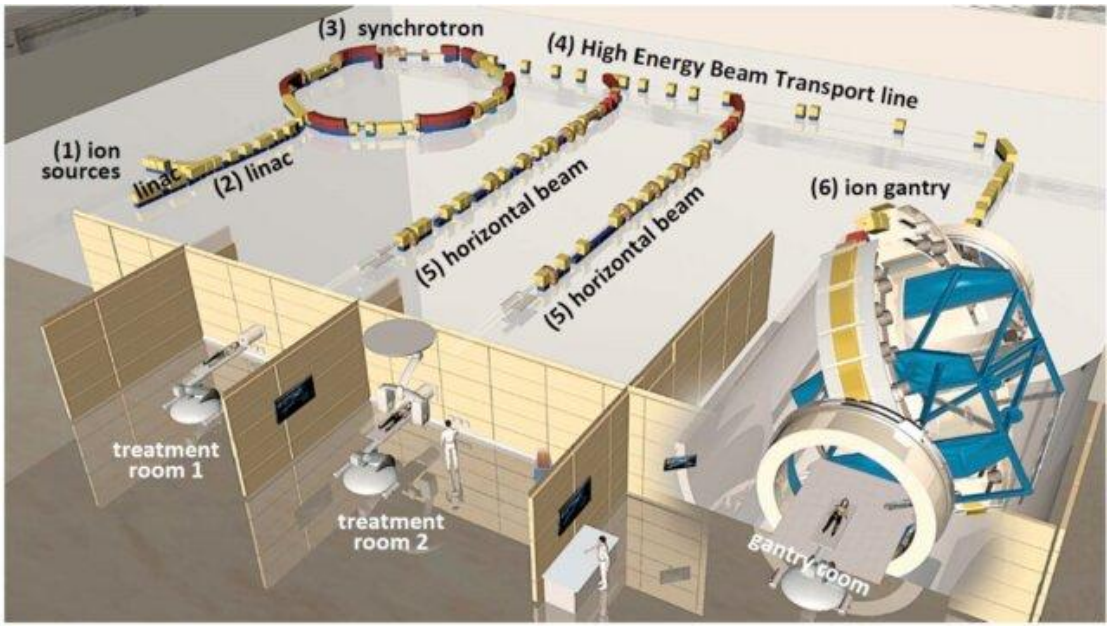

Figure 10. Design of the Heidelberg Ion-beam Therapy (HIT) facility[50].

Since medicine is moving towards the era of high-precision and personalised treatment, heavy ion centres would play an ever-more important impact on oncology[44]. Given the fact that the number of oncological patients is constantly growing, we can expect the number of patients that would need carbon ion therapy to grow accordingly[51]. Building next-generation facilities, with smaller and cheaper systems, would certainly help in making carbon ions centres more affordable and to improve their cost-effectiveness. If particle therapy could assure the best possible normal tissue sparing, this would also make another point in favour of it, making it become the safest and most effective treatment option[47].

1.3 Healthy tissues toxicities

The concept of healthy tissue sparing started to be really taken into consideration in the 1930s, when the disciplines of physical modelling and dosimetry started to be used to plan the radiotherapy treatments, also in order to avoid as much as possible healthy tissue irradiation[1].

Acute side effects occur during or within the weeks of treatment up to three months afterwards, while the late effects occur three months to several years after treatment[52]. The acute effects are usually reversible, thus they are generally not dose-limiting, while the late effects tend to become permanent[53]. The reason behind this bimodal response is that the

acute effects result from the death of a large number of cells, occurring within a few days or weeks after irradiation and is thus more relevant for tissues with a faster turnover rate, like gastrointestinal epithelium, hematopoietic system and the epidermal layer of the skin. The damage is repaired thanks to the proliferation of stem cells. Every tissue can be organized in functional sub-units (FSUs), and an important difference stands between structurally defined FSUs, like nephrons in the kidney, and structurally undefined FSUs, like the skin. The difference is in how the clonogenic cells repopulate a tissue: in the first case, they can´t migrate to another FSU, and if this one is completely depleted of them, the entire sub-unit is lost; in the second case, the clonogenic cells can migrate and repopulate all the tissue[2]. Above the tissue level, the organs are divided between parallel and serial: the first are sensitive to the percentage volume receiving radiation, but can tolerate high doses to small areas, while in the latter low doses are well sustained by large volumes, but damage to one sub-unit can affect the overall organ function[54].

Apart from the initial post-irradiation acute effects, which normally manifest in the three months after treatment, patients can develop late toxicities during their lifespan, and every individual has a different radiosensitivity[52]. Since late clinical radiotoxicity has a multifactorial aetiology, and it´s extremely difficult to predict the individual radiosensitivity of each patient, the golden rule is to spare as much healthy tissue as possible, or to reduce it in order to avoid long-term consequences[55]. Figure 11 depicts the timeline of when the biological side effects appear after radiation and their characterisation.

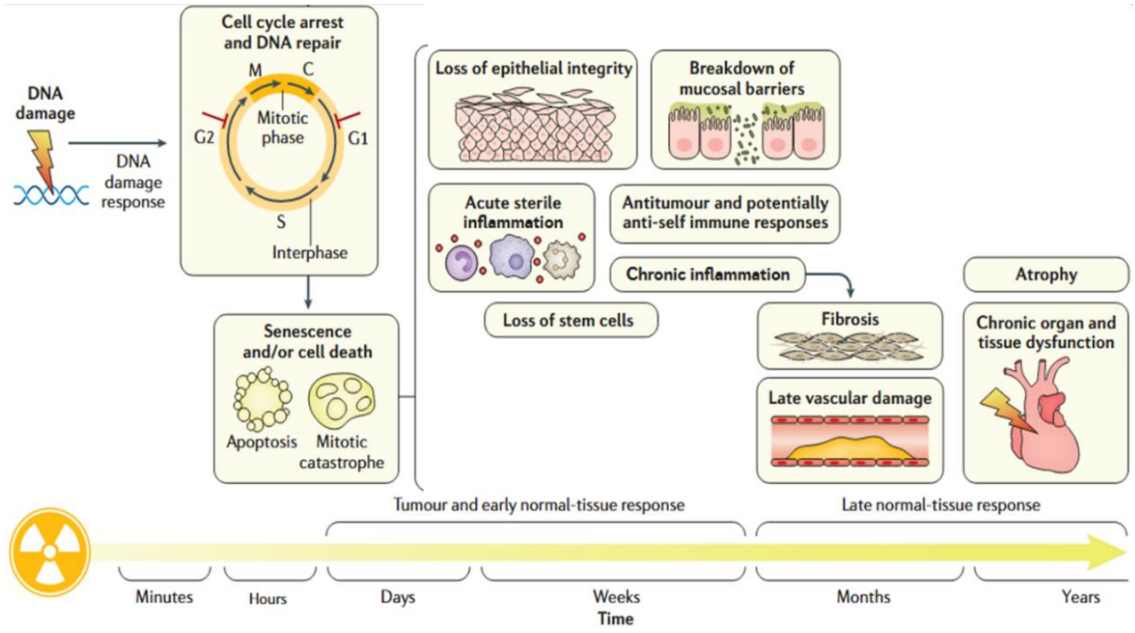

Figure 11. Timeline of biological side effects after radiation, adapted from De Ruysscher *et al.*[52].

In patients undergoing radiotherapy, the scoring criteria adopted to classify acute and late radiation morbidities is the one from the Radiation Therapy Oncology Group (RTOG)[56]. In this thesis, the radiation-induced toxicities of the skin, the oesophagus and the spinal cord were taken into consideration and are here presented; more details about the projects´ aim can be found at Paragraph 1.5.

Radiation-induced skin toxicity (Table 1) can manifest quite often when considering external beam radiotherapy, because there will be at least one beam entering the patient´s body. Skin has no well-defined FSUs, and it responds to damage like parallel tissues while

not showing a volume effect at lower levels of injury, since the surviving clones are scattered throughout the treatment volume. The skin healing process can undergo issues like increased potential for infections, mainly caused by the development of ulcerations; this symptom also prolongs the healing time[2]. The symptoms of radiation induced skin toxicity range from mild redness (inflammation), to erythema, hypersensitivity, dermatitis, painful moist desquamation. ulceration and necrosis[54]. The cells that are the most sensitive to radiation are basal keratinocytes, stem cells in hair follicles and melanocytes[52]. Other reactions, which may occur later, are alopecia, fibrosis and telangiectasia[57].

Table 1. RTOG skin radiation morbidity scoring scheme[56].

	Acute	Late
[0]	No change over baseline	None
[1]	Follicular, faint or dull erythema; epilation; dry desquamation; decreased sweating	Slight atrophy; pigmentation change; some hair loss
[2]	Tender or bright erythema; epilation; dry desquamation; decreased sweating	Patch atrophy; moderate telangiectasia; total hair loss
[3]	Confluent, moist desquamation other than skin folds, pitting oedema	Marked atrophy; gross telangiectasia
[4]	Ulceration, haemorrhage, necrosis	Ulceration

Radiation-induced oesophagitis (Table 2) might occur in the treatment of head and neck cancers, as well as in tumours located in the thorax. Like the skin, also the mucosae show a response similar to the tissues where the FSUs are in parallel and the same healing constraints are present[2]. In the mucosae the stem cells that are lost from the basal layer interfere with the replacement of cells in the superficial mucosal layers, which are normally lost during the normal physiological sloughing. In the case of the oesophagus, the denuding of the epithelium results in mucositis, which is painful and interferes with feeding capability[52] leading to issues in healing, cancer- related cachexia and response to stress[57]. Radiation-induced oesophagitis has an acute phase, up to three months after treatment, and a late phase, manifesting on average six months afterwards[58].

Table 2. RTOG oesophagus morbidity scoring scheme[56].

	Acute	Late
[0]	No change over baseline	None
[1]	Mild dysphagia or odynophagia; may require topical anaesthetic or non-narcotic analgesic; may require soft diet	Mild fibrosis; slight difficulty in swallowing solids; no pain on swallowing
[2]	Moderate dysphagia or odynophagia; may require narcotic analgesic; may require puree or liquid diet	Unable to take solid food normally; swallowing semisolid food; dilation may be indicated
[3]	Severe dysphagia or odynophagia with dehydration or weight loss > 15% (from pre-treatment baseline); requiring N-G feeding tube, i.v. fluids or hyperalimentation	Severe fibrosis; able to swallow only liquids; may have pain on swallowing, dilation required
[4]	Complete obstruction, ulceration, perforation, fistula	Necrosis/perforation; fistula

Radiation-induced cervical spinal cord toxicity (Table 3) is mainly manifesting after treatments revolving around the central nervous system (CNS) and the spinal cord. Late effects typically occur in the slowly proliferating tissues, like the CNS, and the pathogenesis includes the formation of fibrosis, atrophy, loss of parenchymal cells and vascular damage[53]. Vascular damage is not the dominant factor because if it were, the dose-effect relationships would be the same for every tissue. However, this might be true for some tissues, including the spinal cord. In the case of the spine, another important concept explains how the damage might happen in this tissue. The FSUs in the spine are arranged in a series, which means that damage of one FSU leads to complete failure of the organ, since the impulses are passed all the way along the cord. If radiation damage is induced, the expected response would be binary, where below a certain threshold dose the normal function is retained, and above which there is loss of function, like radiation-induced myelopathy[2]. Myelopathy is a highly impairing late effect of the radiation treatments directed to spine, head and neck areas, and the lungs; in the clinical practice the risk of permanent injury is kept very low (between 0.03 and 0.2%) by delivering a dose to the spine which doesn´t exceed 45-50 Gy in 1.8-2 Gy daily fractions.

Late effect consists in demyelination and necrosis of the white matter in the irradiated area of the spinal cord, which manifest as paralysis of the limbs at the organism level[59]. Usually, the irradiation of the cervical spinal cord leads to kyphosis and upper limbs paralysis, while irradiation of the thoracolumbar transition or the sacral areas lead to paralysis of the lower limbs.

Table 3. RTOG CNS and spinal cord morbidity scoring scheme[56].

	Acute	Late
[0]	No change	None
[1]	Fully functional status (*i. e.* able to work) with minor neurological findings, no medication needed	Mild Lhermitte´s syndrome
[2]	Neurological findings present sufficient to require home care or nursing assistance; medications including steroids/antiseizure agents may be required	Severe Lhermitte´s syndrome
[3]	Neurological findings requiring hospitalisation for initial management	Objective neurological findings at or below cord level treated
[4]	Serious neurological impairment that includes paralysis, coma, or seizures > 3 per week despite medication; hospitalisation required	Mono, para quadriplegia

1.4 Treatment and range monitoring with radioactive ion beams (RIBs)

The possibility of causing radiation-induced morbidities in patients is an important topic in healthcare, especially in cancer survivors. There are always uncertainties in RT, but in the case of charged particle therapy the steep dose profile is particularly sensitive to uncertainties in the particles range inside the body[60]. Sources of range uncertainties can be: variations in patient anatomy during the course of the treatment, uncertainties in CT Hounsfield units (HU), conversion of HU into particle stopping power and CT reconstruction (CT acquired with photons, not charged particles), errors in patient positioning and in the beam energy[61,62]. In the case of heavy ions, the sharp dose gradients

in the Bragg peak region are highly desirable to deliver a high dose to the tumour, but on the other hand, the sharpness of the Bragg peak makes them more susceptible to the range uncertainties, as shown in Figure 12.

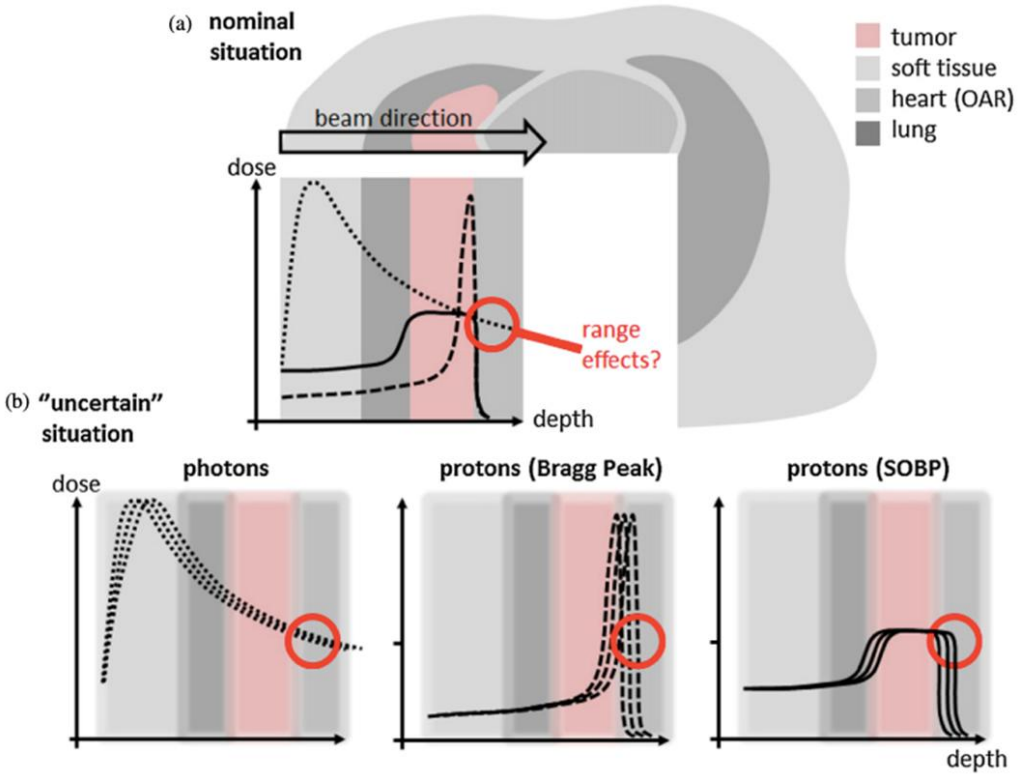

Figure 12. Range uncertainties in heavy ion therapy. A) Potential dose benefit of a proton treatment compared to a photon treatment (dotted line: photon depth dose curve; dashed line: mono-energetic proton depth dose curve known as Bragg Peak; straight line: spread out proton Bragg curve (SOBP) to cover the whole tumour). B) Influence of uncertainties to these depth dose curves. From Knopf and Lomax[63].

These can result in an increased risk of delivering a high dose to the normal tissue and underdose to the tumour, impairing the beneficial effects of charged particle therapy. Much research in particle therapy is therefore aimed at developing new methods, which enable to verify the particle range in patients. This approach should be non-invasive and has to be ideally done *in vivo* to allow for immediate intervention and treatment delivery adaptation during irradiation, to avoid additional dose to the patient[64].

There are different approaches which take advantage of the secondary particles generated by the beam, like range verification based on prompt γ-rays and charged particles trackers, but the first one applied with patients treated with particle beams has been Positron Emission Tomography (PET)[64–68]. Positron emission is the result of spontaneous radioactive decay[69].

1.4.1 Radioactive decay and positron emission

Radioactivity is a natural phenomenon that occurs in the atoms, which spontaneously emit energy in the form of radiation and decay in daughter nuclides. The activity A of a radioactive source is proportional to the number of radioactive nuclei in the sample (N) present at any given instant and the decay constant (λ)[1]:

$$A(t) = \lambda \cdot N(t)$$

The amount of radioactivity in a source is measured by the rate at which atoms undergo radioactive disintegration, with the Becquerel (Bq, 1 disintegration per 1 second) as the unit, from Henry Becquerel, the discoverer of radioactivity[70]. Another unit for the activity is the Curie (Ci, activity of one gram of radium and equal to 37 GBq), named after Maria Skłodowska Curie and her discovery of radium. An important concept in radioactivity is the half-life ($T_{1/2}$) of a radioactive substance. Since the decay constant represents the probability per unit time that a single radioactive atom will decay, the half-life is the time when half of the atoms present will have decayed, following an exponential form dictated by the decay constant[1].

$$T_{1/2} = \frac{\ln 2}{\lambda} = \frac{0.693}{\lambda}$$

The use of radioactive decay in nuclear medicine is important, since it can be used for personalised patient management. One example is PET (see following sections): its applications vary from medical imaging for diagnosis of early-stage diseases, targeted treatments, and in particular monitoring of the treatment of tumours.

1.4.2 Positron Emission Tomography

PET imaging is a nuclear medicine technique used to reveal the metabolic or biochemical function of tissues and organs[66,68]. It requires the injection of a radioactive tracer (usually ^{18}F is attached to molecules like fluorodeoxyglucose (FDG), which behaves like glucose in the body[71]) to show typical and atypical metabolic activity[1]. It´s commonly used to assess the presence of tumour tissue in the body, since tumour cells show an accelerated metabolism that mostly relies on glucose and glycolysis[68]. Due to this characteristic, the ^{18}F-FDG will tend to accumulated in the tissues that require glucose the most – tumours and brain tissues[1,72].

PET imaging is characterized by a high sensitivity and accurate estimation of the *in vivo* concentration of the radiotracers. It has been adopted for oncological, cardiovascular and neurological clinical applications, and also in preclinical studies involving small animals, like murine models[73]. In diagnostics, the combination of PET imaging with the anatomical imaging delivered by X-rays computed tomography (CT) provides the synergistic combination of information about what is seen (from PET) with information about where it is (from CT). The anatomical information deriving from the CT helps in providing estimations of the quantitative corrections needed for accurate PET imaging[74].

The principle of PET is based on the detection of the activity of a β^+-emitting radionuclide[67]. A nucleus with an excess of protons decays to a more stable state by emitting a positron (β^+) and a neutrino (ν). The emitted positron travels a short distance, typically 1–2 mm in the case of ^{11}C (as depicted in Figure 13) for example, before interacting with an electron. Since positrons are the antiparticles of electrons, they annihilate upon contact, releasing two high-energy photons emitted simultaneously in opposite directions (approximately 180° apart)[69]. These coincident photons are detected by the PET scanner's detectors, which are arranged in a ring or other geometric configurations around the patient. The detected signals are then processed to reconstruct a three-dimensional image of the tracer distribution.

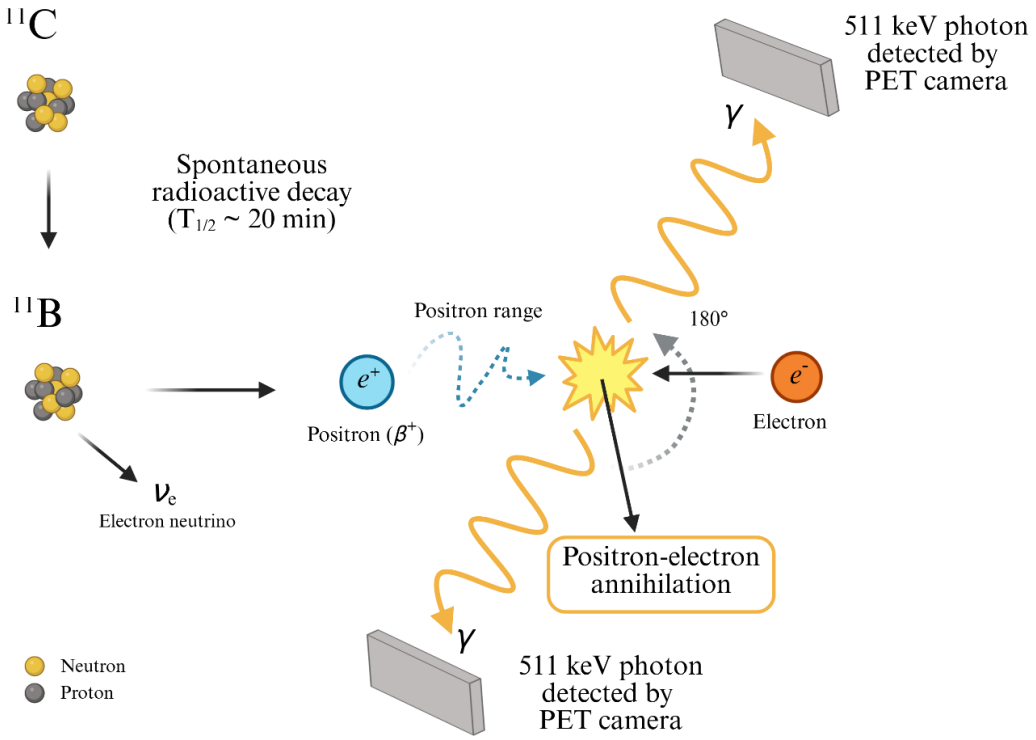

Figure 13. ^{11}C decay and use of PET imaging. Created with BioRender.

1.4.3 PET monitoring in charged particle therapy

Differently from nuclear medicine, there aren´t radiotracers involved in charged particle therapy. Still, if the beam energy is enough to produce nuclear interaction between the ions in the beam and the nuclei in the tissues (≃20 MeV), positron emitters can be produced and subsequently used for visualising the beam range in the tissue[75,76]. The radioisotopes produced from the fragmentation of ^{12}C comprehend ^{11}C, ^{15}O, and ^{10}C, with respective half-lives of 20 minutes, 2 minutes and 19 seconds[77] (see Table 4). They can be produced either as a fragment of the primary particles (beam used for irradiation) when those collide with the biological tissues (autoactivation), or by making a beam hit a target and obtaining fragments from the original particles present in the beam (target fragmentation)[78].

Table 4. Positron emitting isotopes that have been considered for radioactive ion beams therapy[79].

Stable isotope	Positron-emitting isotopes	Half-life
^{12}C	^{11}C	20.33 min
	^{10}C	19.3 s
^{14}N	^{13}N	9.97 min
	^{12}N	11.0 ms
^{16}O	^{15}O	2.04 min
	^{14}O	1.17 min
^{19}F	^{18}F	1.83 h
	^{17}F	1.07 min
^{20}Ne	^{19}Ne	17.26 s
	^{18}Ne	1.66 s
^{31}P	^{30}P	2.50 min
	^{29}P	4.14 s

Three different modalities can be used to monitor treatments with a PET scanner: offline monitoring, where the PET system is located outside the treatment room (data acquired only after treatment); in-room, where the data are acquired shortly after treatment; in-beam, where the PET scanner acquires data during the beam delivery. In the last case, there is no need to reposition the patient after the treatment delivery and no information about the activity are lost (especially considering the short half-lives of some of the radioisotopes), leading to the production of more accurate PET images of the dose deposition[80,81].

In 1997 a pilot project performed at GSI - Helmholtzzentrum für Schwerionenforschung GmbH where cancer patients were treated with ^{12}C between 1997 and 2008, a dedicated in-beam PET system (BASTEI PET[82]) has been developed in the framework of the German Heavy Ion Tumour Therapy Project, in a collaboration between GSI and HZDR (Helmholtz Zentrum Dresden Rossendorf)[83,84]. Newer in-beam PET devices comprehend OPEN-PET[85] at National Institute of Radiological Sciences (NIRS-QST) in Chiba, Japan; ON-LINE[86] at National Cancer Center Hospital in Kashiwa, Japan, and the INSIDE[87] PET at CNAO (Centro Nazionale di Adroterapia Oncologica, Pavia, Italy)

The signal generated during ^{12}C irradiation is, however, not very strong, because the number of $ß^{+}$-emitting radioactive fragments is very low compared to the number of primary ^{12}C ions. PET images can already be obtained during a carbon ion treatment, but since the signal obtained by the detected photons is not so high (low count rates), they lack enough precision; another reason for the low precision is the biological washout, the transportation of the isotopes away from their native location due to the blood flow, which disperses the signal[88]. These factors, added to the broad activity distribution and the mismatch between the activity peak and the dose distribution that can be seen in Figure 14, limit the precision of PET measurements in ^{12}C radiotherapy[89].

1.4.4 Radioactive ion beams

Despite PET being widely in use for imaging in ^{12}C therapy, the low count rates, biological washout, and broad activity distribution still limit its precision. Instead, radioactive beams used directly for treatment would yield an improved signal and a closer match with the dose fall-off, potentially enabling precise in vivo beam range monitoring[89]. The resulting PET image quality could be substantially improved and so is the possibility of adjusting the range of the beam online, while the physical and radiobiological advantages of the stable counterpart should remain[79,85,88,90].

In fact, using a ^{10}C beam would be even better from the imaging point of view, since its half-life is only 19 seconds, making it less prone to the biological wash-out of the radioisotopes. However, it´s technically difficult to produce beams of ^{10}C with an intensity (number of particles delivered in a defined time) high enough to have a therapeutic value, at the moment[88,91]. This is not the case of ^{11} beams, instead, at least for preclinical research. ^{11}C beams can now be produced at high intensities at the Fragment Separator (FRS) at GSI, which is used to produce the fragments by making a stable beam colliding onto a beryllium target and separating the relevant isotopes from other reaction products[92]. The newly reached intensities are sufficient to treat a tumour-bearing murine model, while acquiring the PET signal *in vivo* in a reasonable within-treatment time thanks to the short half-life of these radioisotopes, and opening up the possibility of reaching online range monitoring[88,91].

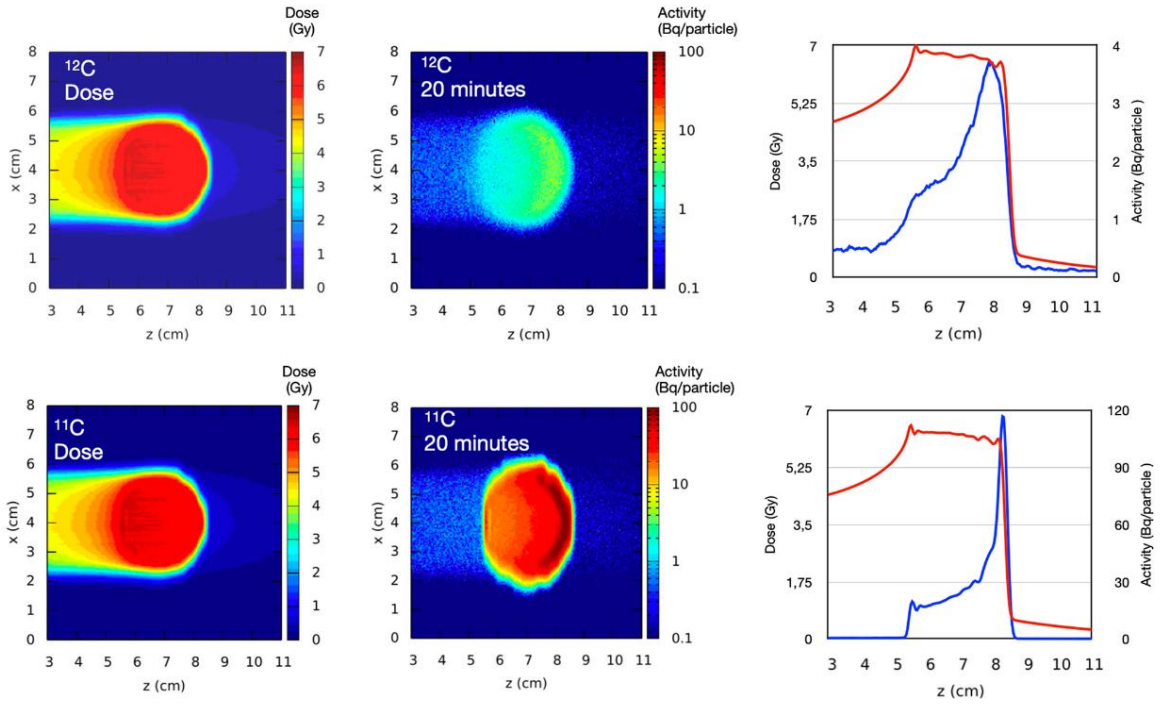

Figure 14. ^{12}C and ^{11}C dose and activity maps. The graphs on the right show the distributions of dose (red curve) and activity (blue curve) along the beam direction (z-axis) showing the shift between dose and activity when stable ions are used. The same does not apply with the radioactive ions, where dose and activity peak show a good match. FLUKA Monte Carlo simulation from Boscolo *et al.*[88].

As it can be seen in Figure 14, there is a shift between the activity peak position and the SOBP dose fall-off for the stable beams (top row), while there is a match between activity peak and SOBP 80% dose fall-off between the two distributions for the radioactive primary ions. Thus, measuring the activity would make it possible to determine the position where a relevant amount of the dose is deposited[88]. By augmenting the precision in the dose delivery, the Planned Target Volume can be dramatically reduced, leading to a substantial sparing of the healthy tissue and thus overcoming the most relevant obstacle still present in carbon ion therapy[47,93]. *In silico* treatment planning studies suggests various benefits of using ^{11}C, like improved outcomes and less severe toxicities for the healthy organs, plus how the annihilation maps of ^{11}C compared with the dose distributions measured in the patients can reflect sub-millimetre shifts in the latter[89].

Another advantage of using radioactive ions beams (RIBs) conjugated with PET could be the possibility of using the measured activity to quantify the biological washout in the irradiated tissues[88]. Several works have been exploring the use of RIBs as *in vivo* radiotracers, for example, to monitor the biological washout of radioactivity in rodent models[78,94–97], both tumour-free and tumour-bearing. Part of this studies were dedicated to explore the use of RIBs and their biological washout as a mean to predict the tumour hypoxic status[98,99].

The application of RIBs might also be useful for understanding with preclinical experiments how single-fraction high dose radiotherapy (SDRT) works. This kind of radiotherapy has been studied recently[100] as a possible replacement of hypofractionation, the delivery of the therapy in 4 or 5 fractions, which is already a reduction in comparison to normal fractionation (around 15-20 fractions). While there are promising studies going in

this direction[101–103], the exact mechanism is unknown. One hypothesis is the early vascular damage induced by a single high dose, which can cause a ischaemia/reperfusion type of injury in the tumour´s tissue[104–106]. If this is the case, the radioactivity will be retained in the tumour instead of being washed away by the blood flow. By implanting a high number of radiotracers in the tumour, their decay can be monitored to observe any alterations caused by the circulation impairment. By adding PET-based monitoring to the course of a treatment[85], the vascular status of the tumour (especially in the case of hypoxic tumours) could be monitored online, without additional radiation exposure or risk from radiotracers-containing drugs administration[93].

1.5 Aim of the project

The use of radioactive ion beams in radiation therapy has been postulated since the beginning of charged particle therapy, and was first explored with ^{19}Ne ions during the pilot project at the Lawrence Berkeley Laboratory (LBL) in 1975, which first used heavy ions to treat more than a thousand patients[107]. In that context, it became clear that RIBs could be used for range verification, by overcoming the uncertainties in predicting the range of heavy ions from the CT images[79]. Given the fact that heavy ions already show a favourable depth-dose distribution and significant radiobiological advantages, it would be of fundamental importance to sweep away the last uncertainties in the dose delivery[91]. In this context, the project "Biomedical Application of Radioactive Ion Beams" (BARB) aimed to demonstrate for the first time the application of ^{11}C ion beams for simultaneous tumour treatment and range verification via PET. Figure 15 shows how the experimental setting was implemented, and the details of the beamline can be found at 2.4.2.3.

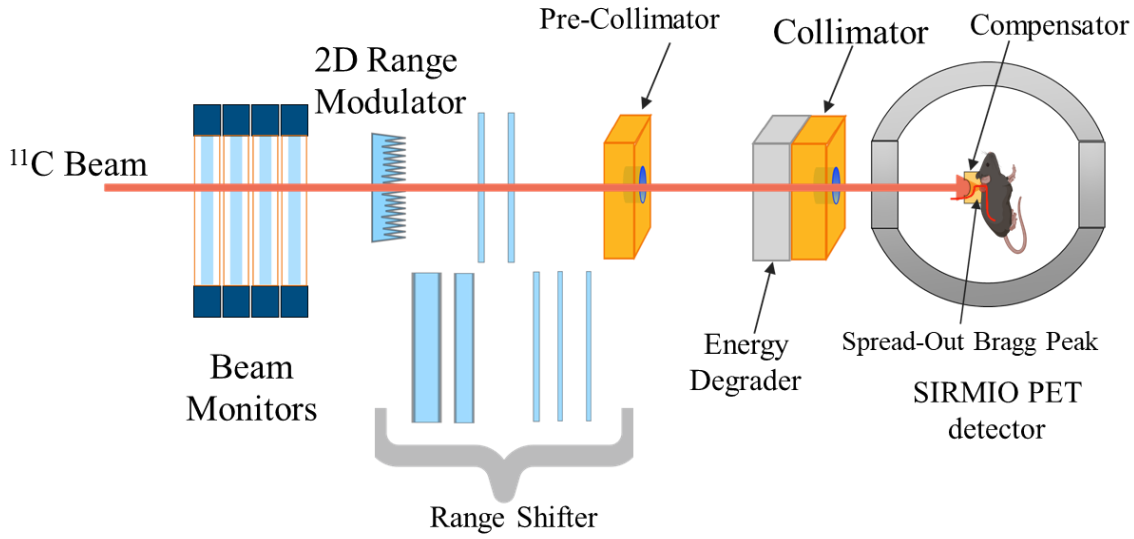

Figure 15. Conceptual representation of the Biomedical Application of Radioactive ion Beams (BARB) project. The components necessary to shape and monitor the ^{11}C beam are depicted, together with the SIRMIO PET system and the mouse that receives the SOBP treatment. From Boscolo *et al.*[108].

The biological hypothesis is that, if the beam range is carefully controlled in a living organism, the tumour would be treated and the side effects minimized, and that the beam stopping position in the animal´s body can be correlated to the early and late side effects. We irradiated tumour-bearing mice with ^{11}C, controlling the beam penetration depth by measuring the PET signal coming from the abundant emission of positrons. The animals

were followed-up for the development of early and late side effects up to six months, when they were sacrificed for histological analysis.

1.5.1 BARB experimental campaign

Exploiting the radiobiological properties of the radioactive ion beams and the online range verification required protocol for the *in vivo* experiments, including a tumour model, which was set up in this thesis work. To obtain tumour-bearing mice, with the tumour located near organs at risk that could manifest toxicity after radiation exposure, the animals were injected subcutaneously with murine osteosarcoma cells above the cervical area of the spinal cord. In this way, both the spinal cord and the oesophagus functioned as organs at risk (OARs) during the irradiation and in the subsequent follow-up phase. To establish the best tumour model, the tumour growth was tested with preliminary experiments. The dose necessary to eradicate the tumour and the possible health side effects were found out through a dose escalation study with X-rays; during this part of the experiments, also the health care that needed to be provided prior and post the carbon ions treatment was established.

Two different biological experimental campaigns ("beamtimes") have been conducted during this thesis work, one in 2024 and one in 2025. In both cases, to produce the radioactive ^{11}C beam used in this study, a dedicated beamline was set up at GSI Helmholtzzentrum für Schwerionenforschung GmbH (Darmstadt) in the context of the ERC Advanced Grant (883425) BARB, granted to Prof. M. Durante[88]. Online range monitoring during the irradiation was achieved by employing the SIRMIO PET detector developed at the Ludwig-Maximilians-Universität München (LMU) and mounted in the irradiation room (Cave M, see Figure 16) of GSI, directly at the treatment position. After the ^{11}C treatment, the animals were monitored for tumour growth and radiation-induced skin toxicity.

In the case of the first campaign, the goals were to assess the tumour growth rates after a treatment with either a low (5 Gy) or high dose (20 Gy), deriving from the results of the X-rays experiment. These doses could also made it possible to look at the biological washout of the ^{11}C radioisotopes in the tumour tissue, and data were collected with the aid of SIRMIO during the irradiation and up to one hour afterwards. The other goal was to gather preliminary information about the healthy tissues' toxicities by following-up the animals up to six months post irradiation[108].

The second campaign, instead, was meant to specifically correlate the online range monitoring with the beam position in the mice′ bodies, and how different beam depths may lead to different biological outcomes, *e. g.* if the radiation field is not covering adequately the tumour volume or if the organs at risk were exposed during the irradiation. Since the irradiation field covered the cervical area of the spinal cord, and the oesophagus is in close proximity, these animals were also kept for six months to monitor tumour growth and health status, especially regarding the development of oesophagus toxicity and radiation-induced myelopathy in the spine.

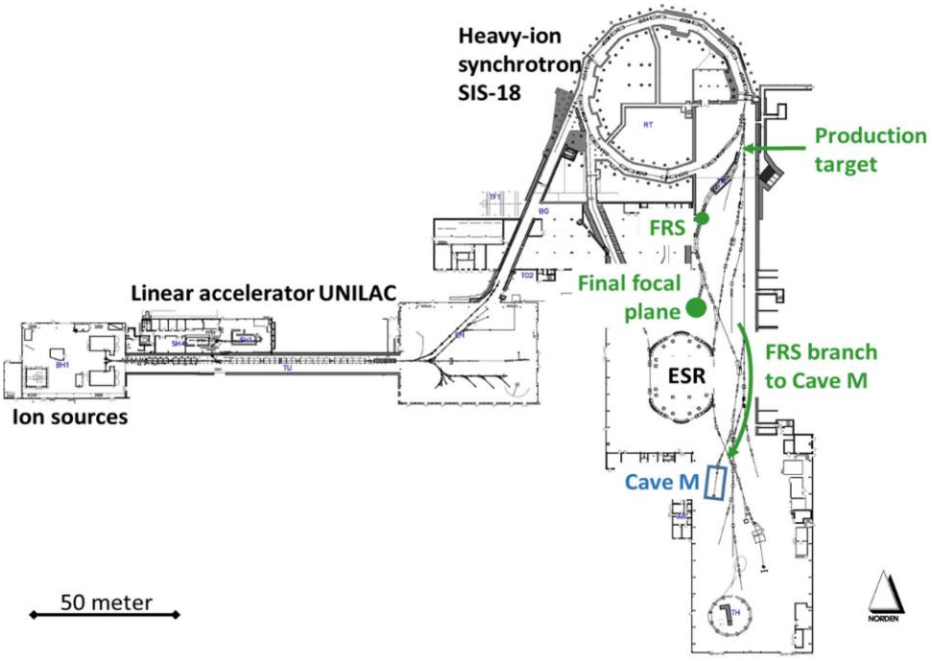

Figure 16. GSI research facility map[88].

2 Materials and methods

2.1 Animal model and ethical disclosure

The experiment was approved by the Hessen Animal Ethics Committee (Project License: DA17/2003, Regierungspräsidium Darmstadt, Germany) and followed the German Federal Law for animal experiments and the 3Rs principle (Reduce, Replace and Refine)[109]. Particular care was adopted on refined handling techniques to reduce as much as possible the stress caused to the animals along the months of experiments.

2.1.1 Animal husbandry and handling

The animals used in all of the experiments presented in this work were 11-12 weeks old female C3H/ HeNRj mice (*Mus musculus*) purchased from Janvier Labs, (France), housed at GSI in a conventional animal facility (non-SPF) at 55% humidity, 22°C and inverted 12 hours light-dark cycle, to ensure the animals were awake during the experimental procedures. The animals had *ad libitum* access to water and standard diet food (Ssniff, Germany). After arrival in the facility, the animals were given a week of acclimatization, during which they were habituated to cup handling to maximize cooperation during the future tests.

2.2 Tumour model

The cell line selected for these experiments was the Dunn LM8 murine osteosarcoma (Riken BioResource Research Centre) originated from the same mouse strain[110] used in this study and had already been used for preclinical research in radiotherapy[111–113]. In those cases, the tumours were located in the hindlimb of the animals. Since the current study required larger beam penetration depths with the possibility of range adjustments, as well as the proximity of healthy tissues that could manifest toxicities, the inoculation was performed above the cervical area of the spinal cord. This area has been selected due to the proximity of the growing tumour to two organs at risk, the spinal cord and the oesophagus, and to minimize the exposure to other organs during irradiation.

2.2.1 Cell culture

LM8 murine osteosarcoma cells that were frozen at passage nr. six were cultured in Dulbecco's Modified Eagle Medium (DMEM 1X + GlutaMAX-I, Gibco, Bleiswijk, The Netherlands) supplemented with 1% Penicillin-Streptomycin (10,000 U/mL Penicillin, 10 mg/mL Streptomycin, Pan Biotech, Aidenbach, Germany) and 10% foetal bovine serum (FBS Superior, Sigma, Brazil). Cells were stored in T75 flasks (Corning Inc. Dunham, USA) in a humidified 5% CO_2 incubator at 37°C, and the passages were performed by rinsing the cells with Dulbecco's Phosphate Buffered Saline (PBS, Sigma Aldrich, United Kingdom). Followed by trypsinization with 1 mL of Trypsin-EDTA (0.05%/0.02%, Pan Biotech, Aidenbach, Germany), they were reseeded with a dilution of 1:20. The passages were done twice per week for two weeks, before injecting the cells in the laboratory animals at passage four post-thawing.

2.2.2 Tumour inoculation and monitoring

The tumour inoculation followed the week of acclimatization, and was performed by injecting ~10^6 LM8 cells suspended in 20 µL of PBS buffer solution. The animals were shaved behind the head just prior the injection, which was administered subcutaneously in the dorsal area of the neck (Figure 17) with a 30G needle (8 mm length, BD Micro™-Fine+ Demi Insulin Syringes 0,3 mL U100, Embecta GmbH, Heidelberg, Germany) at an angle of 30° degrees. Animals were anesthetized by inhaling 2.5% isoflurane mixed in air to maintain the consistency of the injection location. The total anaesthesia time was around 5 minutes per mouse, or even less if the animals were falling asleep fast. The recovery after this short anaesthesia exposure was fast, with the animals starting to move around the recovery cage in less than a minute. One week after inoculation, most tumours were visible and measurable with the calliper and the µCT. The treatment, done with both photons (X-rays) and radioactive carbon ion beams, was delivered two weeks after the tumour inoculation (see 2.4).

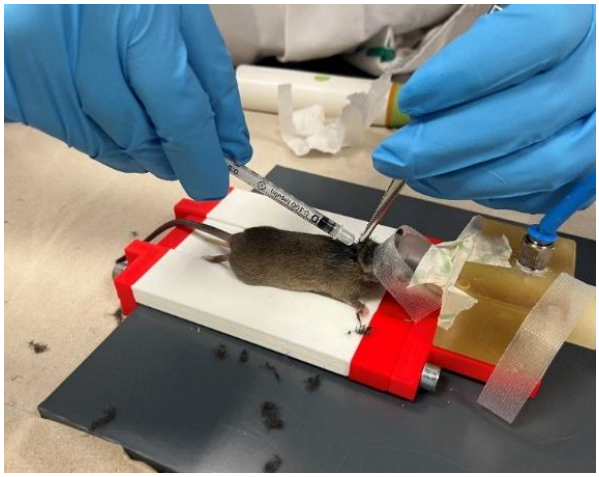

Figure 17. Mouse anesthetised for subcutaneous administration of LM8 cells. The dorsal neck area was shaved prior to the injection.

2.3 CT imaging

Computed Tomography imaging is used to gather information about the anatomy of a subject, and is routinely done in the clinical practice to visualize tumours and prepare treatment plans. This technique was also applied in this work to collect information about the anatomy of the mice and prepare the adequate irradiation treatment plan, monitor the health status (diagnostic CT), and create beamline components based on the anatomy itself (see paragraph below).

2.3.1 µCT horizontal imaging

To scan the mice, we used the preclinical µCT scanner (VivaCT 80 Scanner, SCANCO Medical AG, Switzerland) (Figure 18). Animals were anesthetized with isoflurane before the scan by placing them in a red-walled plastic chamber at an induction dose of 2,5%; once asleep, a cream ointment (Bepanthen, Bayer) was applied to the eyes to avoid desiccation. The animals were then immobilised with surgical tape on a bed specifically designed to fit in SIRMIO, with an incorporated anaesthesia flowing and exhaust gases scavenging system. During the scan, the anaesthesia maintenance dose was 1,5%. A 5 minutes scan was used

for the weekly tumour growth assessment. The neck area (31 mm) was scanned at tube voltage of 45 kVp and current of 177 µA, adding an aluminium filter of 0.1 mm. The acquisition consisted of 250 projections per 180° with 45 ms integration time, resulting in an image with a voxel size of 97.1 µm. After every scan, the animals were let to recover in a separate cage until they were fully awake, before being brought back to the original cage. These scans were also used to extrapolate the anatomical shape of the irradiated area (neck of the animals) and were used to create the anatomical compensator collar used during the ^{11}C irradiation and the health follow-up scans (see 2.4.2.3).

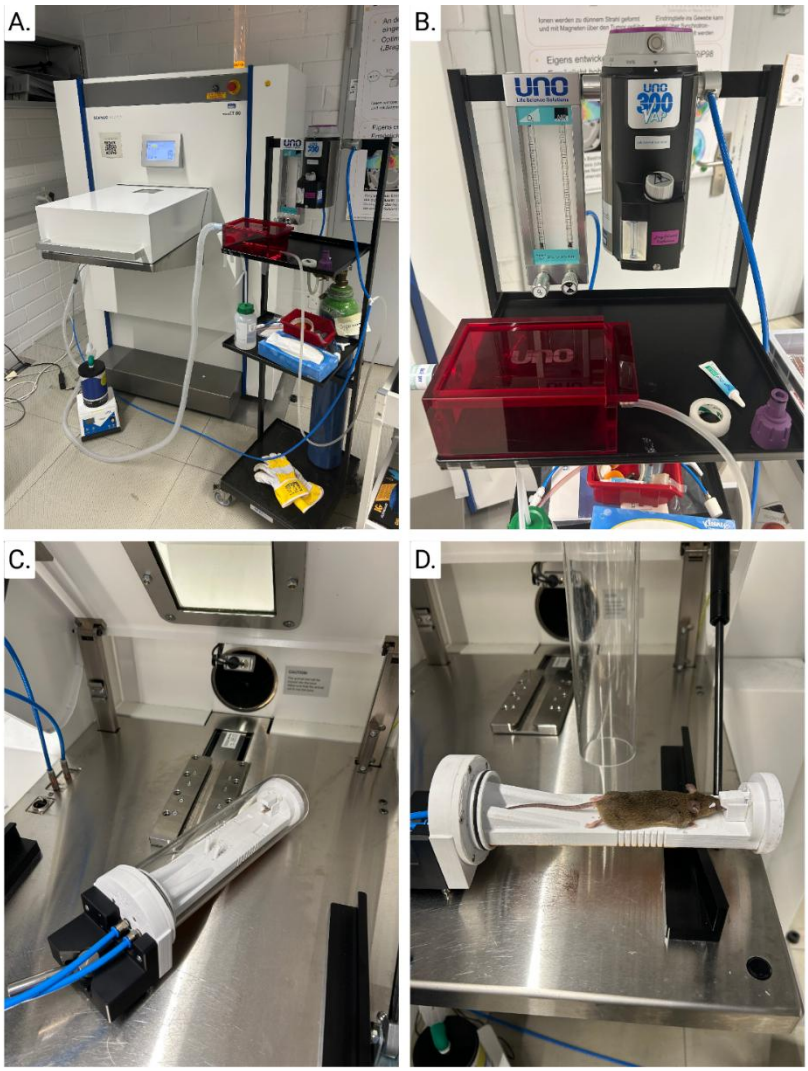

Figure 18. A) µCT system installed at GSI. B) Induction chamber (red plastic box) and isoflurane vaporiser system. C) SIRMIO bed connected to the anaesthesia gas flow and gas scavenger system, equipped with an enclosing cylinder. D) Mouse fixed on the bed prior to µCT scan.

2.3.2 Cone beam CT vertical imaging

The Small Animal Radiation Therapy Platform (SARRP) cone beam CT (CBCT, XStrahl, Germany) was utilised to acquire CBCTs of the animals in vertical position, since this would have been the position of the animals receiving ^{11}C irradiation (Figure 19). As for the µCT scans, the animals were anesthetised with isoflurane (2,5% for induction, 1,5% for maintenance) and fixed to the SIRMIO bed, were also the anatomical compensator was used. The scan at the SARRP acquired 250 projections per 180° at current of 1 mA and tube voltage of 70 kVp, adding a 0.1 mm copper filter; the resulting images had a voxel size of

275 µm. The SARRP was used for both the clarification on the role of the anatomical changes in the treatment planning and the experimental setup in the second experimental campaign (section 3.4) and for pre-irradiation imaging during the second part of the experimental campaign (beamtime in 2025).

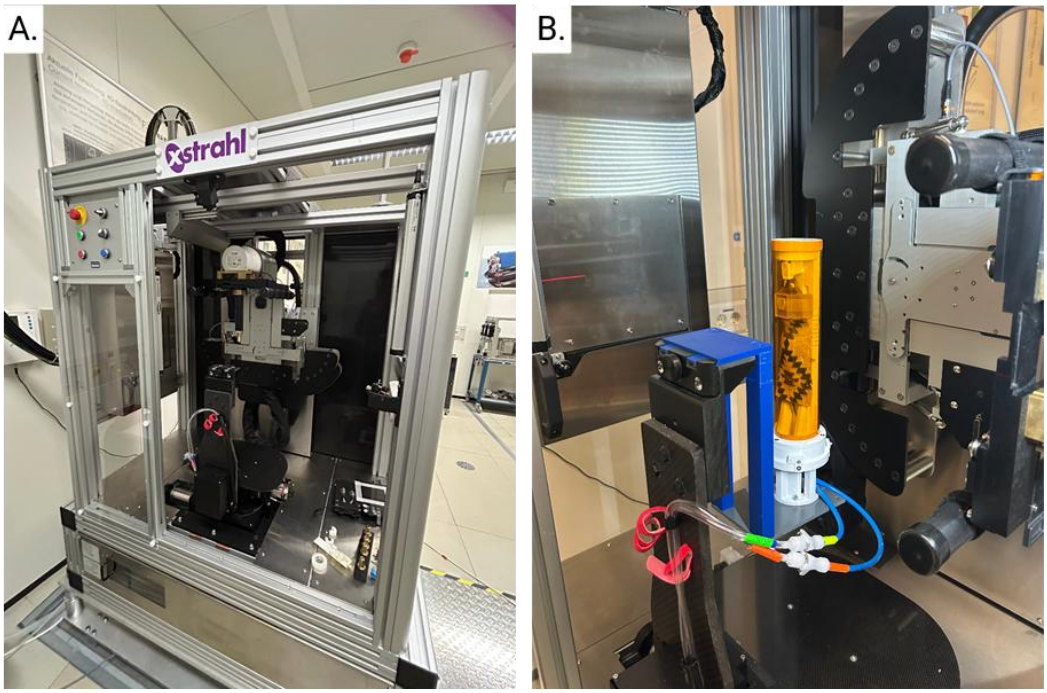

Figure 19. A) SARRP system installed at Cave M at GSI. B) Mouse fixed on SIRMIO bed with anatomical collar to mimic the ^{11}C irradiation setting during SARRP imaging.

2.4 Irradiation modalities

In radiation experiments with heavy ions, it is common practice to first benchmark by conducting an experiment with X-rays, since it's considered to be the reference radiation[1]. Photon irradiation is usually easier to perform because it requires just an X-rays generator, unlike the irradiations with heavy ions and their requirement for a facility equipped with linear accelerator, synchrotron, treatment rooms etc., as shown in Figure 10. Photons were also the first type of radiation to be used in preclinical and clinical settings, before the discovery of heavy ion beams. Lastly, the RBE is usually calculated starting from X-rays as the reference radiation (1.1.4).

Therefore, also in this work a preliminary experiment with photons was performed before the irradiations with ^{11}C.

2.4.1 Photon irradiation

The photon irradiations were conducted using a kilovoltage X-rays generator (Isovolt DS1, Seifert, Ahrensberg, Germany) operated at 250 kVp and 16 mA, with the filtering composed of 7 mm beryllium, 1 mm aluminium, and 1 mm copper. The animals were sedated with isoflurane as previously described, and immobilised in horizontal position with an anatomical collar (see paragraph 2.3.1) and surgical tape inside an isoflurane-filled plastic container with a 2 mm thick lid. The immobilization in a certain position was required to maintain the anatomy as close as possible to the one assumed during irradiation. The beam was coming from the top, arriving to the back of the animal. The dose rate of 5

Gy/min was achieved by adjusting the distance from the source to the animal, and the dose at the animal position was verified using an ionization chamber (PTW, Freiburg, Germany). Brass collimators (2.5 cm thickness) were used to shield the animal body, while irradiating only through a 1.5x1.2 oval opening in the cervical spinal cord area, where the tumours were located. The doses selected in this study were: 0 (sham irradiation), 5, 10, 15, 20 Gy, to find the dose leading to tumour control and the one causing damage to the spinal cord. Figure 20 shows representative pictures of the setup.

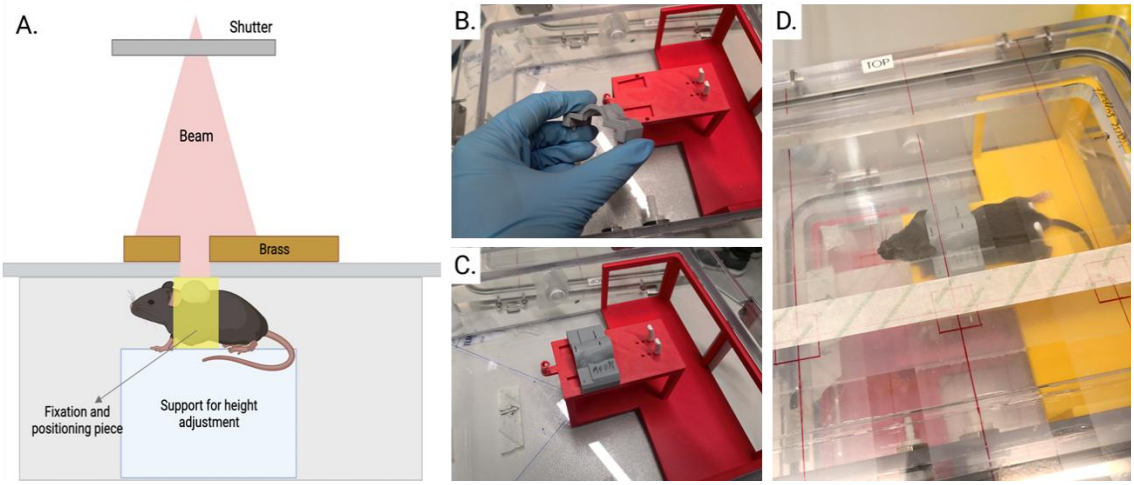

Figure 20. Photon irradiation setup. A) Graphical representation of the photon irradiation setup, where the body of the animal was shielded by a brass collimator to avoid delivery of unnecessary dose. B-C) Height adjustment support created with the SIRMIO bed geometry to resemble the positioning inside the μCT, with anatomical collar for immobilisation. D) Mouse anaesthetised and positioned in the setup. Created with BioRender.

2.4.2 ^{11}Carbon ions irradiation

For the BARB experiment, a specific beamline has been set up at GSI to deliver RIBs with an intensity sufficient to treat a tumour-bearing small animal. An important background regarding beam production and characterization, beamline architecture, dosimetry, Monte Carlo simulations and PET detection has been the focus of the project prior to realizing the final biological experiment.

2.4.2.1 Treatment and beamline planning

FLUKA Monte Carlo[114] is general purpose tool for calculations of particle transportation and interaction with matter, and it was used for delineating beamline components such as shielding, range modulator, collimator, and anatomical compensator (see next paragraphs); it also supported the dosimetry and data analysis.

To prepare the treatment plan, firstly the tumour growth was checked at the CT, and the individual GTVs were manually contoured using the 3D Slicer 5.0.3 software[115]. The sum of all the individual GTVs obtained during the tumour model establishment experiments (3.1) created the generalised CTV, which accounted for the biological variation in tumour locations and dimensions (see Figure 21). The CT scans gave also information about the location of the tumour with respect to the OARs, which were also contoured to create a uniform treatment plan that was used for all the treatments. As mentioned in paragraph 2.3.1, the anatomical immobilisation devices (compensator collar) were created from the CT scan to ensure a reliable and reproducible treatment outcome. They were used to

immobilise the animal during irradiation and to shape the beam entering the body according to the planned CTV, as it can be seen in Figure 22; more details on the production ca be found in 2.4.2.3. Afterwards, the µCT scans and the CTV were imported in FLUKA, to create simulations to define the optimal beam parameters for the irradiation and predict dose and PET signals.

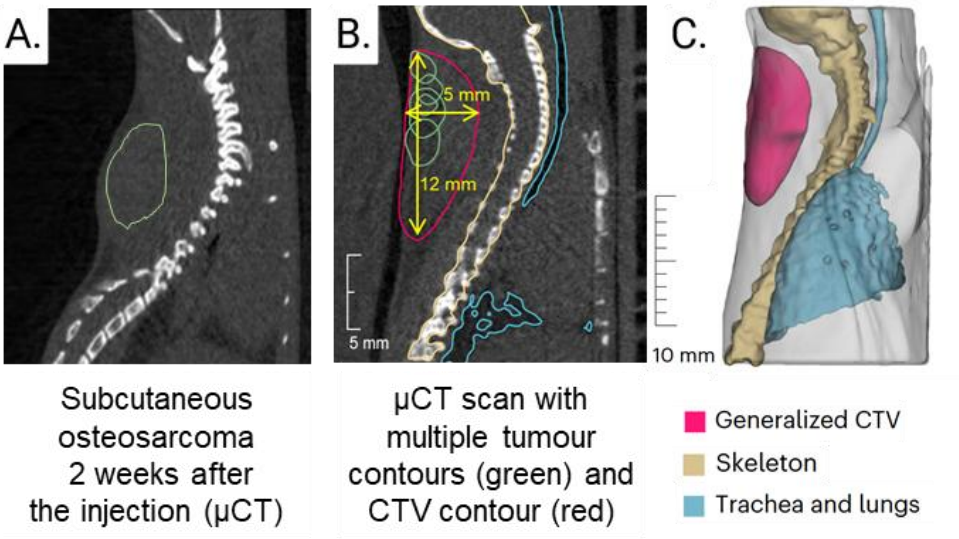

Figure 21. CT scan with tumour and CTV. A) Representative µCT scan of the cervical neck area, with the bones of the spine in white and the body of the mouse in grey; the tumour volume is contoured in green. B) µCT scan depicting the contours of the individual tumour GTVs near to the OARs (spine in yellow, trachea and lungs in blue). The generalised CTV (red) was applied to all the animals. C) 3D representation of the CTV and OARs. The CTV contours were smoothened and made symmetrical with respect to the spine to account for further biological variations, and all the animals were treated using this CTV. Adapted from Boscolo *et al.*[108].

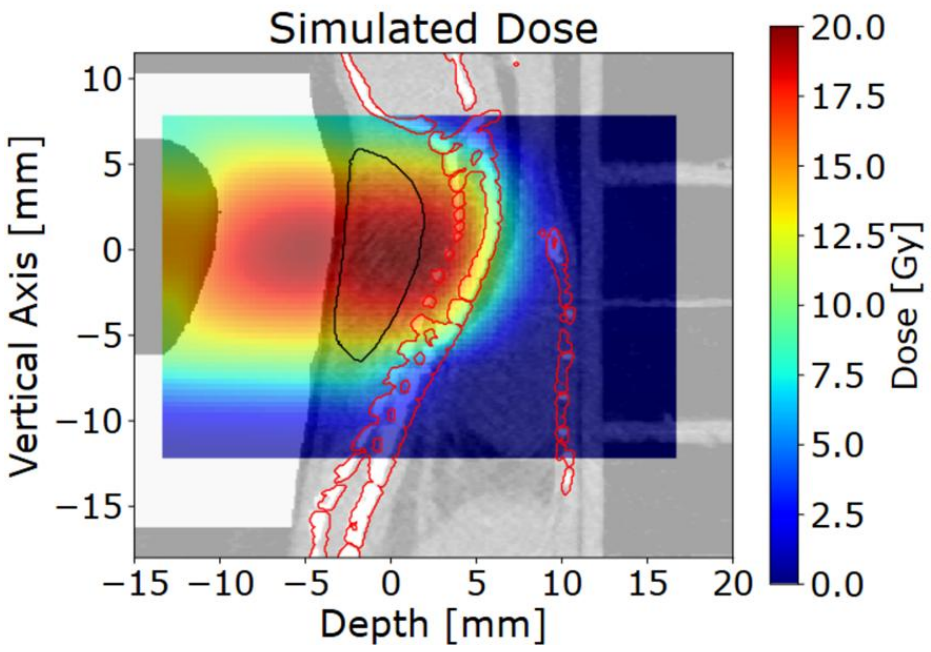

Figure 22. Treatment planning and FLUKA dose simulation. Representative example of a FLUKA simulation of the ^{11}C treatment (expected dose deposition), overlayed with the µCT scan of a mouse fixed with the anatomical compensator collar; the distal part of the SOBP is shaped to the tumour CTV thanks to the shape of the cavity in the collar. Adapted from Boscolo *et al.*[108].

2.4.2.2 ^{11}Carbon beam production

Starting from a 300 MeV/u ^{12}C primary beam generated at the SIS18 synchrotron (intensities up to ~ 1.6×10^{10} particles per spill)[108], the ^{11}C beam was produced via in-flight separation by having the primary beam hit an 8.045 g/cm^2 thick beryllium target at the FRagment Separator (FRS) and undergoing peripheral nuclear reactions, where some of the nucleons are stripped off. The consequence was the production of lighter isotopes, among which the ^{11}C ions were selected based on the magnetic rigidity and the energy loss, using a wedge-shaped degrader located at the central focal plane at the FRS. The resulting isotopically clean ^{11}C beam was then carried to Cave M via the dedicated FRS branch (see Figure 16), with a final intensity of $2.5 \cdot 10^6$ particles per spill and an energy of 209 MeV/u[108].

2.4.2.3 BARB beamline

A dedicated beamline was designed to passively shape and optimize the beam according to the planned treatment, to obtain the right dose-depth distribution, irradiate the animals and acquire the activity data with SIRMIO. To attenuate the beam energy and reach the desired depth in the mouse body, a 28.37 mm thick aluminium degrader was used. A 2D range modulator[116] for generating a 1.2 cm SOBP was 3D-printed with a 3D Systems ProJect MJP 2500 Plus, using VisiJet M2S-HT250 (printing material) and VisiJet M2 SUP (supporting material). The Bragg peak position was further adjusted by using a range shifter equipped with polyethylene plates. To shape the beam laterally, a brass collimator with 15x12 mm elliptical opening was used, and other two brass plates were added to shield the SIRMIO PET from stray radiation.

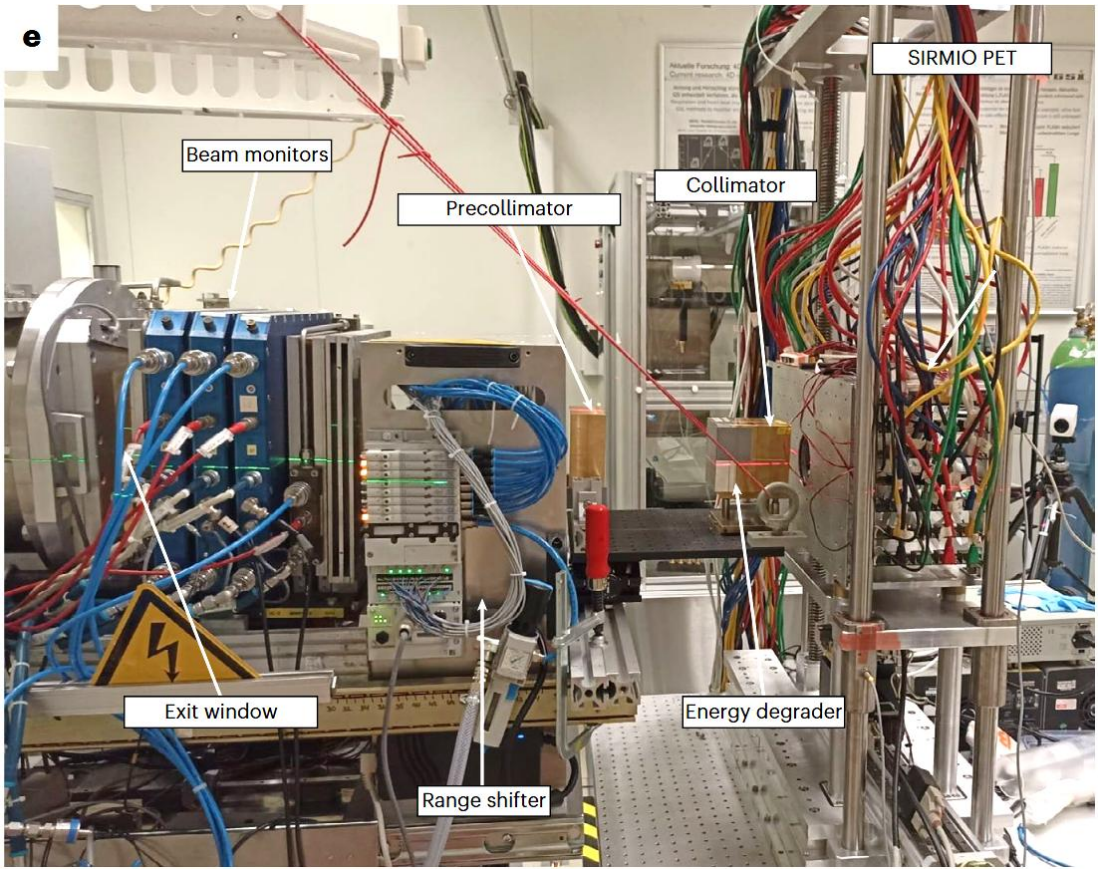

Figure 23. BARB beamline. BARB setup, delineated by modulator, range shifter, energy degrader, collimators and SIRMIO PET (from Boscolo *et al.*[108]).

The tumour CTV was covered by the distal part of the SOBP thanks to the specific design of the anatomical compensator (white shape on the left hand side of Figure 22, Figure 41), which also reduced the energy of the incoming beam in the irradiation area. Multiple copies of compensators were produced in the same way as the range modulator, comprehending the anatomical one to fix the animals during irradiation, to shape the beam according to the treatment plan, and to stop the beam in the necessary position (paragraph 2.4.2.1). Anesthetised mice were immobilized onto an enclosed bed in vertical position; before turning on the beam, the SIRMIO PET was lowered around the bed for the in-beam PET signal acquisition.

2.4.2.4 Dosimetry

Upon reaching the experimental room, the beam was monitored by the means of a large parallel plate ionization chambers and characterized using a PTW Peakfinder (PTW, Freiburg), and a water phantom equipped with an OCTAVIUS 1600 (PTW[117]). The range modulator was tested in this phase to produce the 1.2 cm SOBP in water. To ensure the correct dose delivery to the animals, in the end, a compensator with a custom holder for the small volume PinPoint ionization chamber (PTW TM31023) was used for dosimetry.

2.4.2.5 SIRMIO gamma-PET detector

The SIRMIO PET detector[118] has been developed at LMU (SIRMIO project, ERC grant nr. 725539 to Prof. K. Parodi). It´s a spherical high resolution PET scanner, equipped with 56 3-layers depth-of interaction (DOI) detectors positioned along the internal side of the sphere, which has an inner diameter of 7,2 cm. Each detector is made with a LYSO scintillator block, with a pixel size of 0.9 mm readout by an 8x8 SiPM array.

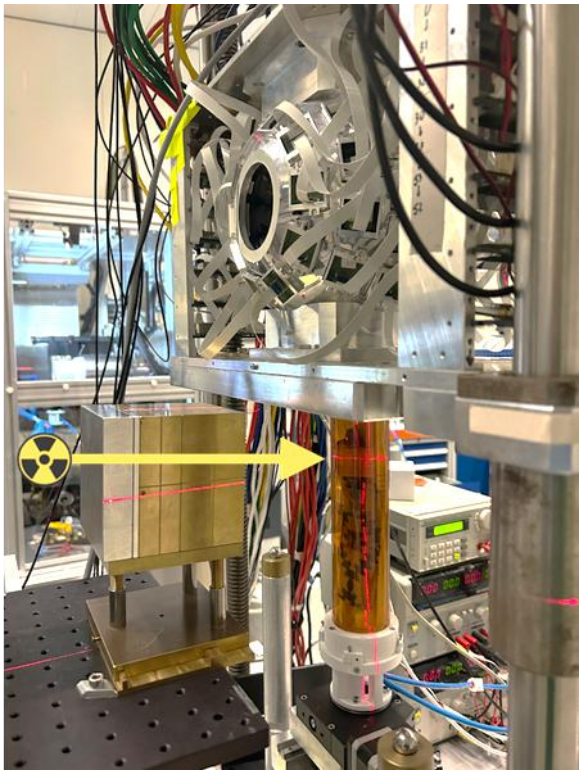

Figure 24. ^{11}C irradiation setup. Mouse fixed on the SIRMIO bed and positioned in front of the beamline, with the back facing the beam exit; the same configuration was used for both the

experimental campaigns. SIRMIO was manually lowered after positioning the mouse bed and before the irradiation, to permit the in-beam PET measurements.

Data acquisition was done using two R5560 digitizers (CAEN, Italy) with a customized software, that was set in order to stream out and reconstruct the list mode data in cycles of 60 seconds. In this way, it was possible to monitor the irradiation build up and decay and to visualize the reconstructed beam stopping position in an almost "real-time" fashion, using an in-house developed Ordered Subset Expectation Maximization (OSEM) algorithm. The resulting 3D activity maps and the wash-out analysis, instead, were obtained with the MLEM algorithm (3D maximum likelihood expectation maximization model). To precisely centre SIRMIO to the rest of the setup, a compensator holding a radioactive source (Na^+) was mounted on the mouse bed to simulate the area where the activity would have been found after irradiation. For this application, the μCT scans were also used for the PET image co-registration and to plan the irradiations, and compared afterwards with the obtained PET experimental data.

2.4.2.6 Pre- and post-irradiation animal healthcare

Mice were prepared for the irradiation by inducing the anaesthesia via 2,5% isoflurane inhalation. Afterwards, an intraperitoneal injection of isotonic saline solution was administered to keep them hydrated during irradiation and PET signal acquisition (approximately 20 minutes + 1 hour), and the eye ointment was applied. Afterwards, they were enclosed in the SIRMIO bed and transferred to Cave M, where they were either directly fixed in front of the beamline (beamtime 2024) or scanned at the SARRP and then moved to the beamline (beamtime 2025). Here the anaesthesia maintenance dose was 1,5%. After irradiation and PET signal acquisition, they were taken out of Cave M and transferred back to the laboratory, where they were let to recover in a cage illuminated by an infrared light for warming them and with HydroGel (ClearH_2O, Westbrook, Maine, USA) available for rehydration. This long exposure to anaesthesia was a stressful procedure, but all the animals recovered without issues and no animals were lost during it.

2.5 Health status and follow-up

The animals were checked daily for their health status, in compliance with the German Federal Law for animal experiments. Any change in appearance, behaviour, social aspects and health was reported and the necessary countermeasures taken. The follow-up periods of the experiments described in this work varied from one week to 6 months, with further details specified in each section.

2.5.1 Weight scoring

The animals were weighted weekly during the scheduled cage changes, using a standard laboratory scale. This moment was used also for inspecting the animal health status. If a decrease in weight was noticed, DietGel® Boost food (ClearH_2O, Westbrook, Maine, USA), a high calories dietary supplement, was supplied in addition to the normal food. If the animal weight dropped below 20% compared to the previous week, termination of the animal was required by law.

2.5.2 Tumour volume measurements

The tumour shape is assumed to be an ellipsoid, with the volume calculated as:

$$V = \frac{4}{3}\pi abc$$

where *a* and *b* are the length and width of the tumour, and *c* (depth) is assumed to be the average of *a* and *b*, respectively. After inoculation, the tumour volume started to be measured with the calliper at week one, once it became visible. Measurements were repeated twice per week up to 28 days post irradiation. For the µCT measurements, instead, these were taken once per week and the tumour mass was contoured manually using Slicer software, as described in 2.4.2.1. The tumours were contoured on several slices, then the volume was extrapolated with the segmentation tool. Both measurements (calliper and CT) were plotted and compared to double check the growth trends.

2.5.3 Metastases presence check

Given the possibility of metastatic growth in this model, the animals were weekly checked for the presence of metastasis by palpation of the abdominal area in the case of metastases growing in the liver, intestine or kidneys. For the lungs, instead, monthly µCTs with the usual protocol were taken to control if some metastases started to grow in this location, or around the head and neck area.

2.5.4 Skin toxicity scoring

The toxicity of the skin in the irradiated area was scored using a simplified grading system of the Gesellschaft für Versuchstierkunde (GV-SOLAS) guidelines, divided by five grades (Table 5).

Table 5. Scoring system used to determine the radiation-induced skin toxicity in irradiated animals, adopted and simplified from the Gesellschaft für Versuchstierkunde (GV-SOLAS) guidelines.

Grade	Manifestation
0	No effect
1	Mild inflammation and dry skin, or white fur regrowth post irradiation
2	Moderate inflammation, desquamation
3	Acute inflammation, closed wounds or crusts
4	Open wound failing to heal
5	Necrosis

From a grade 2 the animals were monitored daily and treated with a topical treatment (Bepanthen®, Bayer) to avert the worsening of the skin condition, if the dry skin started to demonstrate signs of inflammation. Grade 3 burns were still reverted with the application of the topical cream, while in the case of open wounds (grade 4) the topical treatment was ineffective, and lead to the termination of the animal. Grade 5 was never observed. During the six months follow-up some animals partially lost patches of fur all over the body, but upon investigation this was unlikely a sign of stress (no wounds, all the whiskers still

present) but rather a combination of the natural tendency of this strain to develop alopecia areata with aging, especially in females[119], and a systemic effect caused by irradiation.

2.5.5 Oesophagus toxicity scoring

The toxicity of the oesophagus in the irradiated area was scored using a simplified grading system of the Gesellschaft für Versuchstierkunde (GV-SOLAS) guidelines, divided by four grades (Table 6). The supportive care (*e. g.* administration of Boost food) was initiated when a grade 1 was showing, while the termination criteria applied upon reaching grade 3.

Table 6. Scoring system used to determine the radiation-induced oesophagus toxicity in irradiated animals, adopted and simplified from the Gesellschaft für Versuchstierkunde (GV-SOLAS) guidelines.

Grade	Manifestation
0	No weight loss compared to the previous week; breathing undisturbed
1	10% weight loss; breathing undisturbed
2	15% weight loss; accelerated breathing
3	20% weight loss; marked breathing difficulties

2.5.6 Paralysis and spinal cord damage assessment

Since the cervical spinal cord served as the late-responding organ at risk in this study, several tests have been implemented to observe and quantify the development of radiation-induced side effects. Considering the irradiation of the cervical area of the spine, we expected to observe the majority of the side effects in the front limbs of the animal and in the posture[120,121], as it can be seen in the example in Figure 25.

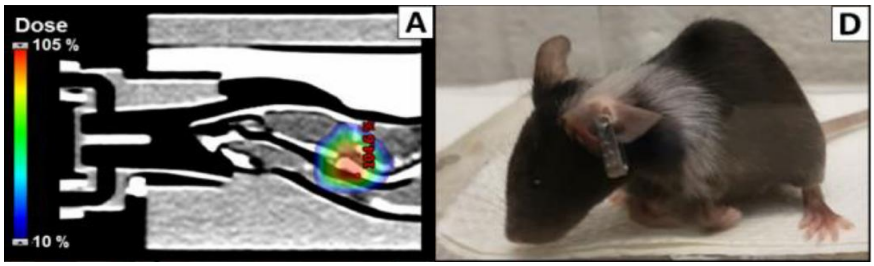

Figure 25. Mouse treated with proton irradiation in the cervical spinal cord. The side effects include paresis of the forelimbs, splaying of the hindlimbs and kyphosis. Adapted from Denbeigh *et al.*[120].

2.5.7 Grip strength test

This motor-function test takes advantage of the natural tendency of rodents to grab any kind of supporting surface they are presented to when suspended by the tail. The purpose is to measure the strength of the animal´s limbs by letting it grab a bar or a mesh surface while pulling it backwards by the tail, up to the point where the strength of the animal cannot counterforce the strength of the operator pulling it back[122]. To measure the strength, the Grip Strength Meter-47200 form Ugo Basile® was used. The device has a selection of objects the animals can grab, which are connected to a Newton meter and a recording device. Upon

release of the grasp, the device measures the peak force in Newtons. The provided software records the peak forces, which can be exported for further analysis. To ensure collaboration, the animals were trained five times on two different days on the device prior to irradiation. After the treatment, the test was repeated every two weeks to avoid habituation, and three successful trials (both front paws grabbing the bar) were recorded and averaged for each animal. Figure 26 shows an example of the grip meter and how the test is conducted.

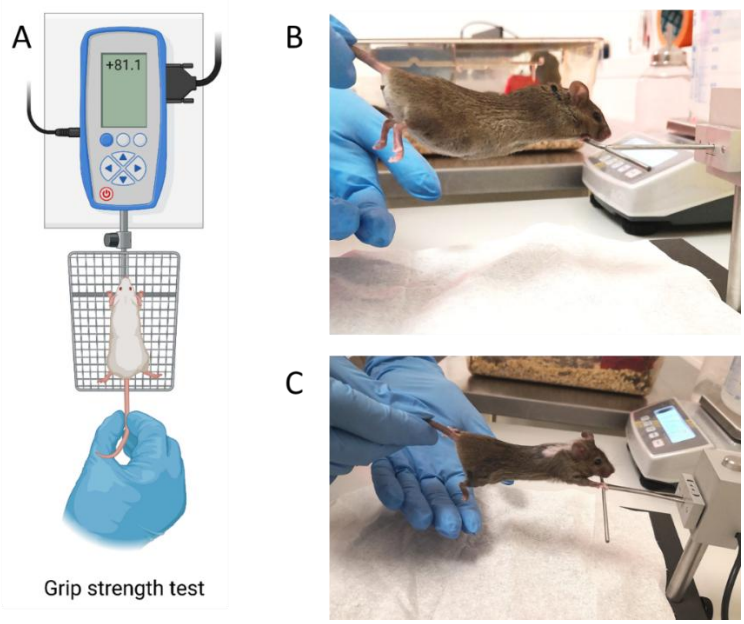

Figure 26. Mice on grip meter performing the grip strength test (A). In B and C, a control mouse an and irradiated one (recognisable because of the white fur growing in the irradiated area) are shown from the lateral and top view. Created with BioRender and published in Boscolo *et al.*[108].

2.5.8 Walk test

To observe the movement capability of the animals after treatment, an in-house setup was created based on the rat mobility testing apparatus PRanCeR (Paw Print analysis of Contrast-Enhanced Recordings, Bounds *et al.*)[123]. The setup was modified to accommodate mice experiments and is described in Figure 27. A video was recorded for each animal every two weeks and analysed with the software developed in the publication, with some changes to the code to adapt it to the changes made in the setup. The test is made by recording the animals walking, and investigating the significant differences in the gait pattern between control mice and treated ones. Animals were taken from the home cage and placed in the entrance area, allowing them to freely walk along a transparent corridor that ended in a loop structure, designed to make them walk back to the corridor. The camera (GoPro Black 7) was placed underneath the corridor, that was lit with LEDs along the side and covered in white matte paper. These specific light conditions and matting of the floor of the corridor allowed to create shadows of the paws, while excluding the shadow of the bodies of the animals. This criterion was required in the PrAnCER software used for the automated analysis of recorded videos, which specifically analyses the "paw-prints" created by these shadows. This test comes from what is known historically as "ink test", where the paws of the test animals were painted in different colours before letting the animals walk on stripes of white paper, leaving a printed image of the gait pattern that could be further analysed for changes in step length, stride length, positioning of the rear paws relatively to the hind paws etcetera[124].

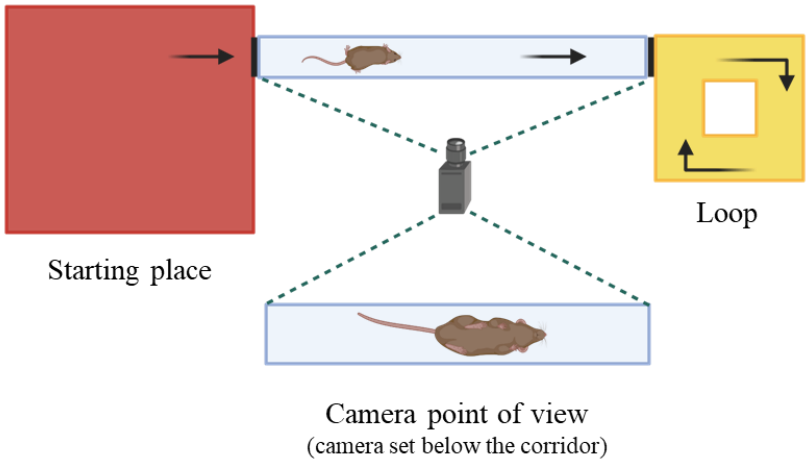

Figure 27. Mouse mobility testing apparatus used for the walk test. In this case, the camera is set below the corridor to record the paws during walking. Adapted from Bounds *et a.l*[123]. Created with BioRender.

Acclimatized and non-stressed animals normally took two minutes to complete the test, which consisted in recording at least three successful runs along the corridor; in any case, the total time the mice were left in the setup never exceeded five minutes. A run was considered successful if the animal wasn't stopping or going back along the way.

2.5.9 Kyphosis

Using a small modification of the setup described in 2.5.8, the mice were filmed from the side of the corridor while walking, grooming, rearing; their overall posture was observed as in Figure 28.

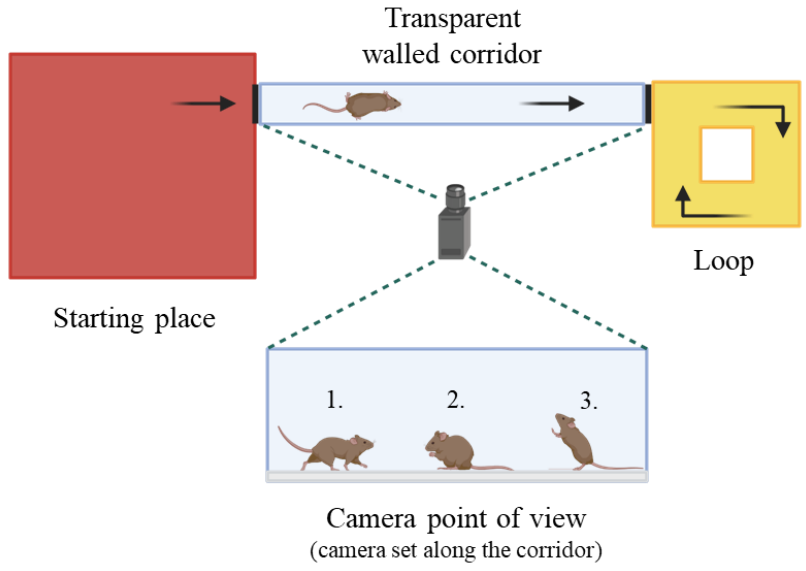

Figure 28. Mouse mobility testing apparatus for kyphosis scoring. In this case, the camera is set parallel to the corridor to observe a full set of behaviours and to score the mobility of the spine. Adapted from walk test apparatus (Figure 27). Created with BioRender.

The kyphosis manifested in the symptoms described in scoring system of Yerger *et al.*[125], and the details can be found in Table 7. None of the animals had severe ambulatory difficulties and could always walk, groom and turn around. The scoring mainly describes the effect on the animal´s posture and curvature of the spine because the development of this feature is gradual, while the paralysis shows a bimodal absence-presence appearance.

Table 7. Scoring system using to determine the radiation-induced side effects caused to the cervical spinal cord, adopted from Yerger *et al.*[125].

Grade	Manifestation
0	The mouse is able to easily straighten the spine in both stationary and locomotory phase, kyphosis is not permanent.
1	The mouse exhibits kyphosis during the stationary phase, but can extend the spine during locomotion.
2	The mouse can´t straighten the spine completely, maintaining persistent mild kyphosis in both phases.
3	The mouse shows persistent and pronounced kyphosis in both phases.

2.6 Histology and immunohistochemistry

Histology and immunohistochemistry are techniques that permit to analyse tissues or entire organs, considering the size of the organs of mice. Through a series of staining steps, it´s possible to highlight different parts of the tissues, distinguish the structures and different layers and to score the presence of pathological features.

2.6.1 Euthanasia and histological samples collection

To harvest the organs for further analysis, the animals were sacrificed via *ex vivo* intra-cardiac perfusion. Following one 20 minutes long final µCT scan (the longer time was needed to achieve a higher resolution) under 1,5% isoflurane, an overdose of 3% isoflurane was administered, combined with an additional overdose of 0.15 mL ketamine/xylazine (120 mg/kg ketamine + 20 mg/kg xylazine) injected intraperitoneally. The withdrawal reflex was checked before spraying the mouse with ethanol and cutting open the abdominal cavity. The necessary cuts to open the ribcage and expose the heart were performed, then a butterfly needle connected to a peristaltic perfusion pump (Schenchen LabV1-III, Baoding Schenchen Precision Pump Co., Ltd, Shanghai, China) was positioned in the left ventricle. After cutting the right aorta, the pump was turned on to clear the blood out of the body with heparin sodium salt (Sigma-Aldrich, Missouri, USA) dissolved in PBS, and to fix the tissues with formaldehyde 4% (ROTI ®Histofix, Carl Roth, Karlsruhe, Germany). After fixation, the selected organs (tumour, lungs, cervical spinal cord, oesophagus) were collected. Tumours, lungs and oesophagus samples were preserved in formaldehyde 4%.

In the photon experiment and the first beamtime, the cervical spinal cord area was excised including the surrounding muscle, bone and fat tissues, and the samples were later fixed in formaldehyde 10% overnight. In the second beamtime, instead, only the cord itself was excised and preserved in formaldehyde 10%.

2.6.1.1 Vascupaint perfusion and µCT imaging of tumour vasculature

Samples for the tumour vasculature analyses were taken after perfusion of the animals with warm heparin dissolved in PBS and formaldehyde 4%. In the case of the tumours collected only for histology, the same fixation and embedding protocol of the other samples was adopted, except for the decalcification passage. If the animal was used for *ex vivo* vascularization imaging at the µCT, the Vascupaint^{TM126} contrast agent was injected via perfusion (yellow colloidal bismuth suspension, MediLumine, Canada). In this case, the samples were dissected after 24 hours to allow the compound to polymerize. Afterwards, extracted tumour and spinal cord samples were scanned at high resolution (10 µm) with tube voltage of 55 kVp, current of 145 µA, 0.5 mm aluminium filter, 1500 projections per 180° with 600 ms integration time per projection. To obtain a 3D reconstruction of the vasculature, the scans were analysed using the 'Bone trabecular morphology' analysis module of the Scanco built-in software, based on the protocol found in literature[127].

2.6.2 Preparation of frozen sections

The frozen sections were prepared for the samples collected up to the first beamtime, since at that time it was not possible to perform the preparation of paraffin sections. The fixed samples were dehydrated in growing gradients of sucrose solution (10%, 20% and 30% in PBS, Roth, Karlsruhe, Germany). An additional treatment step was required for the spines, which contained bone parts that needed decalcification. This was done by placing the samples in 14% EDTA solution (Carl Roth, Karlsruhe, Germany) for three weeks. After the last solution, all the samples were embedded in the Optimal Cutting Temperature Compound (OCT Embedding Matrix for Frozen Sections, CellPath, Roth, Karlsruhe, Germany) by first being cut into slices and then placed into cryomolds (vinyl Tissue-Tek® Cryomold®, Sakura Finetek Inc., Torrance, CA, USA). The cryomolds were let to cool down to -22˚C for at least four hours, and then transferred to the -80˚ C freezer for long-term storage. To soften the samples for cutting, they were taken out of the -80˚ C freezer at least two hours prior and transferred to the cryostat, with the temperature set at -22˚C. Upon use, they were mounted on the cryostat holder to cut slices of 8 µm, then were collected on glass slides (Microscope slides, adhesive and silanized, 75x25x1 mm, LABSOLUTE) and let dry at room temperature for 30 minutes. Afterwards, they were stored at -22˚C until staining. For every staining described, the frozen sections were taken out of the freezer, let soften at room temperature for 10 minutes, fixed in formaldehyde 4% for 15 minutes, rinsed in PBS for 5 minutes and then stained.

2.6.3 Preparation of paraffin sections

This protocol was used for the samples of the second beamtime. The fixed samples were preserved overnight in formaldehyde 4% (10% for the spinal cords) and then transferred to EtOH 70% as a pre-dehydration step. The full dehydration process was performed using the HistoCore Pearl dehydration station (Leica Biosystems, Germany) in the following sequence: 4% formalin, water, 70% EtOH, two times 95% EtOH, three times 100% EtOH, three times xylol. After dehydration, the samples were embedded in ParaPlast Plus (Leica, Germany) and positioned in histological cassettes for cutting. The samples were sectioned in 5 µm thick slices with a microtome (Leica RM2235, Germany) equipped with C35 Type blades (Feather, Japan) and mounted using the floating method on glass slides. After overnight drying, the slides were stained with different staining protocols, according to the type of samples. For every described staining, the slides were first deparaffinized, re-

hydrated trough ascending gradients of ethanol (100%, 96%, 70%), then rinsed in deionised water; the only exception was the Luxol Fast Blue staining (paragraph 2.6.8).

2.6.4 Haematoxylin-eosin staining (HE)

The haematoxylin (Haematoxylin Solution, Gill No. 3, Merck) and eosin (Eosin-G Lösung 0.5% in water, X883, Roth, Germany) protocol was used for staining all the samples (tumours, lungs, spinal cords, oesophagi) and obtain information about the morphology. Haematoxylin stains nucleic acids in deep blue-purple, while eosin stains cytoplasm and extracellular matrix in pink[128]. After the water rinse, the slides were quickly immerged in haematoxylin for 3 seconds, then rinsed for 2 minutes under tap water. The next step was in eosin for 2 minutes, to which a drop of glacial acetic acid was added to each 100 mL of solution. To remove the excess of eosin, the slides were quickly rinsed in three changes of ethanol 80%, before being dehydrated in ethanol 95% and 100% for 5 minutes each. The last steps were two washes in xylol (5 minutes each) for clearing, and mounting with Eukitt (Eukitt® mounting agent (non-aqueous), Merck, Germany) by covering the slides with coverslips (Cover Slips, 24x60 mm, Epredia, Germany) after which the samples were let to dry overnight under the chemical hood.

2.6.5 Perls' Prussian Blue staining

To check for the presence of haemosiderin deposits, which are a sign of haemorrhage, the Iron stain kit (Sigma-Aldrich, Germany) was used. Perls' Prussian blue is a dye that binds to the non-haeme iron contained in haemosiderin deposits and is used to detect haemorrhage sites[129]. After the water rinse, the slides were kept for 10 minutes in the iron stain solution, washed under tap water for 2 minutes and counterstained for 3-5 minutes in pararosaniline solution. After a quick rinse in deionized water and a 1-minute wash in ethanol 80%, the slides were dehydrated in ascending ethanol solutions, cleared in xylol and mounted with Eukitt.

2.6.6 Goldner trichrome staining

To assess the presence of fibrosis in the oesophagus and the spinal cords surrounded by muscle, bone and fat tissues samples, the Goldner Trichrome Stain (Sigma-Aldrich, Germany) was used. The nuclei are counterstained with haematoxylin, the cytoplasm and muscle fibres in red, erythrocytes in orange and the connective tissues in green[130]. The procedure up to EtOH 95% were the same as described before. Afterwards, a pre-set in Bouin fixative solution (Carl Roth, Germany) for 1 hour in an oven set at 37˚ C was performed to prepare the slides for the trichrome differentiation. The slides were then rinsed under tap water for 2 minutes, stained with haematoxylin for 3 seconds, and rinsed under tap water for 2 minutes. Next, samples were quickly washed of 30 seconds in acetic acid 1%, and a similar step was performed between all the three other stains used in this protocol. The first is an azophloxine solution, kept for 10 minutes, followed by 1 minute of tungstophosphoric acid orange G solution and 2 minutes of Light green SF solution. After the last acetic acid wash, the samples were washed for 30 seconds in ethanol 70%, ethanol 96%, twice in ethanol 100%. To conclude, a wash of 2 minutes in ethanol 100% was followed by the steps in xylol and the mounting with Eukitt.

2.6.7 Luxol Fast Blue myelin differentiation

Luxol Fast blue (Sigma-Aldrich, Germany) was used to stain the spinal cord samples and to assess the presence or absence of the myelin. The dye binds to the myelin sheath found around nerve fibres and stains them in blue; demyelinated areas appear white[131]. The slides were deparaffinized and rehydrated up to 95% EtOH. The slides were stained in LFB overnight at 60°C, rinsed in 95% EtOH and distilled water, then differentiated in lithium carbonate for 5 seconds and rinsed in two changes of 70% EtOH for 10 seconds each. This step was repeated until the white matter was clearly distinguished from the grey matter. After another wash in 70% EtOH, the slides were stained in Eosin for a minute, rinsed in distilled water, counterstained in Cresyl violet for a minute (nucleic acids stained in light purple), rinsed in water and then dehydrated through ascending ethanol solutions and cleared in xylol, then coverslipped.

2.6.8 Immunohistochemistry (IHC)

Immunohistochemistry has been used to assess the expression of specific markers in a tissue. The paraffin-embedded sections were used, and the protocol started with the deparaffinization and rehydration, as described above. The Akoya staining kit was used through the procedure, starting by the antigen retrieval step using an antigen retrieval chamber (DCARC0001, Biocare Medical) at 95°C with AR9 buffer (Akoya 10xAR9, pH = 9, Akoya, Marlborough, MA). The slides were then cooled down and the samples circled with a hydrophobic marker before blocking with 0.3% H_2O_2 for 15 minutes. After 3x3 minutes washing with TBST, the slides were treated with blocking buffer for 15 minutes, washed once in TBST and then incubated with the primary antibody at the necessary dilution for 1 hour. Afterwards, the slides were washed 3x3 minutes with TBST and then incubated with an HRP-conjugated secondary antibody (1:1000, Goat Anti-Rabbit IgG H&L HRP, ab6721, Abcam) for 1 hour. At the end of the incubation, the slides were washed as before and stained with DAB chromogen (BD Biosciences, San Diego, CA) for 5 minutes, then rinsed in tap water, counterstained with haematoxylin for 3 seconds and rinsed in tap water for other 2 minutes. The resulting slides were coverslipped with Aquatex® and let dry before acquisition. The cell nuclei are stained in blue because of the haematoxylin, while the cells expressing the selected marker become brown following the deposition of the DAB chromogen.

Table 8. List of antibodies used in IHC staining.

Primary antibody	Technical details	Concentration
Ki67 – Marker of Proliferation Ki67	Cell Signalling Technology, Inc., d385 Rabbit mAb	1:400 in IHC (Paraffin sections)
Beta-catenin	Abcam, AB32572 Rabbit mAb	1:500 in IHC (Paraffin sections)
MBP – Myelin Basic Protein	Abcam, AB218011 Rabbit mAb	1:5000 in IHC (Paraffin sections)
NF – Neurofilament	Abcam, AB207176 Rabbit mAb	1:1000 in IHC (Paraffin sections)

2.7 Histological pictures acquisition

The photographs of the histological samples were taken with either the optical microscope Olympus BX61 (camera: Olympus EP50; ocular lenses: WH1010×; objective lenses: UPlan FL N 20×/0.50 Ph1∞/0.17/FN26.5), or the automated scanning microscope Metafer (CoolCube4 camera, Neon software version 4.3.7, MetaSystems, Germany), or the Akoya PhenoImager (Akoya Biosciences, Marlborough, Massachusetts, USA) with the Fusion 2.3.1 software, using a 10x or 20x magnification.

2.8 Statistical analysis

To determine the sample sizes in the animal irradiation experiments, sample sizes were chosen to obtain an expected effect size (Cohen´s *d*) of d=1 using the online G*Power software (version 3.1.9.7). Animals were randomly allocated in the experimental groups.

Statistical analyses were performed using the GraphPad Prism 10.4.1 software, with differences in the values of $p < 0{,}05$ considered to be significant. For the tumour growth curves and weight curves, a 2-way ANOVA was used for the data analysis. For the grip test in Figure 68, the DataGraph software version 4.5.1 was used, and the analysis comprehended the Mood´s test, Mann-Whitney test, Pearson´s test, and 2-way ANOVA.

Another software used is the open-source software for bioimage analysis QuPath[132], version 0.6.0. QuPath was used to measure the thickness of the epithelial layer in the oesophagus slides, and to analyse the histological sections from IHC by observing the presence of positive cells. For the plots in Figure 79, data visualization and analysis were performed in Python 3.10 using the Seaborn and SciPy libraries. Python was also used (itertools library) to perform a non-parametric permutation test comparing the full distribution of per-mouse normalized probability density curves. In the figures with column plots, instead, the unpaired two-tailed t test was used, with difference between values considered to be significant when $p < 0{,}05$ The statistical analyses are specified in each figure caption.

3 Results

The tumour model required for the irradiation experiments and presented in this work needed to exhibit specific characteristics, including proximity to an organ at risk, the presence of a vascular network capable of supporting blood flow (even if irregular, as it´s usually the case for tumours), and the possibility to distinguish its borders to enable accurate measurements. The following paragraphs will describe the preliminary experiments for creating and characterising the tumour model (3.1), the photon irradiation experiment used to establish the dose for tumour eradication and induction of toxicities (3.2), and the results from the two experimental campaigns, which demonstrated respectively the feasibility of treatment with ^{11}C (3.3) and the application of in-beam PET-guided adaptive therapy (3.4).

3.1 Tumour model establishment

Three different models have been proposed and tested: a tumour in the lung, in the leg[133,112,113], or on the back of the animals. Known from these antecedent studies, the LM8 cells injected subcutaneously in the limb generate a tumour that was visible and measurable with the calliper in one week. The first trial was conducted by injecting 20 µL of PBS buffer containing approximately $1 \cdot 10^6$ LM8 cells subcutaneously in the dorsal area of the neck in a group of animals (N = 8) and in the right lung (N = 8), with the tumour growth been followed up for 7 days. In this first week of growth, the sizes and positions of the tumour relatively to the spinal cord showed a variability that was taken into account in the treatment planning process (Figure 29). All the different tumours were manually contoured and the contours summed up to create a generalised GTV, as shown in Figure 21 in the Materials and methods section (2).

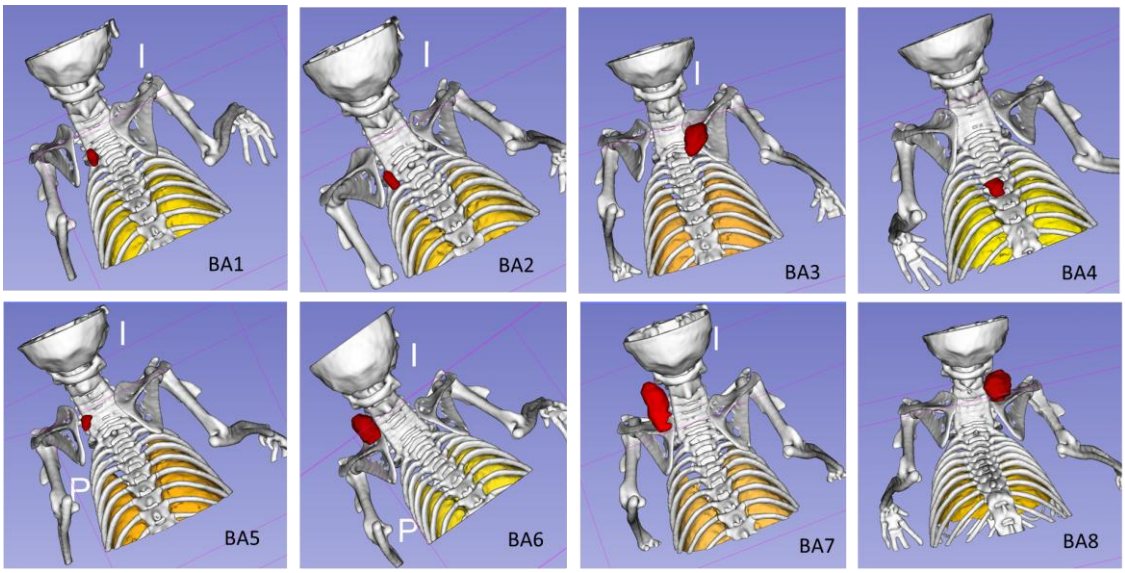

Figure 29. µCT scan Slicer 3D reconstructions of tumours. The reconstructions show the dimensions of the back tumours (red, N = 8) 7 days after inoculation as seen from the dorsal side, and their variability in position. The skeleton (including the spine) is represented in white and the lungs in yellow.

The injection in the lung was performed by mixing the cells with Matrigel as described in Zaun *et al.*[134]. However, in our case this method did not produce a tumour that could meet all the requirements, since the outcome consisted in small lesions dispersed along the inside of the pleural cavity. In the case of the back model, instead, all the animals developed a

tumour that was very small in size, so it was decided to perform another experiment with a longer follow-up (4 weeks, N = 4). In concomitance, also the limb model was tested (N = 4) for 4 weeks of growth. Figure 30 and Figure 31, respectively, show the µCT scans of the limb model and the back model.

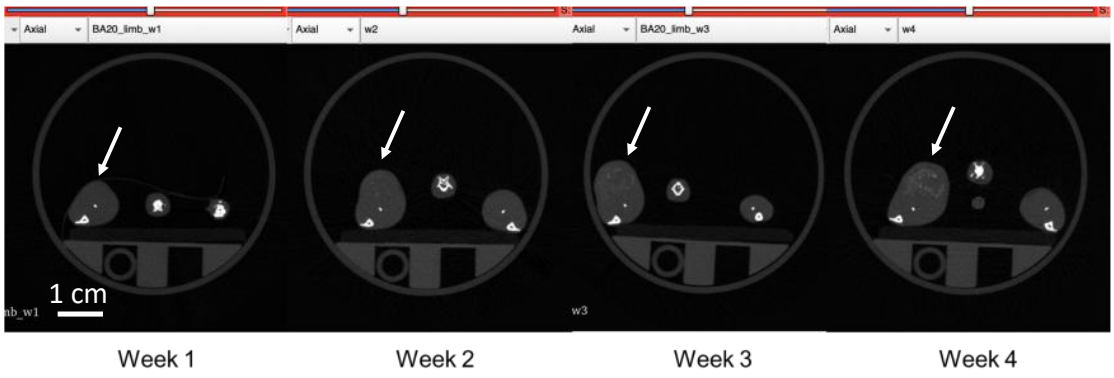

Figure 30. µCT scan (axial view) showing the growth of the LM8 limb tumour (left limb) in 28 days. Resolution: 100 µm. The white arrow indicates the tumour.

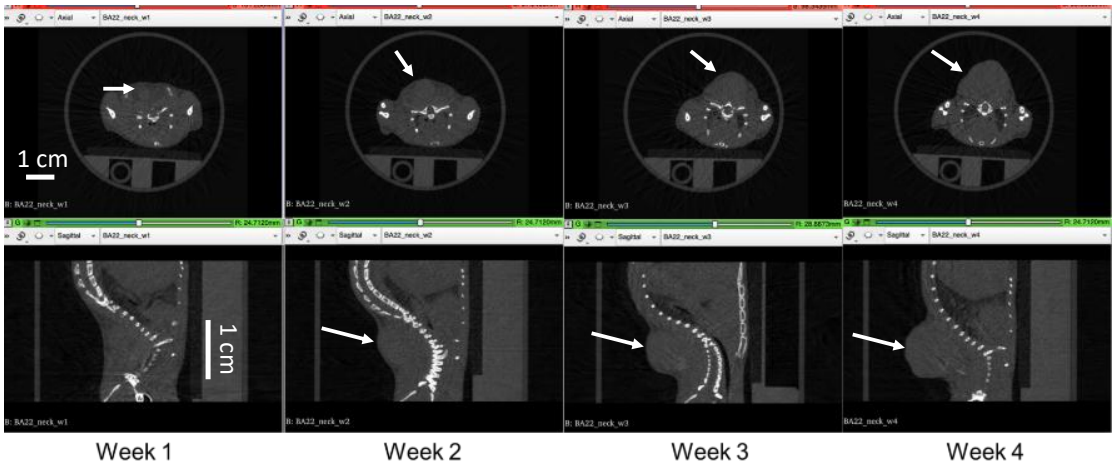

Figure 31. µCT scan (axial (above) and sagittal (below) views) showing the growth of the back model in 28 days. Resolution: 100 µm. The white arrow indicates the tumour.

3.1.1 Preliminary tumour growth curves

For all the animals receiving an LM8 cells injection, the tumours were measured by collecting two measurements with the calliper (twice per week) and by manual contouring of the tumour mass at the µCT (once per week) as described in the paragraph 2.2. In the second experiment, where four animals were injected in the limb and four in the cervical area, all the animals of the limb group grew a tumour, while two in the back group failed to grow it. A reason for this might be the clearance of the tumour cells by the immune system of the animals: the animals used in this study were immunocompetent, so even if the tumour cells were syngeneic, there might be cases in which the tumour cells are eliminated by the immune system. The immune system of mice becomes mature around 6-8 weeks post birth[135], and the animals used here received the tumour cells injection at 10-11 weeks of age. Another reason might be the location where the injection is performed, and the vascularisation present in the area that can be exploited by the growing tumour[136].

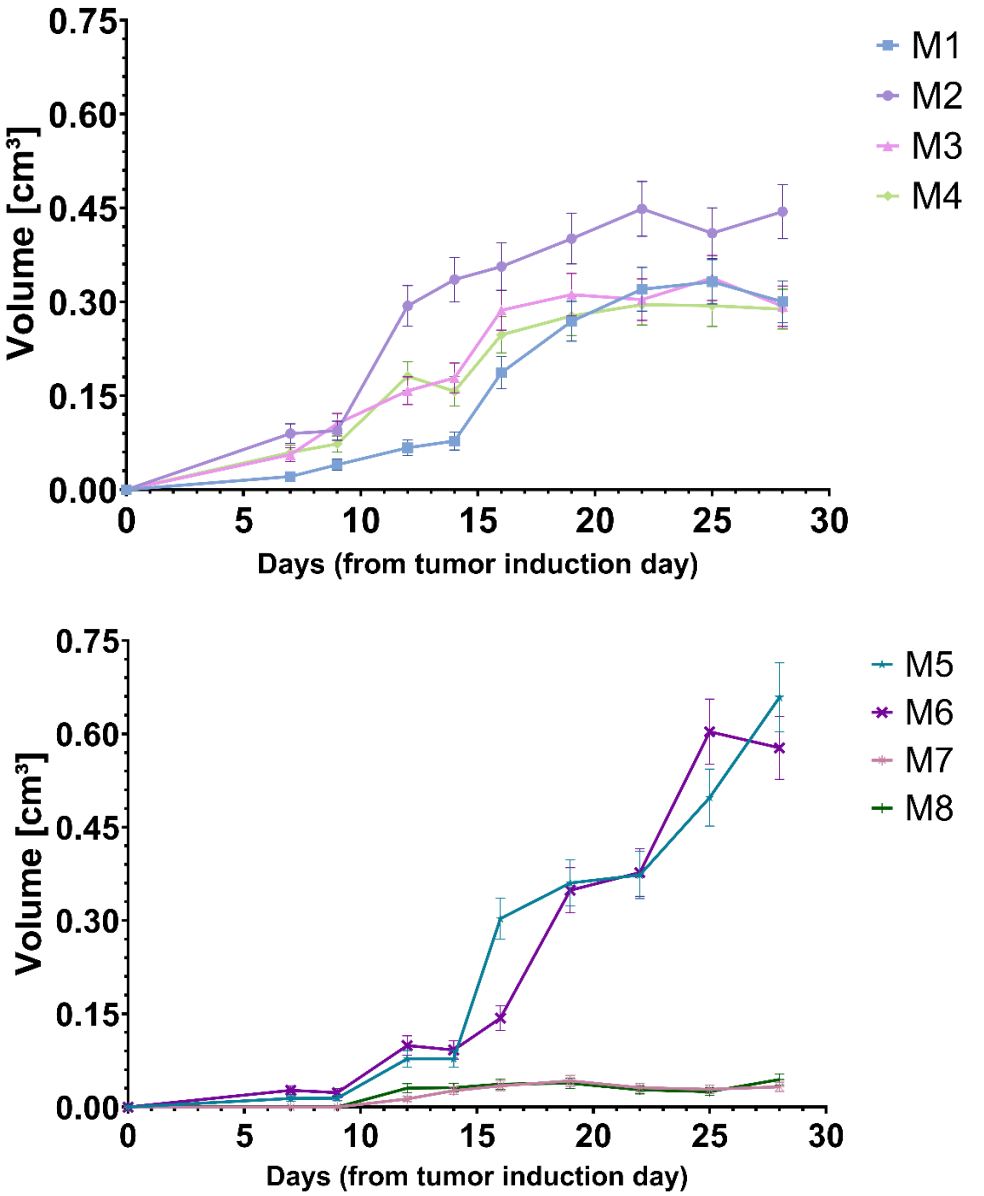

Figure 32. Tumour growth curves of the limb (above) and back (below) tumour models. The measurements were taken with the calliper for 28 days. Error bars represent the error propagation of the error of the calliper (0.01 cm) on the two measurements taken for every animal.

The limb model showed a consistent growth rate and dimension between all the animals in the group. For the back model group, instead, two animals grew a large tumour in exponential fashion from 2 weeks post injection, reaching approximately 1 cm in diameter; in the other two animals, instead, the tumour remained very small, and the area of skin above it experienced hair regrowth. Upon dissection, it was possible to find a small malignancy below the skin.

Since the tumour was not showing in all the injected animals by week two, for the photon irradiation experiment (see 3.2) it was decided to let the tumours grow up to week three post inoculation before performing the irradiation, to be sure in the cases where the tumour was apparently not developing. In the figure below, a 3-dimensional visualization of the tumour and skeleton volumes from the µCT images, contoured in 3D Slicer, shows the volumetric difference between the tumours scanned two and three weeks after injection.

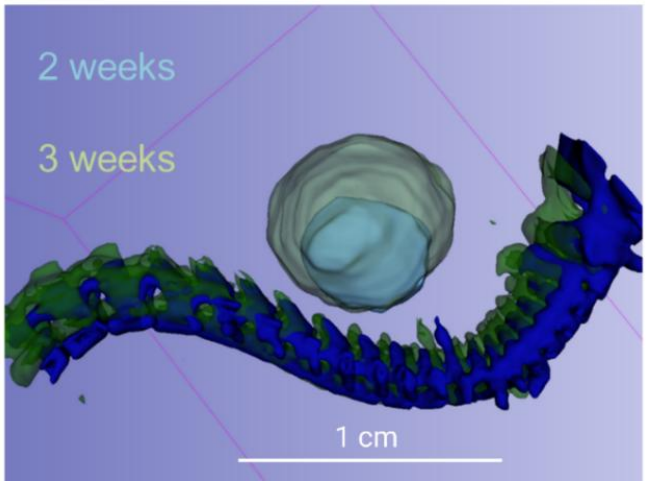

Figure 33. Slicer 3D reconstructions of the back tumour volumes. The reconstructions show the sizes at week two (light blue) and (light green) three post inoculation, with respect to the spine (blue and green).

Other three trials to assess the back tumour model viability have been performed, for a total number of 36 animals. Two animals were excluded from the analyses because of nerve damage caused during the injection, which led to premature euthanasia (1 week post injection). Of the 34 remaining animals, 5 didn't show a tumour growing, which represents the 15% of the total.

3.1.2 Examination of tumour vasculature with µCT and histology

After having recorded the back and limb model growths, the vascularisation has been studied by injecting a contrast agent for the µCT in the animals via *ex vivo* perfusion. Briefly, Vascupaint™ was injected after the formaldehyde fixation step, filling up the vasculature system of the animal. After an overnight polymerisation, the organs were extracted and scanned at the µCT at high resolution (approximately 10 µm voxel resolution). The contrast agent is bismuth-based, making vessels appear like dense structures on the CT scan and easy to distinguish from surrounding soft tissues, and permits an accurate 3D reconstruction of the vascularisation. The process is represented in Figure 34.

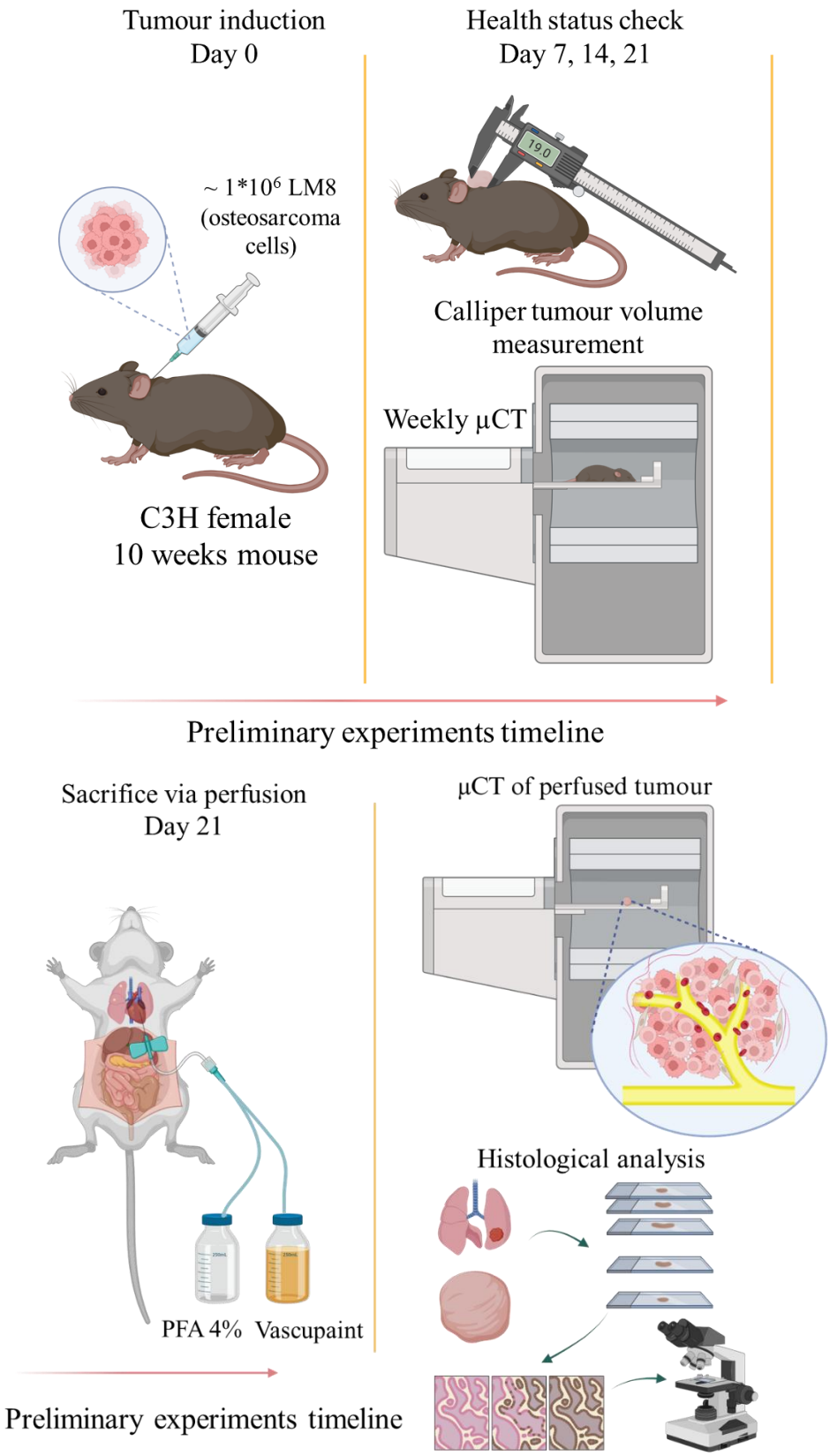

Figure 34. Preliminary experiments workflow to obtain information about the tumour vasculature. Created with BioRender.

The tumours from both models were analysed and visually compared to the kidney, a healthy organ with a clear and organised vasculature system (Figure 35).

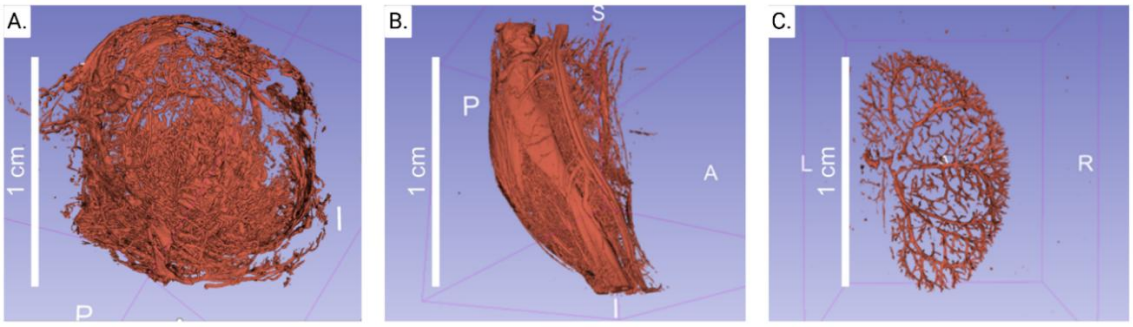

Figure 35. Vasculatures of the tumours perfused with Vascupaint. A) Back tumour model, B) limb tumour model, C) kidney µCT reconstructions obtained with the use of the Vascupaint™ *ex vivo* contrast agent.

As it can be seen in those reconstructions, the kidney vasculature showed an organised structure, with the main vessels branching into the minor vessels. In the limb model, the presence of a full network of vessels can be appreciated, but it also grew all around the tibia and the fibula. Since it was difficult to extract the bones from the samples without ruining the vascular network, this process was avoided, with the result of the 3D reconstruction showing both bones and vessels in the same way. This was also due to the fact that the Hounsfield Units for bones and Vascupaint are the same, making them impossible to distinguish from one to another. Additionally, it was difficult to discern the tumour vasculature from the one of the surrounding muscles. The back model tumour, instead, could be extracted without the presence of other organs inside of it, and it also showed a vasculature distributed both around and inside the tumour, which could be easily separated from the rest of the surrounding tissue and considered as tumour vasculature only.

After preservation, the tumour and lung samples were stained with HE staining to characterise their morphology. HE staining is the golden standard of histology[130], and is daily used in pathology laboratories to analyse biopsies. In this staining, the nuclei of cells are stained in dark blue because of the presence of DNA, which is acidic (haematoxylin), while the extracellular matrix and cytoplasm are stained in various shades of pink (eosin). In general, the structures that are basophilic stain in dark blue, while the pink ones are acidophilic.

In Figure 36 the histology of limb and back tumours (sampled at week 4 post injection) shows the unorganised structure of the organ, with no clear differentiation of the tissues. The strong presence of dark purple shows a high number of cells nuclei, meaning the tissue was actively proliferating: in fact, these tumours grew quite fast, reaching a diameter of approximately 1,5 cm in one month. The pink area reveals a zone of high content of extracellular matrix, which function is to create the structural support of the organs and to sustain the vessels. Osteosarcoma cells have osteocytes as progenitor cells[137], which come from osteoblasts. The osteoblasts produce osteoid[138], which contains type I collagen (stained in pink in HE).

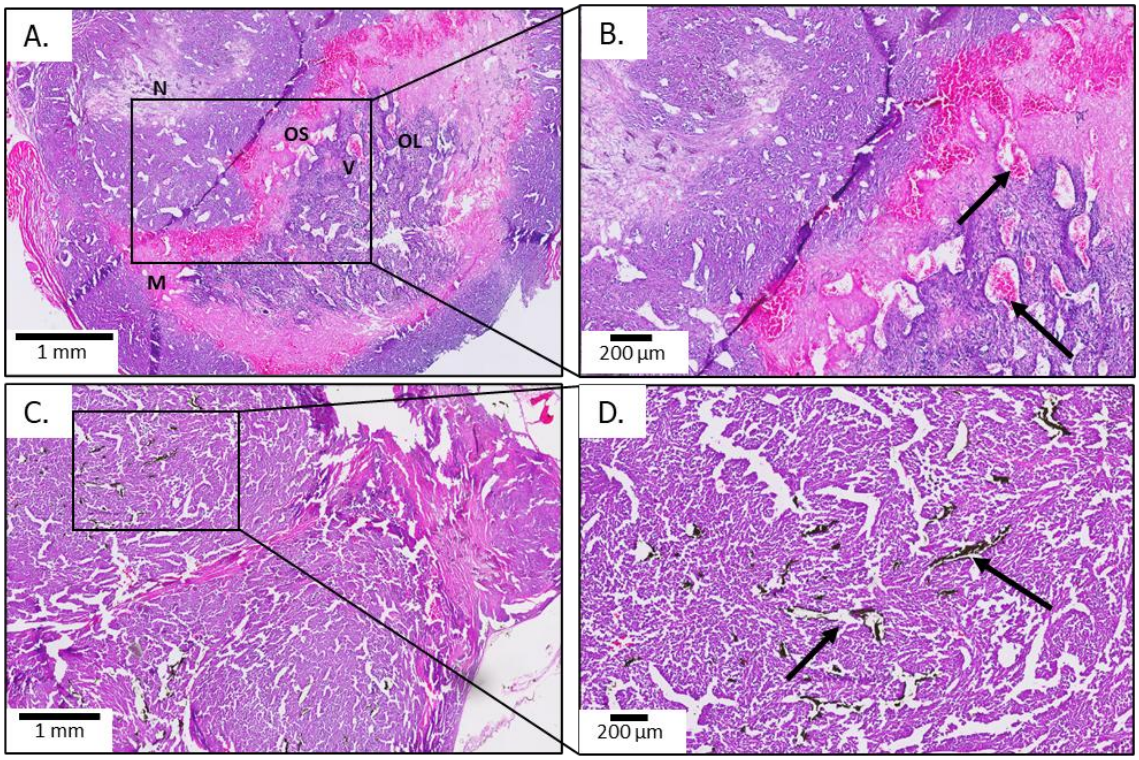

Figure 36. HE histology of osteosarcoma tissues. Tumour tissues from the limb (A-B) and the back model (C-D). The vessels are indicated by the black arrows in the magnified pictures, and show the vessels filled with red blood cells (B) and with residuals of Vascupaint (D). Usually, the perfusion clears away the blood from the circulation, but since the vessels of tumours are chaotic and leaky not all of them are emptied during the process. The same happens in the samples perfused with Vascupaint, were the compound can´t reach every vessel. Images were analysed through the program QuPath-0.6.0 to gather knowledge on the expected tissue composition and colocalising vessels containing Vascupaint. Representative images are depicted. Legend: OL, osteon-like structure; M, muscle fibres; V, vessel; OS, osteoid; N, necrosis.

The HE staining can reveal the presence of the vessels (white holes in the samples) and their content. Figure 36 show the presence of Vascupaint in part of the vessels (blackened dye); since those samples had to stay overnight in the fridge to allow the polymerisation of the compound, the tissue in C-D appears to be slightly dehydrated (larger white cracks in the tissue) but the vessels containing Vascupaint and the extracellular matrix (pink) can still be identified. Figure 37 shows magnifications of the vessels containing erythrocytes and the presence of haemorrhagic areas, where the erythrocytes have leaked outside of the vessels. This is commonly found in tumour tissues due to the leakiness of the newly formed vessels that characterise them[24].

The LM8 cells, when injected subcutaneously in the limb of the animals, are known to produce metastases in the lungs[113]. This was checked also for the back model with HE histology, as shown in Figure 38, with metastases forming in the lungs of both back and limb model mice. In the case of the irradiation experiments, the presence of metastases in the lungs was monitored during the follow-up with monthly µCT scans; if lesions were to become visible at the macroscopic level, this would have required the termination of the animal according to the ethical protocol.

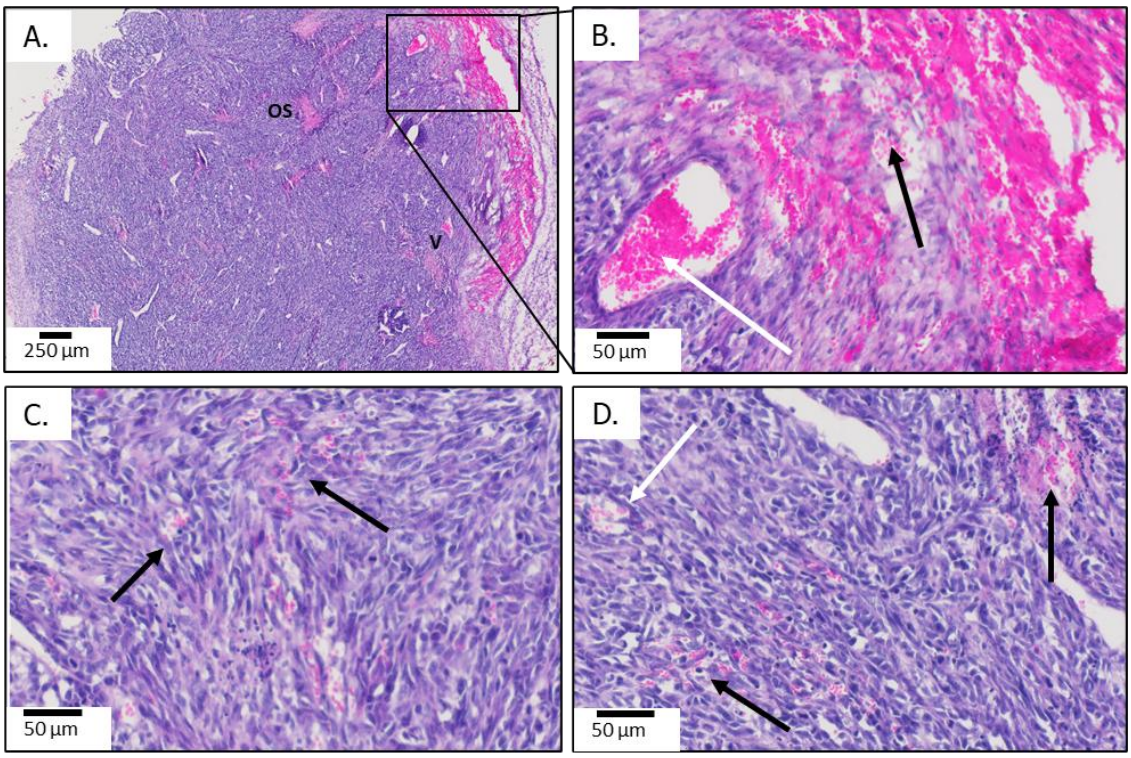

Figure 37. HE histology of back tumour tissue. A) Tumour tissue. B) A magnification of A shows the erythrocytes (pink circles) inside a vessel (white arrow) and a large haemorrhagic area (black arrow). C-D) Areas where the vessels present a chaotic structure, leading to blood leaking in the tissue. Images were analysed through the program QuPath-0.6.0 for sample dimensions and haemorrhagic areas identification. Representative images are depicted. Legend: V, vessel; OS, osteoid.

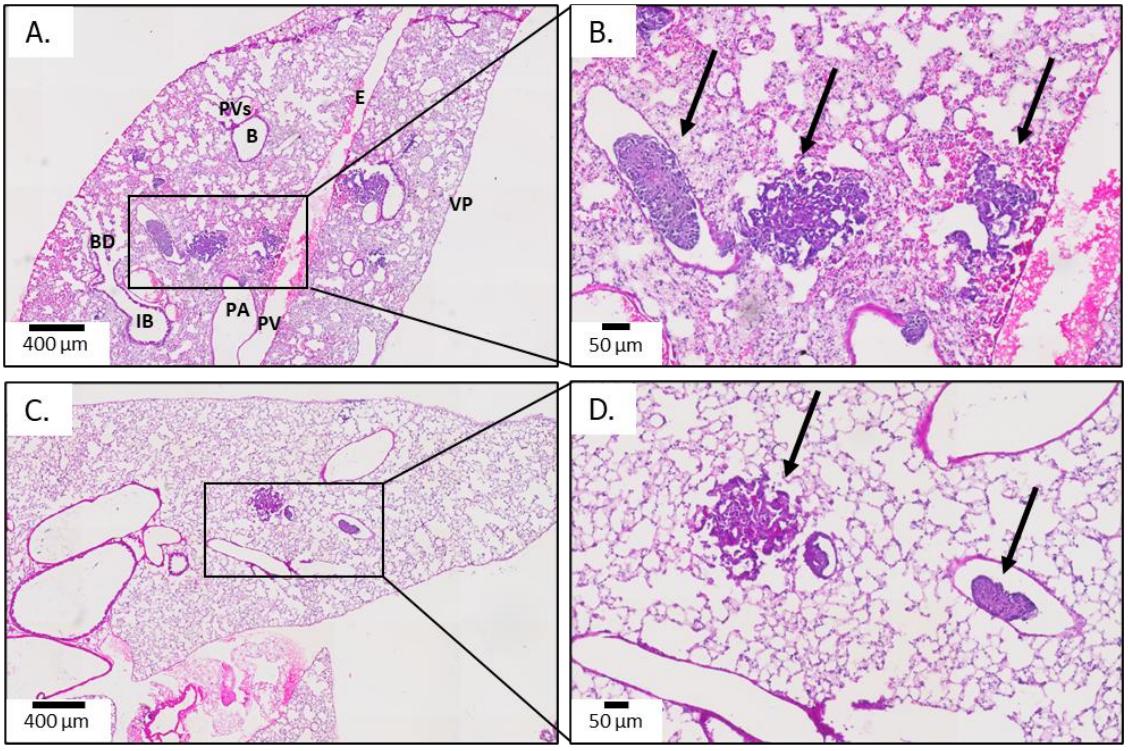

Figure 38. HE histology of lungs with metastases. The tissues were taken from rom the limb (A-B) and the back model (C-D). Metastases were found in both the models, showing similar structures and distribution patterns, and are a characteristic sign of the LM8 cell line. They can be distinguished from the surrounding pulmonary tissue for their dark colour, given by the presence of a high number

of cells in a small area. Images were analysed through the program QuPath-0.6.0 for metastases localisation. Representative images are depicted. Legend: PV, pulmonary vein: E, erythrocytes; IB, intrapulmonary bronchus; B, bronchiole, BD, bronchiolar duct; PVs, pulmonary vessels; PA, pulmonary artery; VP, visceral pleura.

3.1.3 Selection of the tumour model

For the irradiation experiments, the tumour model needed to have some specific characteristics, which have been described in the previous paragraphs. To make it easier to contour on the μCT scans for the treatment planning, the tumour needed to have defined borders. In this case, the back model was developing subcutaneously without growing on other parts of the body, unlike the limb model. For the same reason, the limb model was also affected from the point of view of the vascularisation reconstruction with Vascupaint; the presence of the bones and of the surrounding muscles' vessels was interfering with the reconstruction of the tumour vessels only. Even if the tumour was vascularised, the back model had a vasculature that could be attributed to the tumour only, which was more useful to this study.

The location was also an important factor: the back model was close to two organs at risk, *i. e.,* the spinal cord and the oesophagus, while the limb wasn't in close proximity to any organs at risk. From the histological point of view, the tissues were looking similar and showed a similar metastatic phenotype, with both models producing metastatic lesions in the lungs; this showed how, regardless of the location of the injection, the LM8 cells retained their phenotype. The presence of vessels perfusing the tumours was shown by both Vascupaint perfusion and histological analyses, where vessels of different dimensions can be observed in Figure 37. The presence of such a developed network can be useful in treatments that target the vasculature, like anti-angiogenic therapy used for tumour vasculature normalisation[139]. In the case of this study, the role of the vasculature is explored in the paragraphs about the biological washout and the relevant experiment during the first experimental campaign (3.3.1).

Because of these reasons, even if there was a small failure probability (15%) in the growth of the back model, it was still selected because of the three relevant criteria explored in this study.

3.1.4 Preparation of anatomical immobilisation devices

After the back model was selected for the rest of the experiments, immobilisation devices were developed to ensure a reliable positioning for all the animals used in the irradiation experiments. The weight of the animals was measured to understand the inter-variability and, if necessary, to prepare different versions of the restrainers to accommodate differently sized animals. During these preliminary experiments, the weights of the animals were recorded as part of weekly health check-ups. According to the ethical protocol, if an animal loses more than 20% of its weight compared to the previous week, it should be euthanised to prevent further suffering. An example of the inter-mouse weight variability is represent in Figure 39.

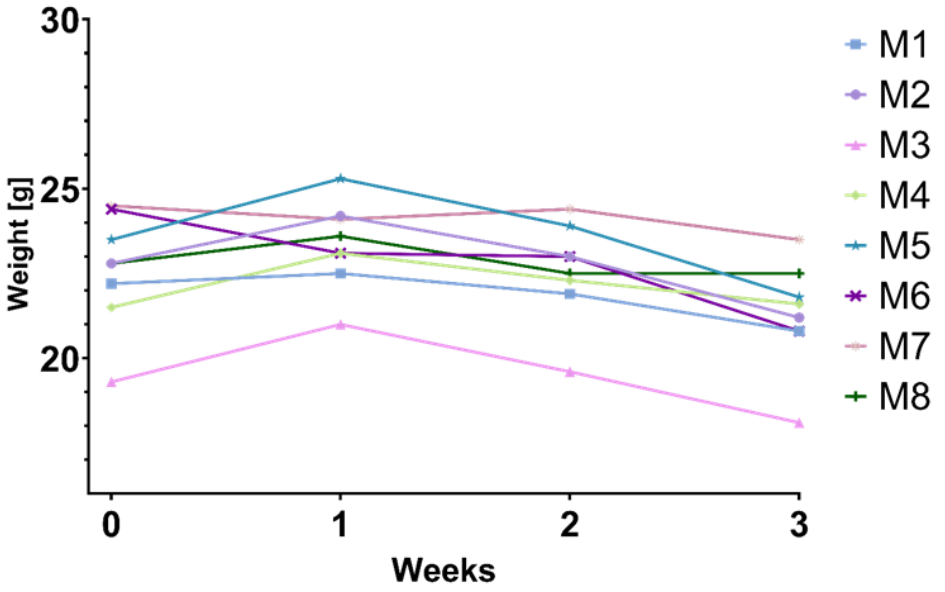

Figure 39. Example of the weekly fluctuation of the weight of the mice. The gain and loss of 1-2 grams per week has been observed thorough all the experiments presented in this work and is considered to be normal.

These measurements, coupled with the scans obtained with the µCT, were used to create the anatomical collars that were adopted for the irradiation experiments (Figure 40). Since they slightly restrained the breathing motion of the mice, they helped to reduce streak artifacts on the µCT scans, which helped in contouring of the tumours. The template of these immobilisation devices was used to produce a thin collar to fix the mouse in position for the photon experiment (Figure 20) and the compensators used in the experimental campaigns, which had different designs based on the function they were used for. Some examples are: shaping the beam accordingly to the CTV (Figure 41); reducing the energy of the incoming beam; holding a radioactive source for the alignment of the SIRMIO PET to the place where the mouse would have been positioned inside of it and to the rest of the irradiation setup.

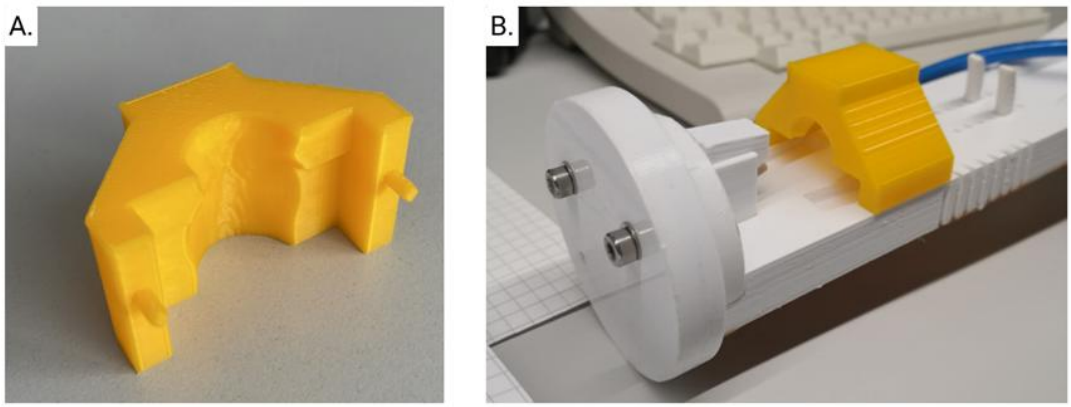

Figure 40. Production of the anatomical collar. A) Example of anatomical collar and B) anatomical collar fixed on SIRMIO µCT bed.

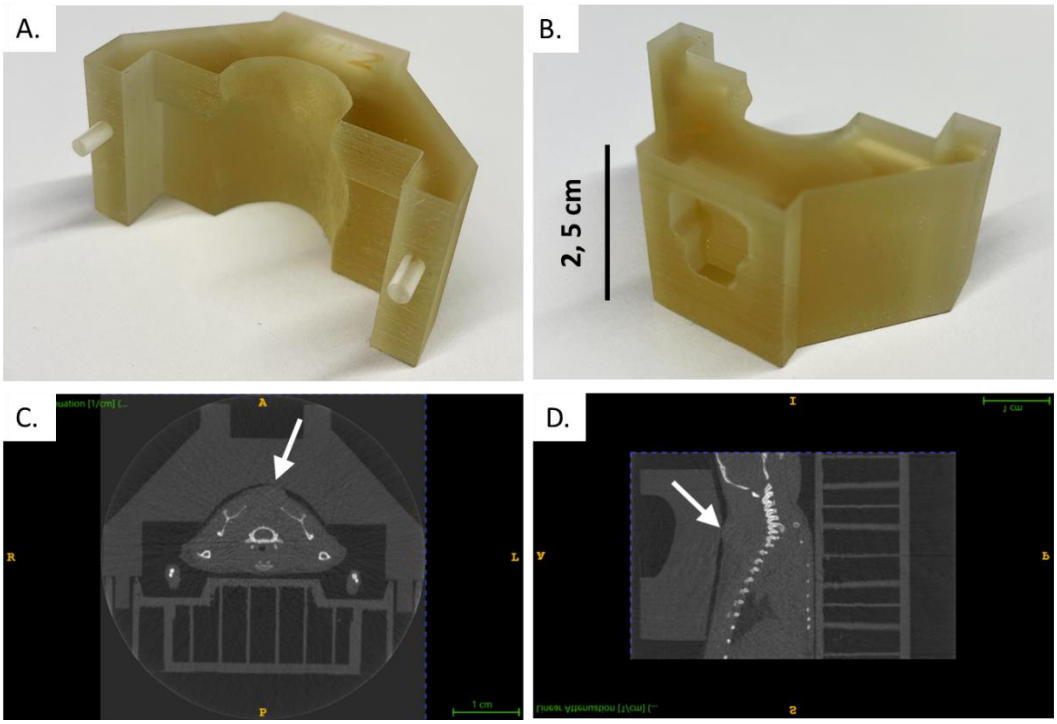

Figure 41. Anatomical compensator. A, B) Pictures of the plastic compensator (left, inner side with anatomical cut; right, dimple corresponding to the distal edge of the CTV). C) Axial and D) sagittal view of µCT scan of a tumour-bearing animal immobilised with the anatomical compensator. The tumour is the small protuberance indicated by the white arrows. The dimple in the compensator shapes the beam to cover the CTV according to the treatment plan. Resolution: 100 µm.

With the data collected about the tumour growth, the histological characterisation, the expected weights and the production of the immobilisation devices, it was possible to continue the experiments with the photon irradiation for testing the overall experimental architecture required by the upcoming experimental campaigns.

3.2 Photon irradiation – Dose escalation study

The aim of this experiment was to find two dose types for the tumour irradiation, a lower one achieving uncontrolled tumour growth, and one high enough to control the growth, but also cause spinal cord toxicity, since the irradiation field goes all the way through the tumour and the healthy tissue present behind it.

Osteosarcoma is generally regarded as radio-resistant[140] and therefore needs a high dose to achieve local control. Because of this high dose, a certain degree of skin toxicity[141,121] was expected during the course of this experiment, and the preventive measures were taken as explained in paragraph 2.5.4. The preparation of the animals was executed as explained in the previous paragraphs, and since some of the tumours were still not visible at week 2 post injection, the irradiation was performed at week 3 post injection, where the majority of the tumours became visible. In four cases, the injected cells failed to produce a measurable tumour: these animals where therefore excluded from the tumour growth analysis but are still represented in the layout in Figure 42 (mouse IDs with asterisk).

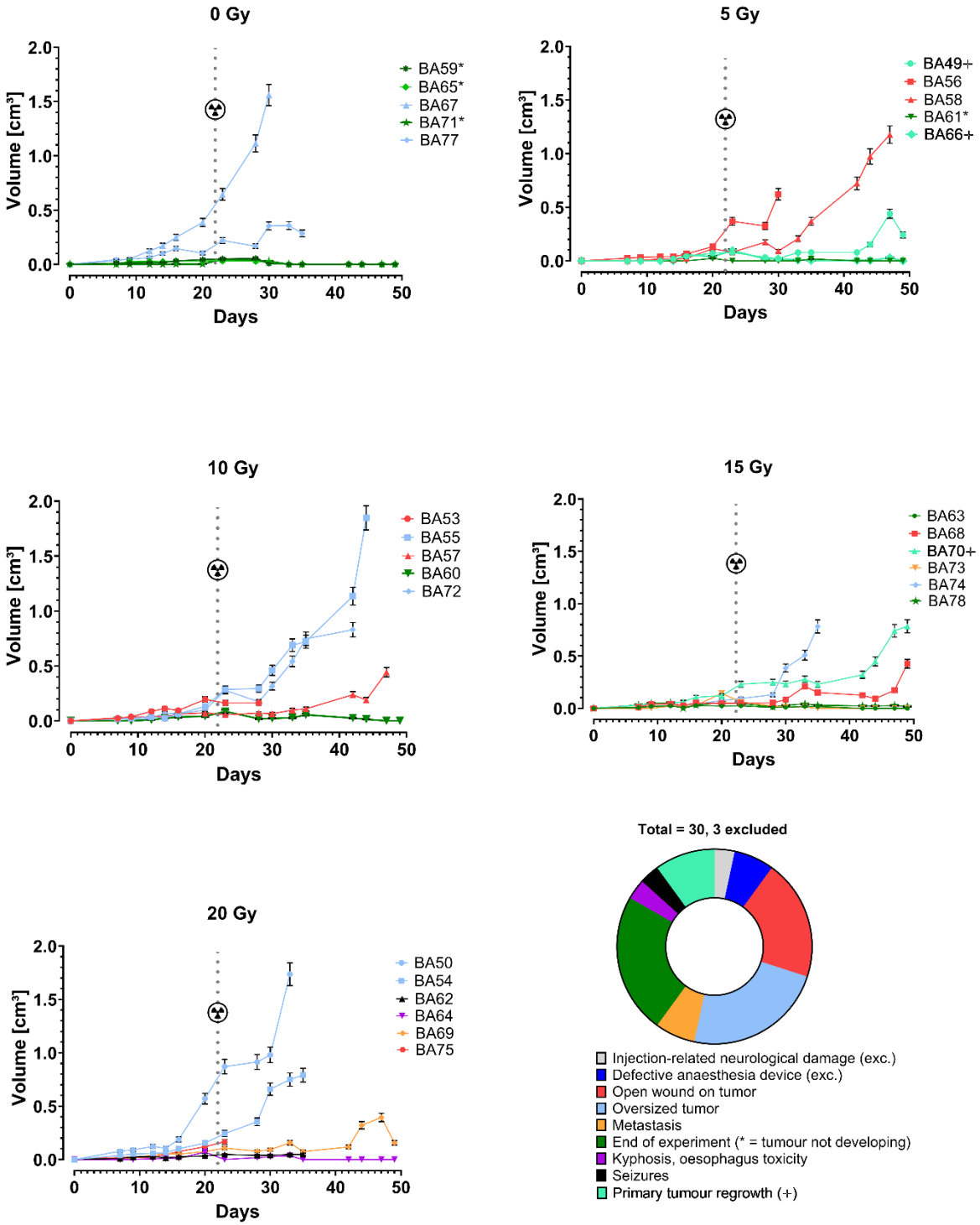

Figure 42. Photon irradiation experiment tumour growth curves and death causes. This panel shows the tumour growth curves for each animal involved in the study (also the ones in which the tumours failed to grow). An example of this phenomena is the 0 Gy graph, where all the animals didn´t receive radiation and were therefore supposed to show uncontrolled tumour growth, but instead show failed growth (mice IDs marked with asterisk, *). The irradiation was performed at day 22 post-injection (radiation symbol and dotted lines in the graphs). The wheel chart at the bottom-right corner summarises the death causes that were observed during the course of the experiment; the colours in the graphs match the reason of sacrifice. The mice marked with a cross experienced tumour regrowth after day 50 and were euthanised for that reason (┼).

The number of animals surviving the tumour growth was low, as shown in Figure 42, and in the groups of sham-treatment (0 Gy) and the lower doses (5, 10, 15 Gy) they were likely

to be the ones in which the tumour failed to grow, or where it was possible to achieve local control. A number varying from one to three per each group arrived at the end of the experiment (24 weeks post-irradiation), with the only survivor of the 20 Gy group living up to week 16 post-irradiation. This animal presented radiation-induced toxicities symptoms in the oesophagus, *e. g.* a strong and rapid weight loss (> 20%) manifesting in a timeframe where all the other animals were constantly gaining weight. This event served as an important indication of normal tissue complications, and will be further discussed in section 3.4.

Since the numbers were reduced to values below the ones which could be used to assert statistical significance, these results were mainly used as a preliminary overview to plan the experimental campaigns with ^{11}C and to understand which kind of side effects, normal tissue complications, survival rate and other possible issues could present in the following experiments.

After the first part of the experiment, where the major endpoint was the tumour growth, it was possible to understand that 5 Gy were just delaying the tumour growth, as it can be seen in the panel in Figure 42. The 20 Gy dose, instead, treated successfully the two animals that survived the timeframe in which the other animals in the group did not. However, one of the two animals experienced metastatic growth in the abdominal cavity. Therefore, it had to be sacrificed 49 days post-injection, while the other one remained tumour-free up to week 16 post-irradiation.

It might also be possible that some tumours shifted out of the treatment area during the positioning of the animal in the X-rays irradiation setup. This couldn't be seen due to the presence of the anatomical collar used to immobilise the animals; hence it was not possible to adjust their position before the irradiation.

To avoid the loss of many animals due to the late irradiation time-point, in the experimental campaigns with ^{11}C it was decided to perform the irradiation two weeks after the tumour cells injection. To draw a conclusion about which doses should have been used for the ^{11}C experiments, the tumour growth curves gave some hint about the use of 5 Gy as the lowest (to observe uncontrolled growth after the irradiation) and 20 Gy as the higher dose. Before drawing further conclusions on the higher dose, though, the normal tissues toxicities were explored to collect data about the normal tissue complication probability (NTCP).

3.2.1 Skin toxicity

In the case of the photon irradiation, the scoring of the skin toxicity was complicated due to the early deaths caused by the tumour growth, the partial lack of tumour control given by the different doses and the late irradiation time-point (Figure 42); in these cases, if the tumour reaches 1,5 cm in diameter, the animals needs to be sacrificed according to the ethical protocol. Especially when manifesting before the irradiation, symptoms such as inflammation of the skin and the opening of lesions could be related to the tumour growth. The highest grade reached was grade 4 (open wound, see Figure 43) which required the termination of the animals in the case the wound wasn´t healing.

These lesions were most probably caused by the animal during grooming and worsened by the other animals present in the cage. To try to manage them, a small amount of disinfectant (Betaisodona® Lösung, 100 mg/mL) and ointment (Bepanthen®) were applied

to promote wound closing, and the animals were treated with Carprofen (dose: body weight multiplied by five to obtain the number of µL to administer) injected subcutaneously as a painkiller. Unfortunately, even with these treatments the lesions were not resolving, which led to the termination of the animals to stop the suffering. These lesions appeared around week 3 post-injection and were not observed during the preliminary experiments on the tumour model selection.

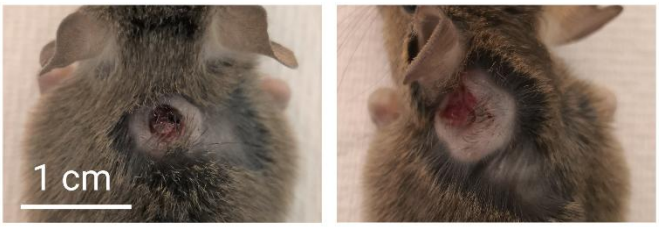

Figure 43. Example of lesions forming on the tumours.

Since necrosis (grade 5, maximum) was never observed during the course of this experimental campaign, grade 4 was deemed as the highest tolerable grade the animals could be exposed to. Figure 44 summarises the causes of skin toxicity observed in this experiment.

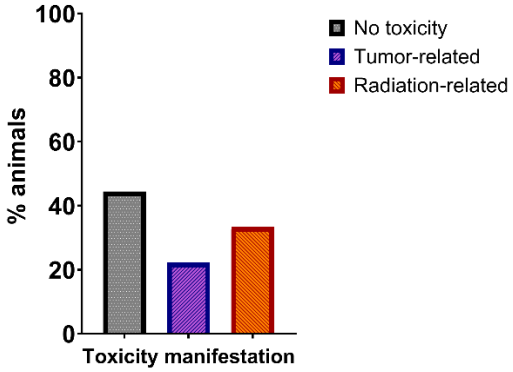

Figure 44. Photon irradiation experiment skin toxicity. Around half of the animals (12, 45%) didn´t manifest toxicities, while 22% (6 animals) needed to be euthanised due to tumour-related issues, and a third manifested radiation-induced skin toxicity (9, 33%) which was managed and healed with the application of topical treatments.

After the irradiation, the discrimination between tumour-related and radiation-related skin issues was still troublesome, since part of the animals continued to open lesions on the tumours. Radiation-induced skin toxicity, instead, manifested as inflamed skin and radiation dermatitis, with some crusts developing on site but no open lesions.

In the cases in which the tumour was actually treated, the application of the above-mentioned healthcare procedures led to the healing of radiation-induced damage, even in the animals treated with 20 Gy. The choice for 20 Gy, and not higher, comes from studies[141,121] that show how 19 Gy can already produce a significant radiation-induced skin toxicity, and it can become more severe with higher doses, where a significant fraction of the animals need to be sacrificed due to skin toxicity, interfering with other relevant endpoints (*e. g.* spinal cord toxicity). However, in this work, the healthcare ensured that no animals had to be sacrificed due to radiation-induced skin toxicity. This experiment helped in setting the foundation of post-radiation care for the two ^{11}C ions irradiation experiments

and demonstrated that 20 Gy was a dose that could be well-tolerated by the skin with acceptable and manageable side effects.

3.2.2 Weight gain patterns

The weights of the animals were recorded as part of the health scoring. The panel in Figure 46 reports the weekly weights recorded for each animal divided by dose groups.

In general, the weight tends to increase with time, but it can quickly drop in case the animals are stressed or suffering. If the weight loss was larger than the usual 1-2 grams weekly weight fluctuation, an enriched soft diet was provided to avoid weight losses above 20% of the weight of the previous week.

The exception to this weight-gain pattern was the only animal surviving from the 20 Gy dose group, which experienced a severe weight loss between week 15 and 16. The animal was showing accelerated breathing, kyphosis, and even after the dietary enrichment administration it failed to gain weight again, as it can be seen in the sharp drop in the dedicated graph. Upon dissection, the oesophagus revealed to be anatomically changed and the gastrointestinal tract was empty, hence the altered food-intake. Since the radiation field covered the oesophagus, it could be hypothesised that this was caused by radiation-induced toxicity developing in the oesophagus. Unfortunately, since there was no suitable control animal to compare at that time-point, no histological analyses were conducted on this sample.

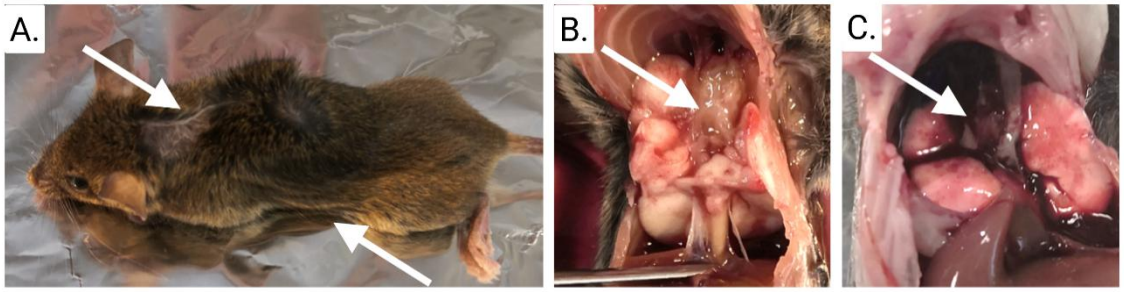

Figure 45. Animal exposed to 20 Gy of photons in the cervical area. In A) the white arrows indicate the altered curvature of the spinal cord (kyphosis) and the empty flanks with soft folds of skin, which shows the drastic weight loss. In B) the dissected thoracic cavity of this animals is compared with a control (C), showing a mass of tissue that is absent in the control.

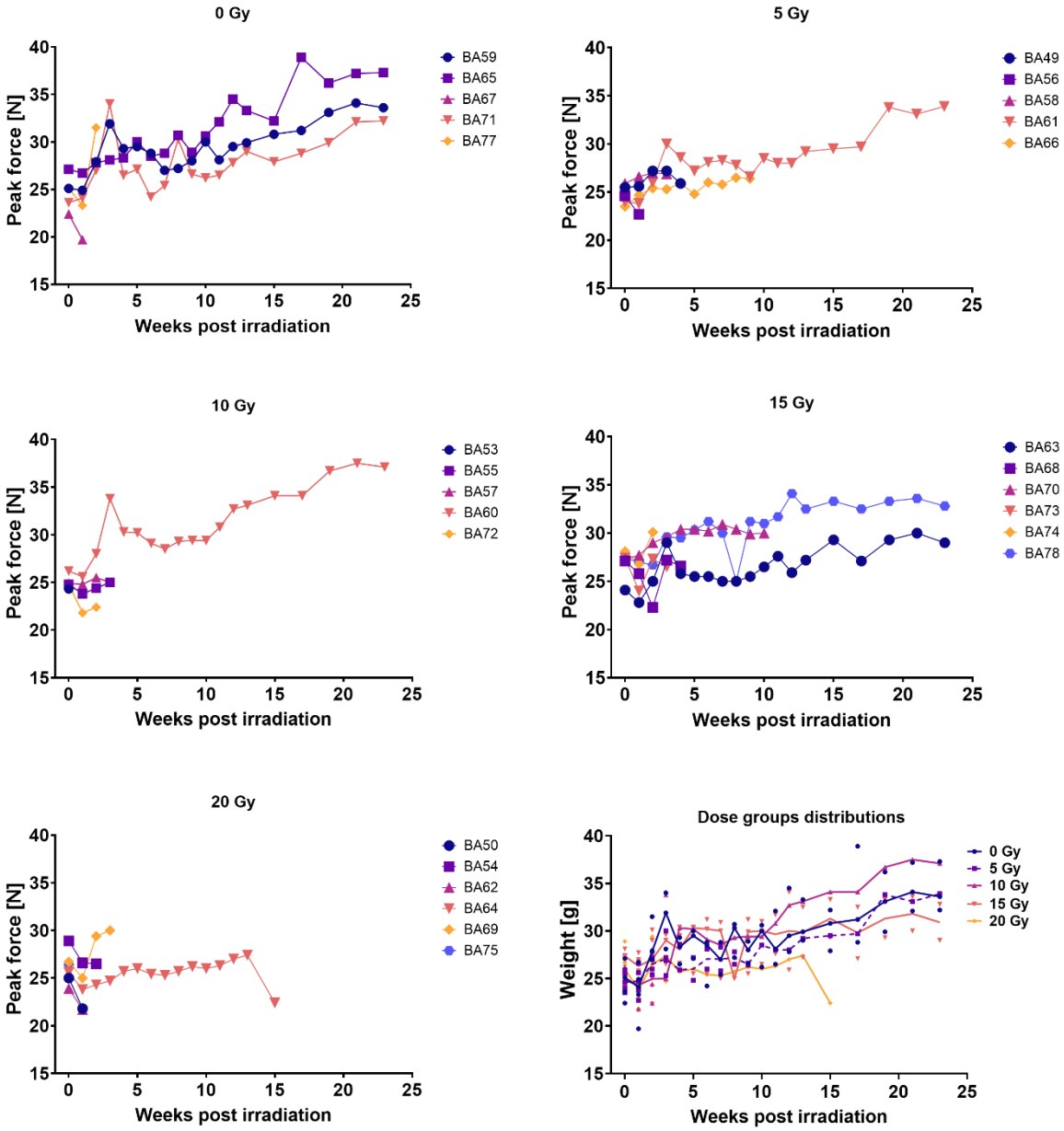

Figure 46. Photon irradiation experiment weights distribution. The animals present in each group gained weight during the follow-up, with the exception of the animal that received 20 Gy of irradiation. The lines represented in the "Dose groups distributions" panel are group medians.

These plots, when compared with the information obtained in the tumour growth panel, show which animals survived because of tumour growth failure (0 and 5 Gy survivors), and which because of tumour eradication (10 and 15 Gy groups) after successful tumour development. This data will be further discussed in the paragraph 3.2.4.

3.2.3 Motor function impairment

As a part of the daily health check-up, the animals were scored for general wellbeing, changes in behaviour (*e. g.* isolation, excessive grooming, pain-showing, etcetera) and posture. Since the cervical spinal cord was irradiated, changes in posture, mobility and function of the forelimbs (see Figure 25) were monitored as telling signs of radiation-induced morbidities.

3.2.3.1 Grip strength test

The grip test was used to assess the development of radiation myelopathy. The test was repeated weekly and 5 measurements were collected for each animal. During the course of the follow-up, though, it became clear that the animals were habituating to the task, which hindered their cooperation. It was then decided to reduce the number of tests to every two weeks. Since this was the first time this test was performed in the context of this work, it helped in understanding how much biological and operator-related variability were to be expected during the data acquisition.

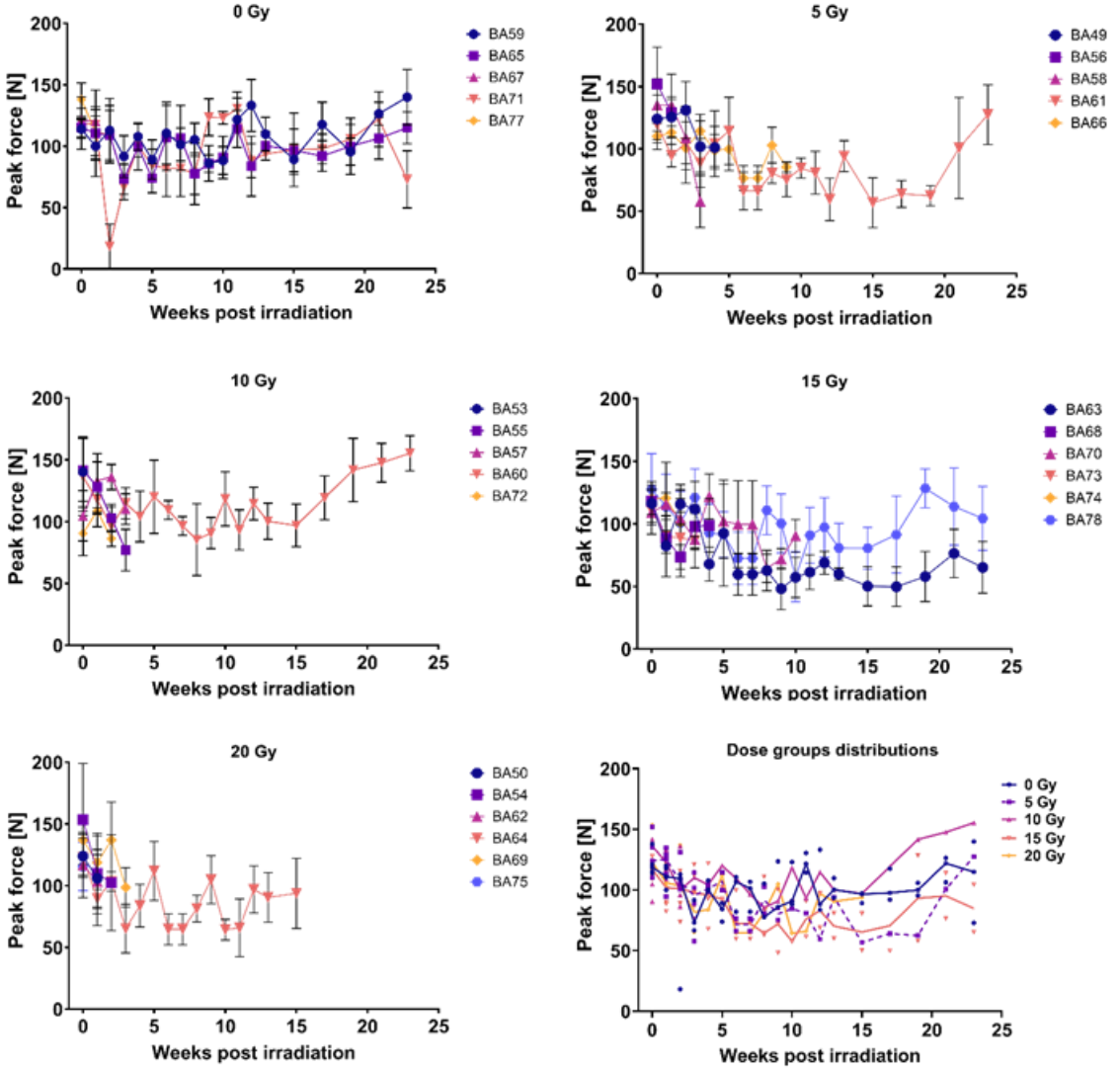

Figure 47. Photon irradiation experiment grip test panel. The dose groups plots show the individual curves for each animal, and the error bars are the standard deviations. In the dose groups distributions plot the average values for each animal are represented by a point, and the curves depict the median for each group.

As it can be seen in Figure 47, the inter-individual variability was quite wide, as well as the intra-individual one. For example, it can be seen that the variation in peak forces can vary between 150 and 50 N in almost all the plots. In the 0 Gy group, three animals survived until the end of the observational period: by averaging all the average peak forces recorded along the six months, the average peak force of the group is 101,7 N, with an average

standard deviation of 10,9 N. As an example of inter-individual variation, on the last day of measurement the difference between two of the three animals in the group ranged from 72,9 to 139,9 N. Regarding the intra-individual variation, instead, the 5 Gy and 10 Gy groups can be taken as examples. The 5 Gy survivor showed and average peak force of 87,2 N (std. dev. 20,4 N) through the six months, with a range going from 56,8 N to 127,5 N. The 10 Gy survivor, instead had a six-month averaged peak force of 113,6 N (std. dev. 19,5 N), with a range between 85,5 N to 155,34 N. Nevertheless, the reduced number of animals present in each group doesn't permit to draw any statistical conclusion.

Also a correlation between grip strength and weight of the animals was explored: theoretically, mice that weight less are supposed to have less muscle mass, hence less grip strength[142]. In this study, though, part of the animals with increased body weight tended to try to avoid the test. When the results were normalised to the body weights, these animals were showing a decrease in performance, even if they were belonging to the control group, which were not expected to show signs of radiation-induced spinal cord impairments. The body weight normalisation was therefore excluded from the following analyses, and the same applies for the experimental campaigns described in 3.3 and 3.4.

3.2.3.2 Motor-function impairment test

The so-called "walk-test" used in this work was used to perform video recording and motor-function analyses of the animals. The video acquisition was performed every two weeks from the irradiation time.

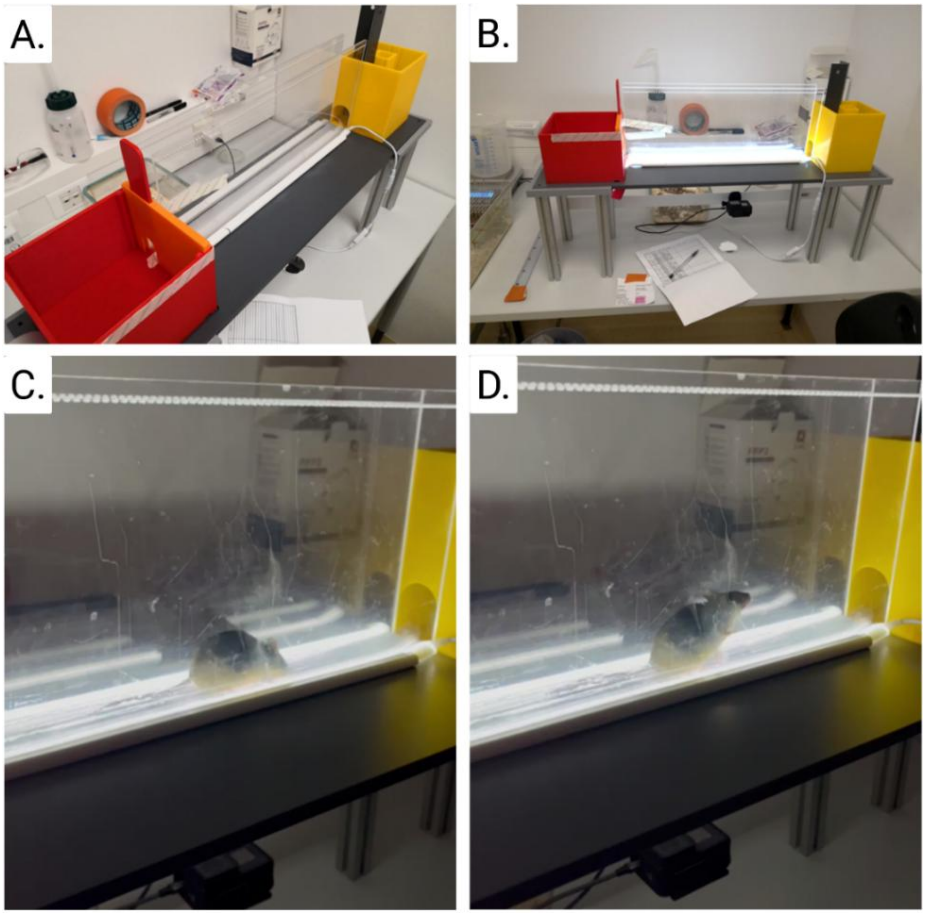

Figure 48. A-B) Walk test apparatus, adapted from Bounds *et al.*[123]. C-D) Mouse walking and rearing inside the corridor.

Also in this test, the animals were trained prior to video acquisition by being frequently handled to get them used to the procedure and to minimise stress. The videos were taken in the apparatus described in Figure 48 with the room lights off, since the animals were kept at inverted cycle (dark during the day, light on during the night). If they were scared of the new environment, they were "freezing" in the corridor, thus preventing a proper analysis of the gait pattern. Keeping the lights off helped in preventing fear-related behaviours, as well as recording in a quiet environment with no noise disturbances. The test was considered successful when the animals were walking along the corridor without stopping or turning back in the middle of a run. The high walls of the corridor, though, permitted the possibility or rearing, a standard behaviour adopted by the animals when they are exploring. This behaviour was a sign of health, and it permitted to assess the spinal cord mobility, as it will be further discussed later in this paragraph.

The expected change in motor function was the development of paralysis caused by radiation induced myelopathy, which translates in the loss of function of the limbs as they start to be dragged during locomotion. This severe morbidity was never observed during this work, thus leading to the search of other biological effects to explore for determining the amount of neurological damage. One effect was the manifestation of body length reduction, caused by the development of kyphosis, which tends to make the spine shorter during movement and stationary phases. It's not a parameter that is automatically calculated in PrAnCER (see Table 9). In Figure 49, the body length was calculated thanks to the presence of a ruler in the setup, and the pixel to centimetres conversion that is calculated by giving a reference measurement as input before the video processing part.

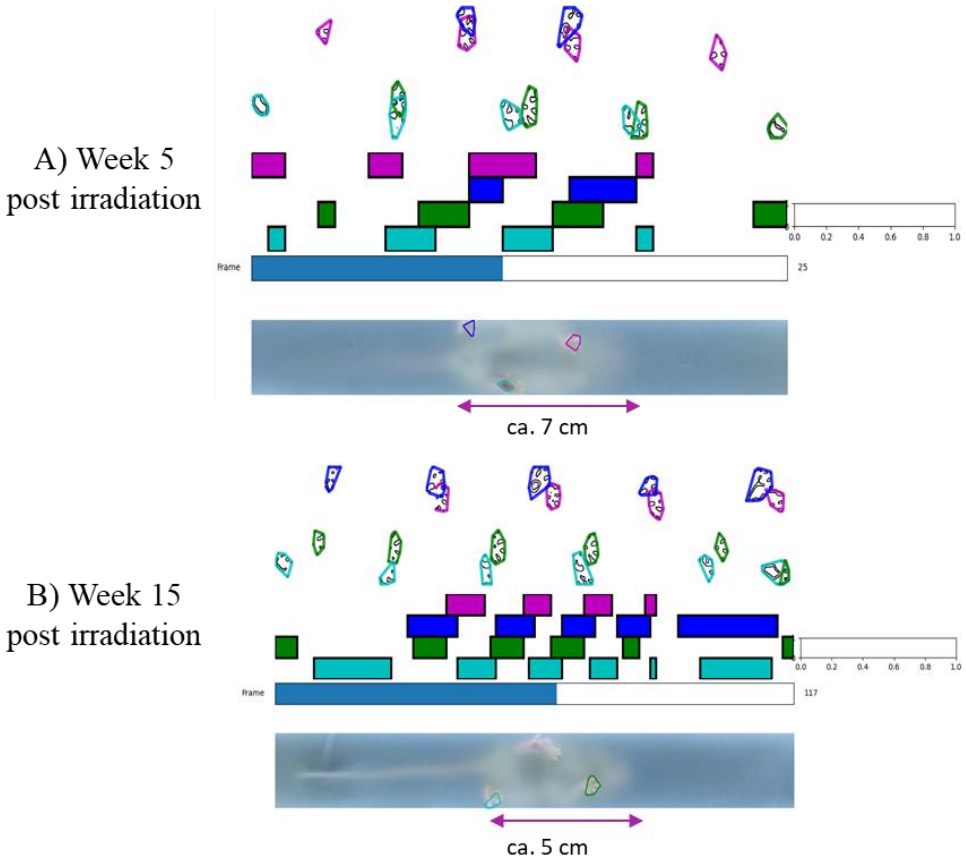

Figure 49. Output of the PrAnCER software from Bounds *et al.*[123]. The gait patterns of the animal irradiated with 20 Gy of photons after 5 and 15 weeks. From top to bottom, the paw-prints are printed are identified, then the time they are recorded is represented with the 4 different coloured blocks.

The last part shows the camera point of view from below the corridor: the body of the animal is visible and the length can be measured. Legend: cyan = hind left paw, green = front left paw, blue = hind right paw, magenta = front right paw.

Table 9. Table with parameters from PrAnCER (Bounds *et al.*[123]).

Description of gait parameters.

This table describes the most commonly used gait parameters; those used in this study are indicated in bold.

Gait Parameters	
Parameter	**Definition**
Stride Length	Distance between successive contacts of the same paw
Step Length	Distance between successive contacts of contralateral front or hind paws along the axis of the direction of motion
Base of Support (BOS)	Distance between successive contralateral front or hind paws perpendicular to axis of the direction of motion
Maximum Contact Area	The maximum detected area of a hind print
Interlimb distance	Distance between ipsilateral front and hind paws
Stance Duration	The length of time a paw was in contact with the ground
Swing Duration	The length of time a paw was not on the ground
Stance to Swing Ratio (SSR)	Stance duration/swing duration
Discrete Speed	Stride length/(stance duration + swing duration) for a paw
Average Speed	Average of discrete speeds in the period used in analysis
Speed Variability	Percent change in discrete speeds during a run
Run Speed	Time to cross the tunnel/length of tunnel

The software can give a wide number of parameters to choose from and analyse, some examples of which can be found in Table 9. For each animal, one maximum five minutes long video has been recorded every two weeks, and at least three successful runs were analysed and averaged. These measurements were then averaged with the rest of the same dose group.

These parameters were affected by the behaviour of the animal in the testing apparatus. If in a certain week the animals were stressed, *e. g.* in the weeks following the irradiation, it was difficult to remove the stress factor from the analysis and find a true signal. For this reason, the data up to week 6 post irradiation (end of the tumour growth recording) have not been considered. Another reason for not considering this period of time in this analysis (up to six weeks post irradiation) is because it´s not relevant for the observation of spinal cord toxicity. Additionally, it wasn't always possible to record three successful runs for each animal during every test day, fact that reduced the number of possible data available for the analysis. Hence, no significant differences were found in these parameters. The variability caused by the behaviour of the animals in the testing apparatus could be a reason, which couples with the fact that the symptoms were not showing in a strong and clear way. In case, additional experiments may be needed to discern the effect of the testing environment on the behaviour and on the exhibition of the symptoms.

In the specific case of the 20 Gy irradiated animal (depicted in Figure 50), the only parameter that showed a statistically significant change was the base of support, which is defined as distance between successive contralateral front or hind paws perpendicular to axis of the direction of motion (Figure 51).

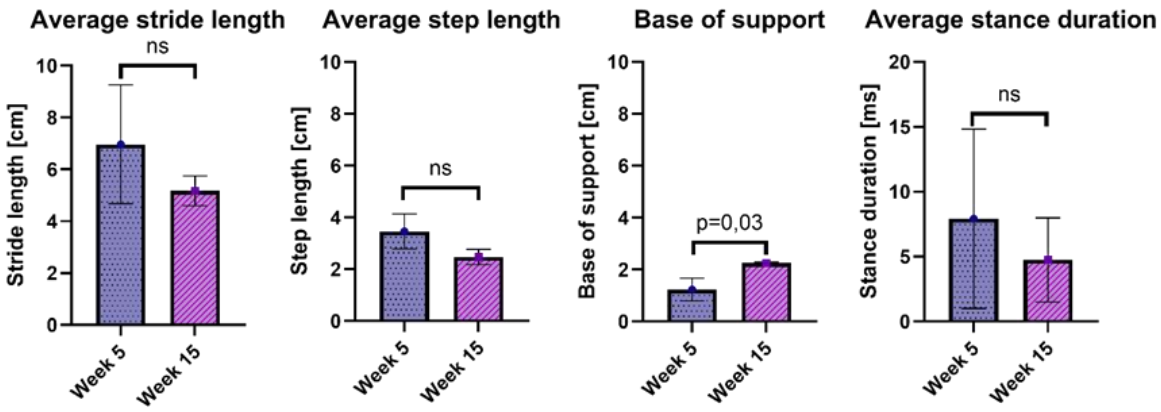

Figure 50. Analysis of stride length, step length, base of support and stance duration comparing the video recorded during weeks 5 and 15 of the 20 Gy irradiated animal. The parameters from three different successful runs are averaged (error bars: standard deviation) and the unpaired two-tailed t test was used to assess statistical significance, with the differences considered to be significant if p-value < 0,05.

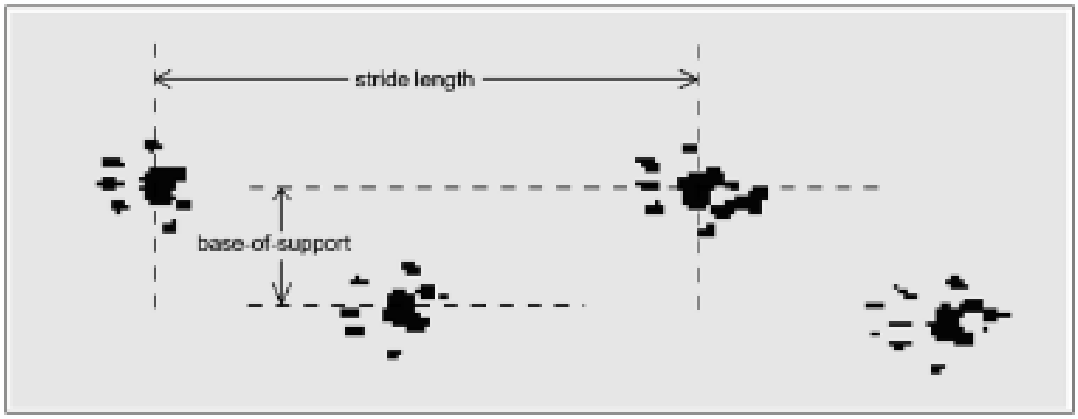

Figure 51. Schematic visualisation of the base of support and stride length parameters from Hamers *et al.*[143].

This small difference could be explained when we look at the posture of the animals. The base of support becomes larger when the limbs are splayed, and this might happen in the case of kyphosis development (Figure 52).

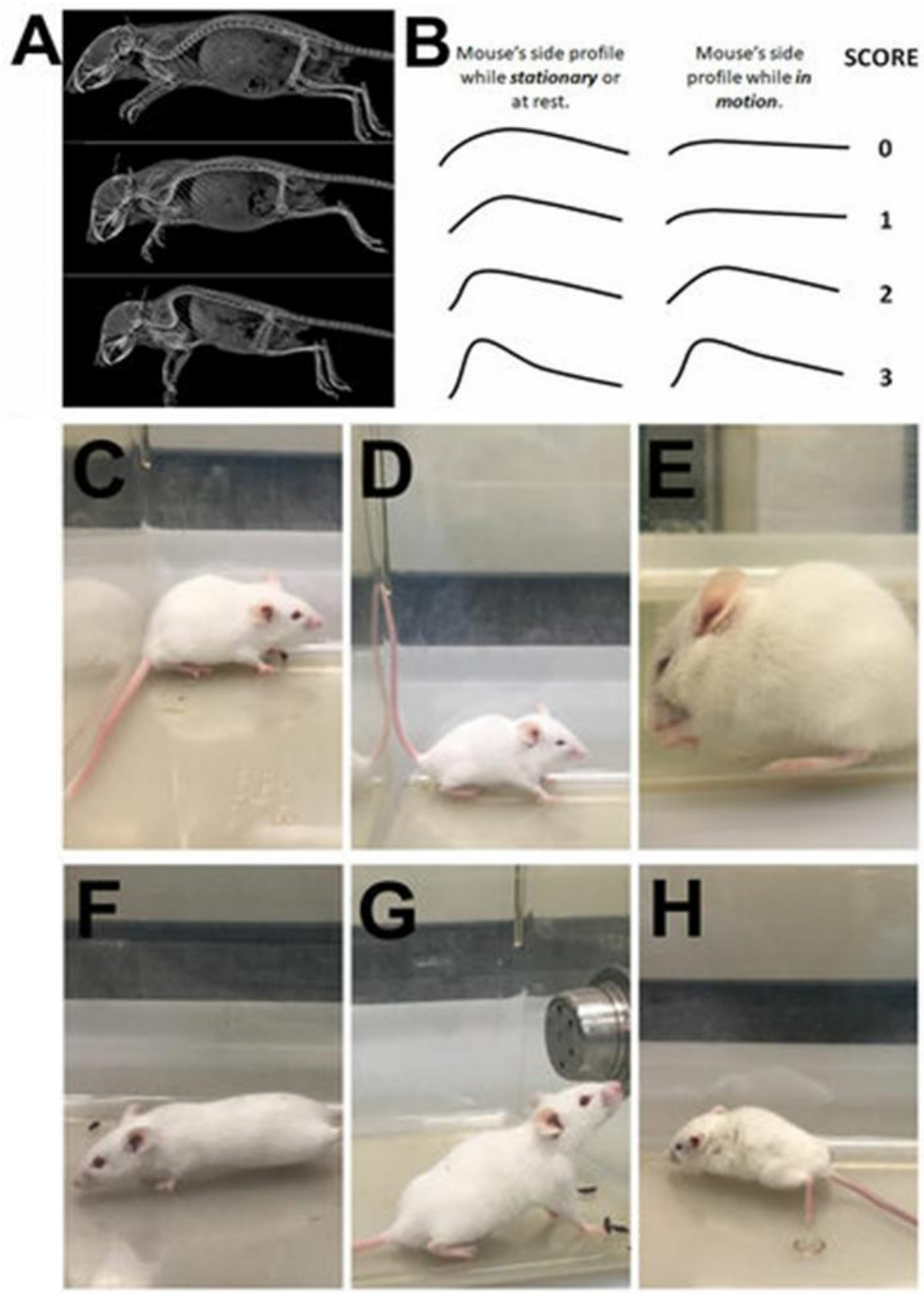

Figure 52. Kyphosis scoring system from Yerger *et al.*[125]. Kyphosis scoring system from Yerger *et al.*[125]. In A) the μCTs of the animals can be seen and the curvature of the spine appreciated. The spine curves are represented during the stationary and motion phases in B), while the figures from C to H show the severity from a control animal to one representing grade 3.

The animals were visually scored for their kyphosis development using the above-mentioned system from Yerger *et al.*, and the one in the 20 Gy dose group was scored with a grade 3 (the mouse shows persistent and pronounced kyphosis during both stationary and motion phase), since it was comparable to the score 3 of the system of Yerger.

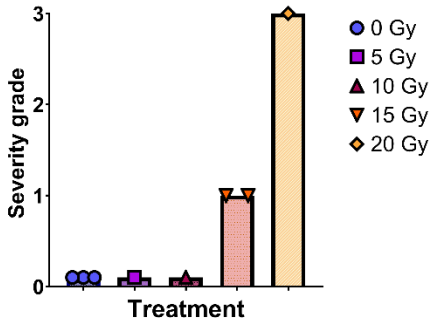

Figure 53. Kyphosis severity grading of photon experiment. The points in the columns represent individual animals.

Since paralysis never manifested during the course of this work, the visual scoring of the kyphosis was the only effective way to quantify the presence of spinal cord toxicity during the follow-up phase. As it can be seen in Figure 53, the animal that received 20 Gy manifested the highest grade (3), while grade 1 (the mouse exhibits kyphosis during the stationary phase, but can extend the spine during locomotion) was observed in the two animals that received 15 Gy. No other effect was observed in the animals treated with lower doses or sham irradiation. Compared to the possibility of developing paralysis, grade 1 is a mild side effect which neither impaired the general life and well-being of the animals nor lead to early euthanasia; in fact, both the animals survived until the end of the study.

3.2.3.3 Histological evaluation of spinal cord toxicity

The absence of severe side effects was confirmed by the histology of the spinal cords, which revealed no particular differences between animals belonging to the 0 Gy dose group and the animal treated with 20 Gy (Figure 54).

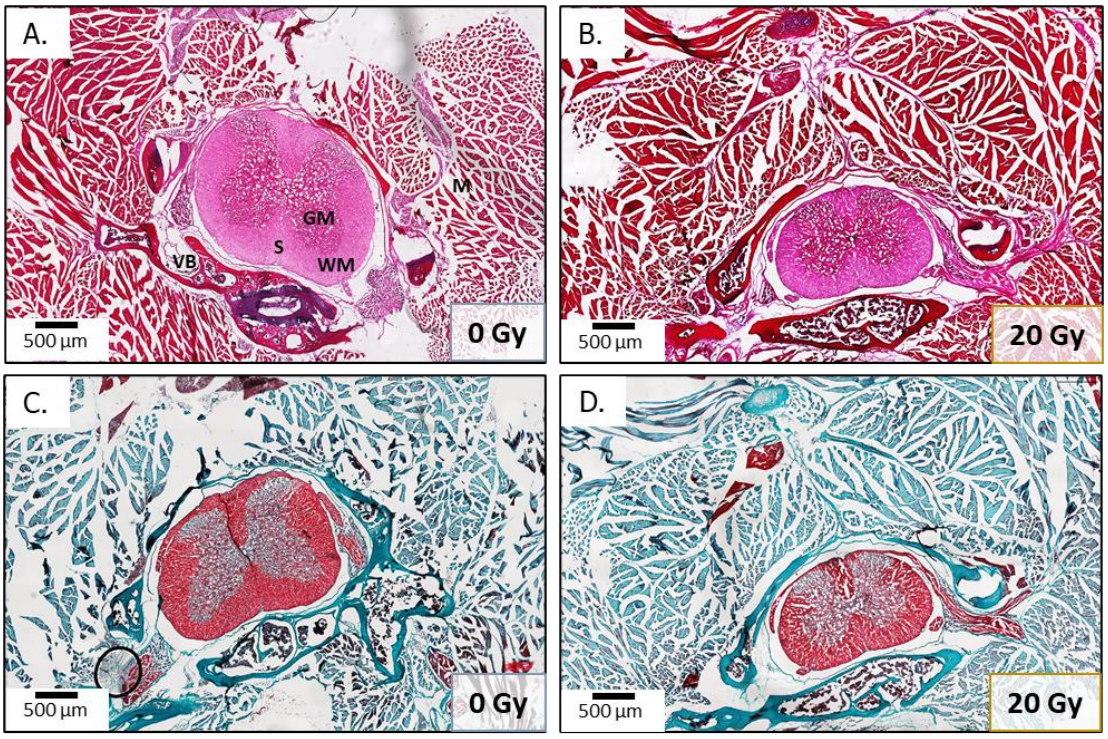

Figure 54. Histological panel representing a comparison between sham irradiated (A-C) and 20 Gy X-rays irradiated cervical spinal cords with surrounding tissues. The top figures (A-B) are

Haematoxylin and Eosin staining, the bottom (C-D) Masson Goldner staining, used to assess the presence of fibrosis in the tissues. Images were analysed through the program QuPath-0.6.0 for pathological changes and overall tissue architecture. Representative images are depicted. Legend: S, spinal cord; M, muscle tissue; VB, vertebral body; GM, grey matter; WM, white matter.

The structures of the spinal cords and the surrounding tissues (bones, muscle, fat layers) remained similar. A common side effect of irradiation of the spinal cord is demyelination[59], the loss of the myelin sheath that surrounds the axons and helps in conducting the signals along the cord to the limbs. If demyelination happens, this is reflected in the paralysis of the limbs below the site of injury; in the case of this experiment, though, paralysis was never observed, which is explained by the preservation of the myelin in the white matter in Figure 54.

3.2.4 Selection of the doses for tumour treatment and normal tissue toxicity

Out of the different doses tested during this dose escalation experiment, two doses were important to be selected - one for treatment of a tumour and inducing normal tissue toxicity, and the second one to not stop the tumour growth. The presence of lesions forming in the tumour and the irradiation time caused the loss of part of the animals before the end of the experiment, complicating the interpretation of the results. Nevertheless, from Figure 42 and Figure 46 it's possible to see that the animal developing the tumour could be at least partially treated with the doses starting from 10 Gy. The animals surviving in the 0 and 5 Gy groups, instead, were those were no tumour developed, and all the other ones belonging to those groups were euthanised either for lesions formation, tumour not controlled or primary tumour regrowth. The 5 Gy dose was therefore selected as the dose that shouldn't stop the tumour growth (low dose in the washout experiment of the first experimental campaign, paragraph 3.3.1). With regards to the higher dose, we have selected 20 Gy since it resulted in the highest degree of kyphosis that we observed over the duration of the follow-up. Additionally, the skin could tolerate 20 Gy without severe complications, with no excessive toxicity observed and its reversion with appropriate care.

To avoid losing animals due to the late irradiation time point, the irradiation in the experimental campaigns was performed at two weeks of tumour growth, instead of three as in the photon experiment. This would have meant that part of the tumours might have not been measurable by the irradiation time, but if present, the tumours would have continued to grow for some day after the irradiation (further discussed in paragraph 3.3.2) and eventually become measurable. To prevent bias, the animals were randomised based on tumour size in the irradiation groups of the experimental campaigns, including animals with both small and large tumour volumes in all the groups.

The radiation-induced myelopathy was not exhibiting with a strong phenotype, even if the photons dose distribution was completely covering the cervical part of the spine. The ^{11}C irradiation was planned to have a different dose distribution than the photon one, with the dose only partially covering the spine (Figure 22), but owing to the higher RBE of heavy ions (Figure 9), we still expected to detect and quantify the spinal cord toxicity.

3.3 First demonstration of *in vivo* efficacy of tumour eradication with ^{11}C

The first biological experimental campaign using ^{11}C has been preceded by physics experimental campaigns[91,144], which were not part of this work but set the foundations for it. The objectives for this campaign were: the verification of the range of the particles inside the body of the animals by PET monitoring, and the observation of the biological washout of the β^+-activity and its implications with tumour treatment. The results and pictures found in this section are published in Boscolo *et al.*[108]. For the experiments, the animals were divided into five treatment groups, which are described in Table 10.

Table 10. Description of the experimental groups of the first experimental campaign with ^{11}C.

Experimental group	Nr. of animals	Dose (Gy)
Tumour-free control	8	0
Tumour-bearing control	27	0
Range verification study	17	20
High dose – Washout study	8	20
Low dose – Washout study	7	5

As explained in 2.2, the animals were injected with LM8 cells subcutaneously to form a tumour. However, after the photon dose escalation experiment, where the tumour was treated three weeks after inoculation and part of the animals experienced treatment failure, for the two experimental campaigns the irradiation was performed two weeks post-inoculation. To account for the growth failure rate that was observed during the previous experiments, higher numbers of animals were injected and the ones that could not be treated due to limited irradiation time were used as controls (see Table 10, tumour-bearing control group). Also in this experiment, the tumour implantation success rate was 85%. The animals were imaged at the μCT the day before irradiation as described in 2.3.1. On the irradiation day, the animals were anaesthetised as described in 2.4.2.6 (see Figure 55), brought at the beamline and treated for approximately half an hour with an SOBP of ^{11}C ions.

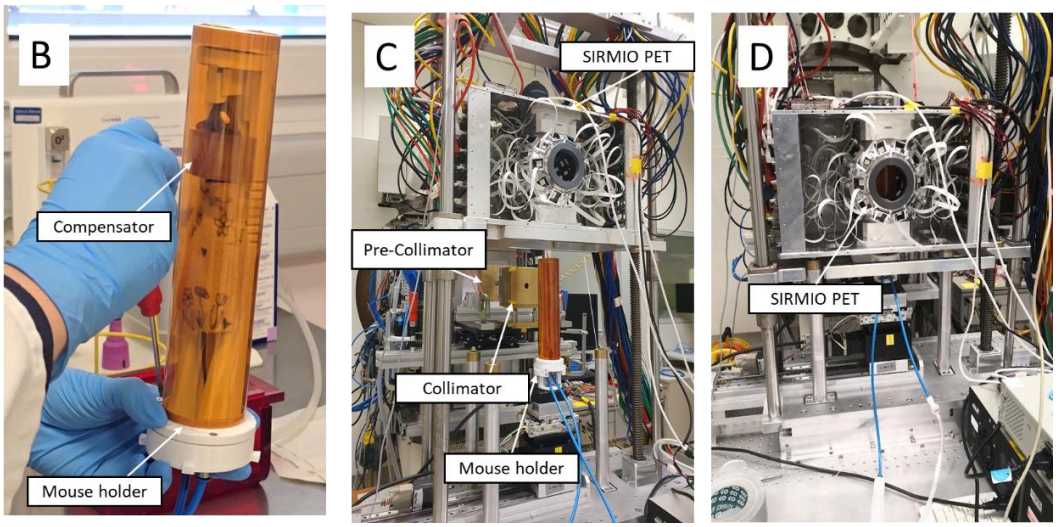

Figure 55. Preparation of the animals for ^{11}C irradiation. The animals were anaesthetised and fixed with the anatomical compensator on the SIRMIO bed, which was closed with a protective foil

to avoid gas leakage. The holder was then positioned in front of the beamline exit, and SIRMIO was lowered around it for the PET signal acquisition.

In the case of the low-dose washout group, the animals were left inside SIRMIO for the PET signal acquisition for one hour. The animals where the tumour appeared to be out of the treatment field at the moment of dose delivery were also moved to the tumour-bearing control group. The same treatment plans (see Figure 22) were applied for the irradiation of all the animals, with the only difference being the different dose delivered to the low dose group.

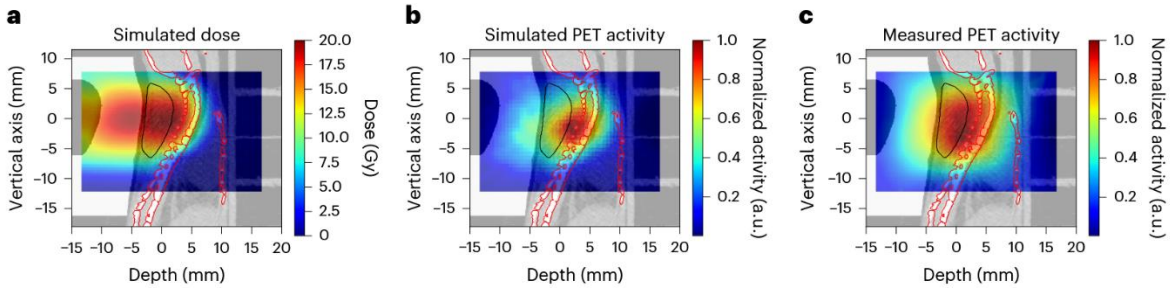

Figure 56. PET imaging for the first ^{11}C experimental campaign. A) FLUKA simulation of the expected dose overlaid on the mouse µCT (sagittal view). B) Corresponding Monte Carlo simulation of the PET activity and C) online SIRMIO PET image of the positron activity distribution measured during the ^{11}C irradiation. The black line represents the treatment area while the spine is highlighted in red.

Figure 56 shows the PET data overlayed with the µCT scans of the animals and the treatment area. The average tumour size at the moment of treatment was roughly 0,8 cm^3 (Figure 62), and the treatment area (generalized CTV) accounts for the small variations in tumour growth locations and size observed in Figure 29. In Figure 57 the dose and activity profiles along the beam path (z-axis) are depicted: the CTV area (light pink) was planned to receive a dose of 20 Gy, while the spine, receiving the end of the SOBP, received on average a lower dose, descending from 20 Gy to 15 at the end of the dose distribution (light red area, solid blue lined profile). The dose deposition in the spinal cord will be further discussed in the paragraph 3.3.5.

It's worth to notice the difference between the simulated and measured PET activity profiles (Figure 57, a, blue dashed line and red solid line). This happens because during the first experimental campaign all the treatment planning was prepared based on the µCT of the animals acquired in the horizontal position, but the irradiations were performed by keeping the animals vertically in front of the beamline. A small experiment was performed after the end of the first experimental campaign, when the SARRP became available. This helped in understanding if the horizontal versus vertical positioning could lead to major changes in the mouse anatomy with consequences on the dose delivery.

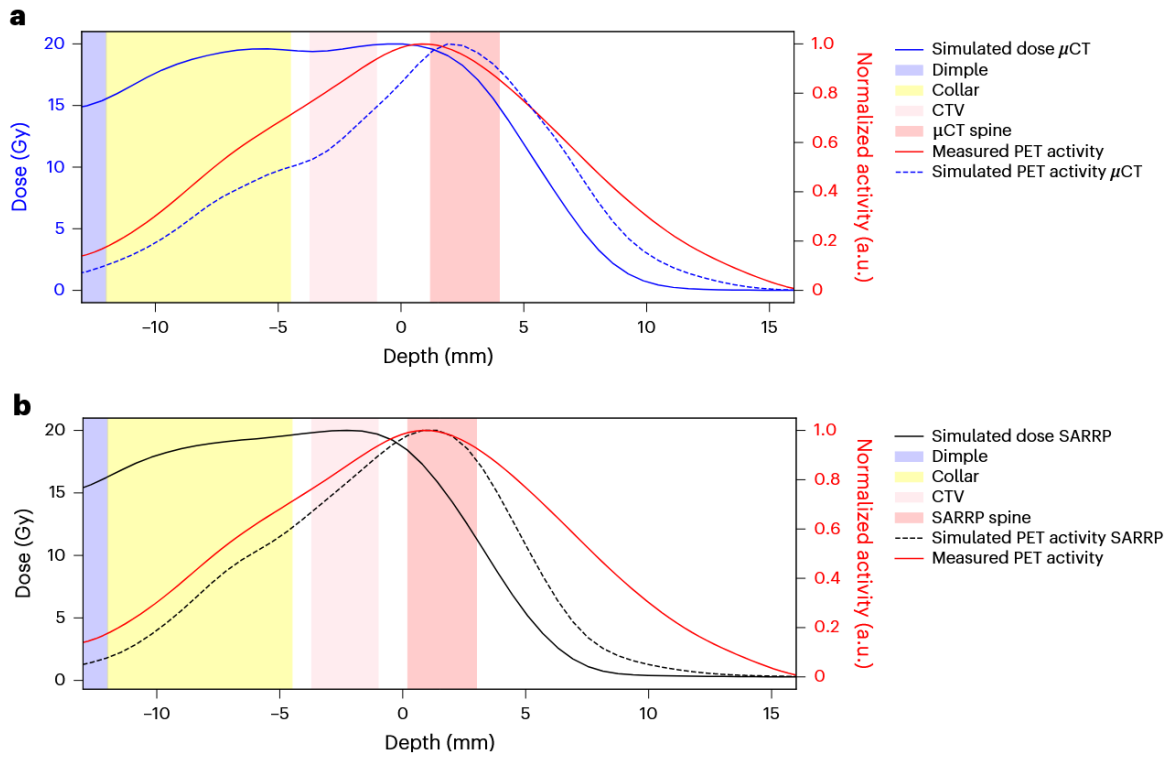

Figure 57. Activity profiles in mice from the first experimental campaign. A) The same mouse represented in Figure 56 is used to show the z-axis depth profiles of the simulated dose (normalised to the target dose, in blue), the simulated PET activity (dashed blue) and the measured (red) PET activity profiles.

A total of 5 animals were injected with LM8 cells as previously described and imaged at the µCT and SARRP just afterwards. This showed small but consistent differences (Figure 58) in the curvature of the spinal cords, which were taken into account in the simulations and measured activity calculations for the second experimental campaign.

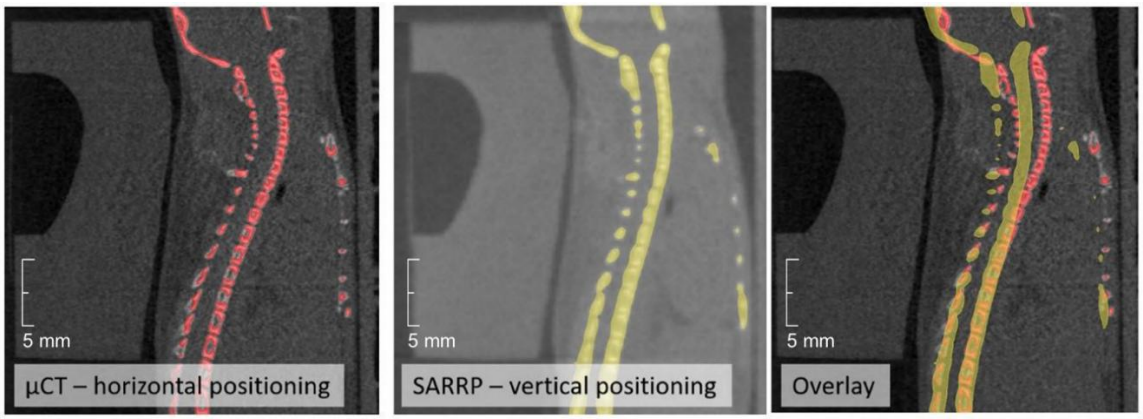

Figure 58. µCT versus SARRP imaging. The µCT and SARRP scan are compared to show the difference in the spinal cord curvature, which led to incongruences between the simulations of the dose and the experimental data obtained about the measured activity peak.

This anatomical difference reconciled the simulated and measured PET activity profile, as it can be seen in Figure 57b (back dashed line and red solid line), where the peaks match exactly. These findings highlight the importance of imaging performed just prior the dose delivery, and the acquisition of a SARRP scan will be routinely done during the second experimental campaign (3.4).

When the activity data were correlated with the grip test results, it was possible to observe a match between the highest measured activity value in the spinal cord with the worst performance on the grip meter (further details can be found in 3.3.5). This result was important for the prediction of the development of future side effects, but it was made on the assumption that the spinal cord anatomy during irradiation was maintained as on the diagnostic µCT acquired the day before. After the short experiment on the difference of the spine curvature between µCT and SARRP, also the activity measured during the beamtime was compared to understand the impact of the anatomical change on the dose deposition and the activity measured subsequently, as shown in Figure 59.

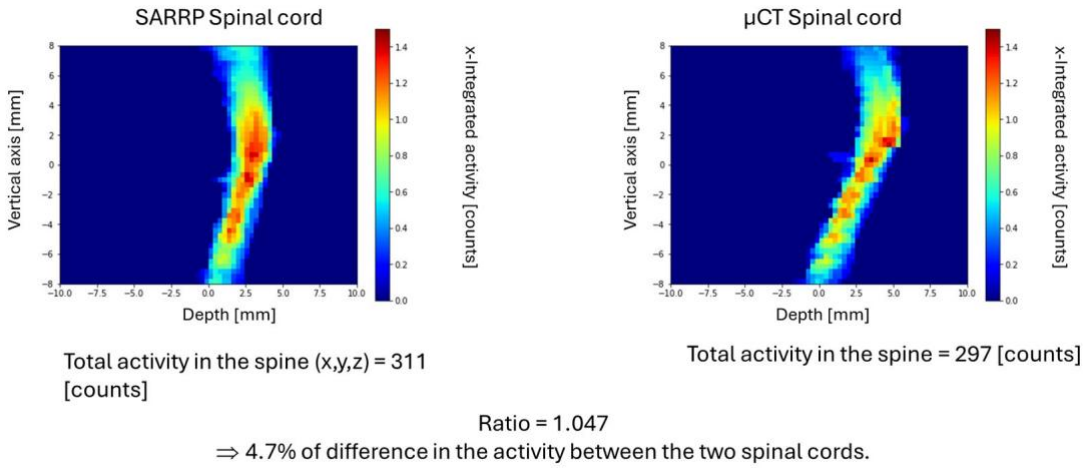

Figure 59. Activity in the spinal cord (µCT vs SARRP). Activity in the spinal cord (µCT vs SARRP). The Monte Carlo Simulation of the PET activity observed in the spinal cord shows a small difference in the activity counts between horizontal µCT and vertical CBCT (SARRP). The images were reconstructed with the MLEM algorithm and the activity counts in the spine are normalised to the total activity in the image. From Boscolo *et al.*[108].

When positioned vertically, the activity in the spine showed always slightly higher counts, but the value was in the 2-5% range and these differences didn't affect the correlation observed in Figure 68, where the scatter of the points is mainly caused by the high variability of the grip test results. The anatomical changes, then, didn't yield to major changes in the late side effects prognosis, but were tested to create a solid base on which it was possible to align the physics and the biology part of the study, fine-tuning all the simulations before the next experimental campaign and understanding the resolution power of the SIRMIO PET system.

3.3.1 Differences in the biological washout of PET signal in the tumour following high- and low-dose irradiations

The radioactive decay measurements were first tested in a plastic phantom, where only the physical decay of the activity is expected. This process gave the baseline for the physical activity decay expected during the experiment, where also an unknown biological decay is expected because of the blood flowing in the tumour. The blood circulation removes the radioactive isotopes from the decay site, especially if the tumour is highly vascularised and there are no major impairments to the flow. Since this tumour model is highly vascularised (Figure 35), a measurable biological washout was expected.

The animals belonging to the washout experiment were imaged in SIRMIO to collect the activity decay data. A model based on studies in a rat glioma model performed in Japan[97],

points to a double-exponential model for the biological washout, which could also be used for the data collected after the above-mentioned irradiation. The following equation describes how the measured activity data were analysed and fitted:

$$A(t) = A_{phys} \times A_{bio} = A_0 \sum_i w_i e^{\frac{-ln2}{T_{1/2i}}t} \times [W_s e^{-k_s t} + (1 - W_s) e^{-k_f t}]$$

where A_0 is the activity at the end of the irradiation, W_s is the relative weight of the slow component, and k_s and k_f are the slow and fast time constants, respectively. $T_{1/2i}$ is the half-life of the *i*th contributing radioisotope and w_i is its fraction in the total number of fragments. The model was adapted for this study, with the contributing isotopes considered were 96% ^{11}C, 3% ^{10}O, and 0,5% ^{15}O (based on the FLUKA Monte Carlo simulations). The physical and biological components of the decay were taken into account during the data analysis, with the results of the data fit depicted in Figure 60.

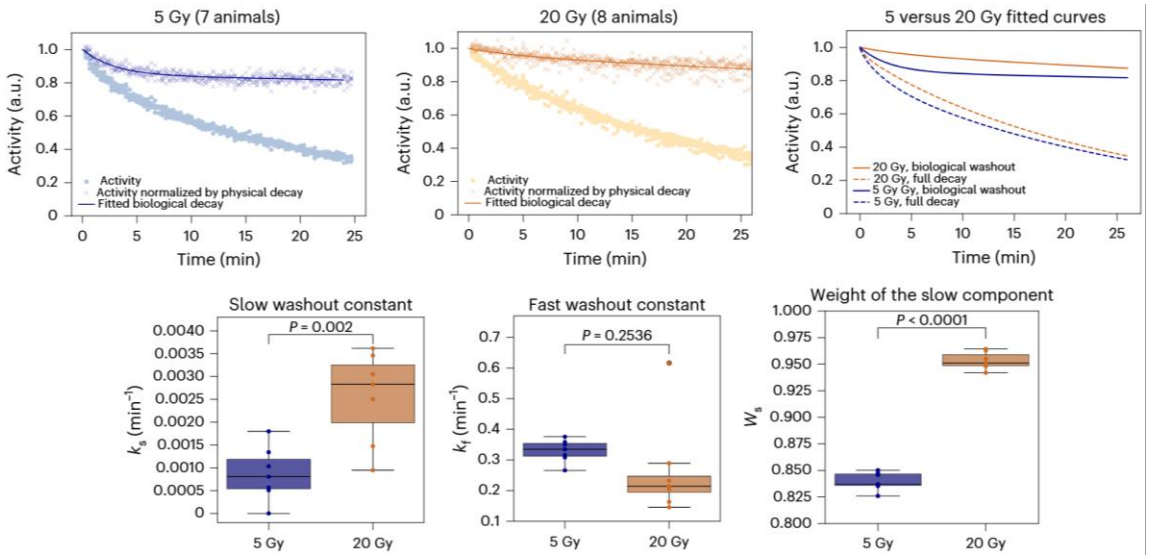

Figure 60. Radioactive washout curves. On the top line, the graphs represent the individual activity data from the 5 Gy dose group (blue) and the 20 Gy dose group (orange), with the fitted curves depicted in the figure on the right. On the bottom line, the double-exponential decay rates (k_s for the slow washout constant and k_f for the fast washout constant) and the weight of the slow component (W_s) from the activity equation for 5 Gy and 20 Gy. Box plots display the median (line), interquartile range (box spanning the 25th–75th percentiles) and whiskers extending to the furthest data points within 1.5× the interquartile range. Circles display the individual data points and the statistical significance was tested with the unpaired two-tailed t test.

In the analysis it can be seen that two different components are present in the data fit: the fast one, visible as the slope that steeply fades in the 5 Gy curve, and the slow one (the continuation of the curve, which characterised the second part of it). In the 20 Gy curve, the fast component is basically not present, and the washout is described only by the slow component. This difference suggests a vascular injury happening really quickly after the high dose irradiation, which delays the washout process.

To further investigate the presence of the vascular injury in the tumours, a Perls Prussian blue staining for presence of haemorrhage was performed. This method permits to highlight the presence of iron deposits in the tissue in bright blue, and in this case the iron deposits derive from haemosiderin. This iron-containing protein complex derives from the degradation of the haemoglobin contained in red blood cells by macrophages[130,145], which

are engulfed after haemorrhage. Part of the animals from the wash-out experiment were sacrificed immediately after the irradiation to assess the presence or absence of haemorrhage. The staining revealed hemosiderin deposits only in the high-dose irradiated group, hinting to a possible biological explanation for the slower biological wash-out of the PET signal. However, due to the limited size of the samples, it was not possible to draw further statistically significant conclusions.

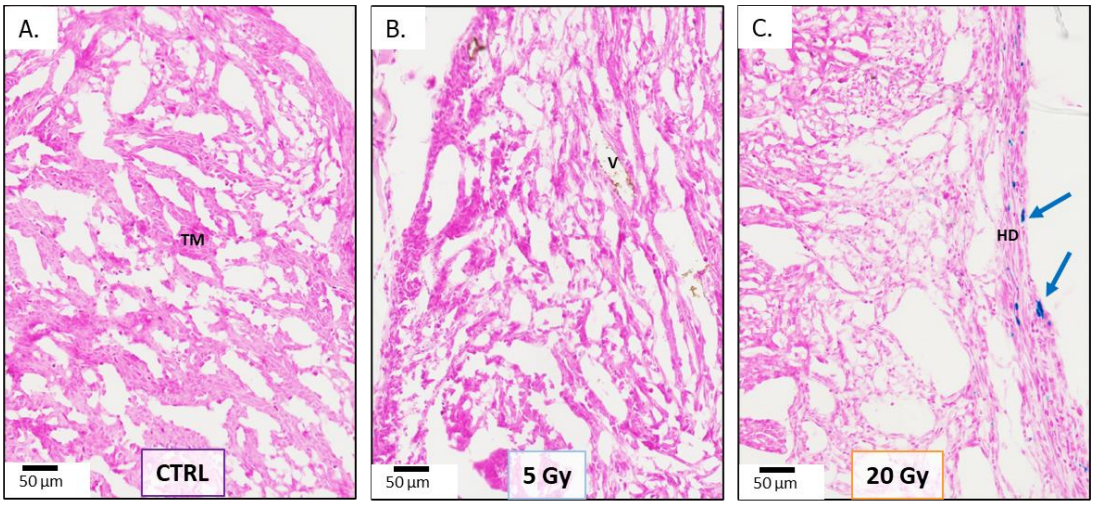

Figure 61. Haemorrhage presence in control, 5 Gy and 20 Gy tumours 1 hour post irradiation. Perls Prussian Blue staining for hemosiderin deposition. A subgroup of the animals belonging to the wash-out experimental groups were sacrificed 24 hours after the irradiation (CTRL N = 2, 5 Gy N = 1, 20 Gy N = 2) to check the presence of hemosiderin deposits, a sign of haemorrhage, indicated by the blue arrows. The tissue is stained in pink, while the deposits appear blue. Images were analysed through the program QuPath-0.6.0 for hemosiderin deposits localisation. Representative images are depicted. Legend: TM = tumour matrix; V = vessel, HD = hemosiderin deposit.

3.3.2 High doses of ^{11}C lead to tumour eradication

As described in 2.5.2, the tumour growth measurements were taken twice per week with the calliper (starting from the injection day) and once per week with the µCT (starting from the day before irradiation). These measurements were taken until the euthanasia of the animal, and in the case of the animals euthanised before the end of the experiment the last measurement was propagated to plot the growth curves for the following days.

Overall, tumours were eradicated with the high dose (20 Gy), while in the low dose (5 Gy) treatment the tumour growth is slowed down for two weeks, but then these tumours started to grow again by the end of the observational period. While the low dose was not enough to eradicate them, as expected, these data show the fact that one single high dose of ^{11}C managed to successfully halt the tumour growth. This experimental setting could be approximated to the one of single fraction high-dose RT that is being tested in the clinics, since only one dose was delivered instead of a fractionated treatment, and its aspects will be further discussed in 4.3.

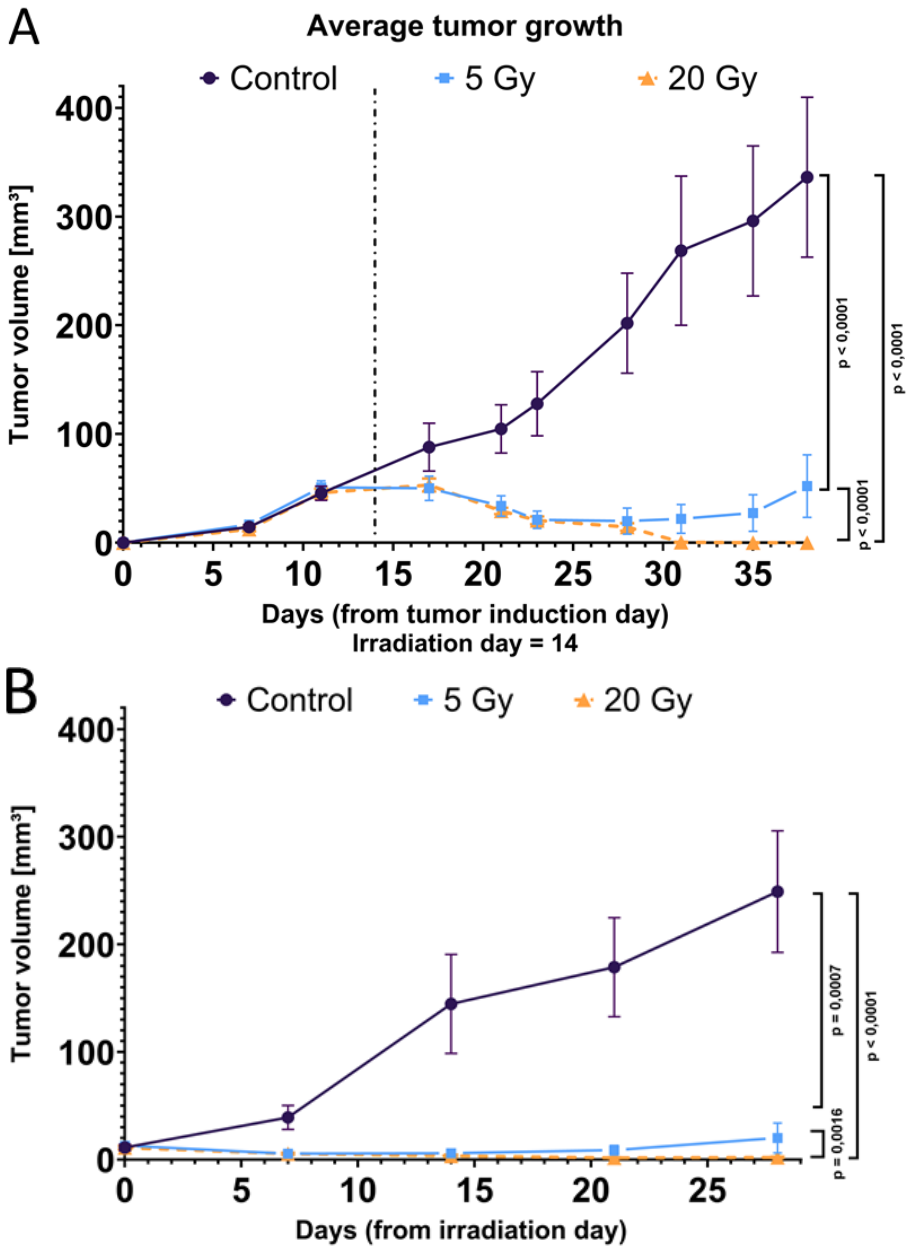

Figure 62. Average tumour volumes of the first experimental campaign with ^{11}C. A) Tumour growth curves measured with calliper, with the irradiation day marked by the dashed line. B-C) µCT growth curves and relative plot magnification. The 2-way ANOVA has been used to measure the difference between the curves, with the differences considered to be significant if p-value < 0,05.

3.3.3 Skin toxicity

Some animals were lost due to the development of lesions on the tumours (grade 4) also in the case of this experiment (Figure 63). In the case of radiation-induced skin toxicity, instead, this was resolved as previously explained and was sustained without major issues by the animals (Figure 64). Around 2 months post irradiation all the animals healed and either grew white fur, or remained hairless in the irradiation area.

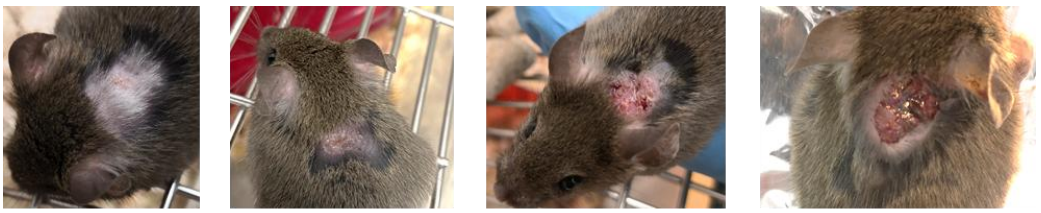

Figure 63. Representative pictures of skin toxicity scoring system. Grade 1 shows an animal where white fur is growing back after irradiation, with a small area of mild inflammation. Grade 2 shows moderate inflammation and desquamation, and grade 3 acute inflammation and development of crusts. Grade 4 was only observed in tumour-bearing animals that opened lesions in the tumours and was not caused by irradiation, since it could manifest before the treatment.

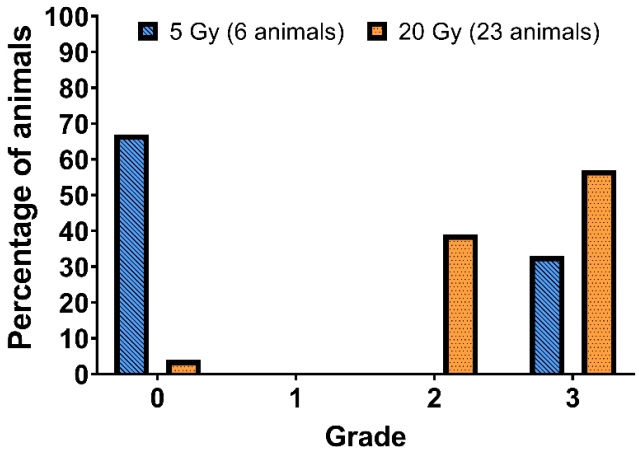

Figure 64. Radiation-induced skin toxicity of ^{11}C treatment. The columns show the percentage of animals showing toxicity. In both low (33%) and high dose treatment (57%) the animals manifested a grade 3.

3.3.4 The ^{11}C treated animals showed increased weight gain compared to the photon treated animals

In Figure 65, the weights from the animals belonging to the 15 and 20 Gy groups (X-rays experiment) were plotted together with the animals used for the long-term health status follow-up in the ^{11}C experimental campaign. The settings of the photon experiment and the experimental campaign were partially different (*e. g.* treatment setup, time of irradiation after tumour inoculation) and the sizes of the groups were reduced to small values in the photon-treated groups, but the graph is still useful to visualise the different distributions. In the experimental campaign, the losses in the tumour-bearing animals were caused by lesions or metastases development, and no animals were lost due to irradiation-related issues.

Weight-gain is a criterion commonly used to assess the general animal well-being. All the treatment groups showed differences, and in both the cases of ^{11}C and 15 Gy X-rays the animals survived until the end of the experiments without major morbidities, unlike the animal from the 20 Gy X-rays group. The cause of death of that animal was most probably radiation-induced oesophageal toxicity, since the dose distribution of the photons transversed the whole cervical area, from the back to the oesophagus. The same applies to the 15 Gy group, but in this case the dose was probably not enough to cause an extremely severe toxicity. In the case of the ^{11}C group, instead, the dose profile suggests that the oesophagus was at least partially covered by the tail of the SOBP. On the other hand, in the

case of this experiment, when the diet was enriched in the week after irradiation to prevent stress-induced weight loss, the tumour-free sham controls rapidly gained additional weight. This weight was never lost during the rest of the follow-up period, partially explaining why the controls weight distribution was skimmed towards higher values.

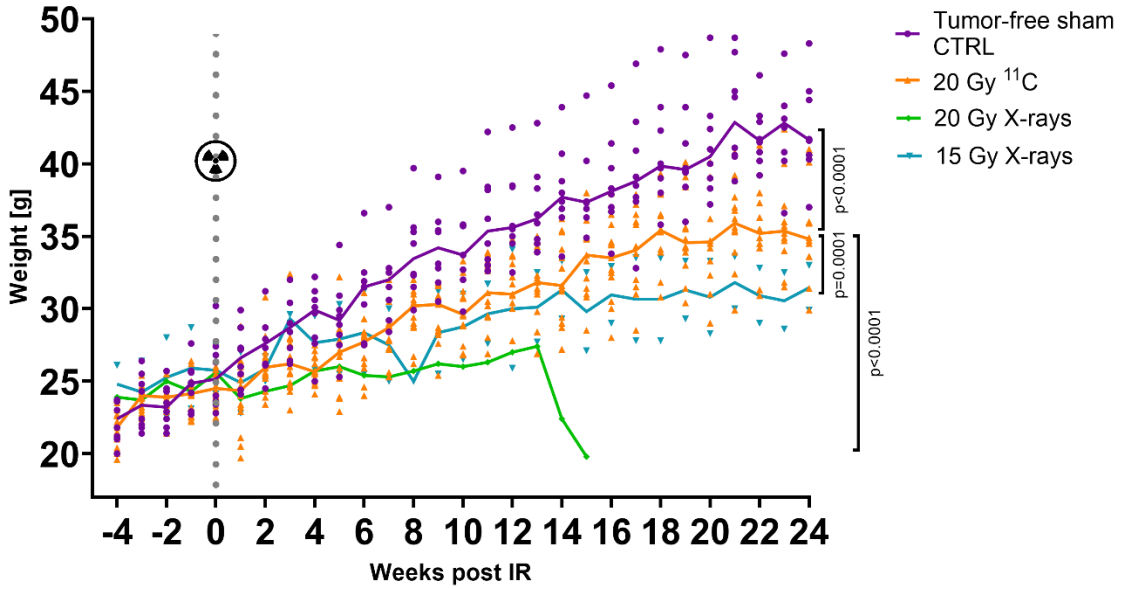

Figure 65. Weight-gain patterns of the animals from the first experimental campaign (tumour-free sham controls and 20 Gy ^{11}C irradiation) compared with the animals from the photon experiment (15 and 20 Gy groups). Every dot corresponds to one animal. The 2-way ANOVA has been used to compare the curves, with the differences considered to be significant if $p < 0,05$.

3.3.5 The PET-based monitoring of the beam range can predict late health side effects in the animals

The tumour-free sham-irradiated group was kept for 6 months post irradiation, together with the group treated with 20 Gy ^{11}C. They were compared not only for the general wellbeing (*e. g.* weight, skin toxicity) but mainly for the development of kyphosis and minor signs of neurological impairments, since the photon experiment suggested that paralysis would not have developed in this experimental setting.

Figure 66 shows the development of mild kyphosis in the irradiated animals. Also in this experiment, paralysis of the forelimbs was never observed, which led to all the animals reaching the planned end of the follow-up. As it can be seen in the plot below the scoring-system figure, the majority of the ^{11}C-treated animals exhibited a grade 1 kyphosis, which is not life-impairing and still permits to the animals to feed without issues (the food is usually located in the grid that closes the cages, above the animals, which means they have to stand up and reach for the food to eat).

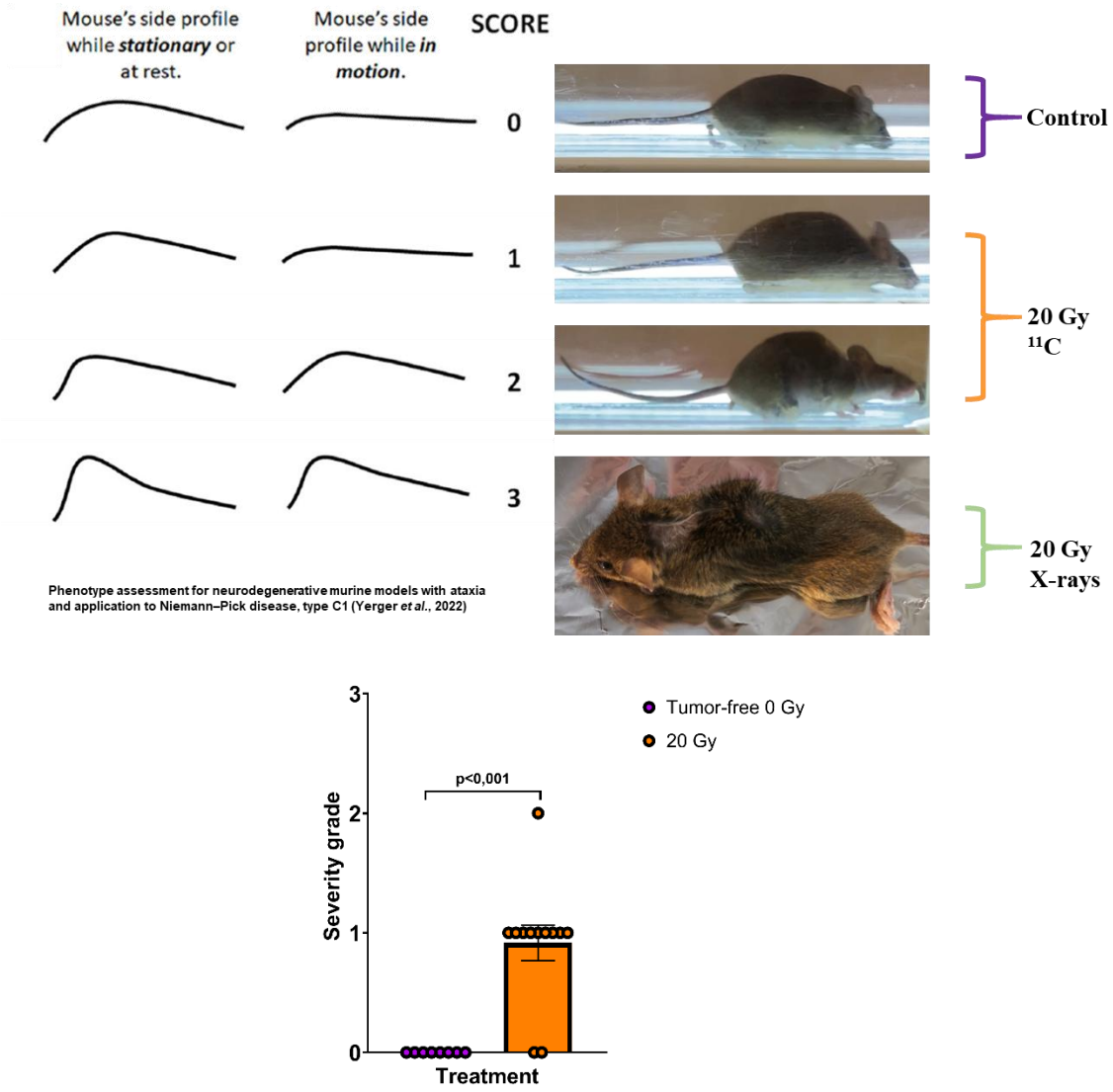

Figure 66. Kyphosis scoring of the first experimental campaign. The scoring system from Yerger *et al.*[125] was used to score the animals for the development of kyphosis during stationary and movement phase. The unpaired two-tailed t test was used to assess statistical significance, with the p value considered to be significant if $p < 0,05$.

The walk test has been performed also during this experiment, but since the animals tended to gain weight in a steady fashion, this led to some difficulties in the video analysis of the paw-prints, because the software could not distinguish between the paws and the shadow of the body of the animals. Since it did not prove to be significant during the photon-experiment, it was decided to not utilise those data.

The grip test, instead, proved to be a useful test to assess neurological impairments, especially when combined with the kyphosis scoring. It was performed as already described in 2.5.7 and showed that the animals exposed to ^{11}C had a decreased forelimb strength when compared with the controls (Figure 67).

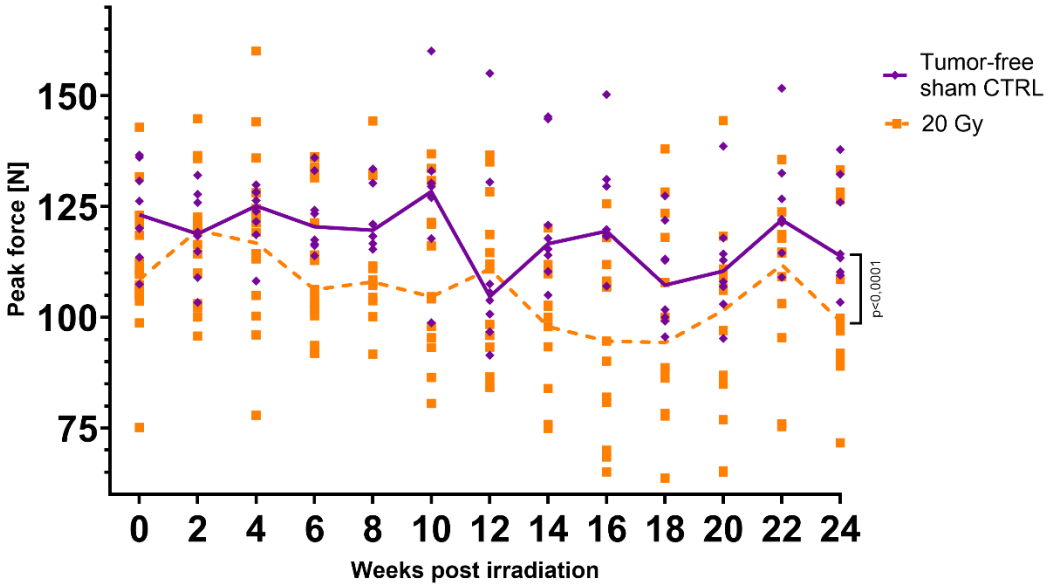

Figure 67. Grip test results of the first experimental campaign. The purple line represents the median values of control group, while the orange represents the animals treated with ^{11}C. Every point in the distribution represents the average of three measurements taken for one animal on the test day. The 2-way ANOVA has been used to compare the curves, with the difference considered to be significant if $p < 0,05$.

Because of the proximity of the tumour to the spinal cord, it was inevitable to have some dose deposited in the spine itself, which means that some activity was observed in the spinal cord (Figure 57). The PET-imaging data acquired during the irradiation moment were correlated with the performances of the animals during the grip test. The activity counts were measured for each animal, thus permitting to understand the relationship between the activity in the spine of the animal and the manifestation of later side effects. Since the spinal cord is an organ that shows a later response to radiation, for the plots in Figure 68 only the data from week 6 have been considered, assuming no radiation effects in the first month of follow-up.

These results show that the irradiated animals had a tendency to perform with lower grip strength values compared to the controls. A negative correlation has been found between the total activity and the grip strength: the higher the activity, the lower the strength (Figure 67c). The opposite applies with the fraction of test with $F < 100$ N, where the higher the activity, the more that animal showed values of force below 100 N. Back-correlating these findings with the irradiation moment, these data support the idea that knowing the position of the activity peak measured in the body can help in predicting the late radiation-induced side effects.

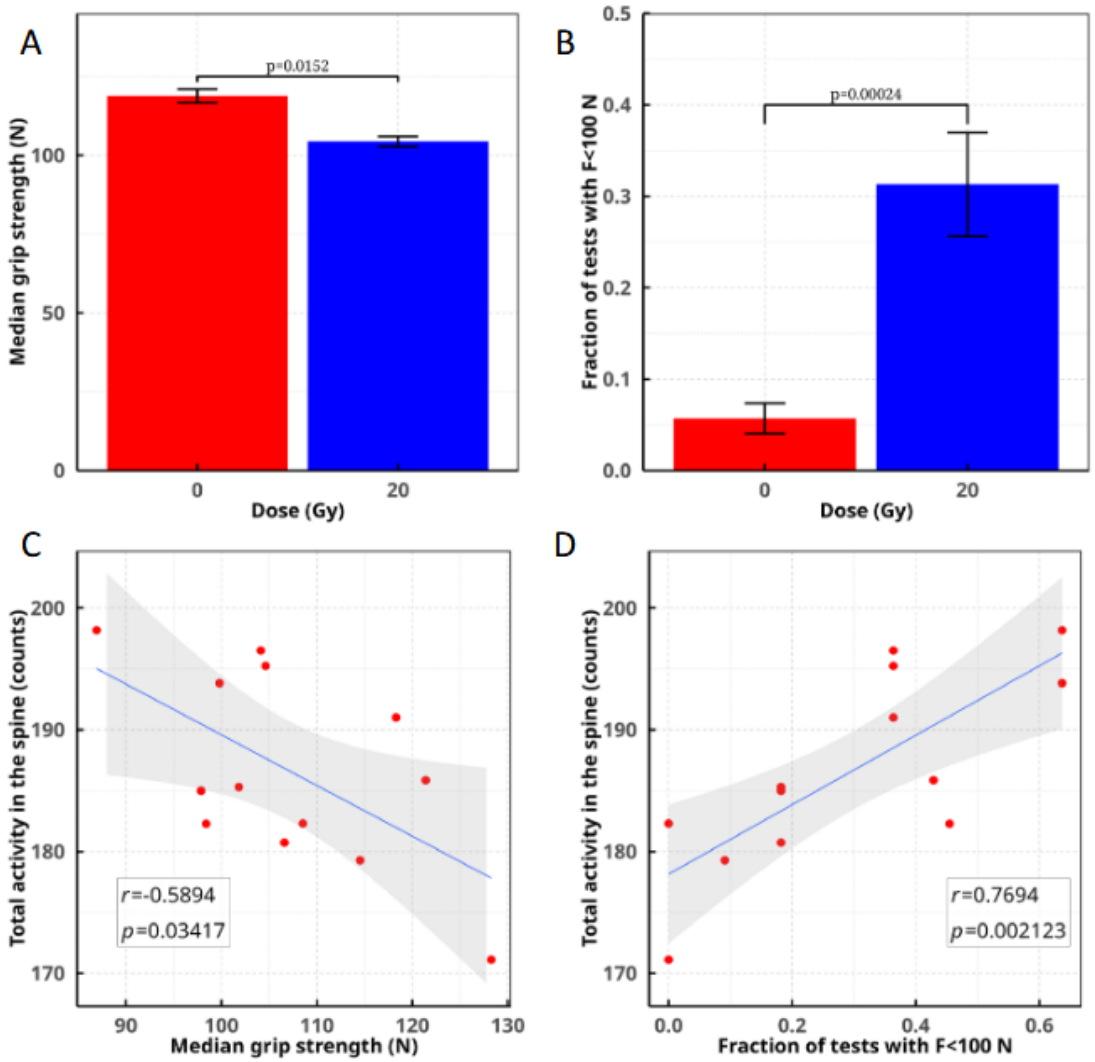

Figure 68. Correlation between measured activity and grip test strength. The ^{11}C treated animals are represented in blue and the controls in red. A-B) Column plot of the median grip strength for each treatment group, bars are standard errors of the median values and the Mood's median test was applied. B) Fraction of time points where the measured peak force (F) was lower than 100 N; bars are standard error of the mean and the Mann-Whitney test was used. C-D) Median grip strength and fraction of tests with F<100 N are correlated with the total activity (counts) measured in the spine. The grey area is the 95% CI around the regression line, r is the correlation coefficient and the significance of the correlation was evaluated by Pearson's test.

Also for this experiment, a histological analysis has been conducted on the spinal cord and surrounding tissues, but like as in the photon experiment, no significant differences were found between control and ^{11}C treated animals. Different structures, which can be identified with the different colours present in the staining and are described in Figure 69, generally maintain their integrity. No differences are present in the myelin (in the white matter, WM, external part of the spinal cord) where the radiation-induced damage is expected to happen[131]. The Goldner Trichrome staining (bottom panels) was performed to observe signs of fibrosis[146] (collagen fibres deposition) in the irradiated area, but also this was not observed.

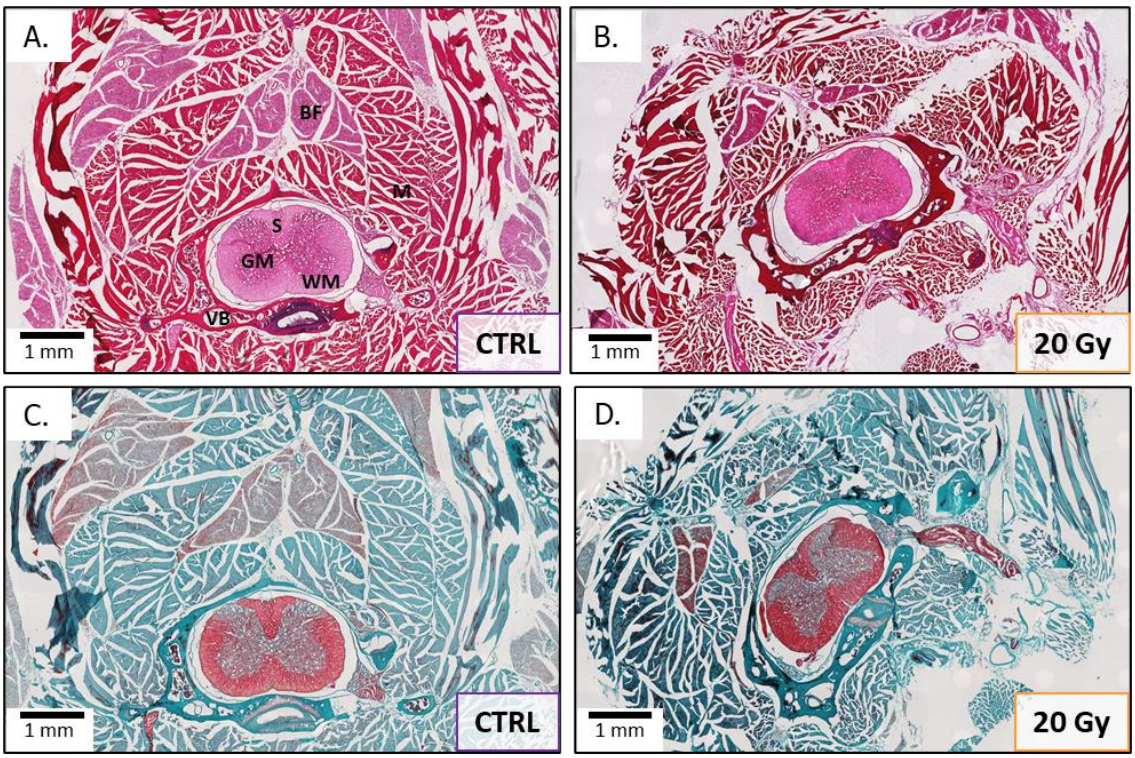

Figure 69. Histological panel representing a comparison between sham irradiated and 20 Gy ^{11}C irradiated cervical spinal cords with surrounding tissues. The top figures (A-B) are Haematoxylin and Eosin staining, the bottom (C-D) Masson Goldner staining for fibrosis. As in the photon experiment, 20 Gy were not sufficient to cause serious histological alterations. Images were analysed through the program QuPath-0.6.0 for pathological alterations. Representative images are depicted. Legend: S, spinal cord; M, muscle tissue; VB, vertebral body; GM, grey matter; WM, white matter, BF, brown fat tissue.

The manifestation of neurological symptoms at the histological level will be further discussed in 4.2, but as in the photon dose escalation experiment, it seemed clear that 20 Gy were not sufficient to cause serious ailments in the motor-functions of the animals (*i. e.* paralysis). Also, the spinal cord was covered only partially with 20 Gy, with an average value closer to 17 Gy as shown in Figure 57, which might also be the reason of the mild side effects.

In conclusion, the first experimental campaign demonstrated the feasibility of tumour eradication with 20 Gy of ^{11}C, the measurement of the biological washout *in vivo* at the same time of treatment and the presence of minor neurological side effects in the survivors, which could be correlated with the activity measured inside the body of the animals.

3.4 In-beam PET monitoring with ^{11}C beams enables adaptive *in vivo* tumour treatment and normal tissue toxicities prediction

The goal of this experimental campaign was to prove how in-beam PET can be used for real-time dose verification and treatment adaptation in particle therapy, with the contribution of RIBs. The results and pictures found in this section are published in Moglioni, Vitacchio *et al.*[147]. RIBs already proved to be useful in producing spatially resolved images to give information about the beam depth reached in the body of the animals during the first experimental campaign. In this case, the aim was to prove how the beam can

be dynamically repositioned to achieve different treatment outcomes. Regarding the biological endpoints, the experiment aimed at producing three different effects that could correlate exactly with the beam position in the body of the animals. In Figure 70, this concept is illustrated in the following way: when the range of the beam is too short (S), the tumour will not be completely covered by the SOBP, and the expected outcome is tumour recurrence; when the range is too long (L), instead, the tumour will be treated, but toxicity will develop in the healthy tissues behind it. The optimal scenario would be the one where the radiation field covers the tumour in the "just right (R)" way, eradicating it but sparing the healthy tissues behind. In literature, this term originates from the fairy-tale "Goldilocks and the Three Bears" where the character Goldilocks chooses the "just right" porridge, chair, and bed. The term generally refers to something being "just right" or in the ideal or optimal state, avoiding extremes. Lastly, the Long beam range was planned to traverse tumour, spinal cord and reach the oesophagus, to potentially cause a toxicity that was easier to confirm than the one of the spinal cord during the sixth months of follow-up.

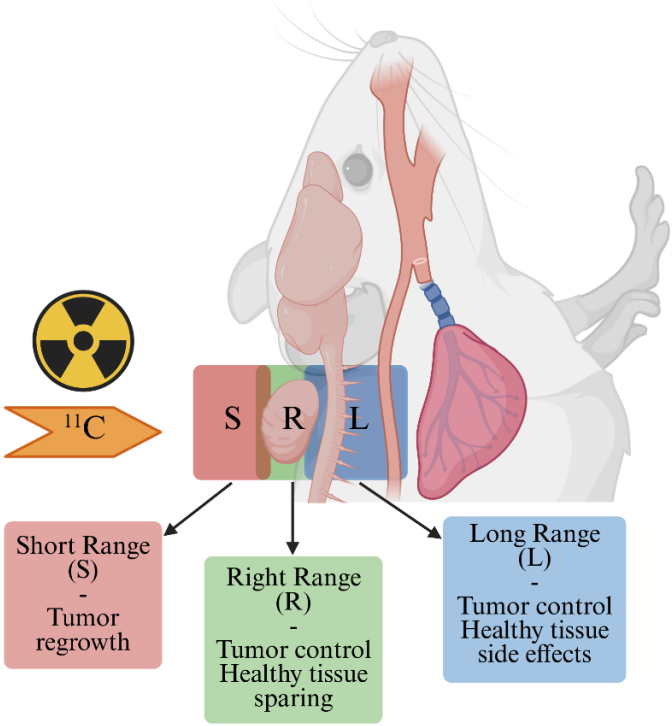

Figure 70. Goldilocks range concept. The three different beam ranges are represented together with the OARs and the mouse sagittal plan, and are linked with different biological outcomes. Created with BioRender.

The irradiation and control groups are described in Table 11.

Table 11. Description of experimental groups of the second experimental campaign with ^{11}C.

Experimental group	Nr. of animals	Dose (Gy)
Tumour-bearing control	9	0
Tumour-free control	8	0
Short Range	7	20
Right Range	8	20
Long Range	10	20

Unlike the first experimental campaign, as explained in 3.3, this time the animals were scanned at the μCT the day prior to irradiation, and then scanned at the SARRP just before the irradiation to get the exact image of the anatomy as in the irradiation setup. The utility of this process will be further discussed in 3.4.1, but as already explained in Figure 57, it was important to obtain the exact match between simulated and measured PET activity data. For the irradiation, the animals were anaesthetised as already described in paragraph 3.3 and enclosed in the SIRMIO holder, then they were transferred at the SARRP for a quick (5 minutes) scan. Afterwards, they were positioned in front of the beamline, where first the ^{11}C monoenergetic beam was used to verify the range that was planned for each animal by overlapping it with the CT scan obtained at the SARRP. The dose used for this beam was 5 Gy, but since the irradiated area was around 7 mm^2, this was considered to be negligible for the tumour treatment part. The in-beam PET images were produced in approximately 25 seconds, providing instantaneous feedback on the range of the beam. The normal 20 Gy SOBP was delivered afterwards, in the same way it was done during the first experimental campaign, with the only difference being the three treatment scenarios.

To produce this different biological endpoints, three different FLUKA simulations were prepared to plan the ^{11}C dose distributions in the mouse based on the anatomy obtained with the vertical CT scan (Figure 71) and to ensure that the monoenergetic beam ranges reached the desired depths in the targets and surrounding healthy tissues. Regarding the beamline, a stainless-steel collimator with a 3 mm aperture was positioned along the beam path and used with the ^{11}C monoenergetic probe beam to verify the range of the beam prior to full target dose delivery. This component was mounted inside SIRMIO and as close as possible to the mouse holder to avoid beam scattering. The three ranges, instead, were obtained during the irradiations by selecting combinations of plastic plates with a remotely controlled range shifter, adding or removing plates to have a shorter or longer reach of the beam inside the body of the mouse.

Figure 71 shows the simulated dose distributions (left side) and the respective 1D dose profiles and measured activity profiles on the right side. The simulations were used for real-time range verification. In A and B, the Short range information can be seen, where the simulated dose deposition (dashed line) of the SOBP was planned to fall in the compensator collar, with a fraction of the dose covering the tumour and basically no dose received after it. In C and D, the Right range plots show how the SOBP was planned to cover the tumour, with minimal dose deposition after it. In E and F, ultimately, the information about the Long range show how the SOBP covered the CTV, but also the oesophagus with a high percentage of the planned dose (around 80%). The simulations were performed on the CBCT scans (obtained with the SARRP) of the animals, with the same anatomy of the irradiation moment; the measured PET activity profiles where therefore confirmed to be correct, as shown in the example obtained during the first experimental campaign (Figure 57).

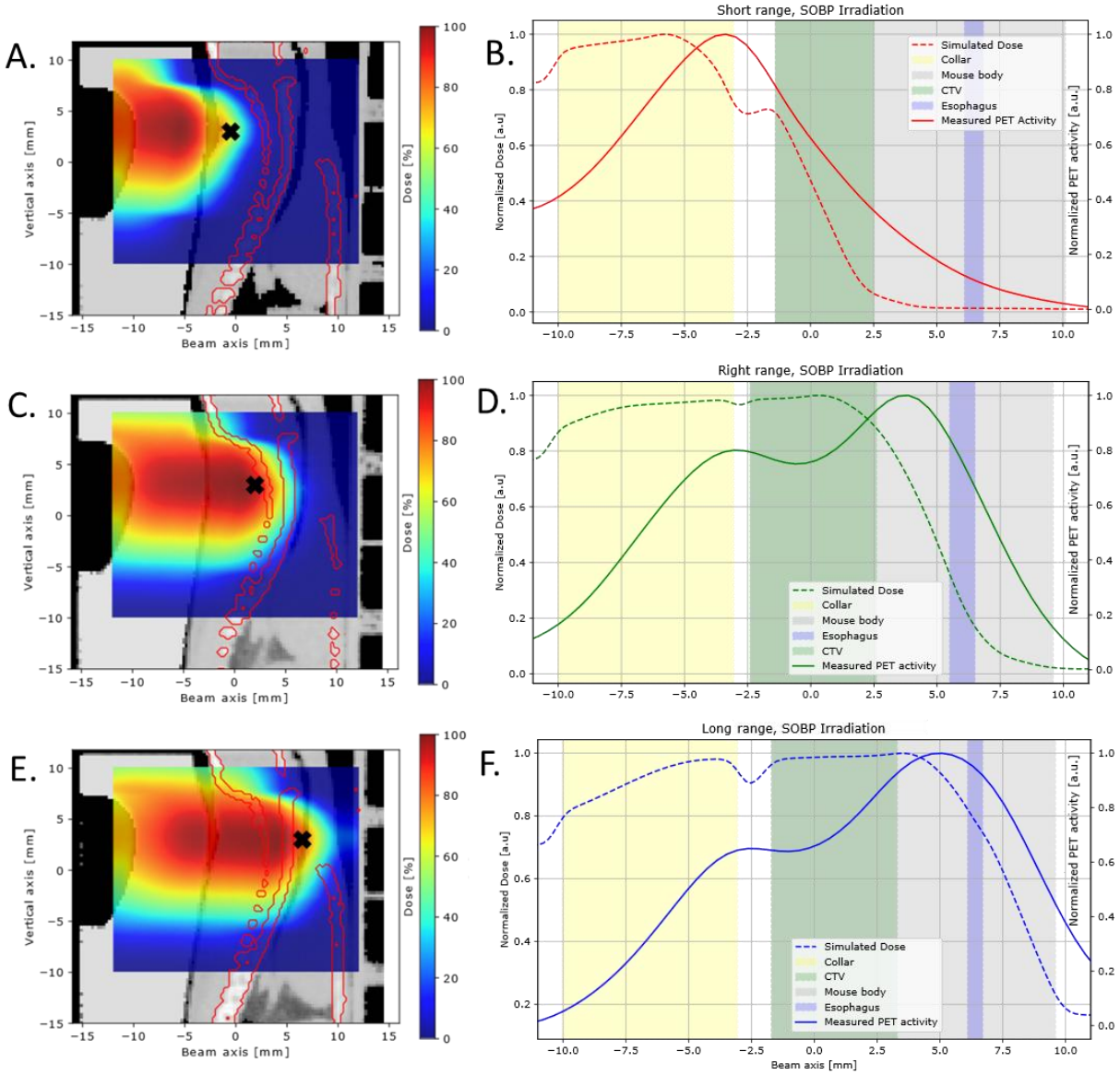

Figure 71. FLUKA simulations and dose and measured activity profiles of the second experimental campaign. A, C, E) FLUKA simulations showing the planned ^{11}C-ion dose distribution (in percentage of the maximum dose value) for the Short range (A), Right range (C) and Long range (E) in the SARRP scan of a mouse in the sagittal view. B, D, F) Plots representing the simulated doses (dashed lines), measured PET activities (solid lines), collar (yellow band), CTV (green band), mouse body (grey band), oesophagus (blue band) for the Short range (B), Right range (D), and Long range (F).

3.4.1 In-beam range monitoring can predict tumour control

As already described in 2.5.2, the tumours were measured twice per week. Also during this experiment several animals were lost due to the development of lesions on the tumours, and for those the last tumour measurements were propagated until the end of the follow up. The first notable result is the tumour regrowth in the Short group, which exhibited an initial growth delay of approximately two weeks before tumour progression resumed, ultimately reaching a trajectory comparable to that of the control group. Secondly, the tumours were instead eradicated in the Right and Long range groups. These results confirm the precision of the irradiation when image-guidance is applied, and that the minimal deviation from the treatment plan might lead to tumour recurrence (case of tumour under-coverage or missed target, represented in this experiment by the Short range). The large error bars in the control

group are explained by the loss of animals intra-experiment, while in the Short range group they are caused by the presence of tumour with different dimension, as it can be seen in Figure 72.

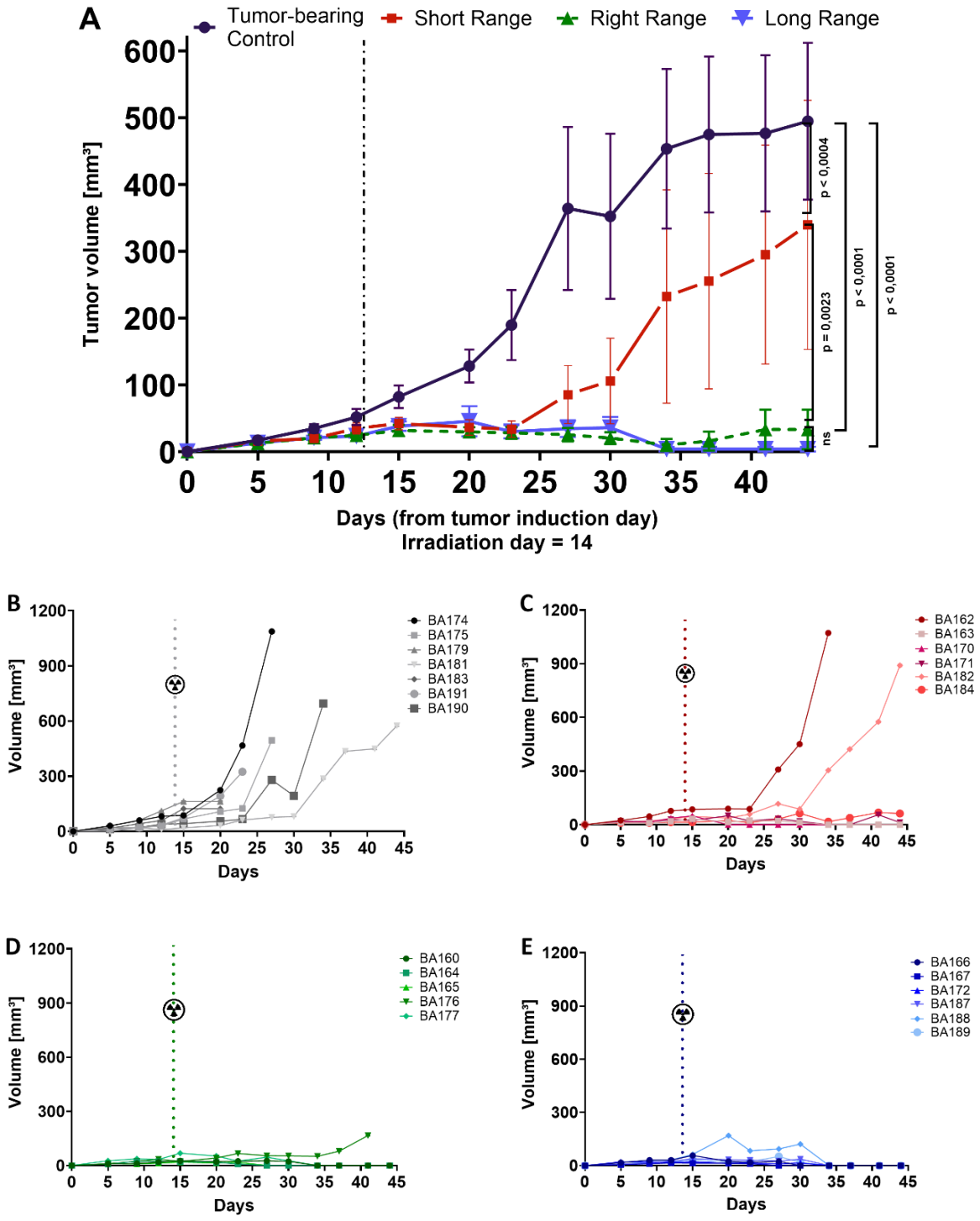

Figure 72. Average tumour volumes of the second experimental campaign with ^{11}C. The bars are standard error of the means, the differences between the curves were analysed with a 2-way ANOVA and were considered significant when $p < 0,05$. The irradiation was performed at day 14 (radiation symbol and dotted lines in the graphs). A) Group-averaged growth curves; B) single curves of tumour-bearing controls; C) single curves of Short range group; D) single curves of Right range group; E) single curves of Long range group.

It can be noticed that there is a small sign of regrowth in the Right range curve in Figure 72D. This is due to a tumour regrowth in mouse BA176, that needed to be euthanised one month after irradiation with the animals remaining in the control and Short group. The Right group size is small compared to the other one, and is due to the fact that some of the animals in the group (N = 3) experienced a shift of the tumour between the day before irradiation (μCT acquisition) and the moment of irradiation, where a CBCT was acquired just before. As it can be seen in Figure 73, the tumour is shifted outside of the treatment area. Since the beamline is fixed, it was not possible to make the necessary adjustment to treat these animals, which eventually had to be euthanised before the end of the experiment and were excluded from the tumour growth analyses.

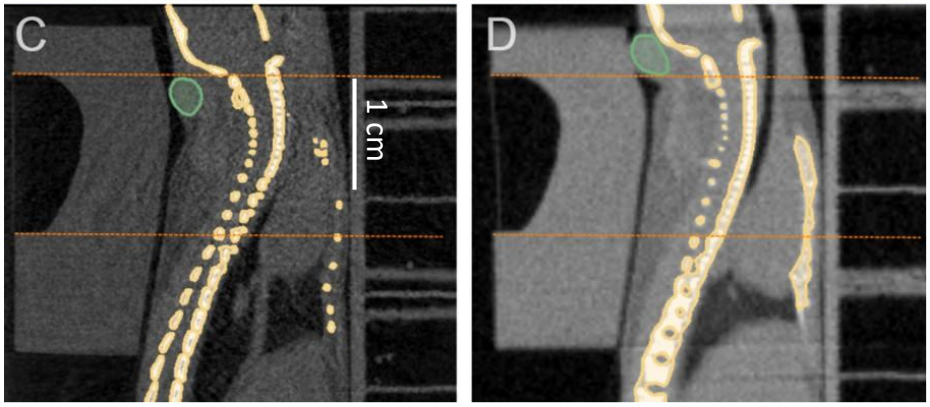

Figure 73. Comparison between horizontal μCT (C) and vertical CBCT (D) scans with tumour shifted outside treatment area during repositioning of the same animal.

The workflow of the experiment followed the setting of online adaptive radiotherapy, where the imaging data acquired just before treatment were used for in-beam PET-based beam delivery verification. These pictures show how in a clinical setting it would be convenient to acquire a new CBCT just before delivering a treatment, but this is usually difficult to do before every fraction due to availability of the machines, dose limits recommendations, treatments times etc. Range verification can help in this regard, since the beam stopping position and therefore the activity peak are expected to be in a certain area based on the planning CT. If activity peak deviations appear, this can suggest that anatomical or positioning variations happened, raising the need for either slight shifts in the beam depth or, with large variations, the need to acquire a new CT and replanning the treatment.

The histology of the tumours of the animals that needed to be sacrificed before the end of the observational period (*e. g.* because of lesions formation) revealed the same conclusions (Figure 74). The control tumours showed the normal structure of the osteosarcoma, with the presence of osteon-like structures and a high quantity of extracellular matrix. In the Short group, the tumour is showing damage attributable to radiation (necrosis, loss of structural integrity) but the sizes were still comparable to the tumours of control group. The Right and Long tumour samples, instead, show large areas of radiation-induced damage, compatible with the effect of the received treatment.

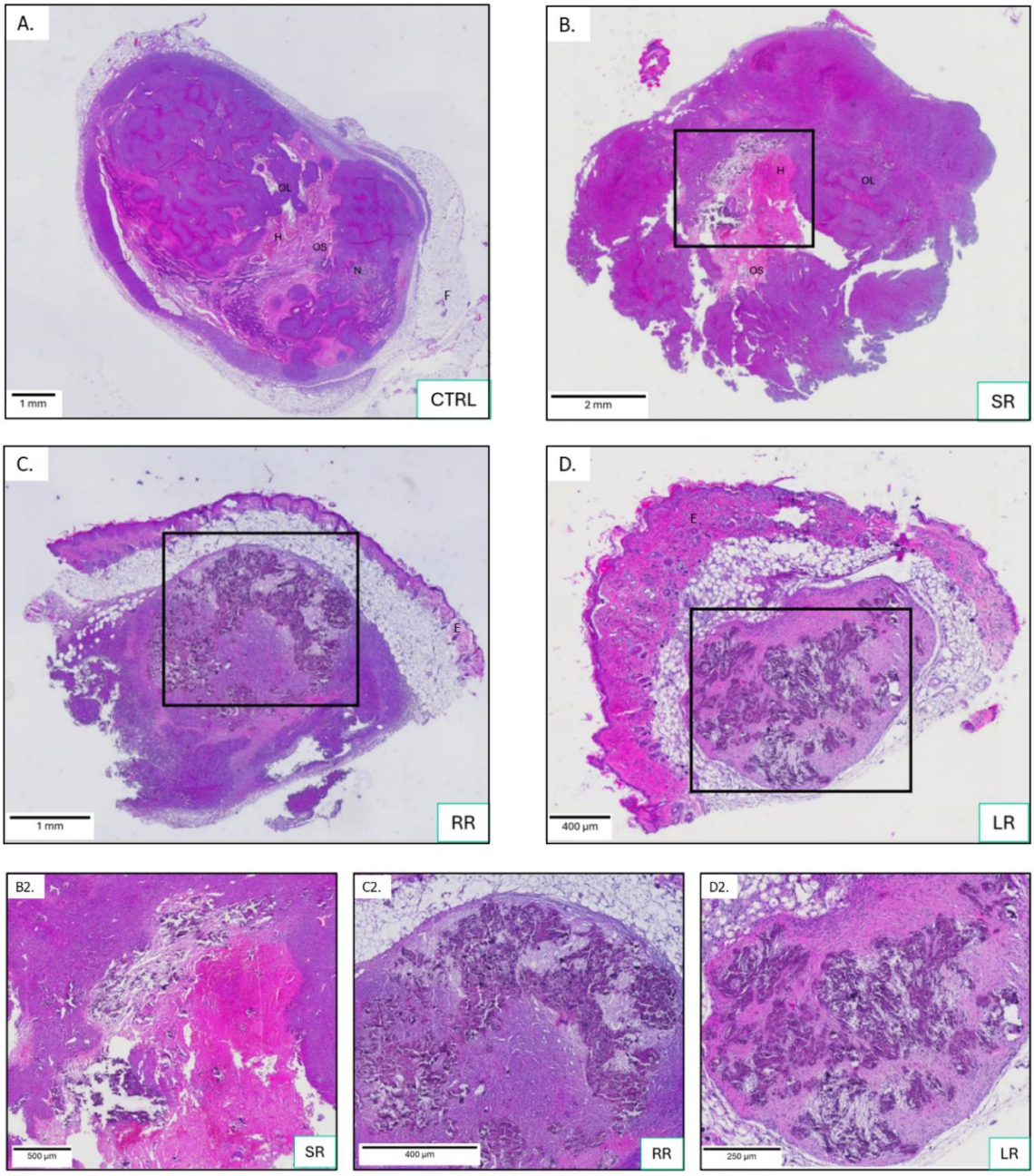

Figure 74. Tumour HE histology from the second experimental campaign. The cell nuclei are stained in deep purple, the extracellular matrix and other types of fibres in pink. Zoom-in images (B2, C2, D2) show radiation-induced lesions in all irradiated samples. Images were analysed through the program QuPath-0.6.0 for presence of necrotic areas and sample dimensions. Representative images are depicted. Legend: CTRL, tumour-bearing control; SR, Short range; RR, Right range; LR, Long range; OL, osteon-like structure; E, epidermis; F, adipose tissue; H, haemorrhage; OS, osteoid; N, necrosis.

3.4.2 Skin toxicity

As for the previous experiments, the grade 4 corresponds to the manifestation of open lesions on the growing tumours. The toxicity expressed by the control animals, therefore, refers to this case. In the case of the irradiated animals, the majority of the toxicity was caused by irradiation exhibiting with a grade 2, and never went above grade 3. The necessary health care was given and all the animals healed from radiation-induced dermatitis without issues. Figure 75 summarises the findings about skin toxicity in this experiment.

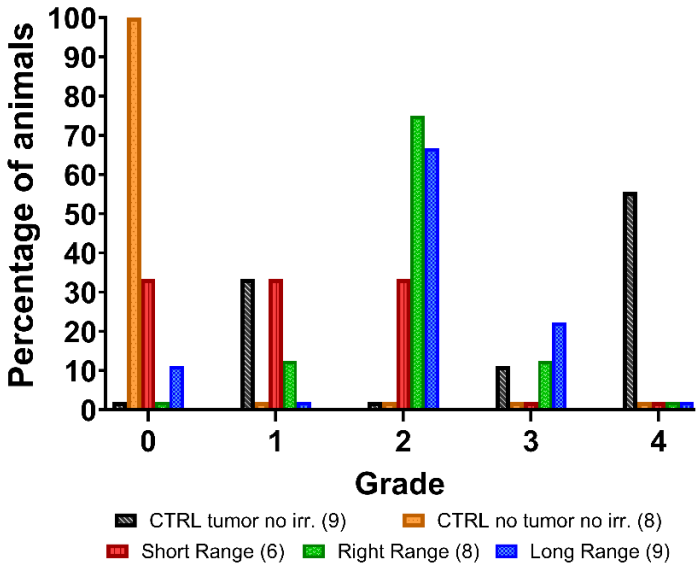

Figure 75. Radiation-induced skin toxicity of the second experimental campaign.

3.4.3 Late toxicities

Except the mild skin toxicity, in this experiment no health complications were expected for the Short and Right groups. Due to the tumour regrowth, the animals belonging to the Short group were euthanised one month after irradiation, but no notable toxicities were observed in this timeframe except the skin toxicity. The normal tissue complications were expected to occur in the Long range group and should have involved the spinal cord and oesophagus. Oesophagus toxicity was not explored before in this work, but the reference scoring system can be found in Table 6. In human patients the radiation-induced oesophagus toxicity is normally associated with pain during swallowing and altered food intake, which can lead to weight loss. Therefore, for the animals treated during this experiment, the main parameter observed was the weight gain during the course of the follow-up.

3.4.3.1 Histological examination of an example of acute radiation-induced oesophageal toxicity

The effect of the Long range irradiation was particularly clear in the extreme case of one animal, which showed a grade 3 oesophagus toxicity and had to be sacrificed due to rapid and severe weight loss (>20%), breathing issues and pain-showing hunched posture just two weeks post irradiation. When scanned at the μCT, the image revealed the empty gastrointestinal tract, indicating an impaired food intake.

The scoring system for describing oesophageal toxicity in this work has been adapted from the Eosinophilic Esophagitis histologic scoring system (EoEHSS) from Alexander *et al.*[148]. Upon histological examination of the oesophagus of the animal manifesting grade 3 toxicity, the oesophageal tissues revealed several pathologic features. A marked increase in the basal cells layer proliferation (hyperplasia, BZH) was present, and surface epithelial alteration (SEA) characterized by partial loss of the keratinized layer and organizational disruption were found. The basal cells layer usually consists in a monolayer of cells, the function of which is to constantly replenish the oesophageal epithelium consumed by the passage of the food bolus during eating. When hyperplasia takes place, it means the epithelium is in an altered condition and the top layers are losing more cells than necessary[149], hence the necessity to repopulate the tissue. In Figure 76, it is clear that the oesophagus was subjected

to loss of epithelial integrity and breakdown of the mucosal barriers, two phenomena that tend to occur in the timeframe between days and weeks post irradiation, as shown in Figure 11. The keratinised layer, the top one of the epithelium which faces the lumen (inside of the oesophagus) is being eroded and it´s losing the connection to the rest of the epithelium, as demonstrated by the presence of cellular debris in the lumen.

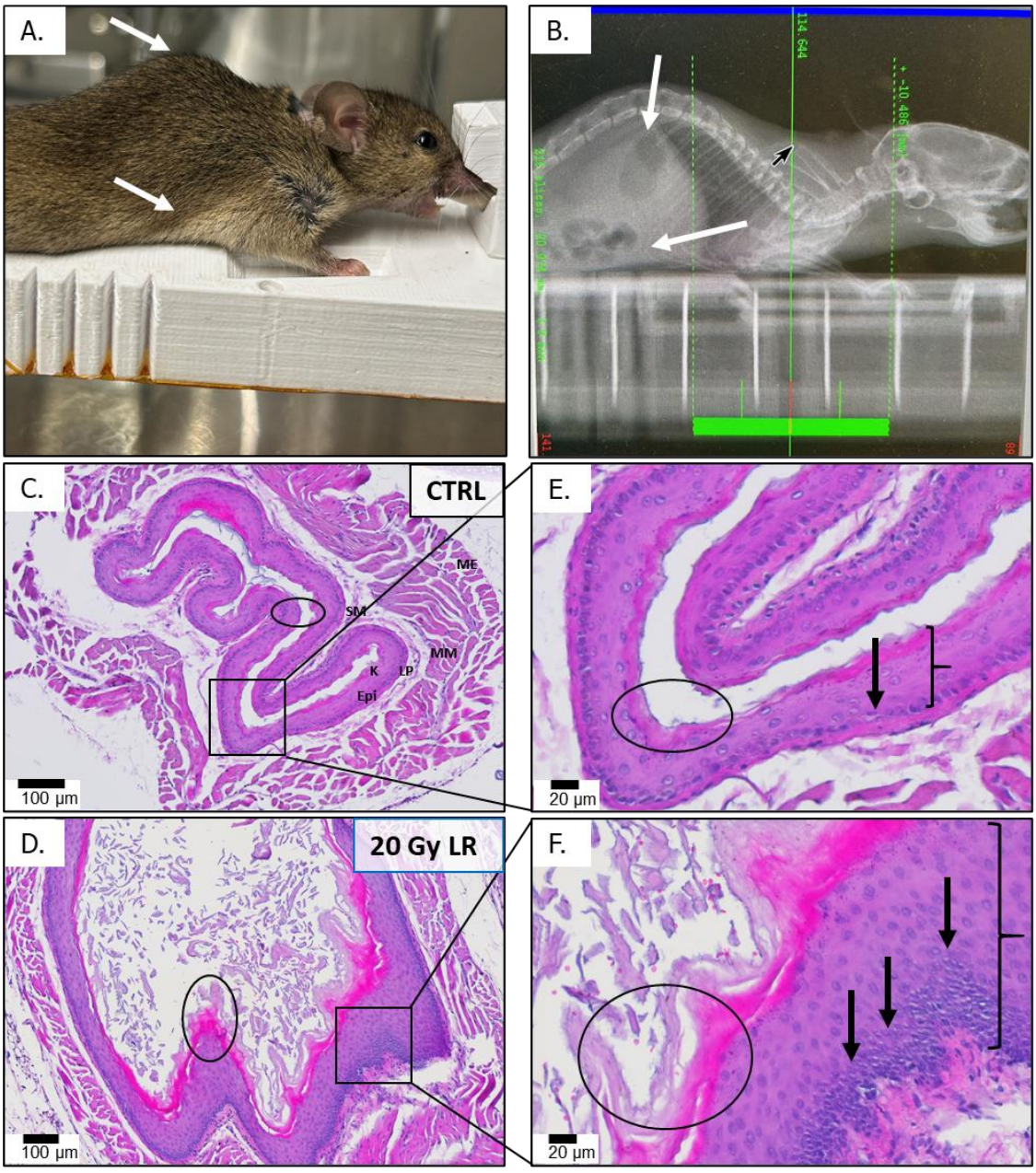

Figure 76. Acute radiation-induced oesophageal toxicity. Panels A-B show the photo and the X-ray scan of a mouse from the long range (LR) group two weeks after irradiation, exhibiting breathing issues, severe weight loss, and altered food intake, which was indicated by the hunched posture and air-filled areas of the gastrointestinal tract seen on the CT (white arrows). The panels from C) to F) show haematoxylin-eosin staining of the oesophagus of a control animal and the animal showing signs of acute radiation-induced oesophagus toxicity. E-F) are magnifications of C-D). The circles indicate the difference between the normal keratinized epithelium of the oesophagus (E) and the surface epithelial alteration (F), with the partial loss of the keratinised layer. The arrows show the normal monolayer of basal cells (E) and the basal zone hyperplasia (F). The curly brackets show the normal epithelium thickness (E) and the consequence of the hyperproliferation of the basal cells layer, resulting in a thickened epithelium (F). Images were analysed through the program QuPath-

0.6.0 for sample dimensions and pathological characteristics. Representative images are depicted. Legend: K, keratinised epithelium; Epi, epithelium; LP, lamina propria; SM, submucosa; MM, muscolaris mucosa; ME, muscolaris externa.

The acute reaction exhibited by this animal was expected to be similar for the Long Range animals kept for the long-term study about the post-irradiation toxicities. Since the only 20 Gy X-rays animal surviving until 16 weeks post-irradiation was most probably manifesting a similar oesophagus toxicity, a similar timeframe was expected for the Long range group.

3.4.3.2 The weight-gain patterns correlate with the beam position inside the body of the animals

The weights were measured weekly and plotted in Figure 77, where the tumour-free controls (N = 8) are compared with the Right and Long groups. Since some animals from the Right and Long group have been lost during the course of the experiment because of the development of metastases, the final number of the survivors were N = 3 for the Right group and N = 5 for the Long group. Along all the follow-up period the weights of the Right group tend to align with the one of the controls, while the one of the Long group diverged. While the weight of the animals depends on many factors (*e. g.* stress level, position in the social hierarchy inside the cage, number of animals present in the cage, diet) the averaged weight distributions suggest the Long range received the planned irradiation and had the oesophagus covered by the beam.

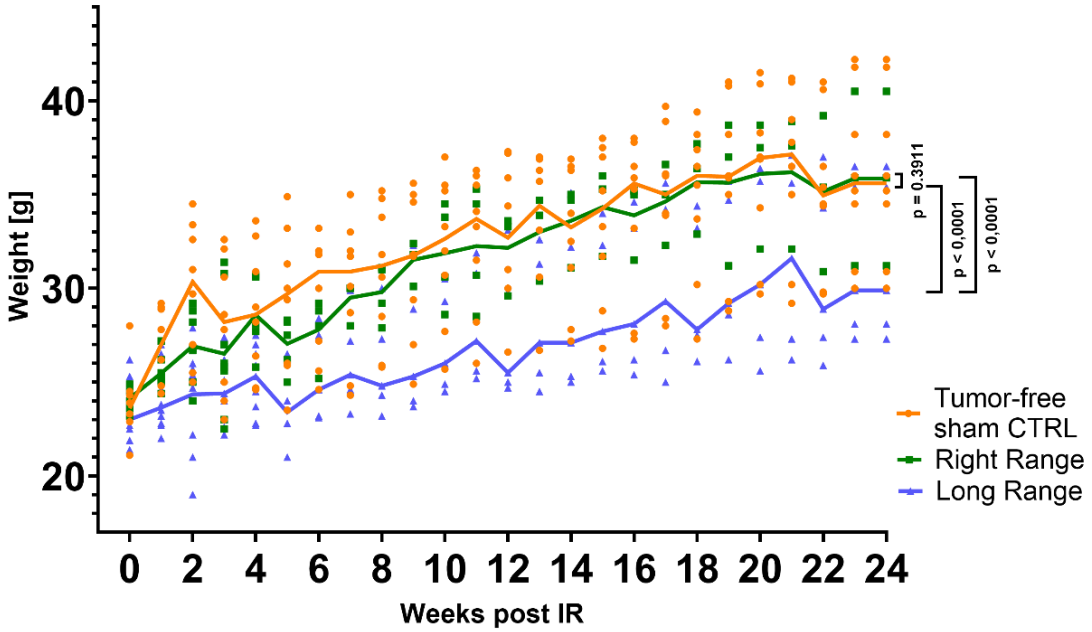

Figure 77. Weight-gain patterns of the animals from the second experimental campaign. Each point represents one animal and its respective measurement taken on a certain day, while the curves are connected by the medians. The difference between the distributions has been analysed with a 2-way ANOVA, with the p-value considered to be significant when $p < 0,05$.

On the long term, the animals of the Long group survived until the end of the experiment (six months) with minor signs of oesophagus issues. The oesophageal staining was scored using a simplified version of the EoE Histologic Scoring System (EoEHSS)[148], with basal zone hyperplasia (BZH), surface epithelial alteration (SEA), and correlation of the hyperplasia areas with the presence of Ki67-expressing cell being the explored parameters. The oesophagus histology panel (Figure 78) revealed focal areas of increased epithelial

thickness and differences in the stratification of layers of cells, which were not observed in the control and Right groups. These regions of thickened epithelium coincided with an elevated density of Ki67-positive cells, which is normally expressed by the cells of the basal cell layer as they are actively proliferating. The basal cells layer is typically a monolayer of cells, but when more cells start to accumulate this is a sign of active hyperproliferation in the tissue, which is usually associated with a pathological state[150].

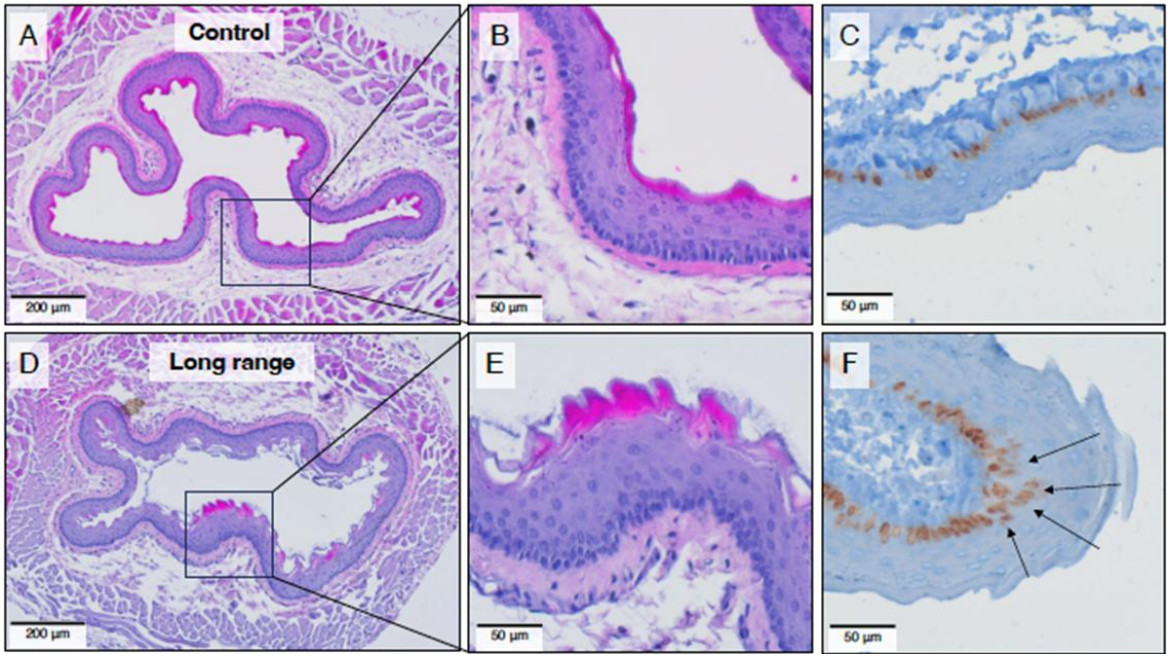

Figure 78. Chronic radiation-induced oesophagus toxicity. Representative pictures of haematoxylin-eosin staining (A, B, D, E) and Ki67 immunohistochemistry (C, F) of the oesophagus of the sham irradiated tumour-free controls (A-C) and animals treated in the L (Long range) group (D-F). Samples from the Long group are characterised by local areas of active cell proliferation in the basal layer with proliferating cells indicated by black arrows in (F), which explains the increased thickness of the epithelium (D). Images were analysed through the program QuPath-0.6.0 for pathological characteristics and overexpression of Ki67. Representative images are depicted.

For each animal, at least five sections taken at different positions along the oesophagus (from rostral to caudal) were examined using QuPath. The degree of epithelial thickening was quantified by measuring the distance from the basal cells layer to the top of the keratinised layer at regularly spaced intervals (60-80 µm) all along the epithelium circumference in each section. Multiple measurements from each animal were pooled and the resulting distributions are plotted in Figure 79, where they were used to generate histogram-based probability density curves for group-average curves, as well for single animal curves (not depicted).

As it can be noted, the distribution curve of the Long range group is skewed towards larger epithelial thickness values. In the pictures in Figure 78 it's possible to see how this happened in focal areas of increased thickness, while in Figure 76 a large part of the epithelium appears to be enlarged. This difference is probably a contributing factor in why the survivors of the Long group arrived at the end of the experiment, contrary to the case of the animal described in paragraph 3.4.3.1, which showed a severely altered oesophagus. These results suggest that the radiation-induced toxicity in the L group became chronic, rather than affecting all the animals in a severe way during the acute stage, as it happened for the animal

that manifested this stage 2 weeks post irradiation. The chronic condition, even if not life impairing, still produced a visible result on the food intake capability of the animals of the Long group by slowing down the weight gain, while it didn't cause notable issues in the R group.

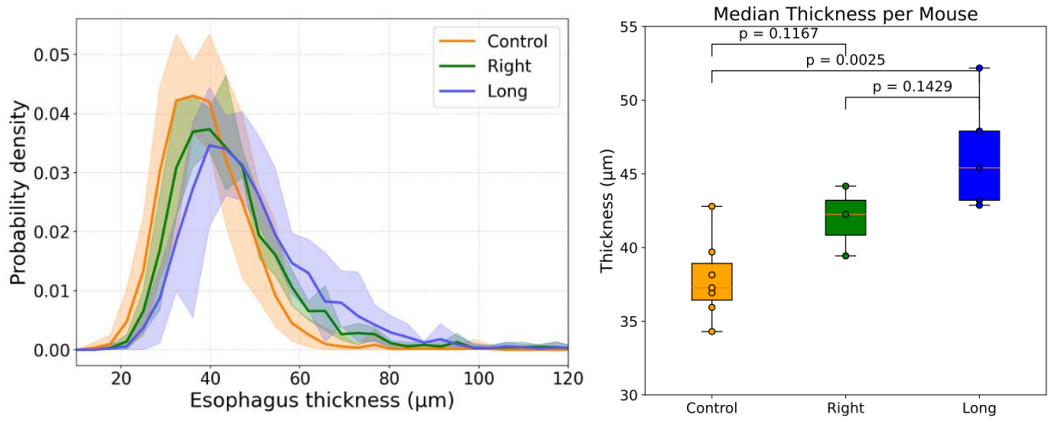

Figure 79. Oesophageal epithelium thickness. The distribution of the oesophageal thicknesses for each experimental group and normalised histogram-based probability density curves were plotted. For each group, the solid line represents the mean probability density across all mice, and the shaded region indicates the range spanned by individual animals. A non-parametric permutation test revealed a significant difference between control and L mice (p = 0.0025), but not between control and R (p = 0.1167) mice. Boxes represent the interquartile range (25th–75th percentiles), central orange lines are group medians, and whiskers indicate the full measurement range (minimum to maximum).

3.4.3.3 Spinal cord toxicity manifests only in the Long Range treatment

The grip strength test was conducted as in the rest of this work, and the resulting distributions can be seen in Figure 80. All the animals arriving at the end of the experiment did not manifest severe symptoms like paralysis, but rather aligned with the mild spinal cord toxicity observed in the previous experiments.

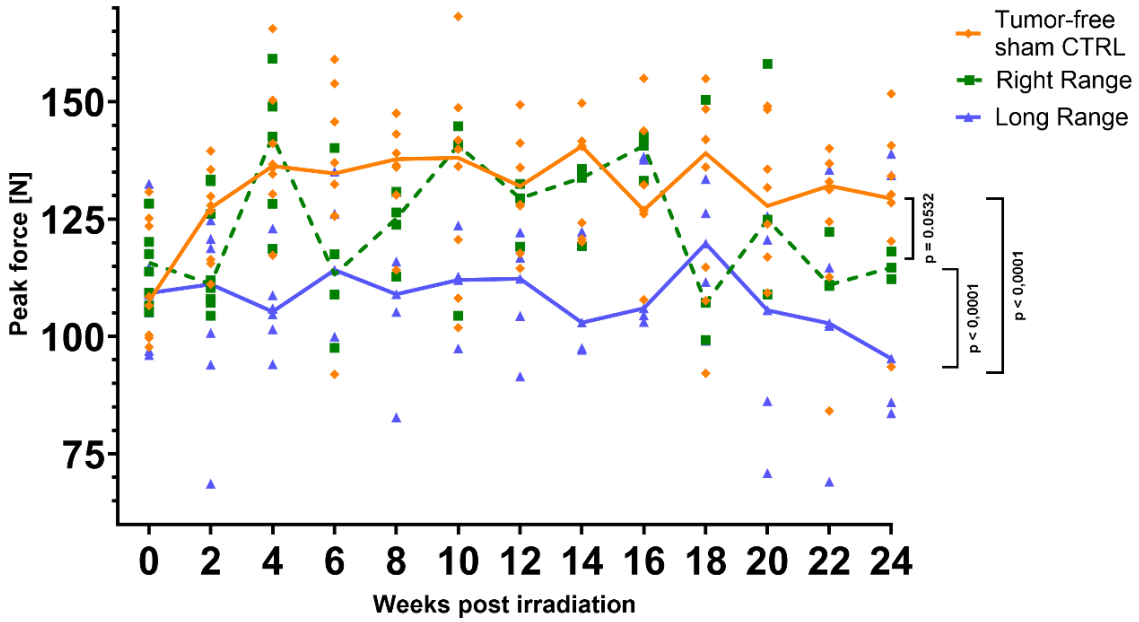

Figure 80. Grip test results of the second experimental campaign. The lines show the medians, every point in the distribution represents the average of three measurements taken for one animal on

the test day. The 2-way ANOVA has been used to measure the difference between the curves, with the p-value considered to be significant if $p < 0,05$.

By comparing the grip test data of the three groups (Figure 80) with a two-way ANOVA test it was possible to conclude that grip strength differed significantly between L group and both R and control groups ($p < 0.0001$), while no significant difference was observed between control and R groups ($p = 0.0532$). With regards to the kyphosis development, as shown on the column plot in Figure 81, the only group that significantly exhibited kyphosis when compared with the controls was the Long range group.

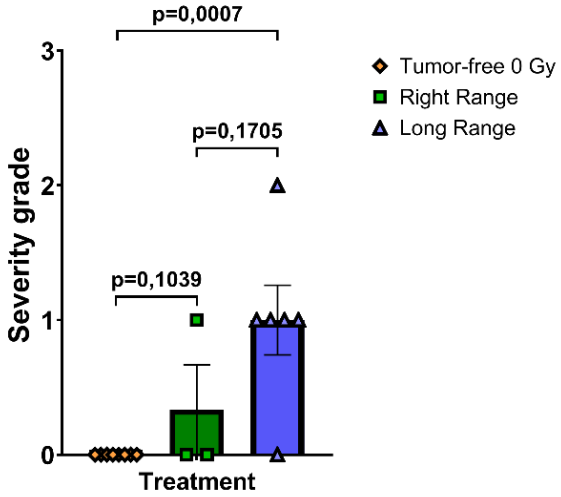

Figure 81. Kyphosis scoring of the second experimental campaign. Every point represents one animal. The unpaired two-tailed t test was used to assess statistical significance, with differences between groups considered to be significant if $p < 0,05$.

Also in this case, regardless of the presence of signs of mild damage to the spinal cord, the histology did not reveal characteristic signs of radiation-induced damage (Figure 82). Some antibodies against the myelin fibres (Beta catenin, Myelin Basic Protein, Neurofilament) were tested to check for demyelination, but the expression was not changed across the treatment groups.

One example can be found in Figure 82, where an immunohistochemistry panel shows the expression of neurofilament (NF) in brown. Neurofilament is commonly expressed in the myelin sheaths surrounding the axons. NF plays a role in axonal development, in their radial growth and in the transmission of electrical impulses along them, and an aberrant deposition of NF usually happens in pathological conditions[151]. The immunohistochemistry against NF, though, did not reveal signs of modified deposition or demyelination, as it happened in the previous experiments performed in this work. The possible reason for this lack of demyelination after radiation exposure will be discussed in 4.2.

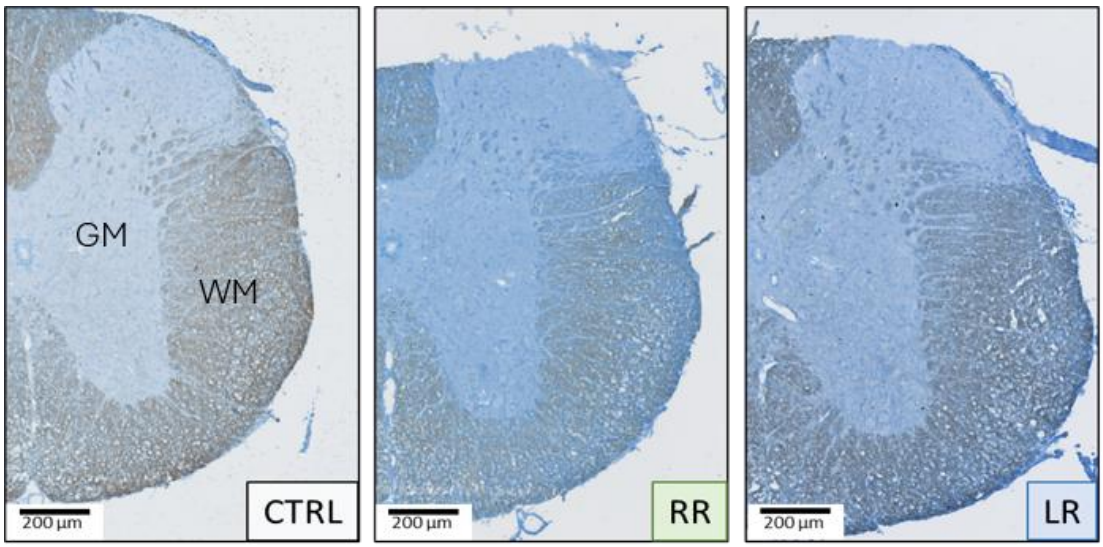

Figure 82. Panel of immunohistochemistry for Neurofilament representing a comparison between sham irradiated, Right range and Long range 20 Gy ^{11}C irradiated spinal cords. The panel shows three representative sections obtained from the first thoracic vertebrae of the mice[152], but all the spinal cord from the first cervical vertebrae to the first thoracic ones has been completely sectioned and analysed. Images were analysed through the program QuPath-0.6.0 for changes in expression of NF and presence of pathologically altered areas. Representative images are depicted. Legend: CTRL, tumour-free sham irradiated control; RR, Right range; LR, Long range; GM, grey matter; WM, white matter.

To conclude, the symptoms that were found during this experimental campaign support the hypothesis that different beam ranges depths can be tracked with in-beam PET imaging and produce distinguishable biological endpoints in an adaptive treatment setting. Skin toxicity was expected and was observed in all the treatment groups, since the dose was delivered from an external beam source, but it was healed with appropriate care.

In the case of the Short range group, tumour recurrence was found, due to planned insufficient dose coverage. The Right range group had the tumours treated, except for the case of three animals where the tumour position was shifted during the preparation for irradiation: this was confirmed by the CBCT acquired just prior to irradiation. It was not possible to adjust the positioning of these animals before delivering the SOBP. On the other hand, no late healthy tissues toxicities were observed in the animals that survived tumour-free until the end of the observation period. The Long range group, instead, also survived tumour-free, but showed signs of chronic radiation-induced oesophageal changes and the signs of starting mild spinal cord toxicity.

4 Discussion

Charged particle therapy is a relatively new and ever-growing clinical practice, which holds great potential for treating malignancies that are deep-seated in the body of patients and resistant to conventional photon radiotherapy, with heightened healthy tissue sparing[46]. This happens thanks to the increased relative biological effectiveness of heavy ions, *e. g.* their capability to cause more severe damage to the internal structures of the cells, in particular the DNA[1,47]. Heavy ions are also known for their peculiar energy deposition, known as the Bragg peak, where the majority of the energy of the particles is released in a small area. This phenomenon is used in radiotherapy because it permits to deliver a high dose to the tumour, while minimising the dose to the surrounding healthy tissue[1]. In this way, it´s possible to increase the precision of the treatment, and the therapeutic ratio as a consequence[42]. This translates in the reduction of the number of treatment fields: in the case of photons, their dose is deposited more in the entrance of the beam than in the tumour volume (see Figure 8). This requires the superimposition of multiple fields to deliver the dose, especially in the case of deep-seated malignancies. Heavy ions, instead, require less fields to deliver the necessary dose to the tumour because of the Bragg Peak, fact that leads to reduced dose deposition in normal tissue[43]. However, this also increases the risk to miss the tumours due to organ motion and patient setup variations in between the planned treatment fractions.

The uncertainties in dose deposition during charged particle therapy aren´t just caused by changes in the anatomy of the patient, but also because of uncertainties in the conversion of CT numbers to the particles stopping power, the quality of the CT and how the dose deposition can be measured. One way to confirm the location of the dose deposition is to collect information about the fragmentation of the particles in a tissue, which produces radioisotopes that decay (activity) by emitting positrons. These positrons annihilate with the electrons present in the tissue, and this reaction emits two anti-parallel photons that can be measured with a PET scanner. On the other hand, the number of positrons generated by the fragmentations of the original particles is not high, so their signal is not very strong. Moreover, the dose and the activity peaks are not spatially matching, because the measured activity is not the one coming from the original particles, but their fragments.

Therefore, even with PET imaging, the position of the particles reaching the tissues of the patient is not known with the necessary accuracy, which would be at the sub-millimetre to millimetre level[153]. This issue could be overcome by using positron emitting particles as the primary source of irradiation, which can lead to a higher measured PET signal and better match between dose and activity peaks. The activity, in this scenario, comes from the decay of the implanted particles themselves, not their fragmentation products.

In the context of the BARB project held at GSI, we used ^{11}C beams instead of ^{12}C (commonly used in heavy ion therapy clinics) to treat a tumour-bearing murine model. The use of the SIRMIO PET detector permitted to obtain the activity maps of the ^{11}C beam, which confirmed a close correlation of the dose and activity peaks and enabled precise treatment ([108,147]). The findings of this study show how it was possible to treat a murine tumour with ^{11}C for the first time, how image-guidance with PET was used to check the beam range inside the bodies of the animals and how this correlated with the biological endpoints, *i. e.,* tumour eradication and development of normal tissue toxicities.

This chapter provides a broader context about the latest developments in heavy ion radiotherapy and the niche this work fulfils, discussing the usefulness of its data and the contribution to the relevant research fields. In the following paragraphs, the findings of this project are discussed and taken into account considering the state-of-the-art of RIBs radiotherapy. This work has been highly dependent on the two "beamtimes" (yearly moment of accelerator usage at GSI) that were planned for the BARB project, referred to as "experimental campaigns" throughout the whole thesis. RIBs can only be produced at sufficient intensity only at GSI and at NIRS-QST in Japan[79], limiting the possible amount of beamtime that could be accessed. This is due to the fact that several improvements need to be made to a linear accelerator to produce such exotic beams, effectively pushing the boundaries of the actual most advanced nuclear physics techniques and technologies. Some animals could not receive the planned irradiation due to technical issues experienced during the beamtime, hence the different numbers in the treatment groups.

Paragraph 4.1 discusses the creation of a specific murine model for the experiments present in this work, and how to correlate biological endpoints with the necessity of demonstrating a physics proof-of-concept.

Paragraph 4.2 examines the need for an X-rays benchmarking experiment prior to the ^{11}C irradiation, especially in the context of limited amount of the latter and the knowledge value it has represented in this work.

Paragraphs 4.3 and 4.4 explore the findings of the two experimental campaigns, focusing first on the achievement of the first preclinical treatments done with ^{11}C, then the improvements of the experimental setting. Both the experiments produced results that permitted to demonstrate the feasibility RIBs radiotherapy in a murine model by using in-beam PET for real-time image guidance.

Finally, in paragraph 4.5 the discussion will focus on the role of RIBs radiotherapy and the future improvements of this sub-field, contextualising these findings between the important achievements in charged particle therapy.

4.1 Initial tumour model characterization

The final model used in this work started with testing three different ones. The one in which the injection of LM8 cells[134] was performed in the lung didn't produce a viable tumour mass, while the one injected subcutaneously in the hindlimb, based on these models[112,133] was well-vascularised, but located far away from an organ at risk. It could be argued that the limb model would have been useful for the vascularisation study with high- and low-doses of ^{11}C, but this would have meant a complete change in the irradiation setup and the GSI beamline is fixed, so normally the experiments are done by maintaining the same setup. Using only the back tumour model, instead, it was possible to study the biological washout, the tumour eradication and the normal tissue complications with just one model.

After finding a suitable model with a reproducible growth, no other tumour cell lines have been considered due to the reduced number of experiments programmed for this project. This can be considered a limitation of the study, but it should also be considered that this work was a biological proof-of-concept of a physics theory. The idea was that high-precision image-guided RIBs therapy can be used to spare healthy tissues and control tumours at the same time, and this applies to a wide range of solid tumours. Of course, the same doesn't apply to blood cancers like leukaemia, but in these cases radiotherapy is not

the first choice because it would require the irradiation of a large part of the body, which usually results in lymphopenia[154]. The concept behind this study is that RIBs radiotherapy can potentially be applied in general to solid tumours that are close to organs at risk and radioresistant[155]. Therefore, also other tumour cell lines should be explored in future studies with RIBs, even if the ones in which carbon ions already showed a higher cell killing capability, like the 4T1 breast cell line[156], should yield the same survival results. The main point would be testing other tumour cell types injected in different locations, with more complex anatomical arrangement and close to organs at risk with different radiosensitivity.

The fact that the LM8 cell line has a highly metastatic potential[110] resulted in being a nuisance during the study, because of the animals that had the tumour eradicated, but died some weeks after the disappearance of the malignancy because of metastases. They could be find in the liver, ovaries, lungs, intestines, lymph nodes around the jaws, spinal cord and brain, in a timeframe from 1 month to 2 months and a half post inoculation. This is, on the other hand, closer to the clinical situation with human patients. Osteosarcoma, for example, is both radioresistant[46] and metastatic[157], and it's the same for other malignancies like melanoma[46] or breast cancer with acquired radioresistance[158]. It's still not clear which role radiotherapy plays in metastases formation: on one hand, it seems like it can promote the mobilisation of circulating tumour cells (CTCs) and enhance their dissemination, which ends in the formation of metastases[158]. We tried to correlate the deaths caused by metastatic growth during our experiment, but since the losses were happening at very different timepoints and with not comparable control animals, this data collection could not be implemented.

On the other hand, the *abscopal* effect seems to be a process that can induce the regression of metastases after a radiation treatment[159,112]. It was theorised in 1953 to describe an immune-mediated response to radiation by tumour cells located distant from the irradiated site[160]. It is rare and mechanistically remains under study, although recent case reports have seen an increasing incidence of the effect with the administration of immunomodulatory agents[161], also in case of carbon ion treatments.

There is now a growing consensus from several studies indicating that combining radiotherapy with immunotherapy provides an opportunity to boost *abscopal* response rates[161,162]. Immunotherapy is a therapeutical approach that centres around using the patient´s immune system to eradicate cancer and prevent recurrence, and it was tested already in the 1890s[163]. Cancer cells can escape the immune system surveillance through various mechanisms, such as restricting antigen recognition, inhibiting the immune system, and inducing T cells exhaustion[164]. By targeting the immune checkpoints (immune-cell surface receptors controlling either the activation or the inhibition of immune responses), it´s possible to make the cancer cells visible again for the immune system. Since CIRT combined with immunotherapy has emerged as a promising strategy for managing metastatic disease[165], this combination has become clinical practice in the recent years, and it´s usually done by using immune check-points inhibitors[166]. The optimal combination of check-point inhibitors and radiation dose for boosting the *abscopal* effect and targeting metastases are currently under research in *in vivo* models[167,168].

To summarise, in the clinical practice there is a growing tendency to move towards patient-specific high-precision medicine[44]. This approach requires the use of adjuvant therapies after the initial treatment, which is usually surgery. Cancer is a multifaceted

disease, and there are various hints pointing at the need to find the right combination of radiotherapy, surgery, chemotherapy and immunotherapy to properly treat this complex malignancy.

4.2 Selection of radiation doses

In the dose escalation experiment (3.2), the tested doses were sham (0), 5, 10, 15, and 20 Gy. The doses tested in this experiment were later used for the experimental campaigns, as described in the paragraphs 3.3 and 3.4.

4.2.1 Tumour treatment dose selection

The tumour control in the photon irradiation experiment (3.2) was complicated by the late irradiation timepoint and the development of lesions on the tumours. The irradiation was performed at three weeks post inoculation to account for the few tumours (15%) that were not showing signs of growing, but this instead caused issues in tumour control. Since part of the tumour were already large in size at the irradiation moment (see Figure 42, from 0,5 cm^3 to almost 1 cm^3), they eventually quickly reached the size limit for euthanasia (1,5 cm in diameter), before the radiation-induced cell death could actually occur, leading to volumetric regression. Figure 42 also shows that one mouse receiving 10 Gy and two receiving 15 Gy experienced tumour eradication, while the mouse surviving from the 5 Gy group was one were the tumour failed to grow, and the other animals died for tumour regrowth or lesions. This indicated that 5 Gy were not sufficient to eradicate the tumour, and therefore this dose were selected as the low dose for ^{11}C experiment. To observe a clear tumour remission, and also normal tissue side effects (which will be discussed in the following paragraphs, 4.2.2 and 4.2.3), it was decided to have 20 Gy as the high dose in the following ^{11}C experimental campaigns.

4.2.2 Radiation-induced skin toxicity

Some degree of radiation-induced skin toxicity has been observed, but as already described, it was managed with the use of a topical treatment. This toxicity is usually observed after a radiation treatment, and with the correct management it can be healed without severe complications. The skin of mice can heal after doses up to 50 Gy[169], but 20 Gy was considered to be enough to eradicate the tumours – as it was demonstrated in the two experimental campaigns. This limit was reasonable, since it´s preferable to avoid causing severe side toxicities which might end up in having to euthanise additional animals. Considering the fact that various animals have been lost due to metastases, it was better to select a dose that wasn´t adding additional side effects to the post-treatment phase. Acute skin toxicity can be strong enough to require the termination of the animals, or can become cronic[121], but during this work, in the long term, it was only manifesting as epilation or fur discoloration. Table 12 describes some examples of studies about radiation induced skin toxicity in murine models. Week-old is shortened in w.o., days of follow up are counted from post irradiation day. In the dose column, where the articles specify certain doses these are reported as “1-2-3 Gy (for example)”, otherwise if the range is very wide with a certain interval in between doses they’re reported as “from 20 to 80 Gy (with intervals of 2 Gy)”, for example.

Table 12. Examples of studies about radiation induced skin toxicity in mice.

Author	Strain	Dose	Fractionation scheme	Follow-up	Effect
Pisciotta *et al.*[141], 2020	7 w.o. C57BL/6 male mice	Protons, 12-15-17-19 Gy	Single fraction	Up to day 40	Up to grade 5 (necrosis)
Denbeigh *et al.*[121], 2024	8 w.o. female C57BL/6J mice	Protons, from 18.2 to 118 Gy (intervals of 2 Gy on average)	Single fraction (18.2 – 82.4 Gy) and fractionated exposures (18x, 28 – 118 Gy)	Up to day 365	Up to grade 5 (necrosis), chronic toxicity in survivors
Sørensen *et al.*[170], 2015	10–14- w.o. female CDF1 mice	Photons, 37.8 to 41.8 Gy	Single fraction	Up to day 322	Up to grade 3.5 (moist desquamation)
Sørensen *et al.*[170], 2015	10–14- w.o. female CDF1 mice	Carbon, 23.1 to 30.1 Gy	Single fraction	Up to day 322	Up to grade 3.5 (moist desquamation)

4.2.3 Radiation-induced spinal cord toxicity

The literature contains different examples about radiation-induced spinal cord toxicity, but it there seems to be a lack of experimental evidence on the right dose to induce a strongly manifesting spinal cord toxicity in mice, and also the time frame for it to become noticeable. It's possible to find examples for mice, but it should be noted that several studies involved rats[171–174]. According to Denbeigh *et al.*[121] mice were found to have a higher radiation tolerance than rats in spine proton irradiation studies, which makes the comparison of rat and mice studies misleading.

Most of the mice studies focused on fractionation[175,176,121], which is not the same case of the single dose treatment given to the animals in this study, or analysed the effect of combined treatments, not just radiation[177,178]. Methods wise, the majority of the scoring systems come from studies regarding spinal cord injury[179–181] or neurodegenerative diseases[182–184]. A study where the animals received 20 Gy X-rays at the thoracolumbar transition showed the development of epidural fibrosis and increased expression of transforming growth factor beta 1 (TGF-ß 1), but no data about the manifestation of this histological findings at the organism level are presented[146]. In general, throughout all of the mentioned studies there is a wide range of doses, endpoints, timeframes and murine models used. Various studies focused on the dose escalation, but the number of doses explored was too wide for drawing any comparison with this work. Some examples can be found in Table 13, where paresis is defined as the incomplete loss of voluntary movement (weakness), while paralysis is the complete loss of voluntary movement (plegia). Week-old is shortened in w.o., days of follow up are counted from post irradiation day. In the dose column, where the articles specify certain doses these are reported as "1-2-3 Gy (for example)", otherwise if the range is very wide with a certain interval in between doses they're reported, for example, as "from 20 to 80 Gy (with intervals of 2 Gy)".

Table 13. Studies exploring radiation-induced spinal cord toxicity in rodents.

Author	Strain	Dose	Fractionation scheme	Follow-up	Endpoint
Ruifrok *et al.*[171], 1994	Female CPB/WU rats, 1-18 w.o.	Photons, 1 w.o. mice received 16 to 21 Gy; 2, 3, 18 w.o. mice received 17 to 24 Gy, 4-12 w.o. mice received 22 Gy	Single fraction or graded doses	Up to 365 days	Up to limb dragging (paresis or paralysis)
Okada *et al.*[172], 1998	Male Wistar rats, 12 w.o.	Carbon, 0-5-15-20-25-30 Gy	Single fraction	Up to 52 weeks	Up to complete paralysis
Philippens *et al.*[173], 2007	Male CPB/WU rats, 12-16 w.o.	^{192}Ir γ-rays with single (15-22) or double (16-24) catheter	Single delivery	Up to 10 months	Up to paralysis
Saager *et al.*[185], 2014	Young adult female rats (no specific age details)	Carbon, 11.5 to 24.5 with 1 Gy intervals	Single fraction	Up to 300 days	Up to both forelimbs showing signs of paralysis
Lo *et al.*[175], 1993	C,Hf/Sed//Kam male mice, 9-13 w.o.	Photons, 2 to 24 Gy per fraction	Fractionation (2, 3, 4, 6, 10 or 20 fractions, 1x day)	Up to 450 days	Up to complete paralysis
Lo *et al.*[186], 1992	C,Hf/Sed//Kam male mice, 9-13 w.o.	Photons, 12 to 75 Gy	Single fraction	Up to 360 days	Up to paralysis
Denbeigh *et al.*[121], 2024	8 w.o. female C57BL/6J mice	Protons, from 18.2 to 118 Gy (intervals of 2 Gy on average)	Single fraction (18.2 – 82.4 Gy) and fractionated exposures (18x, 28 – 118 Gy)	Up to 365 days	Up to paralysis
Lavey *et al.*[176], 1994	C3Hf/Sed//Kam male mice, 9-11 w.o.	Photons, 24 to 70.8 Gy	Fractionation schemes (1.2 Gy 1x day, 1.2 Gy 2x daily, 2 Gy 1x daily)	Up to 365 days	Up to paralysis
Yokogawa *et al.*[146], 2015	ddY mice (sex not specified), 10 w.o.	Photons, 10 or 20 Gy	Single fraction	Up to 24 weeks	Presence of epidural fibrosis in histological analyses, no description of *in vivo* findings

In the case of patients, spinal cord toxicity is mostly expected as a side effect of radiotherapy used as a palliative, to treat spinal metastases or as a consequence of the PTV

covering a part of the spine[187]. The spine is a serial organ, meaning that damage to one part can impact the entirety of the structure below the damaged area. In some cases, it can lead to the development of deformities, like kyphosis[188], neurological manifestations (Lhermitte sign) or mono- and paraplegia[56]. In this regard, the symptomatology of patients is way more clear to observe, and they can also communicate situations causing pain, mobility issues and failures in motor-coordination. The same can't be applied to mice, where the expression of pain is usually controlled and kept at the minimum level, becoming clear only when the pain itself becomes severe[189].

The worst outcome of spinal cord irradiation is radiation-induced myelopathy, which shows demyelination and necrosis confined to white matter, and varying degrees of vascular changes in both white and grey matter at the histopathological level. Following single or fractionated dose delivery schemes to the cervical spinal cord, rats develop forelimb paralysis between 4 and 7 months owing to white matter necrosis[59]. An example of demyelination can be found in Figure 83.

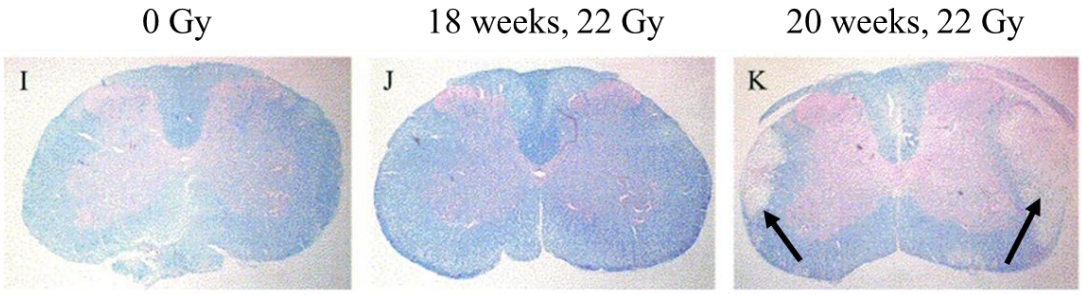

Figure 83. Example of staining for demyelination in the rat spinal cord. Luxol Fast Blue staining in control (I), and irradiated rat spinal cord at 18 weeks (J) and 20 weeks (K) after irradiation with 22 Gy. In K, the focal areas of demyelination and necrosis are demonstrated by the absence of the blue staining in the white matter. Adapted from Atkinson *et al.*[131].

The Luxol Fast Blue staining has also been tried in this work, but it never showed signs of demyelination. However, this is compatible with the absence of paralysis found during the experiments. Usually, in mice and rat studies regarding spinal cord injury or irradiation, the development of paralysis is the data mostly looked for[121], but this is a severe and late side effect of irradiation of the spine. The studies cited in Table 13 considered and explained the observation of the intermediate grade toxicities, like paresis or loss of reflexes, but the reported data are mainly regarding paralysis.

In the context of this thesis, various methods have been taken into consideration for the evaluation of the spinal cord toxicity. One was the Rota-Rod test[190], where mice are walking on a circular support which rotates with increasing speed; at a certain point, the animals can slip, or become tired, or have motion-related impairments which make them fall. This test is commonly used in studies about spinal cord toxicities, but in the case of studies with long time-spans the mice can learn to avoid the test by simply refusing to walk on the support. This can become prevalent especially in animals that tend to accumulate a considerable amount of weight[121]. For this reason, the grip test was instead considered, since there is an operator handling the animals and making them grasp the bar of the grip meter. However, also in this case the animals can refuse to cooperate by not grasping the bar. This happened during this study, and was the one of the reasons why the number of test repetitions was reduced from five to three and why the test started to be performed bi-weekly instead of

every week. The other reason is habituation, which is defined as the waning of a response, elicited by repeated exposure to a novel stimulus not accompanied by any biologically relevant consequence, either positive or negative[191]. The animals learn to ignore repetitive, non-threatening stimuli, meaning their response to a test repeated every week with too many repetitions was sub-optimal.

In motor-function and behavioural tests, though, usually a battery of tests is performed and analysed. This is the reason why, on top of the grip test, also the walk test and the kyphosis scoring were taken into account. These tests could capture a variety of behaviour, motor-function, gait pattern alterations and posture abnormalities that couldn´t be visualised with the grip test only. The walk test might have been proven useful for the manifestation of paralysis, but the timeframe for it to show was probably not long enough. If the maximum duration of the experiment of six months would not be already planned in the ethical protocol, a survival experiment could have been performed. By keeping the animals until the end of their lifespans or at least for a longer period, the development of more severe side effects, such as paralysis of one or more of the limbs, might have been observed. Several studies explored long-term follow-ups, and obtained clear data about the progression of the chronic spinal cord damage and paralysis[121,192]. The kyphosis scoring, instead, still comes from the assessments used for neurodegenerative murine models, but represented a reliable and robust scoring system[125] with a symptomatology that could be correlated to the one manifested by the animals in this study.

Other examples of tests that could be used in spinal cord irradiation experiments are the ones which examine the manifestation or absence of pain-related behaviour, like mechanical allodynia (von Frey test[193]), cold allodynia (acetone test[193]), and thermal allodynia (Hargreaves test[193]). These tests can give a finer indication of growing toxicity in the spinal cord and its functions, also in a relatively short timeframe. It's not described in the Materials and Methods section (2), but also some non-conclusive results were obtained with a preliminary study that investigate the sensitivity of the animals with a von Frey test, which was conducted twice on the animals of the first experimental campaign. The test is performed using thin calibrated plastic filaments that are applied to the plantar surface of the paw, to determine the threshold that elicits a paw withdrawal response to a noxious stimulus. The results were inconclusive, so it was not considered for further trials.

Notably, the C3H mouse strain can exhibit spontaneous absence seizures[194], and this happened during the course of the experiments presented in this work. However, since they were showing regardless of the treatment groups, they were not taken into account in the spinal cord toxicity observations.

Regarding the dose for the induction of paralysis, an interesting example of single fraction irradiation (photons) with notes on the doses for paralysis display can be found in Lo *et al.*[186]. They report the following data: "Findings were: (a) the doses required to paralyze 50% of animals (ED_{50}) were 19.79, 20.77, and 21.85 Gy for mild, partial, and complete paralysis, respectively, as measured 200-360 days after radiation, when at least 2.2 cm of the spine are irradiated". In the case of our study, the length of irradiated spine was approximately 1,5 cm, and the smaller the irradiated volume, the smaller is the expected toxicity. As showed in Figure 57, it also looks like the dose delivered to the spine during the first experimental campaign was not 20 Gy, as was the case of the mouse surviving for 16 weeks after 20 Gy of X-rays, but probably around 16 or 17 Gy on average.

This data makes the comparison with the literature even more challenging, since there is a degree of uncertainty about which dose each animal received. This is shown in Figure 68, where the activity measured in the spinal cords of all the mice shows different values and correlates with the performance during the grip test. If a slightly different dose was received by the spinal cords, it´s even more difficult to explain the biological outcomes and defining the toxicity that was found. By looking into the literature, it seems 22 Gy X-rays could be a dose that can produce toxicity[131], or 30 Gy of ^{60}Co exposure[195], or 20 Gy X-rays are enough to produce demyelination, with doses from 60 Gy necessary to produce forelimb paralysis[196], but all these studies were conducted on rats. Both in preclinical research and in the general clinical practice, the response of the spinal cord seems to manifest above a certain threshold, *e. g.* myelopathy risk increases above 60 Gy in monkey experiments, and the dose limit for patients has been established at approximately 50 Gy given with conventional dose-fractionation schedules[2,54]. Since this threshold was probably not crossed in our experiments, only minor toxicity should be expected and was actually observed.

It should also be noted that the 20 Gy X-rays survivor most probably died because of radiation-induced oesophagitis, since the oesophagus was covered by the X-rays dose distribution. This was not the case of the first ^{11}C experimental campaign, but it was used to plan the irradiation of the Long range group in the second experimental campaign. This helped in ensuring a clear manifestation of normal tissue complications within the follow-up period.

In the end, the aim of this experiment was to find the right compromise between all the biological outcomes that were expected and researched in this work. One of the problems with using a mouse model to study the spinal cord response is death caused by damage to other organs before the onset of paralysis[186], so large groups numbers must be taken into consideration during experimental planning. The same thoughts are reported also in Denbeigh *et al.*[121]. A higher dose to the spinal cord would have produced clearer results about the normal tissue toxicity, but at the risk of also causing worse skin side effects. It is possible that analyses conducted at the molecular level, *i. e.,* sequencing of the spinal cord samples, could have shown a clear effect with differential gene expression or the presence of different proteins in the tissues[197]. Nevertheless, results regarding the toxicity were still found during the experimental campaigns, even if they were not leading to major impairments for the animals[108].

4.3 Feasibility of precise tumour treatment with ^{11}C

The goal of the BARB project was to provide a demonstration of tumour treatment with RIBs coupled with online range verification by PET[108]. With the experiments of the first experimental campaign, it was possible to demonstrate tumour control with ^{11}C. The 20 Gy SOBP was enough to eradicate the tumours, while instead local recurrence was observed with 5 Gy; considering the radioresistance of osteosarcoma, this was the expected outcome. Regarding the skin toxicity, it was manifesting in a similar way in both the photon and ^{11}C experiments. ^{12}C, instead was not used during this study, so it's not possible to compare it with ^{11}C. Some biological experiments, though, might be planned for actually testing if the use of these two different ion beams can lead to biological differences, but this was not the scope of this thesis. One example could be a cell survival experiment, which is commonly used to gain understanding about different radiation qualities and their effect on biological

matter. Other *in vivo* experiments could compare cancer treatments with both ^{12}C and ^{11}C. It should be considered, though, that radioactive ion beams can´t be produced in every facility that uses ^{12}C; this challenge will be further discussed in paragraph 4.5.

The capability of RIBs to predict the distal fall-off position around the 80% of the Bragg peak had been already demonstrated in phantoms and is now confirmed *in vivo*. Therefore, this results provide experimental support to the modelling predictions regarding the benefits of RIBs in particle therapy, particularly for reducing the uncertainties in dose deposition and range monitoring[89,108]. In the murine model used in this work, the tumour was located very close to the spinal cord, which meant a very close match between the dose and activity peaks was desirable for treating the animals based on a reliable range position information. Online real-time PET images were acquired just prior treatment to confirm that the SOBP would have not covered the spinal cord, by first delivering 1 Gy and then then the rest of the dose. Some Monte Carlo simulations of a spine coverage scenario were calculated to have an idea of which dose and activity profiles, if observed during the experimental campaign, would have meant a range correction. This worst case scenario was never observed during the irradiations, so no range correction was applied[108]. If it would have been necessary, this would have shown on the annihilation maps obtained just after delivering the first part of the SOBP, and the necessary correction would have been applied to the rest of the dose. In Sokol *et al.*[89], an *in silico* study which aim was to demonstrate the rationale for using RIBs in the clinical practice, anonymised CT scans from patients were used to study the potential benefit of ^{11}C treatment planning with reduced margins. The study demonstrated that annihilation maps acquired in the patients irradiated with ^{11}C beams can theoretically be used to precisely determine the positions of the SOBP fall-offs, and thus to recognize the shifts in actual dose distributions of about 1 mm. This was practically demonstrated *in vivo* during the first experimental campaign when a mismatch between the simulated dose, simulated activity maps, and measured activity maps was found. The cause of this mismatch was the fact the simulations were run on the horizontal μCT of the animals, while the irradiation and the measured data were made on the mouse positioned vertically (Figure 58). By re-running the simulations on the vertical CBCTs (Figure 59), it was possible to reconcile this millimetre shift. These findings could form a foundation for allowing the application of the necessary plan corrections online or adjust the beam delivery during future clinical treatments.

With regards to the biological washout study, the results of the measured activity decay curves show a clear difference in how the high- and low-dose irradiations affected the washout. Since the fast component, well visible at 5 Gy, disappeared in the 20 Gy case, there's a hint on vascular injury happening quickly after the high-dose treatment. This injury might delay the biological washout by impeding the blood flow through the tumour tissue; a possible cause for this phenomenon is the breakage in the minor vessels, which cause haemorrhages. The presence of haemorrhages was detected via Perls Prussian blue staining in a few animals euthanised the day after irradiation, but since the sample size was small, it's not possible to draw substantial conclusions. It can be discussed that the case of this experimental setup can be considered like the one of single-dose radiotherapy (SDRT), Some *in vivo* results investigating the role of one high dose of radiation in inducing vascular damage and how microvascular endothelial apoptosis affects tumour treatments have been explored[198,199], pointing to an ischaemic-reperfusion mechanism of damage induction[105]. Ischaemia is a phenomenon where a tissue suffers low oxygen concentration due to

insufficient blood supply[200]. Ischaemia-reperfusion damage happens when the blood supply is re-established after prolonged ischaemia, leading to secondary injury caused by local inflammation and ROS production increase. The subsequent cell damage can happen because of different cell death mechanism, such as apoptosis, autophagy, necrosis and necroptosis[201]. The terminal deoxynucleotidyl transferase dUTP nick-end labeling (TUNEL) assay is a common method used to detect DNA fragmentation by labelling the 3'-hydroxyl termini in the double-strand DNA breaks generated during apoptosis, and was used to assess apoptotic cell death in ischaemia-reperfusion rat models in Gujral *et al.*[202].

If this mechanism happened in the tumours just after the irradiation, not only the tumour cells would have been dying because of the radiation-induced damage, but also because of the additional damage caused by the ischaemia-reperfusion injury. If there's an early damage to the vessels just after irradiation, as suggested by the washout findings, then the tissue can become quickly ischaemic and experience reperfusion later, and there are indications on the efficacy of ^{12}C in inducing a fast reperfusion one day after irradiation[203]. From this point of view, this part of the experiment would have benefit from the use of Magnetic Resonance Imaging (MRI)[204], which can produce detailed 3D images of soft tissues, bones and entire organs, but also oedema[174], haemorrhage, tumours and ischaemia. An *in vivo* experiment that comprehends MRI scans prior, just after and weekly after irradiation could observe the changes occurring in the tumour and the surrounding tissues, gathering data about the possible fast induced vascular damage after a high dose of ^{11}C. By euthanising animals at all the timepoints, histological and immunohistochemical analyses could explore the cause and mechanism of this damage and delve deeper in the consequences of tumour growth/control.

On the long term, instead, the low-grade neurological damage that was observed during the first experimental campaign is in line with the findings of the photon experiment, where low toxicity was found in the form of kyphosis. The histology supported this finding by showing the absence of fibrosis and demyelination in the spinal cord and surrounding tissues samples. A correlation between the activity measured in the spinal cord and the grip test performance was found, where the higher the activity, the lower the strength of the animals. Still, the normal tissue toxicity was low and all the animals survived until the end of the experiment without major deficiencies. To find signs of genotoxicity at the DNA level, which then reflect at the phenotype level, the presence of chromosomal aberrations, mutations and DNA lesions could be assessed. Some assays that are commonly used to explore these aspects are flow cytometry, mutation analyses and the Comet assay[205]. These aspects could be explored on digested tissues in the early period following irradiation, while instead molecular analyses such as mRNA-sequencing or Single Cell Sequencing (SCS) could be used for sequencing and decoding differential gene expression[206] at the end of the follow-up of the animals. This approach could have highlighted differences in the pathways expressed in the cells of different treatment groups tissue samples, for example the ones related to inflammation markers and immune response like IL-1, IL-6, TNF-α, and TGF-β. They cause the production of Interleukin-17 (IL-17), a cytokine that plays a role in maintaining immunological homeostasis and is relevant in radiation-therapy induced toxicity[207].

In conclusion, the data obtained in the first experimental campaign were giving very promising result about the use of ^{11}C in an *in vivo* tumour-treatment scenario, setting up the foundations for the second experimental campaign.

4.4 Considerations on beam range monitoring and biological outcomes

The second experimental campaign differed from the first one in the biological endpoints that were looked for, and some technological improvements made to the beamline. The biological aim was to obtain three different treatment outcomes, basically the three possible scenarios that can be obtained during the course of a radiotherapy treatment. These were: tumour recurrence after underdosage or partial mass coverage; tumour eradication combined with normal tissue toxicity due to overdosage to the healthy tissues; tumour eradication and follow-up free of normal tissue complications. As it can be noted, a critical common point in the two negative outcomes is the incorrect dose delivery: this can happen due to incorrect treatment planning, changes in tumour volume and patient anatomy between different fractions, and issues in the positioning of the beam inside the body[61,62].

In fractionated treatments, the anatomical changes occur over timescales ranging from sub-seconds (intra-fraction) to several hours (inter-fraction). Almost 30 year ago, it was proposed that the re-optimisation of the treatment plan could be done by monitoring the anatomical variations, with the aim of creating high precision personalised treatments[208]. Following this idea, nowadays new Cone Beam CTs are acquired to update the treatment plan during the course of treatment[209,210], also because the pre-treatment images are not representing the patient's anatomy at the exact time of irradiation. Visanji *et al.*[211] show how 55% out of 300 patients need to have one CBCT to be reacquired during the treatment course. The number of reacquisitions depends on several factors, *e. g.* tumour size and proximity to body cavities, in-house regulations about the clinical protocol (*i. e.,* maximum dose limits, ALARA principle) and setup variations[211]. The guiding principle is to minimise CBCT reacquisition to avoid additional dose exposure to the patient. For example, over a course of 42 fractions there can be up to 1-2 Gy given by the imaging itself in Kan *et al.*[212] for prostate cancer treatment. Since there is not always the possibility to acquire a new CT scan before the treatment session, the expected activity (estimated from the latest available scan) would be compared with the measured one. If the deviation is too large, this could be an indication of, among others, some anatomical changes, which might require a new CT to confirm and recalculate the plan.

Patient repositioning, weight losses or gains, shifts in the internal organs and presence or absence of liquids in the body cavities are all causing issues in dose delivery, especially in the case of protons and heavy ions, where the SOBP must be carefully positioned to avoid tumour underdosage or normal tissue overdosage[210]. As discussed in 1.4.3, in-beam PET detection could be used to precisely detect the beam range inside the body of a patient. In the second experimental campaign, this was done in a murine model with sub-millimetre accuracy ([147], Figure 71), which enabled the possibility of creating three different biological outcomes in a setting where all the treated organs are in close proximity with each other. This was also possible owing to the high resolution of the μCT (ranging at the μm level[213]), but in the case of patients the resolution is usually at the millimetre level[214]. Nevertheless, a millimetre level of precision in the margins reduction, compared to the organ sizes of patients, would already be a significant improvement[89]. Reductions in proton therapy scenarios for the brainstem from the current range uncertainty of approximately 4% to a potentially achievable level of 1% reduced the probability of brainstem necrosis by up to 1.3 percentage points in the nominal scenario and by up to 2.9 percentage points in the

worst-case scenario, according to Tattenberg *et al.*[215]. In carbon therapy, margin reduction might have a stronger impact on the toxicity outcomes compared to protons, due to the 2–threefold increase of RBE at the distal edge of the SOBP[89].

The hypothesis tested in this experiment was the validation of radioactive ion beams as a powerful tool for in-beam PET-guided adaptive particle therapy. Their high activity counting rate permitted the creation of accurate PET maps, and the combination of their strong correlation with the distal 80% dose fall-off of the beam augmented the precision of the measurement of the beam range. With these known properties, the real-time adaptive approach was enabled by checking the range prior to treatment with a monoenergetic ^{11}C beam. The monoenergetic beam produced clear PET activity distributions maps that were overlapped with the CBCT scan obtained for each animal. This upgrade to the experimental setting is a step that can be taken during the course of an adaptive treatment with in-beam PET, and the applicability of the use of a radioactive monoenergetic ion beam for range verification in a clinical setting will be further discusses in 4.5. Additionally, the possibility to immediately change the range by means of a remotely controlled range shifter permitted a fast change of treatment plan in between the different animals. In a clinical scenario, this means that the beam range can be easily adapted in real-time to the newly calculated treatment plan.

As it was the case for the first experimental campaign, also in the second one the biological endpoints served as demonstration of a physics proof-of-concept. The idea of creating a Goldilocks type of experiment translated complex technological novelties and physics topics in a clear biological experiment, where two of the planned scenarios are non-desirable outcomes (*i. e.* the tumour regrowth after underdosage and normal tissue complications) and the remaining one is the positive outcome (tumour eradication and normal tissue sparing). These results were achieved with modifications applied at the previous setting: the conceptualization of the three ranges (Short, Right, Long) demanded the use of the range shifter and the monoenergetic probe beam. In the Short range case, the result was similar to the one of the animals treated with 5 Gy in the first experimental campaign, demonstrating uncontrolled tumour growth even if part of the malignancy was treated with 20 Gy because of uneven tumour coverage. Figure 71 shows how only the ending part of the SOBP covered the Short range tumours, with a deposited dose that diminished from the 70% to the 10% of the planned dose. Part of the tumours in the group were treated, while some weren't and reached the termination criteria with tumour volumes close to the control group ones.

Even if part of the animals were lost due to the presence of lesions on the tumours and the development of metastases, it was still possible to observe that the Right group achieved tumour eradication and toxicity free-survival. The Long range group, instead, also proved the tumour eradication, but manifested both oesophageal and spinal cord toxicity. In this case, adding the oesophagus to the pool of irradiated normal tissues helped in obtaining clearer data about the normal tissue complications on both the short term (one animal euthanised due to acute radiation-induced esophagitis) and the long term, with clear histological findings found during the follow-up time.

The alterations in the oesophagus were explored in the light of eosinophilic oesophagitis (EoE), a chronic T helper type 2 associated allergic and immune mediated disease, currently globally rising and with an aetiology still undergoing study and exploration[216]. It was not possible to prove that the animals belonging to the L group developed chronic oesophagus

toxicity because of the manifestation of EoE, but the research done about the topic helped in establish the expected toxicity outcomes and the scoring system used to evaluate the histological specimens[148]. To prove the presence of EoE, the oesophagus should have shown the infiltration of eosinophiles in the thickened epithelial layer in the tissue with immunohistochemistry, but this was not found. Some cases of EoE developing after radiotherapy have been found[217,218], pointing to the idea that radiation-induced oesophagitis can manifest after radiotherapy of head and neck and lung cancer. A targeted histological analysis of the biopsies of these patients would be ideal to direct them to the most appropriate treatment[219].

The Right range group, or Goldilocks range, achieved the aim of demonstrating how image-guided beam range monitoring can fully exploit heavy ions in radiotherapy[89], by enabling margin reduction thanks to enhanced reliability in dose delivery with the use of in-beam PET real-time imaging.

4.5 The adoption of new techniques in radiotherapy

Like any other research field, radiotherapy has seen its fair share of important advances since its first use[220]. This is a good premise, especially when we consider the fact that the technological advances made in recent years are now proving theories that were published in the last century, but the science of the time was not ready to demonstrate them. For example, this is the case of the use of radioactive ion beams in heavy ions therapy: when the field started to be explored, the idea was already considered[221], but the particle accelerators at the time could not produce radioactive ion beams with intensities high enough to treat a tumour[88].

Radiotherapy is highly cost effective, accounting for only 5% of the total cost of cancer care[53], while the other costs are divided between surgery, chemotherapy, day hospital medical admissions, emergency admissions, home and hospice care, inpatient and outpatient care[222]. The estimated global economic cost of cancers from 2020 to 2050 is $25.2 trillion in international dollars (at constant 2017 prices)[223], and there are wide differences in the cancer care costs and affordability in different countries.

However, inside the radiotherapy field the economic differences between conventional radiotherapy (photons), proton therapy and carbon therapy are widespread. Not only the construction of a carbon facility is almost six times higher than the one for a photon facility[224], but the same applies for the cost of treatments, with carbon therapy being almost five times more costly than photons[225]. Nevertheless, the consensus about the higher efficacy of heavy ions in tumour control and the lower toxicities produced during the course of a treatment is rising[225]. Conventionally, the course of a radiotherapy treatment is delivered through a high number of daily fraction, but there's a trending shift in heavy ion therapy to move to hypo-fractionated treatments, with a lower number of fractions of higher dose delivered[47,210,225]. With proofs supporting the efficacy of single high-dose radiotherapy[226], then, an ideal scenario forms, where the number of times of necessary treatment times reduces, opening up the possibility of effectively treating the ever-rising number of cancer patients worldwide[225].

The cost-effectiveness of carbon ion radiotherapy is still under discussion, especially because some parts of the facilities (*e. g.* synchrotron) can't be taken out of the equation[49].

One example of the cost-reduction that can be implemented is treating the patients in upright position, instead of laying on a bed (as it's conventionally done). This change removes the need for a gantry, eliminating one of the more costly part of a carbon facility, improving patient comfort and also producing better treatment outcomes in specific cases[227]. Other costs can be saved by looking at the clinical data: CIRT achieves superior local control rates, reducing the need for retreatment or supportive care, which translate in fewer hospitalisations and shorter follow-up durations[225]. For example, in Huang *et al.* a head and neck cancer study showed how both proton beam therapy and CIRT provided therapeutic effectiveness, but adjuvant CIRT was associated with a more favourable acute toxicity profile as compared to proton beam therapy, with significantly lower frequency and severity of acute dermatitis observed[228].

Carbon ions have also proved to be effective in the treatment of radioresistant hypoxic tumours[24], and have been tested for a variety of malignancies, including intracranial malignancies, head and neck malignancies, primary and metastatic lung cancers, tumours of the gastrointestinal tract, prostate and genitourinary cancers, sarcomas, cutaneous malignancies, breast cancer, gynaecologic malignancies, paediatric cancers and recurrent malignancies[49]. Because of its higher relative biological effectiveness (RBE) and linear energy transfer compared to proton beams, CIRT is expected to have superior biological outcomes[229]. This higher effectiveness, on the other hand, can become a double-edged sword when the range uncertainties are taken into account. For this reason, a better range monitoring is one of the main area of improvement in CIRT.

In this context, RIBs can add up to the effectiveness and beneficial aspects of CIRT, when used for adaptive treatments and image guidance. This study tested ^{11}C, but as already discussed in 1.4.4, ^{10}C or ^{15}O would be even more ideal to use because of their seconds to maximum 2 minutes-long half-life. Previous experiments within the BARB collaboration showed that the highest range-resolving power can be achieved with ^{10}C or ^{15}O[144]. ^{11}C was selected as the reference ion because of the daily application of carbon ions in the clinics, and on the other hand, lighter isotopes still require years of testing[108]. At the moment there's no technology that can provide ^{10}C beams with intensities high enough for RIBs radiotherapy in patients. In the near future, the FAIR facility at GSI (Figure 84) will become operational, and the Superconducting Fragment Separator (Super-FRS) will permit the production of high-intensity beams of ^{10}C.

Other facilities where various RIBs can be tested are FRIB (USA), TRIUMF (Canada), ISOLDE (CERN), GANIL (France), SPES (Italy), NICA (Russia), RIBF (Japan), HIRFL (China), and RAON (Korea). Another proposal is the MEDICIS-Promed project at CERN, which consists in Isotope separation on-line (ISOL)[108,230] to produce ^{11}C beams that are injected directly into medical synchrotrons, eliminating the need for investing in power upgrades.

Part of the above-mentioned facilities use the ISOL method, while the others use the in-flight separation method for achieving RIBs, like GSI. The RIBs research is now more active than ever, with possible applications in topics spanning from nuclear astrophysics, nuclear structure, atomic and plasma physics, space-radiation effects, radiobiology, to other interdisciplinary fields, like medical physics, and many others[230,231]. Another facility that uses the in-flight method and can produce RIBs with high intensities is HIMAC at NIRS-QST (Japan)[231]. The fact that these facilities can produce RIBs, though, does not imply that

they can be produced at intensities high enough to be used for radiotherapy in a clinical setting. In our study the animals were treated in approximately 20-30 minutes (dose rate: ca. 1 Gy/min, ca. 1 cm^3 of tumour volume). For patients, higher dose rates are desirable (*e. g.* 3 Gy/min) since bigger volumes need to be considered, therefore the intensities need to be higher.

Of course, medical synchrotrons don't have the same characteristics of the research ones, but by introducing RIBs in them with the ISOL-method they can be used for image-guided radiotherapy. A ^{11}C pencil beam can be used for image-guidance prior to a ^{12}C SOBP delivery, instead of a full ^{11}C treatment. Owing to the high signal-to-noise ratio, this verification can be performed at low beam intensity, minimizing additional exposure and technical requirements for radioactive ion beam production[89,147].

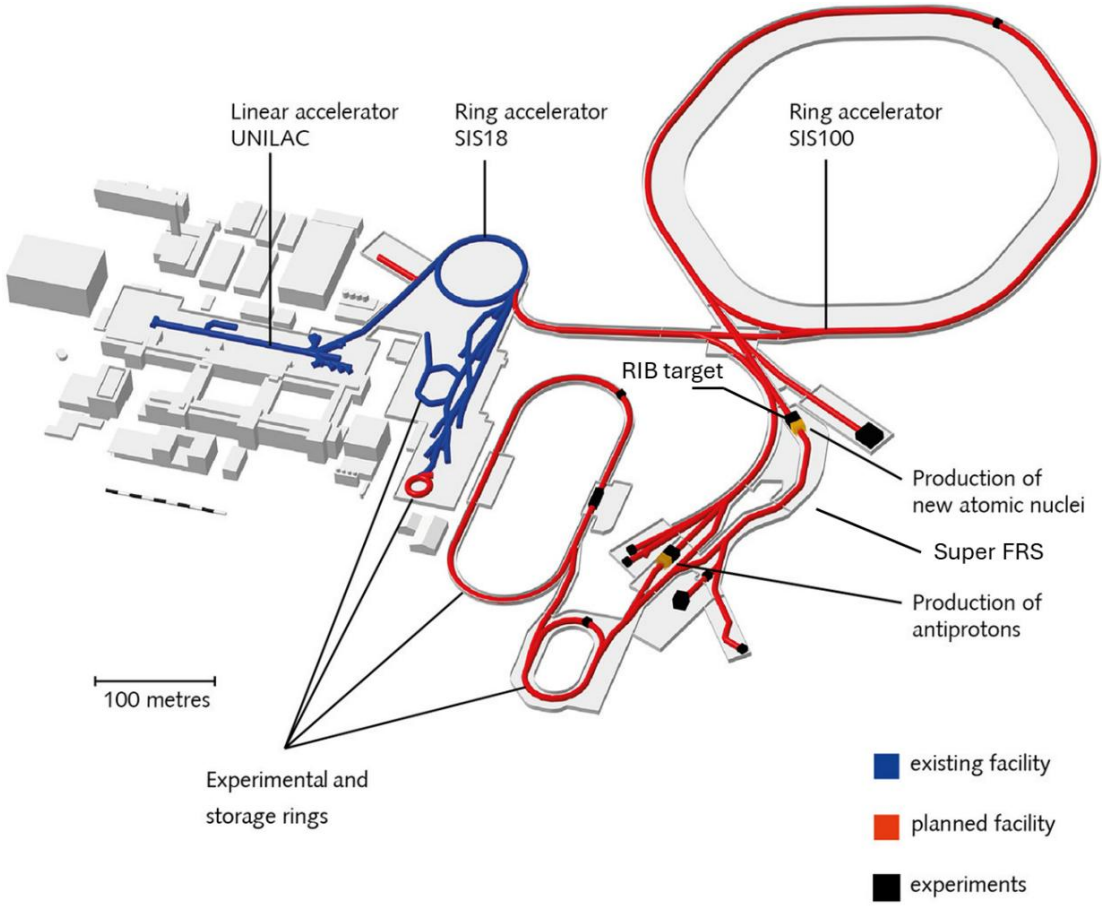

Figure 84. Facility for Antiproton and Ion Research (FAIR). Adapted from https://www.gsi.de/en/researchaccelerators/fair/the_machine, ©GSI/FAIR.

Regarding the use of in-beam PET system with RIBs, also here there are many systems under current implementation. Except for SIRMIO, which is intended to be used in preclinical research, several Open-PET scanners have been developed at the National Institutes for Quantum Sciences and Technology (QST, Japan) and have been used for beam range verification, with a particular focus on radionuclides washout in animal target with applications in ion therapy and in-beam PET imaging[231]. Open-PET has originally been developed for patients, like the BASTEI-PET system used in the GSI clinical trial with carbon ions[82]. The INSIDE in-beam PET used at CNAO (Italy) was used recently used in a clinical trial (NCT03662373)[232] comprehending patients treated with proton and carbon ions; the findings are still preliminary and the second part of the clinical trial is under

analysis, but it shows how the in-beam PET systems are under scrutiny for clinical usage. Another way to augment the reliability of the PET used with RIBs is to compare the planned dose with the predicted dose from PET images, as a direct method for treatment verification; a recently developed method showed good agreement between the predicted dose with the measured doses and a high-accuracy in predicting the distal fall-off positions at 80% of the Bragg peak for ^{11}C and ^{15}O[231].

A topic worth to test in future experiments would be the biological differences between ^{11}C and ^{12}C treatments. In physics theory, there are no expectations about this kind of difference[231] since the track structures of this beams are virtually the same, but this should be confirmed by *in vitro* and *in vivo* experiments. The fact that many radionuclides are implanted in the tissues, for example, may have consequences in the radiobiology of treatments with multiple fractions.

An example of a recently developed radiotherapy technology with a still-to-be-understood radiobiological background is the ultra-high-dose-rate radiotherapy, commonly known as FLASH[233,234]. The FLASH effect main advantage is the sparing of the normal tissue, while maintaining the same tumour control. Several preclinical experiments have demonstrated this effect[112,113], with ongoing efforts in bringing this kind of treatment to the clinical trials level. The normal tissue sparing is currently being investigated, with different theories under exploration about the exact mechanism of action, and the effect of different dose rates, total delivered dose and oxygenation of the tissue[235]. Regardless of the current strong interest in the topic, tough, a more solid radiobiological knowledge is expected to be set before a safe and solid clinical application[210].

This study showed the feasibility of RIBs radiotherapy in a preclinical context, and how the relevant technology is being developed in this context (*e. g.* accelerator developments, PET technologies improvements etcetera). This knowledge aims to pave the way for the future clinical translation[108], where radiotherapy becomes ever-more capable of relieving cancer patients of their burdens with fast, safe and personalised treatments.

5 Conclusions and future perspectives

The aim of this study was to prove for the first time the efficacy of the use of radioactive heavy ion beams for radiotherapy approaches in a preclinical context. The main advantage of using heavy ions in therapy is the Bragg peak, a sharp gradient of dose deposition that minimises the exposure of the surrounding healthy tissue when a malignancy is irradiated, but the uncertainties on the particles range inside the body and the lack of suitable imaging techniques held back the potential of this radiotherapy type[79]. Nevertheless, heavy ion therapy is growing thanks to the higher relative biological effectiveness of heavy ions, its applicability to the treatment of hypoxic and radioresistant tumours. Carbon ions, in particular, are the ones used in the clinical practice for the eradication of radioresistant cancers of various types[45].

On top of that, the use of radioactive ion beams (*i. e.*, positron emitters) could enable real-time imaging with PET, opening the possibility of imaging the beam range during the course of a treatment and permitting adaptation of the treatment itself in case anatomical changes occur. This method could reduce the uncertainties that are limiting the potential application of RIBs. Radioactive carbon ions were selected because of their clinical relevance and due to the possibility of obtaining ^{11}C beams at high intensities, thanks to the progress made in the GSI accelerator in the context of the FAIR-0 Phase project (Darmstadt). These high intensities made the possibility to treat a murine tumour feasible, culminating in the proof-of-concept study that was the Biomedical Application of Radioactive Ion Beams (BARB)[88,108].

To do so, a syngeneic murine osteosarcoma model was purposefully created using LM8 cells, a radioresistant cell line that represent the types of tumours that receive the best benefit when treated with heavy ions. Our model was tested for all the aspects that would have required observation during the irradiation with ^{11}C, including tumour growth, diagnostic µCTs, skin toxicity, spinal cord toxicity (motor-impairment and posture studies), oesophagus toxicity (weight and general wellbeing scoring), and histological analysis for the evaluation of treatment efficacy and normal tissue toxicities. The main outcome was the possibility of testing an in-beam PET system that led to a substantial increase in the measurement precision of the dose and activity peaks of the ^{11}C beam. Owing to the foundational work that demonstrated the feasibility of RIBs production, this study proved that radiotherapy with RIBs is safe and precise during the course of two experimental campaigns.

With the use of SIRMIO PET, it was possible to demonstrate the usefulness of RIBs in an in-beam PET scenario, where the uncertainties were reduced thanks to the high-count rate and strong correlation with the distal dose fall-off of the beam, thus leading to precise image-guidance and clear biological outcomes.

The preliminary experiments were important to establish the tumour model, and the scoring system needed to examine the animals on a daily basis for any kind of sickness-revealing signs. All the motor-impairment test that have been explored throughout the experiments were important to evaluate the degree of spinal cord toxicity, but since this never led to major toxicities (*e. g.* paralysis) in the first experimental campaign, it was useful for reconsidering the treatment plans. Because of the anatomy of the treated area, this led to

adding the oesophagus as the new healthy organ that was observed during the second experimental campaign, and brought a clear demonstration of the normal tissue complications in the Goldilocks range experiment. The extensive histological analyses were fundamental in proving the effects seen *in vivo*, even if larger sample sizes would have been desirable to further explore the biological endpoints. For example, it could have been interesting to add more animals in the pool which could be euthanised just after irradiation to investigate the early-induced radiation damage in the tumour. From this point of view, this is a limitation of this study that couldn´t have been changed.

RIBs have already being tested in mice and rabbits prior to this experiment for studies regarding the biological washout[94,78]. Some examples of biological washout imaging studies explored ^{11}C and protons in mice[78], ^{15}O in rats to measure the biological washout in perfused and hypoxic tumour models[97], and beam-monitoring PET was used to investigate the hypoxia status in rat tumour models[99]. So far, though, no attempts were made to apply these experimental setups for tumour treatment.

This work didn´t delve so deeply into the biological washout topic, but it showed it was feasible to measure it with SIRMIO and ^{11}C with high resolution. Future studies might consider to further explore the information that can be collected during treatment about the hypoxia status of a malignancy. Knowing if the hypoxic regions are present, and where they are inside a tumour, a precise targeting with a local dose boost[236] (dose painting) could increase treatment efficacy in case of hypoxia-induced radioresistance[89], with treatment against highly hypoxic tumours becoming more efficient. RIBs could be used in PET imaging to highlight hypoxic regions in tumours and enable hypoxia PET-based dose painting, which is currently being evaluated in an interventional clinical trial[237].

RIBs, as already discussed, are the best candidates for the treatment of malignancies near organs at risk because that´s the area where image-guided RIBs radiotherapy will test its full potential. They owe to heavy ion particles therapy the effectiveness of disease eradication, but could fulfil the aim of reducing normal tissue complications as much as possible. In this thesis, only serial organs were considered for the post-irradiation toxicity development, but future experiments with RIBs should consider also parallel organs[89], before the translation to the clinical trials. With the technological advancements that are undergoing development in the field of RIBs, and with additional biological proof-of-concepts and studies, RIBs radiotherapy might become the standard clinical practice for safer and long lasting cancer eradication efforts.

6 Bibliography

1. *Radiobiology Textbook*. (Springer International Publishing, Cham, 2023). doi:10.1007/978-3-031-18810-7.
2. Hall, E. J. *Radiobiology for the Radiologist*. (Wolters Kluwer, Philadelphia, 2019).
3. *European Atlas of Natural Radiation*. (Publications Office of the European Union, Luxembourg, 2019).
4. Cléro, E. *et al.* History of radiation detriment and its calculation methodology used in ICRP Publication 103. *J. Radiol. Prot.* **39**, R19–R36 (2019).
5. Borrego-Soto, G., Ortiz-López, R. & Rojas-Martínez, A. Ionizing radiation-induced DNA injury and damage detection in patients with breast cancer. *Genet. Mol. Biol.* **38**, 420–432 (2015).
6. Liu, Y. *et al.* Molecular mechanisms of chemo- and radiotherapy resistance and the potential implications for cancer treatment. *MedComm* **2**, 315–340 (2021).
7. Hänggi, K. & Ruffell, B. Cell death, therapeutics, and the immune response in cancer. *Trends in Cancer* **9**, 381–396 (2023).
8. Varga, T. & Aplan, P. D. Chromosomal aberrations induced by double strand DNA breaks. *DNA Repair* **4**, 1038–1046 (2005).
9. Kumar, K., Kumar, S., Datta, K., Fornace, A. J. & Suman, S. High-LET-Radiation-Induced Persistent DNA Damage Response Signaling and Gastrointestinal Cancer Development. *Current Oncology* **30**, 5497–5514 (2023).
10. Phillips, T. L., Fu, K. K. & Curtis, S. B. Tumor biology of helium and heavy ions. *International Journal of Radiation Oncology*Biology*Physics* **3**, 109–113 (1977).
11. Ballarini, F., Alloni, D., Facoetti, A. & Ottolenghi, A. Heavy-ion effects: from track structure to DNA and chromosome damage. *New J. Phys.* **10**, 075008 (2008).

12. Pacelli, R. *et al.* Technological evolution of radiation treatment: Implications for clinical applications. *Seminars in Oncology* **46**, 193–201 (2019).

13. Jakob, B., Scholz, M. & Taucher-Scholz, G. Biological Imaging of Heavy Charged-Particle Tracks. *Radiation Research* **159**, 676–684 (2003).

14. Jakob, B., Splinter, J., Durante, M. & Taucher-Scholz, G. Live cell microscopy analysis of radiation-induced DNA double-strand break motion. *Proc. Natl. Acad. Sci. U.S.A.* **106**, 3172–3177 (2009).

15. Durante, M. & Loeffler, J. S. Charged particles in radiation oncology. *Nat Rev Clin Oncol* **7**, 37–43 (2010).

16. Weyrather, W. K. & Kraft, G. RBE of carbon ions: Experimental data and the strategy of RBE calculation for treatment planning. *Radiotherapy and Oncology* **73**, S161–S169 (2004).

17. Van Leeuwen, C. M. *et al.* The alfa and beta of tumours: a review of parameters of the linear-quadratic model, derived from clinical radiotherapy studies. *Radiat Oncol* **13**, 96 (2018).

18. Delaney, G., Jacob, S., Featherstone, C. & Barton, M. The role of radiotherapy in cancer treatment: Estimating optimal utilization from a review of evidence-based clinical guidelines. *Cancer* **104**, 1129–1137 (2005).

19. Melia, E. & Parsons, J. L. DNA damage and repair dependencies of ionising radiation modalities. *Bioscience Reports* **43**, BSR20222586 (2023).

20. Gardner, S. J., Kim, J. & Chetty, I. J. Modern Radiation Therapy Planning and Delivery. *Hematology/Oncology Clinics of North America* **33**, 947–962 (2019).

21. Burnet, N. G. Defining the tumour and target volumes for radiotherapy. *Cancer Imaging* **4**, 153–161 (2004).

22. Benson, R. & Mallick, S. Therapeutic Index and Its Clinical Significance. in *Practical Radiation Oncology* (eds Mallick, S., Rath, G. K. & Benson, R.) 191–192 (Springer Singapore, Singapore, 2020). doi:10.1007/978-981-15-0073-2_31.

23. Saberian, F., Ghate, A. & Kim, M. Optimal fractionation in radiotherapy with multiple normal tissues. *Math Med Biol* **33**, 211–252 (2016).

24. Sokol, O. & Durante, M. Carbon Ions for Hypoxic Tumors: Are We Making the Most of Them? *Cancers* **15**, 4494 (2023).

25. Hanahan, D. & Weinberg, R. A. The Hallmarks of Cancer. *Cell* **100**, 57–70 (2000).

26. Senga, S. S. & Grose, R. P. Hallmarks of cancer—the new testament. *Open Biol.* **11**, 200358 (2021).

27. Kuczynski, E. A., Vermeulen, P. B., Pezzella, F., Kerbel, R. S. & Reynolds, A. R. Vessel co-option in cancer. *Nat Rev Clin Oncol* **16**, 469–493 (2019).

28. Wilson, W. R. & Hay, M. P. Targeting hypoxia in cancer therapy. *Nat Rev Cancer* **11**, 393–410 (2011).

29. Anastasiou, D. Tumour microenvironment factors shaping the cancer metabolism landscape. *Br J Cancer* **116**, 277–286 (2017).

30. Quartieri, M., Puspitasari, A., Vitacchio, T., Durante, M. & Tinganelli, W. The role of hypoxia and radiation in developing a CTCs-like phenotype in murine osteosarcoma cells. *Front. Cell Dev. Biol.* **11**, 1222809 (2023).

31. Greaves, M. Nothing in cancer makes sense except…. *BMC Biol* **16**, 22 (2018).

32. Withers, H. R. The Four R's of Radiotherapy. in *Advances in Radiation Biology* (eds Lett, J. T. & Adler, H.) vol. 5 241–271 (Elsevier, 1975).

33. Ripoll-Viladomiu, I., Prina-Mello, A., Movia, D. & Marignol, L. Extracellular vesicles and the "six Rs" in radiotherapy. *Cancer Treatment Reviews* **129**, 102799 (2024).

34. Hanahan, D. & Weinberg, R. A. Hallmarks of Cancer: The Next Generation. *Cell* **144**, 646–674 (2011).

35. Taghizadeh-Hesary, F. “Reinforcement” by Tumor Microenvironment: The Seventh “R” of Radiobiology. *International Journal of Radiation Oncology*Biology*Physics* S0360301623079403 (2023) doi:10.1016/j.ijrobp.2023.09.027.

36. McKeown, S. R. Defining normoxia, physoxia and hypoxia in tumours—implications for treatment response. *BJR* **87**, 20130676 (2014).

37. Tinganelli, W. & Durante, M. Carbon Ion Radiobiology. *Cancers* **12**, 3022 (2020).

38. Liu, Q., Palmgren, V. A. C., Danen, E. H. & Le Dévédec, S. E. Acute vs. chronic vs. intermittent hypoxia in breast Cancer: a review on its application in in vitro research. *Mol Biol Rep* **49**, 10961–10973 (2022).

39. Tinganelli, W. *et al.* Kill-painting of hypoxic tumours in charged particle therapy. *Sci Rep* **5**, 17016 (2015).

40. Wenzl, T. & Wilkens, J. J. Modelling of the oxygen enhancement ratio for ion beam radiation therapy. *Phys. Med. Biol.* **56**, 3251–3268 (2011).

41. Parkins, C., Hill, S., Stratford, M., Dennis, M. & Chaplin, D. Metabolic and clonogenic consequences of ischaemia reperfusion insult in solid tumours. *Experimental Physiology* **82**, 361–368 (1997).

42. Baskar, R., Lee, K. A., Yeo, R. & Yeoh, K.-W. Cancer and Radiation Therapy: Current Advances and Future Directions. *Int. J. Med. Sci.* **9**, 193–199 (2012).

43. Eichkorn, T. *et al.* Carbon Ion Radiation Therapy: One Decade of Research and Clinical Experience at Heidelberg Ion Beam Therapy Center. *International Journal of Radiation Oncology, Biology, Physics* **111**, 597–609 (2021).

44. Rackwitz, T. & Debus, J. Clinical applications of proton and carbon ion therapy. *Seminars in Oncology* **46**, 226–232 (2019).

45. Kim, K. S. & Wu, H.-G. Who Will Benefit from Charged-Particle Therapy? *Cancer Res Treat* **53**, 621–634 (2021).

46. Vischioni, B. *et al.* Radioresistant, Rare, Recurrent, and Radioinduced: 4Rs of Hadrontherapy for Patients Selections. *International Journal of Particle Therapy* **15**, 100737 (2025).

47. Durante, M., Debus, J. & Loeffler, J. S. Physics and biomedical challenges of cancer therapy with accelerated heavy ions. *Nat Rev Phys* **3**, 777–790 (2021).

48. PTCOG - Facilities in Operation (public). https://www.ptcog.site/index.php/facilities-in-operation-public.

49. Malouff, T. D. *et al.* Carbon Ion Therapy: A Modern Review of an Emerging Technology. *Front. Oncol.* **10**, 82 (2020).

50. CERN. CERN Yellow Reports: Monographs, Vol 2 (2019): A Facility for Tumour Therapy and Biomedical Research in South-Eastern Europe. 58.33 MB Preprint at https://doi.org/10.23731/CYRM-2019-002 (2019).

51. Malouff, T. D. *et al.* Estimating the Number of Patients Eligible for Carbon Ion Radiotherapy in the United States. *International Journal of Particle Therapy* **7**, 31–41 (2020).

52. De Ruysscher, D. *et al.* Radiotherapy toxicity. *Nat Rev Dis Primers* **5**, 13 (2019).

53. Barnett, G. C. *et al.* Normal tissue reactions to radiotherapy: towards tailoring treatment dose by genotype. *Nat Rev Cancer* **9**, 134–142 (2009).

54. Wang, K. & Tepper, J. E. Radiation therapy-associated toxicity: Etiology, management, and prevention. *CA A Cancer J Clinicians* **71**, 437–454 (2021).

55. Kerns, S. L., Hall, W. A., Marples, B. & West, C. M. L. Normal Tissue Toxicity Prediction: Clinical Translation on the Horizon. *Seminars in Radiation Oncology* **33**, 307–316 (2023).

56. Cox, J. D., Stetz, J. & Pajak, T. F. Toxicity criteria of the Radiation Therapy Oncology Group (RTOG) and the European organization for research and treatment of cancer

(EORTC). *International Journal of Radiation Oncology*Biology*Physics* **31**, 1341–1346 (1995).

57. Majeed, H. & Gupta, V. Adverse Effects of Radiation Therapy. in *StatPearls* (StatPearls Publishing, Treasure Island (FL), 2025).

58. Baker, S. & Fairchild, A. Radiation-induced esophagitis in lung cancer. *LCTT* **Volume 7**, 119–127 (2016).

59. Wong, C. S., Fehlings, M. G. & Sahgal, A. Pathobiology of radiation myelopathy and strategies to mitigate injury. *Spinal Cord* **53**, 574–580 (2015).

60. Ozoemelam, I. *et al.* Real-Time PET Imaging for Range Verification of Helium Radiotherapy. *Front. Phys.* **8**, 565422 (2020).

61. Lomax, A. SFUD, IMPT, and plan robustness. in *Particle Radiotherapy: Emerging Technology for Treatment of Cancer* 169–194 (2016). doi:10.1007/978-81-322-2622-2_12.

62. McGowan, S. E., Burnet, N. G. & Lomax, A. J. Treatment planning optimisation in proton therapy. *BJR* **86**, 20120288–20120288 (2013).

63. Knopf, A.-C. & Lomax, A. *In vivo* proton range verification: a review. *Phys. Med. Biol.* **58**, R131–R160 (2013).

64. Pausch, G. *et al.* Detection systems for range monitoring in proton therapy: Needs and challenges. *Nuclear Instruments and Methods in Physics Research Section A: Accelerators, Spectrometers, Detectors and Associated Equipment* **954**, 161227 (2020).

65. Belcari, N., Bisogni, M. G. & Del Guerra, A. Positron emission tomography: its 65 years and beyond. *Riv. Nuovo Cim.* https://doi.org/10.1007/s40766-024-00050-3 (2024) doi:10.1007/s40766-024-00050-3.

66. Lin, E. & Alavi, A. *PET and PET/CT: A Clinical Guide*. (Thieme Medical Publishers, Stuttgart, 2019).

67. Internationale Atomenergie-Organisation. *PET/CT Atlas on Quality Control and Image Artefacts*. (IAEA, Vienna, 2014).

68. Lynch, T. *PET/CT in Clinical Practice*. (Springer-Verlag London Limited, London, 2007). doi:10.1007/978-1-84628-504-2.

69. Basu, S. *et al.* The Basic Principles of FDG-PET/CT Imaging. *PET Clinics* **9**, 355–370 (2014).

70. Lawson, R. An Introduction to Radioactivity. (1999).

71. Fowler, J. S. ^{18} F-FDG Radiosynthesis: A Landmark in the History of PET (perspective on "Efficient Stereospecific Synthesis of No-Carrier-Added 2-[^{18} F]fluoro-2-Deoxy-D-Glucose Using Aminopolyether Supported Nucleophilic Substitution" *J Nucl Med.* 1986;27:235–238). *J Nucl Med* **61**, 105S-109S (2020).

72. Ashraf, M. A. & Goyal, A. Fludeoxyglucose (18F). in *StatPearls* (StatPearls Publishing, Treasure Island (FL), 2025).

73. *Small Animal Imaging*. (Springer International Publishing, Cham, 2017). doi:10.1007/978-3-319-42202-2.

74. Vaquero, J. J. & Kinahan, P. Positron Emission Tomography: Current Challenges and Opportunities for Technological Advances in Clinical and Preclinical Imaging Systems. *Annu. Rev. Biomed. Eng.* **17**, 385–414 (2015).

75. Kraan, A. C. Range Verification Methods in Particle Therapy: Underlying Physics and Monte Carlo Modeling. *Front. Oncol.* **5**, (2015).

76. Bey, A. *et al.* Nuclear Fragmentation Imaging for Carbon-Ion Radiation Therapy Monitoring: an In Silico Study. *International Journal of Particle Therapy* **8**, 25–36 (2022).

77. Salvador, S. *et al.* Cross section measurements for production of positron emitters for PET imaging in carbon therapy. *Phys. Rev. C* **95**, 044607 (2017).

78. Ammar, C. *et al.* Comparing the biological washout of β^+ -activity induced in mice brain after ^{12} C-ion and proton irradiation. *Phys. Med. Biol.* **59**, 7229–7244 (2014).

79. Durante, M. & Parodi, K. Radioactive Beams in Particle Therapy: Past, Present, and Future. *Front. Phys.* **8**, 326 (2020).

80. Shakirin, G. *et al.* Implementation and workflow for PET monitoring of therapeutic ion irradiation: a comparison of in-beam, in-room, and off-line techniques. *Phys. Med. Biol.* **56**, 1281–1298 (2011).

81. Pennazio, F. *et al.* Carbon ions beam therapy monitoring with the INSIDE in-beam PET. *Phys. Med. Biol.* **63**, 145018 (2018).

82. Positron-Emission-Tomography for ion beam therapy (PT-PET) - Helmholtz-Zentrum Dresden-Rossendorf, HZDR. https://www.hzdr.de/db/Cms?pOid=45492&pNid=0.

83. Stützer, K. *et al.* Experimental verification of a 4D MLEM reconstruction algorithm used for in-beam PET measurements in particle therapy. *Phys. Med. Biol.* **58**, 5085–5111 (2013).

84. Fiedler, F. *et al.* In-beam PET measurements of biological half-lives of^{12} C irradiation induced β^+ -activity. *Acta Oncologica* **47**, 1077–1086 (2008).

85. Tashima, H. *et al.* A single-ring OpenPET enabling PET imaging during radiotherapy. *Phys. Med. Biol.* **57**, 4705–4718 (2012).

86. Nishio, T. *et al.* The Development and Clinical Use of a Beam ON-LINE PET System Mounted on a Rotating Gantry Port in Proton Therapy. *International Journal of Radiation Oncology*Biology*Physics* **76**, 277–286 (2010).

87. Bisogni, M. G. *et al.* INSIDE in-beam positron emission tomography system for particle range monitoring in hadrontherapy. *J. Med. Imag* **4**, 011005 (2016).

88. Boscolo, D. *et al.* Radioactive Beams for Image-Guided Particle Therapy: The BARB Experiment at GSI. *Front. Oncol.* **11**, 737050 (2021).

89. Sokol, O. *et al.* Potential benefits of using radioactive ion beams for range margin reduction in carbon ion therapy. *Sci Rep* **12**, 21792 (2022).

90. Yamaya, T. *et al.* A proposal of an open PET geometry. *Phys. Med. Biol.* **53**, 757–773 (2008).

91. Boscolo, D. *et al.* Depth dose measurements in water for 11C and 10C beams with therapy relevant energies. *Nuclear Instruments and Methods in Physics Research Section A: Accelerators, Spectrometers, Detectors and Associated Equipment* **1043**, 167464 (2022).

92. Fragment Separator. *GSI* https://www.gsi.de//en/researchaccelerators/accelerator_facility/fragment_separator (2012).

93. Kang, H. & Hamato, A. Prospects for applying radioactive ion beams in particle therapy. *The European Physical Journal Plus* **140**, (2025).

94. Mizuno, H. *et al.* Washout measurement of radioisotope implanted by radioactive beams in the rabbit. *Phys. Med. Biol.* **48**, 2269–2281 (2003).

95. Tomitani, T. *et al.* Washout studies of ^{11} C in rabbit thigh muscle implanted by secondary beams of HIMAC. *Phys. Med. Biol.* **48**, 875–889 (2003).

96. Toramatsu, C. *et al.* Biological washout modelling for in-beam PET: rabbit brain irradiation by ^{11} C and ^{15} O ion beams. *Phys. Med. Biol.* **65**, 105011 (2020).

97. Toramatsu, C. *et al.* Measurement of biological washout rates depending on tumor vascular status in ^{15} O in-beam rat-PET. *Phys. Med. Biol.* **67**, 125006 (2022).

98. Toramatsu, C. *et al.* Tumour status prediction by means of carbon-ion beam irradiation: comparison of washout rates between in-beam PET and DCE-MRI in rats. *Phys. Med. Biol.* **68**, 195005 (2023).

99. Toramatsu, C. *et al.* Prediction of tumour hypoxia status from the washout of positron emitters in beam-monitoring PET: carbon-ion irradiation to tumour rat models. *EJNMMI Res* **16**, 32 (2026).

100. Bartl, A. J. *et al.* Systematic Review of Single-Fraction Stereotactic Body Radiation Therapy for Early Stage Non-Small-Cell Lung Cancer and Lung Oligometastases: How to Stop Worrying and Love One and Done. *Cancers* **14**, 790 (2022).

101. Nicosia, L. *et al.* Long term results of single high dose Stereotactic Body Radiotherapy in the treatment of primary lung tumors. *Sci Rep* **9**, 15498 (2019).

102. Zilli, T. *et al.* ONE SHOT - single shot radiotherapy for localized prostate cancer: 18-month results of a single arm, multicenter phase I/II trial. *Radiotherapy and Oncology* **194**, 110181 (2024).

103. Osti, M. F. *et al.* 30 Gy single dose stereotactic body radiation therapy (SBRT): Report on outcome in a large series of patients with lung oligometastatic disease. *Lung Cancer* **122**, 165–170 (2018).

104. Kalogeris, T., Baines, C. P., Krenz, M. & Korthuis, R. J. Cell Biology of Ischemia/Reperfusion Injury. in *International Review of Cell and Molecular Biology* vol. 298 229–317 (Elsevier, 2012).

105. Bodo, S. *et al.* Single-dose radiotherapy disables tumor cell homologous recombination via ischemia/reperfusion injury. *Journal of Clinical Investigation* **129**, 786–801 (2019).

106. Zhang, M. *et al.* Ischemia-reperfusion injury: molecular mechanisms and therapeutic targets. *Sig Transduct Target Ther* **9**, 12 (2024).

107. Schardt, D., Elsässer, T. & Schulz-Ertner, D. Heavy-ion tumor therapy: Physical and radiobiological benefits. *Rev. Mod. Phys.* **82**, 383–425 (2010).

108. Boscolo, D. *et al.* Image-guided treatment of mouse tumours with radioactive ion beams. *Nat. Phys.* https://doi.org/10.1038/s41567-025-02993-8 (2025) doi:10.1038/s41567-025-02993-8.

109. NC3Rs. https://nc3rs.org.uk/.

110. Asai, T. *et al.* Establishment and characterization of a murine osteosarcoma cell line (LM8) with high metastatic potential to the lung. *International Journal of Cancer* **76**, 418–422 (1998).

111. Helm, A. *et al.* Reduction of Lung Metastases in a Mouse Osteosarcoma Model Treated With Carbon Ions and Immune Checkpoint Inhibitors. *International Journal of Radiation Oncology*Biology*Physics* **109**, 594–602 (2021).

112. Tinganelli, W. *et al.* FLASH with carbon ions: Tumor control, normal tissue sparing, and distal metastasis in a mouse osteosarcoma model. *Radiotherapy and Oncology* **175**, 185–190 (2022).

113. Tinganelli, W. *et al.* FLASH Bragg-Peak Irradiation With a Therapeutic Carbon Ion Beam: First In Vivo Results. *International Journal of Radiation Oncology*Biology*Physics* S0360301624036629 (2024) doi:10.1016/j.ijrobp.2024.11.089.

114. Ferrari, A., Sala, P. R., Fasso, A. & Ranft, J. *FLUKA: A Multi-Particle Transport Code*. SLAC-R-773, 877507 http://www.osti.gov/servlets/purl/877507-sC9S9L/ (2005) doi:10.2172/877507.

115. Kikinis, R., Pieper, S. D. & Vosburgh, K. G. 3D Slicer: A Platform for Subject-Specific Image Analysis, Visualization, and Clinical Support. in *Intraoperative Imaging and Image-Guided Therapy* (ed. Jolesz, F. A.) 277–289 (Springer New York, New York, NY, 2014). doi:10.1007/978-1-4614-7657-3_19.

116. Simeonov, Y. *et al.* Monte Carlo simulations and dose measurements of 2D range-modulators for scanned particle therapy. *Zeitschrift für Medizinische Physik* **31**, 203–214 (2021).

117. Schuy, C., Simeonov, Y., Durante, M., Zink, K. & Weber, U. Technical note: Vendor-agnostic water phantom for 3D dosimetry of complex fields in particle therapy. *J Applied Clin Med Phys* **21**, 227–232 (2020).

118. Lovatti, G. *et al.* Experimental assessment of novel PET detector components for online imaging of radioactive ion beams. *Phys. Med. Biol.* **70**, 195008 (2025).

119. Sundberg, J. P., Cordy, W. R. & King, L. E. Alopecia Areata in Aging C3H/HeJ Mice. *Journal of Investigative Dermatology* **102**, 847–856 (1994).

120. Denbeigh, J. M., Howard, M. E., Debrot, E. K., Remmes, N. B. & Garcia, D. EVALUATING PROTON RELATIVE BIOLOGICAL EFFECTIVENESS FOR SPINAL CORD TOXICITY IN SINGLE AND MULTIFRACTION TREATED MICE.

121. Denbeigh, J. M. *et al.* Characterizing Proton-Induced Biological Effects in a Mouse Spinal Cord Model: A Comparison of Bragg Peak and Entrance Beam Response in Single and Fractionated Exposures. *International Journal of Radiation Oncology*Biology*Physics* **119**, 924–935 (2024).

122. Cabe, P. A., Tilson, H. A., Mitchell, C. L. & Dennis, R. A simple recording grip strength device. *Pharmacology Biochemistry and Behavior* **8**, 101–102 (1978).

123. Bounds, H. A., Poeta, D. L., Klinge, P. M. & Burwell, R. D. Paw-Print Analysis of Contrast-Enhanced Recordings (PrAnCER): A low-cost, open-access automated gait analysis system for assessing motor deficits in the rat. (2019).

124. Brooks, S. P. & Dunnett, S. B. Tests to assess motor phenotype in mice: a user's guide. *Nat Rev Neurosci* **10**, 519–529 (2009).

125. Yerger, J. *et al.* Phenotype assessment for neurodegenerative murine models with ataxia and application to Niemann–Pick disease, type C1. *Biology Open* **11**, bio059052 (2022).

126. Vascupaint Silicone Rubber Injection Compounds (Lead Free) - MediLumine. *https://medilumine.com* https://medilumine.com/product/vascupaint (2024).

127. Downey, C. M. *et al.* Quantitative Ex-Vivo Micro-Computed Tomographic Imaging of Blood Vessels and Necrotic Regions within Tumors. *PLoS ONE* **7**, e41685 (2012).

128. Chan, J. K. C. The Wonderful Colors of the Hematoxylin–Eosin Stain in Diagnostic Surgical Pathology. *Int J Surg Pathol* **22**, 12–32 (2014).

129. Sonoda, A., Nihei, M., Shinkawa, N., Kakizaki, E. & Yukawa, N. Perls' Prussian blue staining and chemistry of Prussian blue and Turnbull blue. *Forensic Science International: Synergy* **11**, 100627 (2025).

130. *Bancroft's Theory and Practice of Histological Techniques - Eight Edition*. (Elsevier, Amsterdam, 2019).

131. Atkinson, S., Li, Y.-Q. & Wong, C. S. Changes in oligodendrocytes and myelin gene expression after radiation in the rodent spinal cord. *International Journal of Radiation Oncology*Biology*Physics* **57**, 1093–1100 (2003).

132. Bankhead, P. *et al.* QuPath: Open source software for digital pathology image analysis. *Sci Rep* **7**, 16878 (2017).

133. Helm, A. *et al.* Reduction of Lung Metastases in a Mouse Osteosarcoma Model Treated With Carbon Ions and Immune Checkpoint Inhibitors. *International Journal of Radiation Oncology*Biology*Physics* **109**, 594–602 (2021).

134. Zaun, G. *et al.* Protocol for the establishment of murine orthotopic lung tumors and the assessment of contralateral pulmonal metastasis by flow cytometry. *STAR Protocols* **6**, 103793 (2025).

135. Holsapple, M. P., West, L. J. & Landreth, K. S. Species comparison of anatomical and functional immune system development. *Birth Defects Research Pt B* **68**, 321–334 (2003).

136. Meschter, C. L., Connolly, J. M. & Rose, D. P. Influence of regional location of the inoculation site and dietary fat on the pathology of MDA-MB-435 human breast cancer cell-derived tumors grown in nude mice. *Clin Exp Metast* **10**, 167–173 (1992).

137. Sottnik, J. L. *et al.* Osteocytes Serve as a Progenitor Cell of Osteosarcoma. *J of Cellular Biochemistry* **115**, 1420–1429 (2014).

138. Franz-Odendaal, T. A., Hall, B. K. & Witten, P. E. Buried alive: How osteoblasts become osteocytes. *Developmental Dynamics* **235**, 176–190 (2006).

139. Goel, S. *et al.* Normalization of the Vasculature for Treatment of Cancer and Other Diseases. *Physiological Reviews* **91**, 1071–1121 (2011).

140. Prudowsky, Z. D. & Yustein, J. T. Recent Insights into Therapy Resistance in Osteosarcoma. *Cancers* **13**, 83 (2020).

141. Pisciotta, P. *et al.* Evaluation of proton beam radiation-induced skin injury in a murine model using a clinical SOBP. *PLOS ONE* **15**, e0233258 (2020).

142. Maurissen, J. P. J., Marable, B. R., Andrus, A. K. & Stebbins, K. E. Factors affecting grip strength testing. *Neurotoxicology and Teratology* **25**, 543–553 (2003).

143. Hamers, F. P. T., Koopmans, G. C. & Joosten, E. A. J. CatWalk-Assisted Gait Analysis in the Assessment of Spinal Cord Injury. *Journal of Neurotrauma* **23**, 537–548 (2006).

144. Kostyleva, D. *et al.* Precision of the PET activity range during irradiation with^{10} C,^{11} C, and^{12} C beams. *Phys. Med. Biol.* **68**, 015003 (2023).

145. Han, Y. *et al.* Hemosiderin deposition in lymph nodes of patients with plasma cell-type Castleman disease. *JCEH* **60**, 1–6 (2020).

146. Yokogawa, N. *et al.* Effects of Radiation on Spinal Dura Mater and Surrounding Tissue in Mice. *PLoS ONE* **10**, e0133806 (2015).

147. Moglioni, M. *et al.* Radioactive ion beam range adaptation in mouse tumors using in-beam PET. *Commun Med* **6**, 393 (2026).

148. Alexander, R. G. *et al.* Eosinophilic Esophagitis Histologic Scoring System: Correlation with Histologic, Endoscopic, and Symptomatic Disease and Clinical Use. *Dig Dis Sci* **68**, 3573–3583 (2023).

149. Ga, B. *et al.* Esophagus - Hyperplasia.

150. Olvera, M. *et al.* Ki67 expression in different epithelial types in columnar lined oesophagus indicates varying levels of expanded and aberrant proliferative patterns. *Histopathology* **47**, 132–140 (2005).

151. Yuan, A., Rao, M. V., Veeranna & Nixon, R. A. Neurofilaments at a glance. *Journal of Cell Science* **125**, 3257–3263 (2012).

152. Watson, C. & Kayalioglu, G. The Organization of the Spinal Cord. in *The Spinal Cord* 1–7 (Elsevier, 2009). doi:10.1016/B978-0-12-374247-6.50005-5.

153. Purushothaman, S. *et al.* Quasi-real-time range monitoring by in-beam PET: a case for 15O. *Sci Rep* **13**, 18788 (2023).

154. Prades-Sagarra, E., Yaromina, A. & Dubois, L. J. Understanding the impact of radiation-induced lymphopenia: Preclinical and clinical research perspectives. *Clinical and Translational Radiation Oncology* **49**, 100852 (2024).

155. Boscolo, D. *et al.* Image-guided treatment of mouse tumours with radioactive ion beams. *Nat. Phys.* **21**, 1648–1656 (2025).

156. Totis, C. *et al.* Induction of Cytoplasmic dsDNA and cGAS-STING Immune Signaling After Exposure of Breast Cancer Cells to X-ray or High-Energetic Carbon Ions. *Advances in Radiation Oncology* **10**, 101783 (2025).

157. Benje, M., Vitacchio, T., Fritsche, D. & Tinganelli, W. Gene Expression Profiling and Phenotypic Characterization of Circulating Tumor Cells Derived from a Murine Osteosarcoma Model. *Cancers* **17**, 1210 (2025).

158. Mageau, E. *et al.* Molecular Mechanisms of Radiation Resistance in Breast Cancer: A Systematic Review of Radiosensitization Strategies. *CIMB* **47**, 589 (2025).

159. Vilalta, M., Rafat, M. & Graves, E. E. Effects of radiation on metastasis and tumor cell migration. *Cell. Mol. Life Sci.* **73**, 2999–3007 (2016).

160. Mole, R. H. Whole Body Irradiation—Radiobiology or Medicine?*. *British Journal of Radiology* **26**, 234–241 (1953).

161. Ebner, D. K., Kamada, T. & Yamada, S. Abscopal effect in recurrent colorectal cancer treated with carbon-ion radiation therapy: 2 case reports. *Advances in Radiation Oncology* **2**, 333–338 (2017).

162. Ngwa, W. *et al.* Using immunotherapy to boost the abscopal effect. *Nat Rev Cancer* **18**, 313–322 (2018).

163. Szeto, G. L. & Finley, S. D. Integrative Approaches to Cancer Immunotherapy. *Trends in Cancer* **5**, 400–410 (2019).

164. Kim, S. K. & Cho, S. W. The Evasion Mechanisms of Cancer Immunity and Drug Intervention in the Tumor Microenvironment. *Front. Pharmacol.* **13**, 868695 (2022).

165. Chen, R. *et al.* Combined carbon ion radiotherapy and immunotherapy: leveraging the immunological advantages of carbon ion. *Front. Immunol.* **17**, 1747607 (2026).

166. Esfahani, K. *et al.* A Review of Cancer Immunotherapy: From the Past, to the Present, to the Future. *Current Oncology* **27**, 87–97 (2020).

167. Liu, R. *et al.* Carbon ion irradiation combined with PD-1 inhibitor trigger abscopal effect in Lewis lung cancer via a threshold dose. Preprint at https://doi.org/10.21203/rs.3.rs-2871494/v1 (2023).

168. Ma, L. *et al.* Optimal radiation dose to induce an abscopal effect by combining carbon-ion radiotherapy and anti-CTLA4 antibody. *Neoplasia* **60**, 101099 (2025).

169. Chang, H. P., Cho, J. H., Lee, W. J., Roh, H. & Lee, D. W. Development of an easy-to-handle murine model for the characterization of radiation-induced gross and molecular changes in skin. *Arch Plast Surg* **45**, 403–410 (2018).

170. Sørensen, B. S. *et al.* Relative biological effectiveness of carbon ions for tumor control, acute skin damage and late radiation-induced fibrosis in a mouse model. *Acta Oncologica* **54**, 1623–1630 (2015).

171. Ruifrok, A. C. C., Stephens, L. C. & van der Kogel, A. J. Radiation response of the rat cervical spinal cord after irradiation at different ages: Tolerance, latency and pathology. *International Journal of Radiation Oncology*Biology*Physics* **29**, 73–79 (1994).

172. Okada, S., Okeda, R., Matsushita, S. & Kawano, A. Histopathological and Morphometric Study of the Late Effects of Heavy-Ion Irradiation on the Spinal Cord of the Rat. *Radiation Research* **150**, 304 (1998).

173. Philippens, M. E. P., Pop, L. A. M., Visser, A. G. & Van Der Kogel, A. J. Dose–Volume Effects in Rat Thoracolumbar Spinal Cord: The Effects of Nonuniform Dose Distribution. *International Journal of Radiation Oncology*Biology*Physics* **69**, 204–213 (2007).

174. Saager, M. *et al.* Late normal tissue response in the rat spinal cord after carbon ion irradiation. *Radiat Oncol* **13**, 5 (2018).

175. Lo, Y.-C., Taylor, J. M. G., McBride, W. H. & Withers, H. R. The effect of fractionated doses of radiation on mouse spinal cord. *International Journal of Radiation Oncology*Biology*Physics* **27**, 309–317 (1993).

176. Lavey, R. *et al.* The extent, time course, and fraction size dependence of mouse spinal cord recovery from radiation injury. *International Journal of Radiation Oncology*Biology*Physics* **30**, 609–617 (1994).

177. Goffinet, D. R., Choi, K. Y. & Brown, J. M. The Combined Effects of Hyperthermia and Ionizing Radiation on the Adult Mouse Spinal Cord. *Radiation Research* **72**, 238 (1977).

178. Sun, Y. *et al.* Transplantation of Oligodendrocyte Precursor Cells Improves Locomotion Deficits in Rats with Spinal Cord Irradiation Injury. *PLoS ONE* **8**, e57534 (2013).

179. Kesslak, P. J. & Keirstead, H. S. Assessment Of Behavior In Animal Models Of Spinal Cord Injury. *The Journal of Spinal Cord Medicine* **26**, 323–328 (2003).

180. Anderson, K. D., Abdul, M. & Steward, O. Quantitative assessment of deficits and recovery of forelimb motor function after cervical spinal cord injury in mice. *Experimental Neurology* **190**, 184–191 (2004).

181. Šedý, J., Urdzíková, L., Jendelová, P. & Syková, E. Methods for behavioral testing of spinal cord injured rats. *Neuroscience & Biobehavioral Reviews* **32**, 550–580 (2008).

182. Guyenet, S. J. *et al.* A Simple Composite Phenotype Scoring System for Evaluating Mouse Models of Cerebellar Ataxia. *JoVE* 1787 (2010) doi:10.3791/1787.

183. Broom, L. *et al.* A translational approach to capture gait signatures of neurological disorders in mice and humans. *Sci Rep* **7**, 3225 (2017).

184. Burrows, D. J. *et al.* Animal models of multiple sclerosis: From rodents to zebrafish. *Mult Scler* **25**, 306–324 (2019).

185. Saager, M. *et al.* Carbon Ion Irradiation of the Rat Spinal Cord: Dependence of the Relative Biological Effectiveness on Linear Energy Transfer. *International Journal of Radiation Oncology*Biology*Physics* **90**, 63–70 (2014).

186. Lo, Y.-C., McBride, W. H. & Rodney Withers, H. The effect of single doses of radiation on mouse spinal cord. *International Journal of Radiation Oncology*Biology*Physics* **22**, 57–63 (1992).

187. Greco, C. *et al.* Spinal metastases: From conventional fractionated radiotherapy to single-dose SBRT. *Reports of Practical Oncology & Radiotherapy* **20**, 454–463 (2015).

188. Mitchell, S. L., Donaldson, C. J., El Dafrawy, M. H. & Kebaish, K. M. Difficulties in Treating Postirradiation Kyphosis in Adults: A Series of Five Cases. *Spine Deform* **7**, 937–944 (2019).

189. Langford, D. J. *et al.* Coding of facial expressions of pain in the laboratory mouse. *Nat Methods* **7**, 447–449 (2010).

190. Deacon, R. M. J. Measuring Motor Coordination in Mice. *JoVE* 2609 (2013) doi:10.3791/2609.

191. Leussis, M. & Bolivar, V. Habituation in rodents: A review of behavior, neurobiology, and genetics. *Neuroscience & Biobehavioral Reviews* **30**, 1045–1064 (2006).

192. Welzel, T., Saager, M., Peschke, P., Debus, J. & Karger, C. P. Effects of Photon versus Carbon-Ion Irradiation in the Rat Cervical Spinal Cord – a Serial T2 and Diffusion-weighted Magnetic Resonance Imaging Study. *rare* **202**, 11–15 (2024).

193. Deuis, J. R., Dvorakova, L. S. & Vetter, I. Methods Used to Evaluate Pain Behaviors in Rodents. *Front. Mol. Neurosci.* **10**, 284 (2017).

194. Tokuda, S., Beyer, B. J. & Frankel, W. N. Genetic complexity of absence seizures in substrains of C3H mice. *Genes Brain and Behavior* **8**, 283–289 (2009).

195. Zhang, J. *et al.* Radiation-induced endothelial cell loss and reduction of the relative magnitude of the blood flow in the rat spinal cord. *Brain Research* **1583**, 193–200 (2014).

196. Bijl, H. P. *et al.* Regional differences in radiosensitivity across the rat cervical spinal cord. *International Journal of Radiation Oncology*Biology*Physics* **61**, 543–551 (2005).

197. Maihemuti, M., Mimi, Mst. A., Sohag, S. M. & Hasan, Md. M. Single-Cell Transcriptomics in Spinal Cord Studies: Progress and Perspectives. *BioChem* **5**, 16 (2025).

198. Garcia-Barros, M. *et al.* Tumor Response to Radiotherapy Regulated by Endothelial Cell Apoptosis. *Science* **300**, 1155–1159 (2003).

199. Fuks, Z. & Kolesnick, R. Engaging the vascular component of the tumor response. *Cancer Cell* **8**, 89–91 (2005).

200. Piotr, W., Aleksander, S. & Waldemar M., P. Influence of Local Temporary Ischemia on Radiotherapy Effects. *Journal of Cancer Therapy* **2011**, (2011).

201. Wu, M.-Y. *et al.* Current Mechanistic Concepts in Ischemia and Reperfusion Injury. *Cell Physiol Biochem* **46**, 1650–1667 (2018).

202. Gujral, J. S., Bucci, T. J., Farhood, A. & Jaeschke, H. Mechanism of cell death during warm hepatic ischemia-reperfusion in rats: apoptosis or necrosis? *Hepatology* **33**, 397–405 (2001).

203. Fukawa, T. *et al.* Differences in pO2 Peaks of a Murine Fibrosarcoma between Carbon-ion and X-ray Irradiation. *JRR* **45**, 303–308 (2004).

204. Wallyn, J., Anton, N., Akram, S. & Vandamme, T. F. Biomedical Imaging: Principles, Technologies, Clinical Aspects, Contrast Agents, Limitations and Future Trends in Nanomedicines. *Pharm Res* **36**, 78 (2019).

205. Graupner, A. *et al.* Genotoxic effects of high dose rate X-ray and low dose rate gamma radiation in $Apc^{Min/+}$ mice. *Environ and Mol Mutagen* **58**, 560–569 (2017).

206. Chaudhry, F. *et al.* Single-Cell RNA Sequencing of the Cardiovascular System: New Looks for Old Diseases. *Front. Cardiovasc. Med.* **6**, 173 (2019).

207. Baindara, P. Targeting interleukin-17 in radiation-induced toxicity and cancer progression. *Cytokine & Growth Factor Reviews* **75**, 31–39 (2024).

208. Yan, D., Vicini, F., Wong, J. & Martinez, A. Adaptive radiation therapy.

209. Brock, K. K. Adaptive Radiotherapy: Moving Into the Future. *Seminars in Radiation Oncology* **29**, 181–184 (2019).

210. Graeff, C., Volz, L. & Durante, M. Emerging technologies for cancer therapy using accelerated particles. *Progress in Particle and Nuclear Physics* **131**, 104046 (2023).

211. Visanji, A., Li, W., Winter, J., Chung, P. & Kong, V. Time toxicity in CBCT-guided radiation therapy: A retrospective analysis of unplanned imaging burden across disease sites. *Technical Innovations & Patient Support in Radiation Oncology* **37**, 100379 (2026).

212. Kan, M. W. K., Leung, L. H. T., Wong, W. & Lam, N. Radiation Dose From Cone Beam Computed Tomography for Image-Guided Radiation Therapy. *International Journal of Radiation Oncology*Biology*Physics* **70**, 272–279 (2008).

213. SCANCO Medical AG vivaCT 80. https://www.scanco.ch/vivact80.html.

214. Veiga, C. *et al.* Toward adaptive radiotherapy for head and neck patients: Feasibility study on using CT-to-CBCT deformable registration for "dose of the day" calculations. *Medical Physics* **41**, 031703 (2014).

215. Tattenberg, S. *et al.* Proton range uncertainty reduction benefits for skull base tumors in terms of normal tissue complication probability (NTCP) and healthy tissue doses. *Medical Physics* **48**, 5356–5366 (2021).

216. Dsilva, A., Avlas, S., Rhone, N., Itan, M. & Munitz, A. A Mouse Model for Eosinophilic Esophagitis (EoE). *Current Protocols* **4**, (2024).

217. Patel, D., Matin, A. & Jaiyeola, D. S1937 Development of Eosinophilic Esophagitis in a Patient With Radiation-Induced Esophageal Strictures: A Case Report. *Official journal of the American College of Gastroenterology | ACG* **115**, S1008 (2020).

218. Bayudan, A. M. & Singh, A. S2050 Eosinophilic Esophagitis: An Unusual Cause of Dysphagia After Radiation Therapy. *Official journal of the American College of Gastroenterology | ACG* **116**, S888 (2021).

219. Laky, K. & Frischmeyer-Guerrerio, P. A. Development and dysfunction of structural cells in eosinophilic esophagitis. *Journal of Allergy and Clinical Immunology* **153**, 1485–1499 (2024).

220. Baskar, R., Lee, K. A., Yeo, R. & Yeoh, K.-W. Cancer and Radiation Therapy: Current Advances and Future Directions. *Int. J. Med. Sci.* **9**, 193–199 (2012).

221. Chatterjee, A., Alpen, E. L., Tobias, C. A., Llacer, J. & Alonso, J. High energy beams of radioactive nuclei and their biomedical applications. *International Journal of Radiation Oncology*Biology*Physics* **7**, 503–507 (1981).

222. Altini, M. *et al.* Assessment of Cancer Care Costs in Disease-Specific Cancer Care Pathways. *IJERPH* **17**, 4765 (2020).

223. Chen, S. *et al.* Estimates and Projections of the Global Economic Cost of 29 Cancers in 204 Countries and Territories From 2020 to 2050. *JAMA Oncol* **9**, 465 (2023).

224. Peeters, A. *et al.* How costly is particle therapy? Cost analysis of external beam radiotherapy with carbon-ions, protons and photons. *Radiotherapy and Oncology* **95**, 45–53 (2010).

225. Bin Sumaida, A., Shanbhag, N. M., AlKaabi, K. & Balaraj, K. Cost-Effectiveness of Carbon Ion Radiotherapy in Oncology: A Systematic Review. *Cureus* https://doi.org/10.7759/cureus.84008 (2025) doi:10.7759/cureus.84008.

226. Kwon, Y.-S., Nguyen, P. A., Dao, H. Y., Jang, H. & Kim, S. Advantages of single high-dose radiation therapy compared with conventional fractionated radiation therapy in overcoming radioresistance. *International Journal of Radiation Biology* **101**, 44–55 (2025).

227. Volz, L. *et al.* Opportunities and challenges of upright patient positioning in radiotherapy. *Phys. Med. Biol.* **69**, 18TR02 (2024).

228. Huang, Q. *et al.* Comparison of the efficacy and toxicity of postoperative proton versus carbon ion radiotherapy for head and neck cancers. *Ann Transl Med* **10**, 1197–1197 (2022).

229. Jang, J. Y. *et al.* A meta-analysis comparing efficacy and safety between proton beam therapy versus carbon ion radiotherapy. *Cancer Medicine* **13**, e7023 (2024).

230. Khasanov, S., Su, Y., Safarov, A., Tedila, H. M. & Mamatkulov, O. Major radioactive ion beam facilities: a brief global overview. *Eur. Phys. J. Plus* **140**, 638 (2025).

231. Yamaya, T., Kang, H. G., Hamato, A., Toramatsu, C. & Inaniwa, T. Prospects for applying radioactive ion beams in particle therapy. *Eur. Phys. J. Plus* **140**, 203 (2025).

232. Kraan, A. C. *et al.* In-beam PET treatment monitoring of carbon therapy patients: Results of a clinical trial at CNAO. *Physica Medica* **125**, 104493 (2024).

233. Weber, U. A., Scifoni, E. & Durante, M. FLASH radiotherapy with carbon ion beams. *Medical Physics* **49**, 1974–1992 (2022).

234. Tinganelli, W. *et al.* Ultra-High Dose Rate (FLASH) Carbon Ion Irradiation: Dosimetry and First Cell Experiments. *International Journal of Radiation Oncology*Biology*Physics* **112**, 1012–1022 (2022).

235. Pogue, B. W., Thomas, W. S., Tavakkoli, A. D., Jarvis, L. A. & Hoopes, P. J. Major contributors to FLASH sparing efficacy emerge from murine skin studies: dose rate, total dose per fraction, anesthesia and oxygenation. *Front. Oncol.* **14**, 1414584 (2024).

236. Popple, R. A., Ove, R. & Shen, S. Tumor control probability for selective boosting of hypoxic subvolumes, including the effect of reoxygenation. *International Journal of Radiation Oncology*Biology*Physics* **54**, 921–927 (2002).

237. Dolezel, M. *et al.* Hypoxia Region Dose Escalation in Head and Neck Cancer: Dosimetric Analysis and Acute Toxicity. *International Journal of Radiation Oncology*Biology*Physics* **123**, e331–e332 (2025).

Appendix

List of contributions

This thesis was part of a wide collaboration between two different institutions, GSI and the Ludwig-Maximilians-Universität München (LMU). The group of Prof. Parodi from LMU created the SIRMIO PET and consisted of Peter Thirolf, Munetaka Nitta, Giulio Lovatti, Francesco Evangelista, Angelica Noto, Gabriele Corbetta, which were present during the BARB biological experimental campaigns. The construction of the SIRMIO PET scanner was partly supported by the ERC Consolidator Grant 725539 SIRMIO to Prof. Parodi.

At GSI, the research was conducted in collaboration with the FRS-SFRS Experiments Department, with the project involving also collaborations with APPA and NUSTAR in the context of the FAIR Phase-0 Research Program (experiments B-22-00046-Durante at SIS18/FRS/Cave-M). The FRS group comprehended Christoph Scheidenberger, Emma Haettner, Sivaji Purushothaman, Daria Kostyleva, Benno Franczak, Hans Geissel.

In the Biophysics Department, Prof. Durante received the European Research Council (ERC) Advanced Grant 883425 for the BARB experiments. The collaborators in the department comprehended Walter Tinganelli, Olga Sokol, Reema Chowdhury, Julius Oppermann, Collin Werkheiser, Beatrice Pretto, Malte Benje, Leonie Hartig, Martina Quartieri, Anggraeini Puspitasari-Kokko, Elizabeth Van der Bijl (Clinical Radiobiology group), Charlot Vandervoorde (Space Radiobiology group), Uli Weber, Daria Boscolo, Martina Moglioni, Andreas Bückner (Particle Therapy Physics group), Christoph Schuy, Tim Wagner (Space Radiation Physics group), Christian Graeff, Lennart Volz, Maria Chiara Martire (Medical Physics group), Alexander Helm (Immune System and Tissue Radiobiology group) and Konrad Lehmann.

More details about the contributions are found in the acknowledgments of the publications listed in the next page.

Regarding specific students' contributions to this thesis, Beatrice Pretto prepared the histological panel in Figure 74. Collin Werkheiser helped in the histological preparations necessary for Figure 78 and tested different antibodies for the immunohistochemistry part, of which Figure 82 is an example.

Related conferences and publications

Conferences

10/2025 First online image-guided treatment of a murine tumour with radioactive ion beams. T. Vitacchio on behalf of the BARB collaboration. *MML Workshop, Karslruhe (Germany); invited speaker.*

09/2025 First preclinical tumour treatment with radioactive ion beams. T. Vitacchio on behalf of the BARB collaboration. *RRS Conference 2025, Puerto Rico (United States of America); poster.*

04/2025 First treatment of a mouse tumour with radioactive ion beams. T. Vitacchio on behalf of the BARB collaboration. *GSI Center Evaluation, Darmstadt, Germany; poster.*

10/2024 The BARB project: first treatment of an animal tumour with radioactive ion beams. T. Vitacchio on behalf of the BARB collaboration. *XXY Convegno Nazionale SIRR, Pavia (Italy); talk.*

10/2023 Preclinical studies with radioactive ion beams: the BARB project. T. Vitacchio, O. Sokol, D. Boscolo, A. Puspitasari, J. Oppermann, W. Tinganelli, M. Durante. *1st INSIGHTS meeting on new horizons in radiation therapy, Pisa, (Italy); invited speaker.*

Relevant publications

2026 Radioactive ion beam range adaptation in mouse tumours using in-beam PET. M. Moglioni*, T. Vitacchio*, F. Evangelista*, M. Nitta*, D. Boscolo, G. Lovatti, O. Sokol, E. Haettner, S. Purushothaman, W. Tinganelli, C. Graeff, U. Weber, C. Schuy, A. Bückner, G. Corbetta, L. Doyle, L. Volz, M. C. Martire, T. Wagner, A. Helm, C. Werkheiser, D. Kostyleva, R. Prajapat, S. K. Singh, E. Rocco, J. Bortfeldt, P. G. Thirolf, C. Scheidenberger, K. Parodi & M. Durante (*shared first authorship). *Communications Medicine,* https://doi.org/10.1038/s43856-026-01786-1

2025 Image-guided treatment of mouse tumours with radioactive ion beams. D. Boscolo*, G. Lovatti*, O. Sokol*, T. Vitacchio, M. Moglioni, F. Evangelista, E. Haettner, W. Tinganelli, C. Graeff, U. Weber, C. Schuy, M. Nitta, D. Kostyleva, S. Purushothaman, P. G. Thirolf, A. Bückner, J. Bortfeldt, C. Scheidenberger, K. Parodi & M. Durante (*shared first authorship). *Nature Physics,* https://doi.org/10.1038/s41567-025-02993-8

Curriculum Vitae

Personal Data

Name	Tamara Vitacchio, M. Sc.
Nationality	Italian

Education and Work Experience

2010-2015	High School in Applied Sciences
2015-2018	Bachelor's studies in Biology at University of Padova, Italy
28.09.2018	Bachelor's Degree in Biology, University of Padova, Italy. Supervisor: Prof. Dr. Luisa Dalla Valle, Department of Developmental Biology and Cytology
2018-2020	Master's studies in Evolutionary Biology, University of Padova, Italy
24.09.2020	Master's Degree in Evolutionary Biology, University of Padova, Italy. Supervisor: Prof. Dr. Nicoletta La Rocca, Department of Vegetal Physiology
Since 03.2022	Ph.D studies in Biology at GSI Helmholtzzentrum für Schwerionenforschung, Darmstadt, and Technische Universität Darmstadt. Supervisor: Prof. Dr. Marco Durante, Biophysics Department

Acknowledgements

The first and foremost acknowledgments of this thesis should go to Walter, group leader of the Clinical Radiobiology group at GSI. Or actually, to Francesco Tommasino, which pointed me out to Walter!

Thank you, Walter, for "adopting" me in the group as your second PhD student, even if it took more than one year for finally meeting in person and having me arriving at GSI (those COVID times…). Thank you for believing that I could make it, and for having given me an opportunity that changed my life.

Of course, none of this would have been possible without Marco! Thank you for trusting me in taking part in such an ambitious and complex, but also very exciting, project. Your insights, knowledge, and your availability for discussing advices and new ideas were absolutely precious. Thank you also for letting me go to the RRS Conference in Puerto Rico! And no, I never overfed the mice on purpose, I swear!

I would also like to acknowledge Prof. Cardoso for her help, support and advices during the PhD committee meetings: it's always helpful to have somebody from out of your topic to help you consider things from a different perspective.

The next acknowledgements go to my amazing group. Thanks to Martina Q., my *senpai*, who showed me the wonders of the Annex lab and introducing me to the world of mammalian cells culture. We had a lot of laughs and funny moments in the lab and outside, and I think you're one of the best lab mates one could ever wish to have! Thanks to Julius, for the additional laughs and all the help with the experiments. Your practical knowledge was very, very necessary during the lab work times! Thanks to Reni, for guiding me through my first mice experiments: it was not an easy task, but you made it easier in stressful moments. Thanks to Reema, for all the chocolate and the post-its with cute motivational support messages, for the company and help during the experiments, especially on those cold hibernation weekend days! Thanks to Leonie, for all the shared moments and the fact that I didn't traumatise you on your first day in our group (you know to what I'm referring to); I wish you the best for your PhD, even if I warned you to not start one! Thanks to Malte for matching my weirdness (maybe you're even beating me at this point) and for being my medieval markets buddy, the one I can always trust for joining such crazy adventures!

Thanks to all of our students, which even if when they stayed for a short period of time, where nice to get to know and collaborate with: Amèlia, Nivida, Nicola, Elizabeth, Dennis, Milkias, Jian Xian. A special thanks goes to Beatrice, for her help during the second beamtime: your presence was calming and supportive in that crazy moment, and your help was fundamental! Another special mention goes to Collin, I would have absolutely never managed to deal with the histological analysis of the second beamtime at that speed-of-light pace without you. I was so glad to meet you and discover how much things we have in common, in between panic and funny moments!

But the most special mention in my group goes to Olga. Let's be honest, I would have never got at the end of the PhD without you. First of all, because of all the physics involved (there's a reason why I choose biology), that you so kindly kept explaining me for four years. Your scientific spirit, dedication, patience, and all the moral support you provided every single day made you the best possible supervisor a student can wish for. I can never thank you enough for everything, and if possible, I wish I could be for any trainee I will

meet in my future what you have been for me. Thank you also for listening to all my weird chatting during the long hours at the CT, the small presents and the daily cat content!

Another important mention goes to Dr. Lotte and her assistants: her work is inspiring, and I believe her way of teaching is the perfect one for future animal experimenters.

More GSI acknowledgments (we're so many!): to Daria, for the additional help regarding the physics part and all the absurd experimental plans with animals (see Megachonker). To Konrad, for his invaluable help and knowledge with the animals, and for the patient demonstrated with all the amendment requests, but also the nice chats about books. To Charlotte, Alex, Claudia, Christoph, for all the help and support and the many little things necessary for organising such large experiments.

Thanks to all the international friends met at GSI in these years, which made it like a fantastic place to share memories and experiences: Warisara, Olivia, Leon, Andreas, Peter, Marie, Tabea, Anastasia, Réka, Ha, and of course all the others that have been already mentioned. A special thanks to Francesca and Laura, for all of our shared passions and interests, the chats about deep and important topics and the common vision we share. Your presence at GSI and outside was always deeply supportive and made me feel understood.

Un grazie di cuore a tutti gli altri italiani lontani da casa, senza il cui supporto questi anni sarebbero stati sicuramente più difficili (e noiosi!): a Gianmarco e Nicolò per le merende pomeridiane, quei piccoli momenti passati in caffetteria che sapevano sempre sollevarmi dallo stress del lavoro (e anche a Vanessa, per i momenti passati assieme fuori dal GSI). A Martina M., Luca e Virginia, per le interminabili risate, le figuracce e le foto imbarazzanti, ma anche perché condividiamo ognuno qualcosa di speciale. A Niccolò, Gaia, Emiliana, Giuseppe, Chiara, Cristina, Valerio, per i momenti di disagio ma anche le belle avventure condivise assieme. Quando in futuro ripenserò a questo periodo della mia vita, sarà con l'affetto di chi sa di aver trovato una comunità in cui sentirsi al sicuro e apprezzati. A Carmine, per essere sempre parte della famiglia italiana all'estero e per le cene tra racconti di viaggi e delle missioni ESA.

Un grazie enorme, poi, alla mia famiglia, che mi ha sempre supportata in tutte le mie scelte, siano esse facili o difficili. Niente sarà mai come tornare a casa sapendo di essere accolti a bracca aperte (o dai miagolii impazienti di Loki!). Grazie per la pazienza, l'affetto e la naturale voglia di imparare che ci contraddistingue, ma anche per la forza che avete sempre dimostrato e che mi avete trasmesso.

Un ringraziamento speciale va a tutti gli amici di casa, che nonostante la distanza ci sono sempre stati per me: a Chicca, per essere mia amica dal primo giorno di asilo e per non esserci mai perse in tutti questi anni. Ad Ari e Sofi, per la loro dolcezza e lealtà. A Giulia e Martina, Francesco e Alessandro, perché siamo ancora uniti nonostante le nostre strade ora siano completamente diverse. A Jessica, per il supporto e l'ascolto. A Diletta, per la sua determinazione e il suo essere incredibilmente tosta. Ad Alice, Thomas, Jack, Sara, per essere entrati nella mia vita in un momento difficile ma creando qualcosa di meraviglioso. Ad Arianna, perché spero di diventare come te un giorno, e per essere una grande fonte di ispirazione. A Sofia, compare di vita in Germania. Al gruppo di Biologia Evoluzionistica, che sono stati compagni di disavventure del dottorato a distanza: Matteo B., Matteo S., Luca, Andrea.

A Federico: perché mi sopporti, mi supporti, e senza di te la vita qui in Germania sarebbe stata decisamente diversa – in peggio. Spero di essere stata per te tutto quello che tu sei stato per me in questi anni, ogni giorno. Grazie per ogni momento, per assecondarmi nelle mie follie, ma anche per darmi sempre un punto di vista differente, per la tua pazienza e per quello che possiamo creare assieme.